

Development of a Novel Bipedal Robot Inspired from Human Musculoskeletal Biomechanics

A thesis submitted to The University of Manchester for the degree of
Doctor of Philosophy
in the Faculty of Science and Engineering

2018

Kunyang Wang

School of Mechanical, Aerospace and Civil Engineering

Contents

Abstract	19
Declaration	21
Copyright Statement	22
Acknowledgments	23
Publications	24
Awards	25
Chapter 1 Introduction	26
1.1 Background and Motivation.....	26
1.2 Methodology and Scope.....	28
1.3 Aims and Objectives	30
1.4 Contributions to Knowledge	31
1.5 Thesis Layout.....	32
Chapter 2 Literature Review	34
2.1 Control Methods of Bipedal Robots	34
2.1.1 Precise Control Scheme	34

2.1.2	Natural Dynamics Scheme.....	37
2.2	Bipedal Robots Emulate Human Behaviours.....	39
2.2.1	Bipedal Locomotion	39
2.2.2	Whole-body Activities	49
2.3	Bipedal Robots to Investigate Human Biology.....	54
2.3.1	Using Bipedal Robots to Study Biomechanics	54
2.3.2	Using Bipedal Robots to Study Neuroscience	70
2.4	Conclusion	76
Chapter 3 Biomechanics of Human Musculoskeletal System		80
3.1	Data Source	81
3.2	Terminology and Kinematics	82
3.3	Segmentation.....	86
3.4	Body Segment Properties.....	91
3.5	Joint Parameters	92
3.5.1	Knee joint.....	97
3.5.2	Ankle joint	97
3.6	Muscle Path.....	100
3.7	Conclusions	104
Chapter 4 Development of the Physical Prototype		107
4.1	Mechanical Design of the Skeletal Structure	108
4.1.1	Foot	108

4.1.2	Leg	109
4.1.3	Trunk.....	112
4.1.4	Arm	114
4.1.5	Joints	114
4.1.6	Assembly	121
4.1.7	Scale.....	123
4.2	3D Printing of the skeletal structure	123
4.2.1	3D Metal Printing	123
4.2.2	General Guidelines of Designing 3D Metal Printed Parts	126
4.2.3	Limitations	128
4.2.4	Problems Occurred in the Printing Process	128
4.2.5	Redesign of the Model.....	131
4.2.6	Material and the Printed Skeleton.....	132
4.2.7	Shoes	134
4.3	Design of a Whole-Body Muscular System.....	135
4.3.1	Background.....	135
4.3.2	Fabrication	137
4.3.3	Material properties of the muscle-tendon unit.....	139
4.3.4	Selecting principle	141
4.4	Integration	142
4.5	Conclusions.....	142

Chapter 5 Simulations in Adams 146

5.1	Development of the Model in Adams	147
5.1.1	Mechanical Body	147

5.1.2	Joints	148
5.1.3	Ground Contact.....	148
5.1.4	Material Properties.....	150
5.1.5	Artificial Muscle	150
5.1.6	Variables	151
5.2	Simulation	152
5.2.1	Model Validation	152
5.2.2	Kinematics	154
5.2.3	Kinetics	160
5.2.4	Cost of Transportation (CoT)	163
5.3	Design of Experiment (DOE)	164
5.3.1	Background.....	164
5.3.2	Parameters and Objective	165
5.3.3	Subtalar Angle	165
5.3.4	Talocrural Angle	168
5.3.5	Correlation for Stable Walking.....	168
5.3.6	Best combination	171
5.4	Conclusions.....	171

Chapter 6 Physical Tests 175

6.1	Variables	176
6.2	Experimental Installation	177
6.2.1	Motion Capture System	177
6.2.2	Force Plates.....	180
6.2.3	The Ramp.....	182

6.3	Preliminary Test.....	185
6.3.1	Launching	185
6.3.2	Roll Motion.....	186
6.3.3	Stopping	187
6.3.4	Falling	188
6.3.5	Frictions	189
6.4	Repeated Test.....	190
6.4.1	Repeated Tests for Passive Walking.....	190
6.4.2	Gait cycle	191
6.4.3	CoM	191
6.4.4	Motion of the Ankle Joint.....	193
6.4.5	Ground Reaction Forces	195
6.4.6	Muscle Settings.....	196
6.5	Functional Analysis.....	198
6.5.1	Uneven terrain.....	198
6.5.2	Pavement friction.....	199
6.5.3	Muscle stiffness	201
6.5.4	Joint axis	201
6.5.5	Foot shape	205
6.6	Conclusion	205

Chapter 7 Conclusions and Future Work 208

7.1	Conclusions.....	208
7.2	Future Work	213

Bibliography 216

Word count: 60609

List of Figures

1.1	Concept of the humanoid research platform.	29
2.1	(a) WL-5, (b) WABOT-I, (c) WABIAN-2, (d) WL-16R. [41, 44]	40
2.2	(a) P2, (b) P3, (c) ASIMO 2000, (d) ASIMO 2004. [52].....	41
2.3	(a) HRP-1, (b) HRP-2 [61], (c) HRP-3, (d) HRP-4 [62], (e) HRP-2M [63].....	42
2.4	H6 (left) and H7 (right) [76].	43
2.5	(a) i-foot (left) [82], (b) Wire-driven robot [83], (c) Running robot [84].....	44
2.6	(a) HUBO [86], (b) Albert HUBO [87], (c) HUBO FX-1 [88].....	45
2.7	Johnnie (left) [94] and LOLA (right) [95].	46
2.8	RABBIT (left) [104] and MABLE (right) [105].....	47
2.9	(a) BHR-01[107], (b) BHR-2 [108], (c) BART-TH, (d) LISA [109], (e) BIP [110], (f) Rh-1 [111], (g) Spring Flamingo, (h) M2 [112].....	48
2.10	SDR-3X (left) [124] and QRIO (right).	50
2.11	NAO [125].	51
2.12	HRP-4C [130].	51
2.13	PETMAN (left) [135] and Atlas (right) [136].....	52
2.14	(a) REEM-C [138], (b) KHR-1 [139], (c) RoboNova [140], (d) HOAP [141, 142], (e) morph3 [143, 144], (f) PINO [145].....	54
2.15	McGeer kneeless (left) and kneed (right) passive dynamic walking robot [149, 150].	55

2.16	Imitation of McGeer developed by Nagoya Institute of Technology [152].....	56
2.17	Passive dynamic walking robot developed by MIT [153].	57
2.18	Passive dynamic walking robot developed by Cornell University [148].....	58
2.19	Passive dynamic walking robot (left) and ankle details (right) developed by Keio University [155].	59
2.20	(a) Stappo, (b) Bob, (c) Baps, (d) Mike, (e) Max, (f) Denise. [158, 161, 169].....	61
2.21	The Cornell biped [170].	62
2.22	A simple passive dynamic robot (left) and Toddler (right) [171].	63
2.23	Cornell Ranger [176].....	64
2.24	Lucy [177].	65
2.25	(a) Kenta, (b) Kotaro, (c) Kojiro, (d) Kenshiro, (e) Kengoro [186, 187].....	66
2.26	JenaWalker II (left) and BioBiped (right) [201].	68
2.27	Athlete Robot [210].....	70
2.28	DB (left) [214] and CB (right) [228].	72
2.29	DB playing air hockey against a human opponent [222, 223].....	72
2.30	RunBot [7].....	73
2.31	iCub [248].	75
2.32	Pneuborn-7II [253].....	76
3.1	Whole body model based on VHP, including (a) skin, (b) skeleton and (c) muscle.	82
3.2	Skeleton model in NX imported from Rhino.	83
3.3	Frontal (Coronal), sagittal, and transverse (horizontal) planes in the human body.	84

3.4	Adjustments to Zatsiorsky-Seluyanov's segment inertia parameters. The adjusted distances are shown on the right of the shaded area [267].	88
3.5	Various body segments in NX including (a) head and neck, (b) upper, (c) middle and (d) lower trunk, (e) upper arm, (f) forearm, (g) thigh, (h) shank, (i) foot.	89
3.6	(a) Front and (b) trimetric view of the coordinate system. Skin is hidden. XC, YC, and ZC represented the global coordinate system; and the red colour X, Y, Z represented local coordinate system.	90
3.7	The 3D whole-body model with 13 segments and 12 connecting joints used for calculating joint parameters. A marker cluster mounted on a plastic plate was attached to each body segment (52 markers in total). The global X-axis is the direction of progression, the Y-axis is vertical, and the Z-axis is to the right [270].	93
3.8	Joint parameters (a) in the ankle and (b) in the whole body including joint centres (hidden in the bones) and joint axes of rotation (blue lines).	94
3.9	Knee joint. (a) Two-joint structure. (b) Joint axis in coronal plane (front view). The axis rises up at a 20.1° angle from the horizontal medial-lateral axis in the frontal plane. (c) Joint axis in transverse plane (top view). The axis is oriented 7.1° with the horizontal medial-lateral axis of the thigh.	96
3.10	Typical motions in the ankle.	98
3.11	Talocrural joint axis. (a) Coronal plane (front view). The axis rises up at a 34.4° angle from the horizontal medial-lateral axis in the frontal plane. (b) Transverse plane (top view). The axis is oriented 13.6° with the horizontal medial-lateral axis of the foot.	99
3.12	Subtalar joint axis. (a) Sagittal plane (medial view). The axis rises up at a 21.4° angle from the horizontal anterior-posterior axis. (b) Transverse plane (top view). The axis is oriented 12.0° medial to the midline of the foot.	100
3.13	The process of generating muscle path. Red lines were the surface profile of the cross-section and blue curve was the muscle path.	101

3.14	(a) Front, (b) Right and (c) Back view of the left part of simplified whole-body muscular system, blue curves representing the muscle paths.	103
3.15	Front (left) and back (right) view of the muscle paths in the left shank.	104
3.16	Front (left) and back (right) view of the muscle paths in the left thigh.	105
4.1	Left foot design in NX.	109
4.2	Left thigh design in NX including (a) main and (b) extra components.	110
4.3	(a) Front, (b) Left and (c) Isometric view of the assembly of left thigh.	110
4.4	(a) Front and (b) Isometric view of left shank.	111
4.5	Assembly of (a) left shank and (b) extra components.....	111
4.6	(a) Front, (b) Left and (c) Isometric view of lower trunk.	113
4.7	(a) Front, (b) Back and (c) Isometric view of middle trunk.....	113
4.8	(a) Front, (b) Left and (c) Isometric view of upper trunk.	113
4.9	Left forearm in NX.....	114
4.10	(a) Main body, (b) Extra weights and (c) Assmbly of left upper arm.....	115
4.11	Configuration of the robot's left ankle. (a) KSTM-05; (b) KGLM-05; (c) The subtalar axis and talocrural axis; (d) Joint angle adjusting mechanism. Various angles of rotating axis can be obtained through four arc columns and the angle between the subtalar and talocrural axis.	116
4.12	Configuration of the robotic left knee. (a) Plain and spherical bearing in knee joint. (b) Joint angle adjusting mechanism.	118
4.13	Configuration of the left hip. (a) angle joint; (b) connection between pelvis and thigh.	119
4.14	Configuration of the left shoulder. (a) angle joint; (b) connections of shoulder joint.	120
4.15	Configuration of the left elbow. (a) clevis joint; (b) connections of elbow.....	120

4.16 Configuration of the robotic spine. (a) connections between the lower and the middle trunk; (b) connections between the upper and the middle trunk (c) simplified robotic spine.....	121
4.17 (a) Front, (b) Back and (c) Isometric view of the assembled robot in NX.	121
4.18 3D printed (a) skeleton-like shank and (b) muscle guide of the robot.....	123
4.19 Schematic diagram of the EOS M280 system.....	125
4.20 Fracture (red circle) between the part and the support during printing.....	128
4.21 Distortion and fracture in the part during printing.	129
4.22 Failure caused by collision between the recoater and the parts.	130
4.23 Adjustment of the lower trunk. (a) original design and (b) final design.....	130
4.24 Adjustment of the left shank. (a) original design and (b) final design.....	131
4.25 Adjustment of the left foot. (a) original design and (b) final design.....	132
4.26 3D printed components of the bipedal robot. (top left) and (top right) showed the assembly of the lower body, (bottom left) and (bottom right) showed the assembly of the upper body.....	133
4.27 The design of shoes. (a) isometric view and (b) functional surfaces at bottom.....	134
4.28 Top (left) and bottom (right) view of the 3D printed shoes.....	135
4.29 (a) Fabricating system for muscle-tendon unit and (b) coiled fishing line.	138
4.30 Artificial muscle tendon units using nylon 6 monofilament fishing line. From top to bottom are a non-twist 0.47-mm-diameter fibre, coiled fibre of 0.47-mm-diameter fibre, a non-twist 1.5-mm-diameter fibre and coiled fibre of 1.5-mm-diameter fibre.....	138
4.31 Material property testing of a coiled fibre using a tensile/compression testing machine.	139

4.32	(a) Front, (b) Back and (c) Isometric view of the assembled bio-inspired bipedal robot. Grey solid was the skeletal structure, and white lines represented the artificial muscle tendon units.	143
5.1	Mechanical body of the lower part in Adams.	147
5.2	The ramp in Adams.	148
5.3	Four solutions replacing muscle-tendon unit. (a) Force vector located in the origin and insertion of Tibialis Anterior muscle. (b) Pulley systems. (c) Flexible volumes such as one corresponding to Tibialis Anterior muscle. (d) Springs implemented in the ankle joint.....	151
5.4	CoM of the robot during passive walking in Adams simulation. The global X-axis is to the right (top), the Y-axis is in the direction of progression (middle) and the Z-axis is vertical (bottom).	155
5.5	Velocity of the robot during passive walking in Adams simulation. Left part is the velocity of stable walking from launching to 10 s and right part is the velocity of last few seconds before falling.....	156
5.6	The angle motion of the left (top) and right (middle) talocrural joint during walking in simulation. The bottom is the angle of two joints in 5 gait cycles starting from heel strike of the right foot. Zero value in the talocrural joint means that the robot is in upright position. Positive value means Dorsiflexion....	157
5.7	The angle motion of the left (top) and right (middle) subtalar joint during walking in simulation. The bottom is the angle of two joints in 5 gait cycles starting from heel strike of the right foot. Zero value in the talocrural joint means that the robot is in upright position. Positive value means Eversion.	159
5.8	The angle motion of the right talocrural and subtalar joint during 3 walking gaits starting from heel strike of right foot in simulation. Zero value in the talocrural joint means that the robot is in upright position. Positive value means Eversion and Dorsiflexion.	160
5.9	Ground reaction forces including medial-lateral (top), horizontal (middle), and vertical (bottom) forces in simulation. Key impulses and peaks are labelled.....	161

5.10	Spring forces in the ankle during 2 stable walking gaits including the anterior-posterior (top) and the medial-lateral (bottom) in simulation. Negative value means tension.	163
5.11	Typical plots of the distance travelled as a function of the subtalar angle for passive walking of the robot in simulation.	166
5.12	Typical plots of the distance travelled as a function of the talocrural angle for passive walking of the robot in simulation.	167
5.13	A sketch of the dependency of the distance travelled as a function of ankle joint orientation including the talocrural and subtalar angle for passive walking of the robot in simulation. The left and right face of the are equal to 5.12 and 5.11, respectively.	169
5.14	Distance travelled as a function of the talocrural and subtalar angle for passive walking of the robot in simulation. The best configuration is 16° in the talocrural joint and 23° in the subtalar joint.....	170
5.15	CoM of the robot during passive walking with 16° talocrural angle and 23° subtalar angle.	172
5.16	Spring forces in the ankle during 2 stable walking gaits including the anterior-posterior (top) and the medial-lateral (bottom). The talocrural angle is 16° and subtalar angle is 23° . Negative value means tension.	173
6.1	The Vicon System used to record 3D motion of the robot.	178
6.2	The biped robot attached with reflective markers on the landmark.....	178
6.3	A force-plate array containing three kistler force plates mounted on the ground.	180
6.4	NordicTrack T22.5 treadmill for testing (top) and swing caused by the gap between the belt and the base of the treadmill (bottom).	182
6.5	(a) New design of the ramp including (b) angle adjustment plates, (c) vices and (d) hinges.....	183

6.6	Special design of the ramp for measuring GRFs.	184
6.7	Roll motion of the robot during passive walking on the ramp.....	186
6.8	Lubrication of the right shank using Teflon tape and Teflon tubes.	189
6.9	Walking test of the robot. (A) Centre of mass in the progression direction and right leg angle time trajectories in terms of pitch, roll and yaw motion. (B) State space plot of the limit cycles in the roll axis (frontal plane). Red dot is the initial conditions (around 0.07 rad and 0 rad/s) and plus sign is the end state. (C) Walking sequence of one step.	190
6.10	CoM of the robot during passive walking. The global X-axis is to the right (top), the Y-axis is in the direction of progression (middle) and the Z-axis is vertical (bottom).....	192
6.11	Rotation angle of talocrural joint (top) and subtalar joint (bottom) in the ankle during robot walking. Zero value in the talocrural joint means that the robot is in upright position, positive and negative angle represents that it inclines forward (dorsiflexion) and backward (plantarflexion) in sagittal plane respectively. Zero value in the subtalar joint means that the robot is in upright position, positive and negative angle represents that it tilts laterally (eversion) and medially (inversion) in coronal plane respectively.	194
6.12	Ground reaction forces during one passive walking gait including medial-lateral (top), horizontal (middle), and vertical (bottom) forces in the physical test.	196
6.13	Extensor digitorum longus muscle (a) in human body and (b) in the robot.	197
6.14	Robot walking experiments on 1.4-m-long uneven terrains of MTD 2.0 mm and 1.5 mm. (A) Centre of mass in the progression direction and right leg angle time trajectories in terms of pitch, roll and yaw motion. (B) State space plot of the limit cycles in the roll axis (frontal plane). Red dot is the initial conditions (0.06-0.07 rad and 0 rad/s) and plus sign is the end state.....	199
6.15	Robot walking experiments on low and high friction pavement. (A) Centre of mass in the progression direction and right leg angle time trajectories in terms	

of pitch, roll and yaw motion. (B) State space plot of the limit cycles in the roll axis (frontal plane). Red dot is the initial conditions (0.07-0.08 rad and 0 rad/s) and plus sign is the end state. Walking sequence on (C) low and (D) high friction pavement.	200
6.16 Robot walking experiments configured with three different Gastrocnemius (GAS) musculotendon units in terms of stiffness. (A) Centre of mass in the progression direction and right leg angle time trajectories in terms of pitch, roll and yaw motion. (B) State space plot of the limit cycles in the roll axis (frontal plane). Red dot is the initial conditions (0.08-0.09 rad and 0 rad/s) and plus sign is the end state. Sequence of (C) the Soft-GAS walking and (D) the Hard-GAS walking.	202
6.17 Robot walking experiments with parallel ankle and oblique ankle. (A) Centre of mass in the progression direction and right leg angle time trajectories in terms of pitch, roll and yaw motion. (B) State space plot of the limit cycles in the roll axis (frontal plane). Red dot is the initial conditions (about 0.05 rad and 0 rad/s) and plus sign is the end state.	203
6.18 Robot walking experiments with arc-shaped foot and round foot. (A) Centre of mass in the progression direction and right leg angle time trajectories in terms of pitch, roll and yaw motion. (B) State space plot of the limit cycles in the roll axis (frontal plane). Red dot is the initial conditions (0.07-0.08 rad and 0 rad/s) and plus sign is the end state. (C) Hobbled sequence of round foot. (D) Normal walking of arc-shaped foot.	204

List of Tables

3.1	Estimated segments defined between the respective start points and end points. ...	88
3.2	Local coordinate system of each segment relative to global coordinate system.....	91
3.3	Body segment properties of each major body segment.	92
3.4	Position and orientation of each joint relative to the local coordinate system. Elbow, shoulder, hip, knee, ankle joint and all the limbs are the left of the body. 1st of the joint axis of ankle joint was subtalar axis and 2nd was talocrural.	95
3.5	68 main functional muscle groups including 6 in the head and neck, 20 in the trunk, 10 in two arms, 18 in two thighs and 14 in two shanks. Triceps muscle, as well as Hamstrings and Gastrocnemius muscles was considered as two muscle volumes respectively.....	102
4.1	The oblique angle of the talocrural joint axis.	117
4.2	The oblique angle of the subtalar joint axis.	117
4.3	The oblique angle of the knee joint axis.	119
4.4	Body segment properties of the original robot in the local coordinate system.....	122
4.5	Body segment properties of the scaled robot in the local coordinate system.	122
4.6	Technical data of M280.	124
4.7	Material properties of multi-material composites (VisiJet CR-WT + VisiJet CE-BK)	136
4.8	Material properties of non-annealing coiled fibres twisted from 1.2-mm- diameter fibre under different loads.....	140

4.9	Material properties of non-annealing coiled fibres twisted from 1.5-mm-diameter fibre under different loads.....	140
4.10	Material properties of annealing coiled fibres twisted from 1.2-mm-diameter and 1.5-mm-diameter fibres under different loads.....	141
4.11	Muscle changes during human walking.....	141
5.1	Recommended value of contact parameters in Adams in which k is stiffness, c is the damping, e is exponent, d is penetration depth, vs and vd are static and dynamic friction velocity respectively. The unit is System International (SI) except that the unit of length is millimetre.....	149
5.2	Parameters of initial conditions for simulation.	153
6.1	Definition and position of the markers placed on the robot.....	179
6.2	Technical data of Kistler force plate.	181

Abstract

The University of Manchester

Kunyang Wang

Doctor of Philosophy

Development of a Novel Bipedal Robot Inspired from Human Musculoskeletal Biomechanics

September 2018

Most researchers study biologically inspired bipedal robot by implementing sophisticated control algorithms into a mechanical structure with actuators and stiff or compliant joints, or simplifying robot based on passive dynamics of the body. However, few study focused on the biomechanical view of the musculoskeletal system of human body, namely, the morphological computation of human body. In this thesis, I propose a new approach of developing bipedal robot inspired from human musculoskeletal (MSK) biomechanics.

A three-dimensional (3D) whole-body musculoskeletal model was used as the biological counterpart to inspire the design of the robot. Image processing was used to examine the anatomy, structure and geometry of human MSK system. Reverse engineering was applied to rebuild the 3D musculoskeletal model. With the model, the details of the skeletal and the muscular system were quantified and modified. The anthropometric data, the mechanical properties and muscle arrangements were analysed in the model. Key kinematic parameters were obtained from 3D motion capture system and inverse dynamics technique.

Based on analysis of the body structure and the mechanics of human MSK, Computer-aid design (CAD) and 3D printing technique were adopted to design and manufacture the skeletal body of the robot, assuring the mechanics in accordance with real human body. Human muscles are not isolated from each other, in fact, they are linked by fascia or even connected to the same tendon, e.g., Soleus muscle joins with Gastrocnemius muscles to form Achilles tendon which inserts onto the posterior surface of the heel bone. Therefore, I designed a whole-body muscular system in which the artificial muscle units with similar function are woven into textiles, especially for Soleus and Gastrocnemius because they are the most important muscles during bipedal locomotion.

Computer simulation of passive walking of the robot was conducted in Adams. The kinematic and kinetic data were measured to compare with humans. The effect of the ankle orientation on normal walking was studied using the design of experiment. The best configuration in the ankle is 16° talocrural angle and 23° subtalar angle, where the robot can travel on the ramp up to 4166.2 mm, 17.4 % longer than the distance that the robot can travel with 0° talocrural angle and 0° subtalar angle (parallel to the ground when standing). It can be intuitive thinking that the oblique axis of rotation in the ankle

may facilitate normal walking for biped robots.

Moreover, physical tests getting down a 2.44 *m* ramp were carried out. The robot with 0° talocrural and subtalar angle can passively walk the full length of the ramp in about 95% of launches, whereas inappropriate initial conditions, e.g., slope angle, released roll angle and released velocity, seem to be the primary cause of those launches in which the robot stopped or fell down before reaching the end of the ramp.

Successful walking of the robot validated the feasibility of the new robotic developing philosophy. The presented framework would provide a biomechanics foundation and technical support for the innovative design and manufacture of bio-inspired bipedal walking robot. Furthermore, this paradigm for developing bipedal robot can be also considered as a new approach to develop exoskeletons and prostheses based on human musculoskeletal system.

Declaration

No portion of the work referred to in the thesis has been submitted in support of an application for another degree or qualification of this or any other university or other institute of learning.

Copyright Statement

- i. The author of this thesis (including any appendices and/or schedules to this thesis) owns certain copyright or related rights in it (the “Copyright”) and s/he has given The University of Manchester certain rights to use such Copyright, including for administrative purposes.
- ii. Copies of this thesis, either in full or in extracts and whether in hard or electronic copy, may be made **only** in accordance with the Copyright, Designs and Patents Act 1988 (as amended) and regulations issued under it or, where appropriate, in accordance with licensing agreements which the University has from time to time. This page must form part of any such copies made.
- iii. The ownership of certain Copyright, patents, designs, trademarks and other intellectual property (the “Intellectual Property”) and any reproductions of copyright works in the thesis, for example graphs and tables (“Reproductions”), which may be described in this thesis, may not be owned by the author and may be owned by third parties. Such Intellectual Property and Reproductions cannot and must not be made available for use without the prior written permission of the owner(s) of the relevant Intellectual Property and/or Reproductions.
- iv. Further information on the conditions under which disclosure, publication and commercialisation of this thesis, the Copyright and any Intellectual Property and/or Reproductions described in it may take place is available in the University IP Policy (see <http://documents.manchester.ac.uk/DocuInfo.aspx?DocID=24420>), in any relevant Thesis restriction declarations deposited in the University Library, The University Library’s regulations (see <http://www.library.manchester.ac.uk/about/regulations/>) and in The University’s policy on Presentation of Theses.

Acknowledgments

I would like to sincerely thank my supervisor Dr. Lei Ren for providing me the opportunity and full support to carry out independent research in the promising field of biologically inspired biped robot. This thesis would have not been possible without his constructive criticism and insightful suggestions during the PhD research. I also thank him for the valuable experiences on scientific writing and presentation skills.

I would like to thank Dr. Zhenmin Zou, Dr. Guowu Wei, Dr. Ali Jabran, Dr. Manxu Zheng, Dr. Dan Hu and Mr. Zheqi Hu from the University of Manchester for numerous inspiring discussions about robotics as well as useful feedback about my research. I am grateful for the knowledge they shared with me. It has been a pleasure to work with them.

I wish to express my sincere gratitude to the Key Laboratory of Bionic Engineering, Ministry of Education, Jilin University, China for continuously supporting me by all means to have access to the experimental equipment.

I would like to thank Prof. Zhihui Qian, Prof. Zhihui Zhang, Prof. Chunbao Liu, Prof. Yunhong Liang, Dr. Qingping Liu, Dr. Baoyu Zhang, Mr Zhengyi Song, Mr. Wei Liang, Dr. Jing Liu, Ms. Jianan Wu and Ms. Qiaoli Ji for their friendship and discussions about science, philosophy and life in Jilin University. I have learnt so much from them about different areas in computer modelling, finite element modelling, 3D printing and design of experiments. I wish them good luck and success in their future careers.

Finally, I would like to extend a special thanks to my family and friends. It has been a long journey, but their support and faith has been never ending.

Kunyang Wang

September 2018

The University of Manchester

Publications

1. Wang K, Tobajas PT, Liu J, Geng T, Qian Z, Ren L. Towards a 3D passive dynamic walker to study ankle and toe functions during walking motion. *Robot. Auton. Syst.* 2019; **115**(2019): 49–60. doi:10.1016/j.robot.2019.02.010
2. Wang K, Hosseinnjad SH, Jabran A, Baltzopoulos B, Qian Z, Ren L. Patellar tendinopathy: 3D stress and strain patterns in patellar tendon during knee flexion. *Int. J. Numer. Meth. Bio.* 2018. [Under Review]
3. Liu J, Qian Z., Wang K, Wu J, Jabran A, Ren L. Non-invasive quantitative assessment of muscle force based on ultrasonic shear wave elastography. *Ultrasound Med. Biol.* 2019; **45**(2): 440–451. doi:10.1016/j.ultrasmedbio.2018.07.009
4. Xiu H, Wang K, Wei G, Ren L, Dai JS. A Sarrus-like overconstrained eight-bar linkage and its associated Fulleroid-like platonic deployable mechanisms. *P. I. MECH. ENG. C-J. MEC.* 2018:095440621881634. doi:10.1177/0954406218816343 [Accepted/In press]
5. Liu J, Wang K, Wu J, Qian Z, Ren LQ, Ren L. Noninvasive in vivo study of the morphology and mechanical properties of plantar fascia based on ultrasound. *J. Biomech.* 2018. [Under review]
6. Xiu H, Wang K, Xu T, Wei G, Ren L. Synthesis and Analysis of Fulleroid-Like Deployable Archimedean Mechanisms Based on an Overconstrained Eight-bar Linkage. *Mech. Mach. Theory.* 2018. [Under revision]
7. Wang K, Ren L. Development of a bipedal walking robot inspired from human musculoskeletal biomechanics. *Proceeding of 5th International Conference of Bionic Engineering (ICBE)*, Ningbo, China, June 2016.
8. Xu Z, Luo Z, Ren L, Wang K, Hu D. Three-Dimensional Human Modeling and Dynamics Simulation Based on ADAMS. *2017 9th International Conference on Intelligent Human-Machine Systems and Cybernetics (IHMSC 2017)*, Hangzhou, 2017, pp. 354-358. doi: 10.1109/IHMSC.2017.191

Awards

1. Best Presentation Award in PGR MACE Conference, School of Mechanical, Aerospace and Civil Engineering, University of Manchester, UK, 22 March 2016.
2. Best Student Oral Presentation in 2016 International Conference of Bionic Engineering, Ningbo, China, June 2016.
3. Secondary Prize of the 2017 ISBE Bionic Innovation Competition, International Society of Bionic Engineering, 2017.

Chapter 1

Introduction

1.1 Background and Motivation

Throughout history of science and technology, the human mind and body have inspired artists, engineers, and scientists to accomplish daily tasks. Nowadays, robots could work on Mars and in oceans, in hospitals and homes, in factories and schools, with the purpose of fighting fires, making goods and products, saving time and lives [1, 2], etc. Recently, robots are making a considerable impact on numerous aspects of modern life, from industrial manufacturing to transportation, the deep space and sea exploring, human healthcare. In future, robots will be as personal and pervasive as today's smart phones and personal computers. The dream to create machines that have similar skills and intelligence has been part of humanity from the beginning of time.

Among these robots, bipedal robots usually share similar kinetic and kinematics to humans, as well as similar sensing and behaviour. Bio-inspired bipedal robots have remarkable advantages such as impressive motion performance on complex surfaces (e.g., uneven terrain, stairs and getting over obstacles) and strong adaptability to environment. Besides, due to the convenience that bipedal robots are very suitable to providing cooperative work and service for human in living and working environment without any large-scale reconstruction, they have caught significant worldwide attention and become key research area in bionic robot field. Therefore, it has great scientific meaning and potential application value to develop bio-inspired bipedal robots.

It is fascinating to observe a person walking, swimming, jumping, running and catching a moving object rapidly. However, performing these agile movements requires complex interactions among the peripheral nervous system, the central nervous system,

the musculoskeletal system and the surroundings. The biologically inspired bipedal robots are designed to approach those human behaviours, resulting possible applications in dealing with daily tasks.

Biologically inspired bipedal robots are increasingly contributing back to biology in fields such as biomechanics and neuroscience. Indeed, bio-inspired bipedal robots are becoming important scientific tools [3, 4] to investigate human locomotion and to test hypotheses about the underlying interactions of body, control, and environment [5]. These robots have multiple properties to complement human biology research: their actions are repeatable and accurate, they offer the opportunity to measure parameters, variables or quantities that would be difficult to be gained from human beings, they can perform activities that are unnatural or harmful for human, and their morphology can be systematically changed. In summary, bio-inspired bipedal robots can be used to perform some experiments that would be difficult or impossible to make with human and reduce the risk that experimentation on human may cause. Bio-inspired bipedal robots are providing useful contributions to biomechanics [6], neuroscience [7], prosthetics [8, 9] etc.

The last decades have seen great progress and advance in bio-inspired bipedal robots, and a large number of bipedal robots have been developed with varying complexities. However, very few of them were designed to investigate and explore the fundamental mechanical principles underlying human musculoskeletal system. Indeed, bio-inspired robotics provides a powerful research tool to examine the structure and function interplay of the human body whilst complying strictly with physical rules.

This project will lay a stepping stone towards the design and manufacture of bipedal walking robots inspired from the human musculoskeletal system. The proposed framework would provide a powerful scientific tool to examine biological hypotheses and fundamental mechanical principles of the human body in fields such as biomechanics, neuroscience, physiology and engineering. In addition, other clinical applications are also possible in such fields as sports science and rehabilitation. Many athletes or sports trainers suffer from chronic pain caused by tendinitis or severe injuries, e.g., rupture of Achilles tendon usually occurs in football or basketball players. If the robot can replicate complicated behaviours involving the skeletal and the muscular system, the analysis of corresponding muscle activities during motions will profit them a lot. Furthermore, the humanoid robot gives an alternative perspective to be used in testing exoskeletons and

prostheses which could be used to assist daily life of disabled civilians and accomplish complex tasks in the military.

1.2 Methodology and Scope

Musculoskeletal system. To develop a humanoid robot for studying human musculoskeletal biomechanics, human musculoskeletal system (MSK) should be studied thoroughly as it gives humans the ability to move with elegance and efficiency using the skeletal system and the muscular system. As million-year selection and evolution, the human MSK evolves to be a highly ideal mechanical mechanism to support and transport the human body, which could inspire engineers to develop robots as effective and economic as humans using innovative technology and methodology. Human musculoskeletal system, composed of bones, cartilages, skeletal muscles, tendons, ligaments and other connective tissues, provides form, support, behaviour and stability for the human body. A more systemic methodology (Figure 1.1) was applied in the whole process of developing bio-robots to study human musculoskeletal biomechanics. In this research, the biomechanical measurements of human MSK are quantified using a same human subject.

Biomechanical measurements. The biomechanical measurements of the human subject were attained from the Visible Human Project (VHP), U.S. National Library of Medicine (NLM). Computed Tomography (CT) images, Magnetic Resonance Imaging (MRI) images and cryosection images which were obtained from one male cadaver were used to examine the anatomy, structure and geometry of human MSK. Key kinematic parameters were measured from gait analysis by using 3D motion capture system and calculated by using inverse dynamics technique.

Biomechanical modelling. Reverse engineering using software such as Mimics, Amira and Rhino was applied to rebuild the 3D musculoskeletal model of the human subject. Details of the skeletal and the muscular system were quantified and modified. The anthropometric data (dimensions), the body segment properties (mass distribution, mass centre position and moment of inertia), the joint parameters (joint centre position and axis of rotation) and the 3D musculoskeletal geometries were analysed in the model.

Robot design. On the basis of analysing the biomechanical model of human MSK, Computer-aid design (CAD) and additive manufacturing technology (in this case, 3D

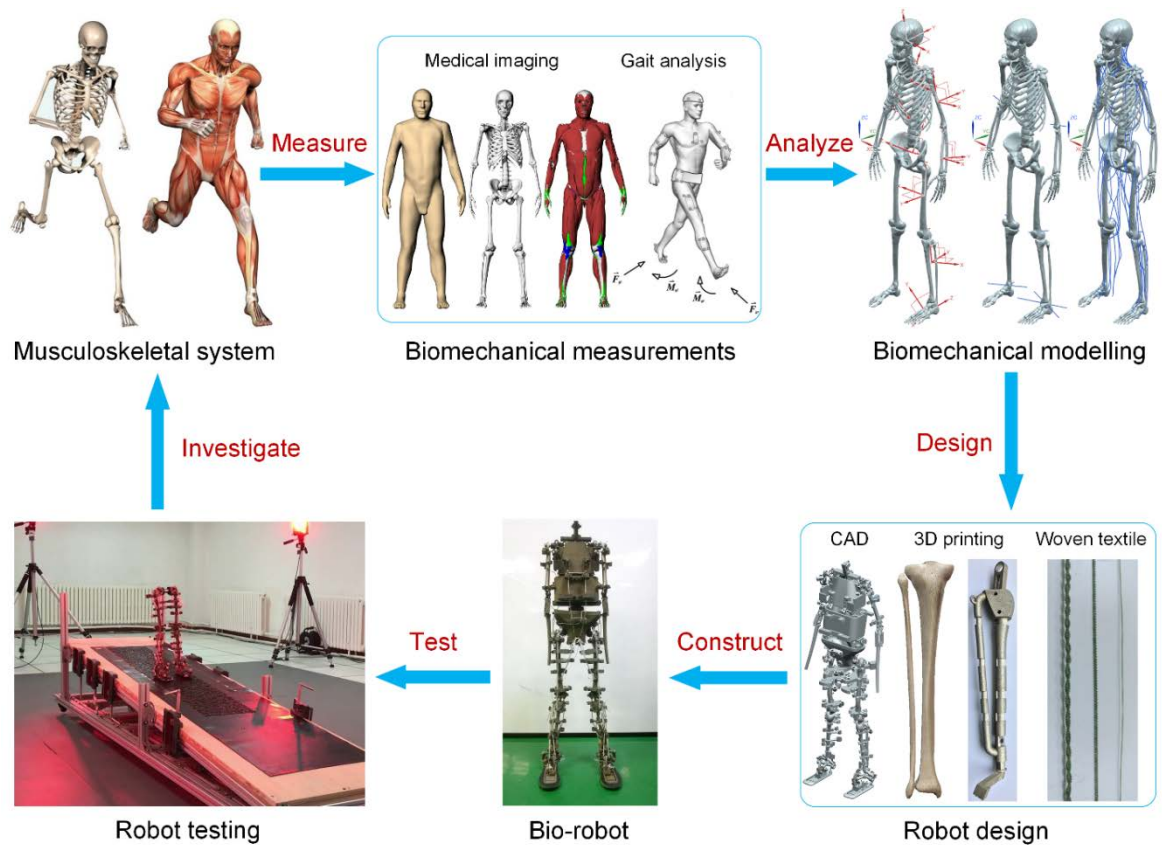


Figure 1.1 Concept of the humanoid research platform.

printing technique) were adopted to design and manufacture the skeletal body of the robot, which assure that the robot has the same anthropometric data, mechanical properties and joint parameters as the subject. Furthermore, a whole-body muscular system was designed and the artificial musculotendon units with similar function to human muscles were woven into textiles, especially for Soleus and Gastrocnemius because they contribute the most during bipedal locomotion.

Bio-robot. The bio-robot platform with a high degree of similarity to human musculoskeletal biomechanics has been constructed, which replicates the whole body of human subject with some simplification in the upper body such as ribs and excluding the head and neck. The mechanics of each body segment (e.g., mass centre, mass distribution and moment of inertia) are almost the same as the human subject, and the kinematics of the key joints (e.g., joint centre and axis of rotation) are as close as possible to that of human subject. The artificial muscular system is designed based on human musculoskeletal geometry, and each artificial musculotendon unit share identical path with corresponding muscle volume of humans. It acts on and equilibrates the skeletal part not

only by itself but also combined with each other, e.g., the units of Gastrocnemius and Soleus have been inserted to the foot by one Achilles's tendon.

Robot testing. To certify the new paradigm of developing humanoid robot platform, repeated tests were conducted on a ramp without any actuation and control in section 4.1. The upper body, including head, middle and upper trunk, and arms, were ignored as the lower body governs bipedal locomotion especially in normal walking and adding the upper body could increase instability. Functional analysis has been tested to demonstrate the potentials of using this robot platform to examine the underlying mechanisms of human agile movements, including internal functions of human musculoskeletal system and external interactions with the environment. Vicon 3D motion capture system (Oxford Metrics Limited, UK) was used to record the kinematic measurements during robot walking at 100 Hz. Each test under different conditions was repeated ten times to allow selection of a representative gait trial.

Biomechanical measurements were made in the University of Manchester, the biomechanical model was built mainly in the University of Manchester and partly in Jilin University, China, and the robot was designed, manufactured and tested in Jilin University, China. All the works were conducted by myself with some help from the technicians.

1.3 Aims and Objectives

The long-term aim of this study is to develop a biologically inspired bipedal robot as a scientific tool to investigate the mechanical design principles underlying human musculoskeletal system.

The objectives includes four aspects as follows:

1. Analysis of the biomechanics of human musculoskeletal system.
 - Build a 3D whole-body musculoskeletal model of a healthy male subject;
 - Predict the body segment properties of each major segment of the subject;
 - Calculate the joint parameters of human subject from gait measurements;
 - Determine the musculoskeletal geometry for each major muscle group.
2. Development of the biologically inspired bipedal robot.
 - Design the main segments of the robot;

- Design the anthropomorphic joints of the robot;
 - 3D metal print the skeletal structure;
 - Design the whole body muscular system of the robot;
 - Fabricate the musculotendon unit;
 - Integrate the skeleton with the muscular system.
3. Computer simulations in Adams.
- Build the computational model in Adams;
 - Conduct preliminary simulation of passive walking on the ramp;
 - Investigate how the ankle configurations affect biped walking.
4. Physical tests of the robot on the ramp.
- Design a ramp for passive walking of the robot;
 - Conduct preliminary test;
 - Certify the new paradigm of developing humanoid robot using repeated tests;
 - Demonstrate the potentials to examine human musculoskeletal biomechanics.

1.4 Contributions to Knowledge

The contributions to knowledge of my PhD study include the following:

- Built a 3D whole body solid model of the human subject;
- Analysed the biomechanics of human musculoskeletal system using the same human subject including segment properties and joint parameters;
- Determined 3D musculotendon paths of major muscle groups using the same human subject;
- Designed a bipedal robot with the same musculoskeletal biomechanics as the human subject;
- Designed a whole body anthropomorphic skeletal structure with the same body segment mechanics as the human subject including mass distribution, centre mass position and moment of inertia;

- Designed anthropomorphic robotic joints with the same kinematic parameters as the human subject including joint centre position and axis of rotation;
- Designed angle adjusting mechanisms where the joint axis of rotation in the ankle and knee can be altered;
- Designed a whole body artificial muscular system with the same musculotendon paths as the human subject;
- 3D metal printed a whole body humanoid robot;
- Built a computational robotic model in Adams including the skeleton and the musculotendon units;
- Predicted the stable region for biped walking with various ankle configurations: no stable walking can be performed for a subtalar angle of more than 29° or a talocrural angle of more than 24° , and the most stable angle for the talocrural joint is $10\text{-}20^\circ$ and for the subtalar joint is $16\text{-}26^\circ$;
- Predicted the best combination of the orientation of ankle axis which could travel the longest distance on the ramp;
- Used a humanoid robot with the same biomechanical properties as the human subject to study human musculoskeletal biomechanics;
- Found that the unevenness of the terrain severely affects the stability of biped walking;
- Found that pavement friction can alter the gait pattern of biped walking by transforming the contact conditions between the foot and the environment;
- Found that proper muscle stiffness is rewarding for the propulsion of biped walking;
- Found that the obliqueness of joint axis in the ankle is beneficial for the capacity of long-distance biped walking;
- Found that the longitudinal arc of the foot makes the robot walk more naturally and stably.

1.5 Thesis Layout

A general outline of the contents of each chapter in this thesis is provided in this section.

Chapter 2 presents a review of the state of the art in biologically inspired bipedal robots and their control methods. According to the ultimate goal, they can be divided into two groups, bipedal robots that emulate human behaviours and that are to investigate human biology.

Chapter 3 studies the biomechanics of human musculoskeletal system. A three-dimensional (3D) whole-body musculoskeletal model based on the Visible Human Project was created to measure and analyse anthropometric data (e.g., mass properties), key kinematic parameters (e.g., joint orientation) and musculoskeletal geometry.

Chapter 4 presents the design and manufacture of the skeletal and muscular system. The design was strictly following the human mechanics obtained in chapter 3 in terms of shape, joint parameters and arrangements for artificial muscles. Coiled fishing lines were used as the artificial muscle-tendon unit in the robot. Fabrication setup and selecting principles of the coiled fishing lines were illustrated. The mechanical body was 3D printed and then integrated with the whole-body muscular system composing the robot.

Chapter 5 shows the simulation results of the robot in Adams. A computational model was developed including the mechanical body, joints and simplified artificial unit (springs). Passive walking on a ramp was simulated in which the kinematic (e.g., centre of mass, velocity) and kinetic (e.g., ground reaction forces and spring forces) data were recorded. The effect of the configuration in the ankle joint on walking performance was explored in depth. The best combination of the talocrural joint and subtalar joint was proposed which made the robot to travel the longest distance on the ramp.

Chapter 6 discusses the results of the physical test on the robot. The experimental installations were introduced including the 3D motion capture system, force plates and the ramp of which the angle can be changed. Preliminary tests were conducted to confirm the variables which affect passive walking. Then, repeated tests were carried out on the ramp. Some key measurements were analysed, e.g., gait cycle, the centre of mass and motion in the ankle.

Chapter 7 concludes the work presented in this thesis and points out the future research directions.

Chapter 2

Literature Review

2.1 Control Methods of Bipedal Robots

To make bipedal robots move, the control method is essential and directly affects the motion trajectory and accuracy. Therefore, numerous control methods have been proposed in the literature. This section presents a review of the state of the art in control of bipedal robots that can be divided into two different methods: precise control scheme using multiple actuators and sophisticated algorithms to control the joints all the time in order to get complex and accurate trajectories; natural dynamics scheme using natural dynamical properties (gravity, free swing motions or inertia) of human body to perform dynamic locomotion.

2.1.1 Precise Control Scheme

The precise control scheme is based on forward dynamics [10]. Using this method, the motions of the joints and segments of bipedal robots are determined by integrating the equations based on predefined joint moment or force data [11-13]. There are several typical schemes being introduced in this section: Zero Moment Point [14], Foot Rotation Indicator [15], Central Pattern Generators [16], Learning Approaches [17, 18], etc.

Zero Moment Point

The Zero Moment point (ZMP) might be one of the most famous criteria used in bipedal robots to obtain joint trajectories. ZMP coined by Vukobratović and Stepanenko in 1972 [14] is the point where the influence of all acting forces on the robot can be replaced by a single force. In other words, ZMP is the point on the ground where the net moment generated from the ground reaction force is zero [19].

In order to obtain the stability of bipedal robots, the ZMP in the body must always reside at the convex hull of the all contact points on the ground. In other words, if ZMP lies on the edge of support polygon, maybe the trajectories are not dynamically feasible, the bipedal robots could fall down. ZMP always coincides with Centre of Pressure (CoP) in a dynamically balanced gait [19]. Nowadays, ZMP has been combined with other control schemes to get more accurate trajectories, such as preview control [20, 21] and offline trajectory generation method considering the constraints, and the relationship between the CoM and ZMP [22].

However, there are some unsolvable drawbacks using ZMP to control the robots that are energy inefficient, low capacity of disturbance rejection and limited motion speed caused by the truth that the robot foot must be fully in contact with the ground. Furthermore, it can be argued that ZMP requires full local controllability which is not a necessary condition for stable walking as it can be seen in limit cycle walkers [23]. In addition, ZMP scheme provides no proper solution after losing balance.

Foot Rotation Indicator

Foot Rotation Indicator (FRI) is introduced as the point on the foot/ground contact surface where the net ground-reaction force would have to act to keep the foot stationary [15]. In fact, a FRI must locate within the support polygon so that the foot of the robots will remain stationary. However, it should be pointed out that FRI method is only applicable when the single support phase and the rotation of the stance foot is the main focus [24]. Aiming at providing a prediction of pure foot rotation, this dynamic control approach is a crucial criterion for the stability of gait. Technically, while the foot of bipedal robot is maintained on the ground, CoP, ZMP and FRI should be all the same point. Yet, if the foot starts rotating, CoP and ZMP are on the edge of the support polygon while FRI is outside this polygon [15]. Therefore, FRI can provide more information than CoP or ZMP and the distance between the FRI point and the support polygon can quantify the gait stability (in terms of both magnitude and direction). Nevertheless, there is a caveat as a recent study reported that, in practice, the distance between the FRI and ZMP is within the measurement accuracy (0.1 % of the foot length) [25].

The FRI point is related to the rotating stability of the bipedal robot as the rate of angular momentum appears explicitly in the FRI formulation [15]. In fact, during standing, walking and running, human tends to maintain or correct balance by appropriately

changing the angular momentum, in addition to taking steps. Since angular momentum can be applied to recover balance after being pushed, it is a good solution for bipedal robots to reject disturbances. Moreover, this approach has been used for walking control of some bipedal robots [24, 26].

Central Pattern Generators

Central Pattern Generators (CPGs) are believed to be a more biologically feasible method of bipedal locomotion [16, 27]. A CPG, a network of coupled oscillators, is widely used to produce stable limit cycles. These oscillators can be tuned to produce periodic and rhythmic signals in accordance with desired frequency, amplitude and phase difference. As to performing bipedal locomotion, a CPG is always tuned to generate the trajectories of joints, corresponding to dynamically stable walking. Trajectory generation based on CPG control is often implemented in open loop without feedback, resulting in toleration of small external disturbances and achievement of little robustness. Applied to real robots, the input to these oscillators can be posture or velocity parameters of robot, and the output the lateral and sagittal position of the leg. Then, the positions of joints can be computed through inverse kinematics [28].

CPGs scheme could be used for balancing and quasi-static walking of robots, but stepping or dynamic walking could not be achieved [29]. The cause of the problems could be the tracking errors and delays of the joints. However, balance controller and speed modulation unit can be combined with CPG to generate a more dynamic motion. Despite the above problem, the main drawback of CPG is the difficulty in applying a particular CPG to achieve periodic motions or perform various tasks. Integrating learning algorithms with CPGs control is an effective way to adapt the trajectories according to different tasks.

Learning Approaches

In the new century, an attractive research idea is utilizing machine learning approaches to achieve stable motion gaits. Usually, a precise robot model is essential to generate motion trajectories in most robotic experiments. Yet, learning approaches could be used to overcome the disadvantages caused by modelling errors that are motivated by the ability to learn through repetition or demonstration. Recently, numerous learning approaches have been adopted in bipedal locomotion: imitation learning [30], reinforcement learning [17], Iterative Learning Control (ILC) [18], and policy gradient reinforcement learning

and particle swarm optimisation [31].

In the case of bipedal robots locomotion, however, directly applying learning methods could not obtain motion stability and safety unless combining with other control methods.

Online Optimization

The ultimate way to adapt the motion of the bipedal robot in real time is to even avoid using any type of precomputed trajectories [32]. This approach requires both the desired motion information and the related control method that can be computed online. Even in some cases, these two steps can be integrated into a single approach to generate real time trajectories. In addition, along with exponential growth of embedded computing ability, it is now imaginable to use more complex optimization techniques to dynamically compute more accurate models in real time.

Model Predictive Control (MPC) is the well-known online optimization technology. If a dynamical model of the bipedal robot is good enough for synthesizing a control scheme, then, the following operations could be achieved at each sampling time: measurement of the actual state; computation of the control that optimizes a given state-dependent cost function on a finite horizon, starting from the current discrete time; application of the control input at the first time index only [32]. However, a main drawback of the approach is the limited theoretical results of stability in the linear or nonlinear systems [33]. Following the parameter adaptation method, an alternative approach Trajectory-Free Nonlinear MPC consists of solving at every time point a constrained optimization problem with a moving horizon [34].

Other Control Schemes

The precise control schemes of conventional robots discussed above are always driven by active electrical actuators which can increase tracking precision. However, for biologically inspired bipedal robots, compliant joint properties can be exploited to store energy and used to generate more human-like properties. Therefore, compliance actuators (such as pneumatic actuator) controlled by pressure or force have been widely used in studying locomotion of bipedal robots.

2.1.2 Natural Dynamics Scheme

Generally, bipedal robots controlled by precise trajectories generation always have a set of

high-torque actuators and complex control algorithms. However, from the biomechanical point of view, these robots are far away from human-like because they require active actuation to perform any motion at any time, as opposed to human walking that relies extensively on natural dynamics of the musculoskeletal system (such as pendulum like swinging movements of the limb) [5]. Therefore, from the energy point of view, they are highly inefficient.

Bio-inspired bipedal robots controlled by natural dynamics scheme are more human-like in terms of biomechanical and energetic aspects. This type of locomotion performed by the bipedal robots is passive due to its passive dynamical properties of the whole body, and active due to its dynamic stability as opposed to static stability. The study of natural dynamic control of bipedal robot has led to a paradigm shift in biped locomotion, going away from precise trajectory tracking control toward locomotion tightly based on passive properties of the body [35, 36]. In this section, two typical control methods have been discussed.

Pendulum

As a typical example of an alternative control mode of bipedal locomotion, some controllers based on inverted pendulum model[37] are used to drive running robots achieving stable gaits. This method can change the landing positions to keep the robots dynamically stable [38]. Using this kind of control scheme, with a well-tuned body morphology made of the bipedal robots, swinging motions of the limbs inspired from pendulum and stable walking could be obtained thanks to gravity and inertia alone [5], without the need for careful joint control to perform bipedal motions.

Cyclic Walking

Bipedal robots controlled by cyclic walking are those that reach, either naturally or with the help from a control, a steady-state behaviour characterised by a cycle in the phase plane. The underlying assumption is that there exists in some sense a more or less hidden set of optimal natural behaviours of the system [23, 32, 39]. The emphasis in the cyclic walking control scheme is on the walking gait periodicity. With the implementation of cyclic walking method, ZMP criterion is violated, thereby proving its conservativeness. Extensively involving in the search of finding periodic and energy efficient walking gait, the cyclic walking control method is not suitable for real time trajectory adaptation.

Moreover, this control method suffers from sensitivity to uneven terrain.

The major drawback of cyclic walking is the limitation about analysis of small perturbations. This has recently been partially addressed in the introduction of active lateral foot placement method [40]. Put it differently, any abrupt change of speed or small perturbations (pushing the robot) cannot be analysed by this criterion. Besides, the stability of the bipedal robots relies on the periodicity which is not a necessary condition for bipedal locomotion. In summary, this method could not provide a feasible solution to achieve robustness, high speed walking and disturbance rejection.

2.2 Bipedal Robots Emulate Human Behaviours

According to the ultimate purpose, bipedal robots are designed to achieve two different objectives: one is taking inspiration from the basic biological principles of human body to perform similar agile movements; the other is using the bipedal robots as scientific tools to investigate theories, experimental methods or principles of biology such as biomechanics and neuroscience. In this section, bipedal robots, which aim at agile movements including bipedal locomotion and whole-body activities, will be discussed.

2.2.1 Bipedal Locomotion

Bipedal locomotion is a key and crucial research topic in bio-inspired bipedal robots. Legged locomotion, especially bipedal locomotion, is an extremely challenging area of bipedal robotics research. Although, some small-size bio-inspired bipedal robots are able to achieve static stable gaits by having a low centre of mass and large feet, other large-size ones with a human-like weight ratio and body dimensions typically need to dynamically balance themselves during bipedal walking or running.

Bipedal Robots Developed by Waseda University

The Bio-engineering group in Waseda University, one of the long-history labs that develop human-like robots, started their research on bipedal locomotion in 1966 with the development of a lower limb model WL-1 [41]. Since then, an impressive row of prototypes has been built as shown in Figure 2.1. Based on WL-5 [42], developed in 1971, the first active robot in the world with bipedal locomotion, the WABOT-1 developed between 1970 and 1973 [43] is known as the first full-scale anthropomorphic robot in the world. It was equipped with a quasi-static walking controller, a visual recognition system

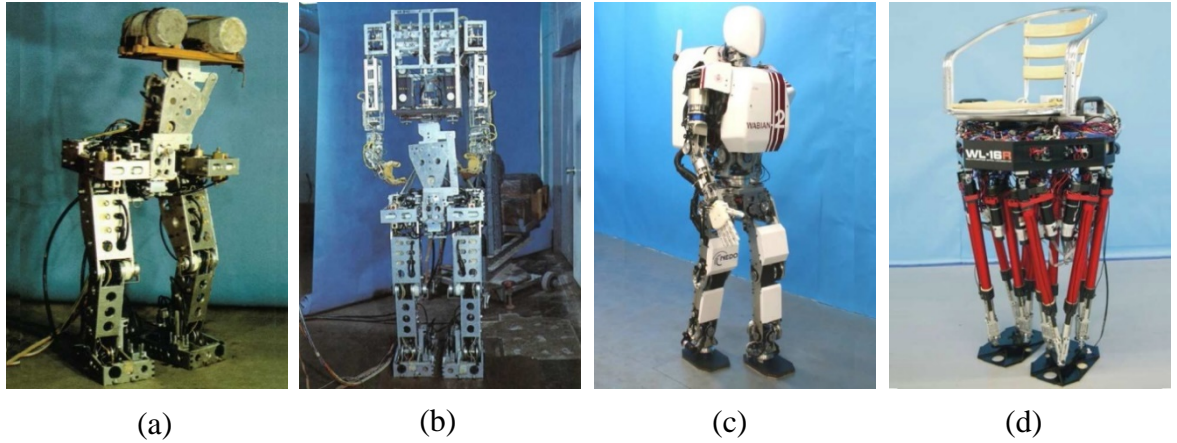


Figure 2.1 (a) WL-5, (b) WABOT-I, (c) WABIAN-2, (d) WL-16R. [41, 44]

and a verbal communication system. The WABOT-I was able to walk with the lower limbs and transport objects with the hands equipped with tactile-sensors. In 1981, the model WL-9DR [44] that used a 16bit microcomputer as its controller was introduced to realize quasi-dynamic walking for the first time in the world, enabling versatile control and making the mathematical solution of a particular walking pattern much more easily attainable (10sec/step).

Afterwards, series models of WL and WABIAN have been developed. Among them, a special design of 7 DOF waist and legs with passive toe joints was adopted in the model WABIAN-2 [45] to investigate stretched-leg walking with heel contact and toe push off and its energy-consumption capacity, while the legs consisting of 6 DoF parallel mechanisms was developed in the model WL-16R, enabling the robot to walk up and down stairs carrying a human[46].

Bipedal Robots Developed by Honda

Honda is a private company in Japan with the longest history in bipedal robotics. After 10 years of secret research, the bipedal robot P2 that could walk stable and climb stairs [47, 48] was unveiled in 1996. This amazing project astonished both the robotic researchers and the society, followed by many other projects started in Japan. Since P2, Honda announced P3 [49] in 1997 and Asimo [50, 51] in 2000 as shown in Figure 2.2. These robots were developed during an intensive research program, leading to ASIMO with 1.3 m tall, 48 kg weight and 57 DoF.

ASIMO is the first bipedal robot in the world to demonstrate remarkable dexterity and

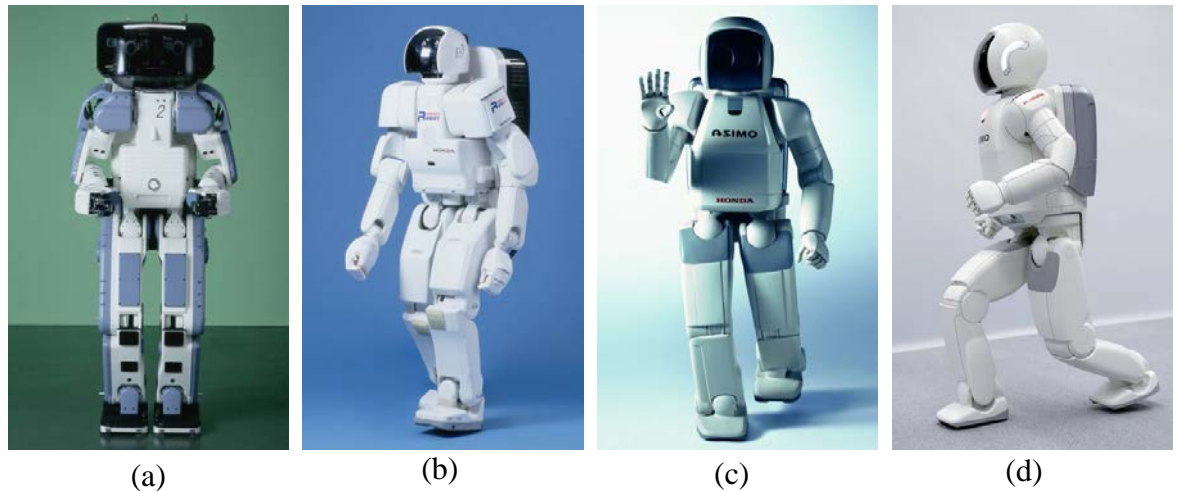


Figure 2.2 (a) P2, (b) P3, (c) ASIMO 2000, (d) ASIMO 2004. [52]

agility in walking at a maximum speed of 2 km/h , with advanced communication ability thanks to recognition technology [50, 53-57]. However, the mechatronic system used in ASIMO is based on stiff joints that are controlled by highly precise independent PID controllers and actuated by powerful direct-current (DC) motors.

After four years of the first generation, the second generation of ASIMO was made public in 2004 with a technology named “posture control” that makes it possible to run in a natural way like human body [48, 58]. The latest version of Asimo is able to demonstrate climbing stairs, grasping, jumping while changing direction, navigation at indoor environment, and even running at a maximum speed of 9 km/h , which makes it the fastest running bipedal robot in the world.

Humanoid Robotics Project (HRP)

While private Japanese companies are investing in bipedal human-like robots, the Japanese government is also providing a large amount of budget for the development. The Humanoid Robotics Project (HRP) was launched in 1998, with a budget of \$40 million funded by the Ministry of Economy, Trade and Industry in Japan. The main goal of the project was the development of general service humanoid robots for tasks in industrial plants and services at home and offices [59, 60]. A series of impressive bipedal robots has been built as shown in Figure 2.3.

HRP-1, enhanced from the Honda P3 robot, was the first robot developed in the HRP project. The legs and arms of HRP-1 could only be controlled separately so that it had to

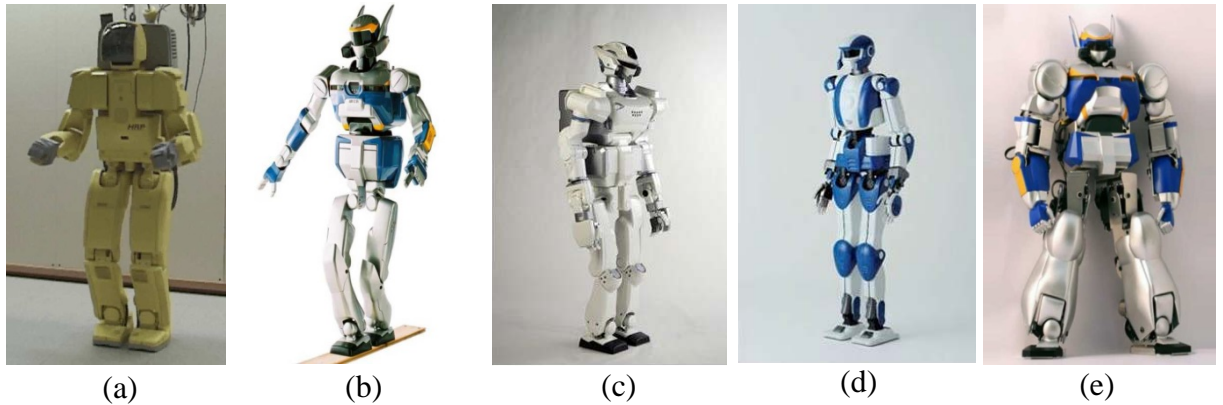


Figure 2.3 (a) HRP-1, (b) HRP-2 [61], (c) HRP-3, (d) HRP-4 [62], (e) HRP-2M [63].

be stopped during walking when arm movements were wanted [64, 65]. Therefore, a lot of practical applications were consequently impossible. Solving this problem, the main control CPU and software were replaced in HRP-1S [64].

Successively, Kawada Industries developed HRP-2 as the main outcome of this project with 154 *cm* height, 58 *kg* weight and 30 DoF [66-70]. As the first finished prototype in this project, the HRP-2 robot was able to demonstrate standing up from a lying position, walking on uneven surfaces, and interaction with humans and help in domestic service tasks, using ZMP scheme for walking at a maximum speed of 2 *km/h*. Since the price to study on a HRP-2 model was too high for research institutes and universities, a small-sized HRP-2M Choromet [63], with 33 *cm* tall, 1.5 *kg* weight and 20 DOF, was revealed in 2006 by AIST (National Institute of Advanced Industrial Science and Technology) and 4 other private companies. It has torque sensors on its legs and accelerometer and gyroscope on its trunk, leading to smooth movements especially the walking pattern.

The HRP-3 [71-73] was subsequently developed with enhanced hand coordination, improved cooling system, additional dust and splash-proof protection, and prolonged operating time. A distributed control system implemented via Controller Area Network (CAN) is used both in the HRP-2 and the HRP-3. Particularly, the prototype of HRP-3 combined a real-time Ethernet communication network in the distributed control system.

In order to improve the function in the domestic circumstances, a new slim, lighter and athletic mechanical design was adopted to the HRP-4 prototype [74, 75], with 151 *cm* tall and 39 *kg*. For upgrading the mechanical system, it has several key improvements



Figure 2.4 H6 (left) and H7 (right) [76].

including LAN and Wireless LAN networks for external and internal communications that is an effective technology to avoid communication errors. Furthermore, Linux open source system and real time software are installed in the HRP-4 to share, reuse, maintain and improve the system by the research community.

However, it should be noted that all the HRP bipedal robots have stiff joints which are controlled by an online trajectory generation based on ZMP and local PID controllers.

Bipedal Robots Developed by the University of Tokyo

The University of Tokyo has developed several bipedal robots to research on dynamic bipedal locomotion, which started with the robot H5 [22] that was created by Jouhou System Kougaku (JSK) Laboratory. An online fast dynamically equilibrated trajectory generation algorithm, together with ZMP criterion, was used to make the robot walk and step down. Followed by H5, the robot H6 [77, 78] was developed in 2000 to achieve whole-body movement. As the last version, H7 improved from H6 (as shown in Figure 2.4) was presented by Kawada Industries and University of Tokyo in 2002 [79].

Using this series of robots, JSK has conducted a large sequence of experiments relating to Dynamic Walking Pattern Generation [80], improvement of locomotion strategies [81] and robot motion planning [79]. However, these bipedal robots all have stiff joints that consist of conventional motors and gears to achieve bipedal locomotion.

Bipedal Robots Developed by Toyota

Since 1970s, Toyota Group has been developing industrial robots, and one of the most important projects is Partner Robot which will embody “kindness” and “intelligence” and

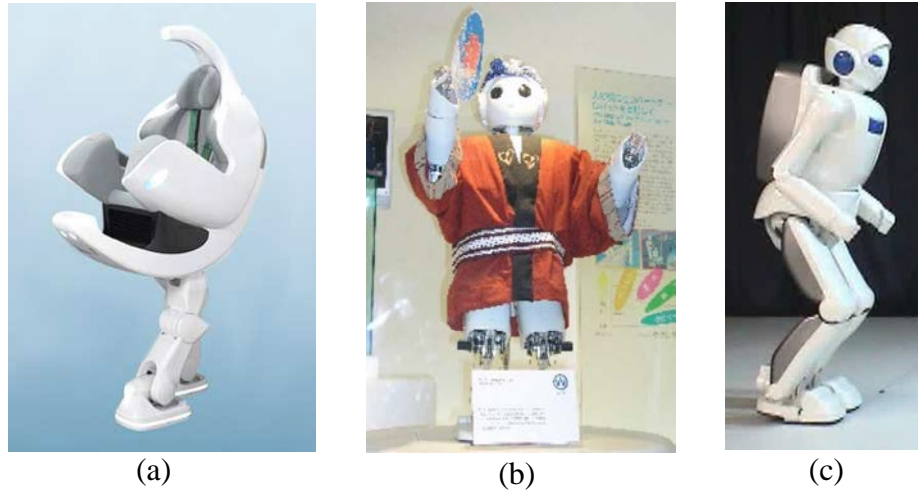


Figure 2.5 (a) i-foot (left) [82], (b) Wire-driven robot [83], (c) Running robot [84].

be able to assist with human activities in applications such as assistance, mobility and elderly care.

In 2006, i-foot [82], a two-legged mountable robot with an egg-shaped cockpit for three-dimensional mobility, was presented to carry a disabled person up or down the stairs. Subsequently, Toyota released a 100 *cm* tall, wire-driven bipedal robot that aimed at reducing the risk of injury and increasing the overall level of safety during interaction with humans [83]. Instead of using direct-driven motors and gears placed at the individual joints to actuate the robot, it placed the motors in the torso and transferred the force by wires that were connected via a nut to a DC motor mounted on a ball-screw. Specifically, there are four wires implemented to drive the knee joints and the ankle joint. One of wires terminates on the posterior side of the knee while the other three wires terminate at the corresponding pitch and roll axes of the foot [83]. This unique design reduces the weight and moment, making the robot safer for human interaction in symbiotic environments. In addition, this robot is envisaged as the new type of mobility besides their cars.

Based on a one-legged jumping robot that was developed by Toyota to investigate the fundamentals of the jumping and running motion [85], a running robot as Toyota's most recent Partner Robot prototype was unveiled in 2009 [84]. The running robot stands 130 *cm* tall and weighs 50 *kg* with 7 DoF in the legs. A motion generation method using ZMP criterion combined with the foot placement scheme was designed to achieve both walking and running. Besides, a balance control method was adopted to maintain balance by dynamically changing the positions of the contact foot during disturbance, consisting of

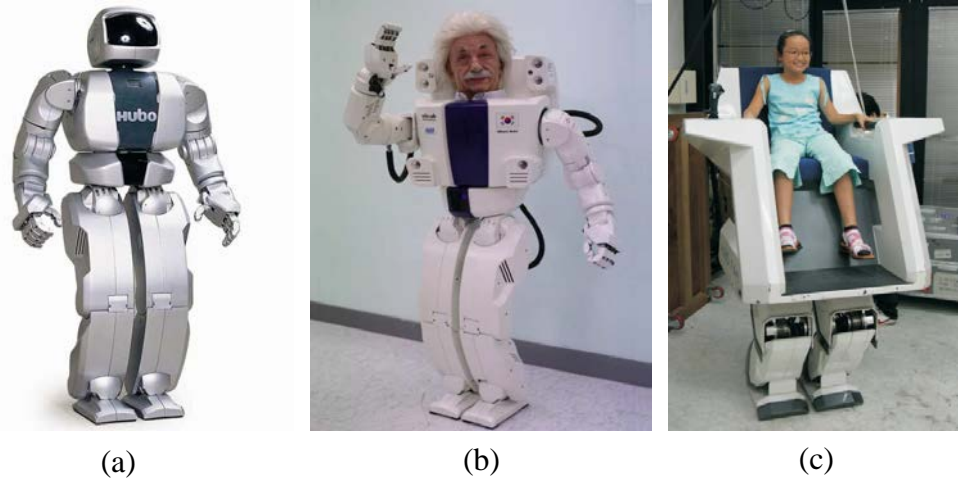


Figure 2.6 (a) HUBO [86], (b) Albert HUBO [87], (c) HUBO FX-1 [88].

compliance control without force sensors and feedback control using the measured orientation of the torso. Finally, this robot can run at an average speed of 7 km/h , which makes it as the second fastest bipedal running in the world. The three types of Toyota Partner Robot are shown in Figure 2.5.

Bipedal Robots Developed by KAIST

Since 2001, Korean Advanced Institute of Science and Technology (KAIST) has developed a series of bipedal walking robots consisting of KHR-0 [89], KHR-1 [90], KHR-2 [91] and KHR-3 (H) [86, 92] with the mechatronic design evolved. The most impressive bipedal robot at KAIST was HUBO project (also called KHR-3) that was developed in 2004 with the aim to provide a reliable platform for achieving dynamic walking, navigation and image processing algorithms based on ZMP criterion and trajectory generation. HUBO is 125 cm tall, 55 kg and has 41 DoF with high stiff joints consisting of planetary gears, harmonic gears and DC motors as shown in Figure 2.6.

In 2006, an android head resembling Albert Einstein that used RC servo motors for facial expression was integrated with HUBO, which led to the robot Albert HUBO (shown in Figure 2.6). Moreover, a running experiment was reported on HUBO in 2009 [93] with the maximum speed of 3.24 km/h , and the tracking control system used in it is based on traditional independent PD position feedback loops.

In addition, HUBO FX-1 [88] was developed at KAIST in 2010 (shown in Figure 2.6) with much larger size and used harmonic reduction gears and high-capacity AC servo motors (400 and 800 Watts) as actuators to carry a human passenger.

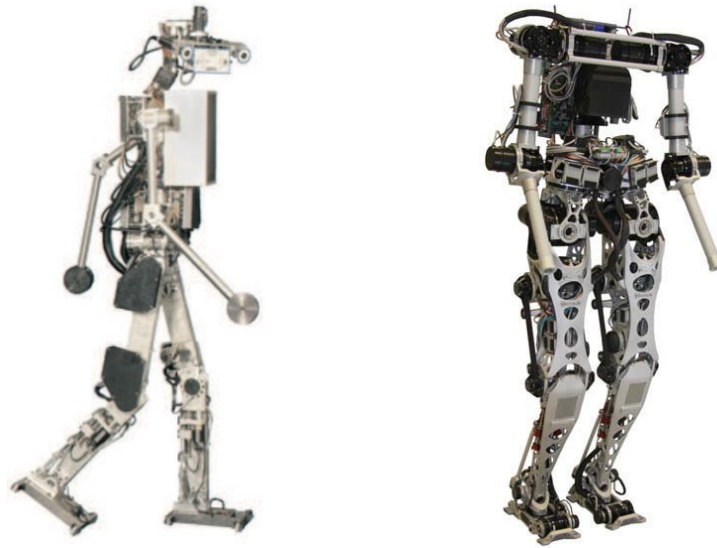


Figure 2.7 Johnnie (left) [94] and LOLA (right) [95].

Johnnie and LOLA

In 2002, an anthropomorphic bipedal robot called Johnnie was developed by the Institute of Applied Mechanics at the Technical University of Munich (TUM) in Germany [96-98], aiming at fundamentally studying and realizing human-like dynamic stable gaits. Johnnie is 180 cm in height and 40 kg in weight with a total of 23 DoF and 17 joints. Joint position sensors attached to the motor shaft, force sensors and attitude sensors were implemented to measure the desired magnitudes. Two control systems that are torque method based on feedback linearization and joint position were implemented in Johnnie. However, it was realized that although computed torque method could work correctly in theory, it did not result in an optimal solution for the real robot, as the computational effort is very high and it requires very accurate sensors with a high bandwidth [97].

Even though Johnnie has demonstrated walking at the maximum speed of 2.4 km/h using joint position control combined with ZMP criterion, higher jogging speeds could not be reached. Therefore, based on the success of developing Johnnie, a new bipedal robot LOLA [99, 100] with enhanced performances was developed in 2006 and unveiled in 2010 (as shown in Figure 2.7) to demonstrate walking and navigation capabilities. The goal of the LOLA project is to increase walking speed and achieve more flexible gait patterns using a light weight structure and powerful stiff actuators. LOLA is characterised by lightweight construction, and a modular multi-sensory joint integrated by brushless motors and gears and sensors using decentralized joint controllers [95, 101-103].

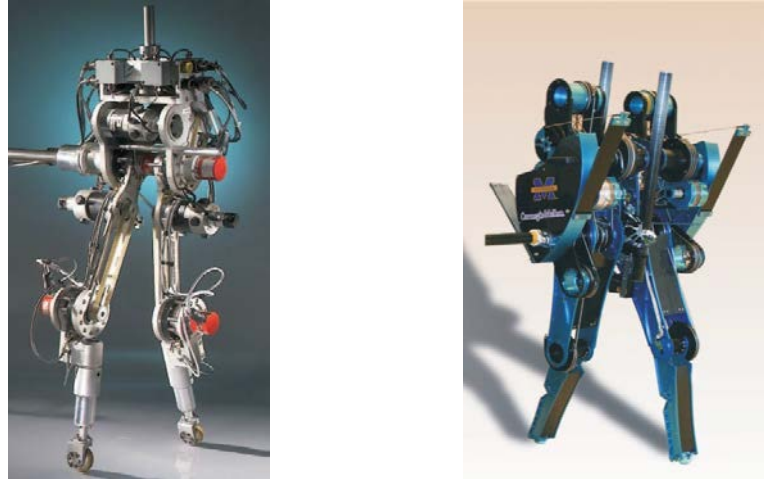


Figure 2.8 RABBIT (left) [104] and MABLE (right) [105].

RABBIT and MABLE

As the result of a joint effort by several French research laboratories and the University of Michigan, a bipedal robot called RABBIT [104] was developed in 2003 to be a testbed for studying advanced motion control theory and achieve high speed walking and running gaits. RABBIT is a five-link, four-actuator bipedal robot with point feet which was to demonstrate that ankles are not absolutely necessary actuating position for asymptotically stable locomotion patterns. Since the ZMP criterion could not effectively be used due to the round feet, in order to achieve high planar walking speed, a running controller based on the new exciting theory of Hybrid Zero Dynamics (HZD) was developed. This theory which made RABBIT execute six consecutive running steps not only provided a completely convincing proof for closed loop stability, but also reduced the debugging and development time existing in present robotic experiments.

However, the running gait of RABBIT that could achieve stable walking gait was not stable, which was mainly caused by the large energy loss during impacts with the ground. In fact, the impacts during the high speed running experiment were much larger than walking and the stiff actuators of the robot always failed to maintain the kinetic energies of the overall bipedal locomotion. Since then, a compliant robot called MABLE [106] was developed in 2009 as an improved version. The robot stands 1 m tall and weighs 58 kg, consisting of a torso and two legs with revolute knees terminated in point feet [105]. All four actuators are located in the torso to keep the legs as light as possible, and for each leg, a collection of cable-differentials is used to connect two motors to the hip and knee joints

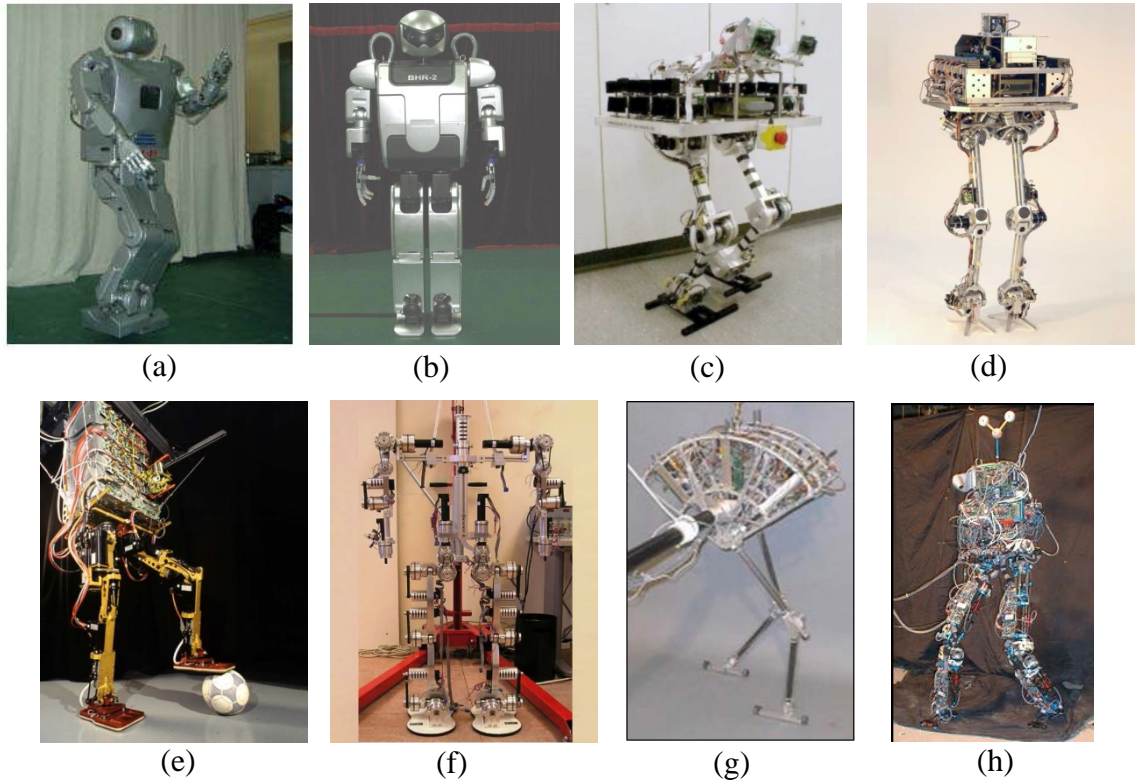


Figure 2.9 (a) BHR-01[107], (b) BHR-2 [108], (c) BART-TH, (d) LISA [109], (e) BIP [110], (f) Rh-1 [111], (g) Spring Flamingo, (h) M2 [112].

in which one motor consists of the line connecting the hip to the toe to control the angle, while the other is connected in series with a spring for the purpose of enhancing energy efficiency and agility of bipedal locomotion. In terms of the control scheme, a compliant HZD controller was designed and implemented to perform efficient, stable and fast walking [105, 113]. Currently MABLE can walk at the speed of 1.5 *m/s* with a stable gait, and Figure 2.8 shows the picture of RABBIT and MABLE.

Others

Apart from the robots above, there are some other representatives in the world as shown in Figure 2.9, including BHR-01 [107, 114] and BHR-2 [108] from Beijing University in China, BART-TH and LISA (Legged Intelligent Service Agent) [109] from the University of Hannover, BIP in France [34, 110] designed for the study of both human and artificial bipedal locomotion, ARNE [115] from a company at St. Petersburg in Russia for playing soccer, Rh-1 [111] in the University Carlos III of Madrid, SILO-2 robot [116] from the Industrial Automation Institute of Madrid, Spring Flamingo and M2 [112, 117] in the MIT Leg Laboratory, etc.

2.2.2 Whole-body Activities

Since bipedal locomotion has been successfully achieved in many cases, researchers wish to enable more bio-inspired bipedal robots to perform more sophisticatedly whole-body activities such as carrying, lifting and catching an object, climbing, or even dancing. Most bipedal robots could achieve these motions using a three-step method that is generating a coarse whole-body motion and transforming it into a dynamically balanced movement, then, using a sensory feedback control system to maintain the stability during the whole-body activity. This feedback might be unnecessary only if the generated motion patterns were perfect and the state of the environment could be exactly anticipated in advance. However, it is very difficult to compute a perfect motion pattern during real circumstances, as the models of both the robot and the environment inevitably have errors, e.g., surface conditions such as friction and compliance. This section focuses on the bio-inspired bipedal robots that can perform whole-body activities similar to human.

Bipedal Robots Developed by Sony

As an international company, Sony has developed a series of bipedal robots with the purpose of entertainment. After studying a commercial robotic dog AIBO for several years, Sony presented the human-like bipedal robot SDR-3X in 2000 [118], SDR-4X in 2002, SDR-4XII [119, 120] in 2003, and the ultimate model well-known as QRIO (i.e., Quest for Curiosity) [121, 122] as shown in Figure 2.10. A Real-time Integrated Adaptive Motion Control has been used in SDR-4X to make an adaptive motion control against external forces interference and walk on uneven surface.

As an entertainment robot, QRIO can perform a lot of amusement activities: dance, throw a ball, fall down and get up again, walk on a wobbling surface, and run. Its moving parts consists of totally 38 degrees of freedom, with each stiff joint (except the joints in the hands and the neck) driven by the Intelligent Servo Actuator (ISA) unit containing a built-in motor driver and communication circuit [122]. Instead of harmonic gear drive, plain flat gears were implemented to obtain back-drivability. There are four force sensors in each foot processing the output data to obtain ZMP position data, achieving stable walking and motion performance. Moreover, QRIO can adapt quickly from being pushed against an external force. SDR Motion Creating System, composed of two parts (the Foot Trajectory Editor to create stable lower body motion and the Motion Editor to edit upper body motion and whole body motion) [123], can produce dynamic and creative motion

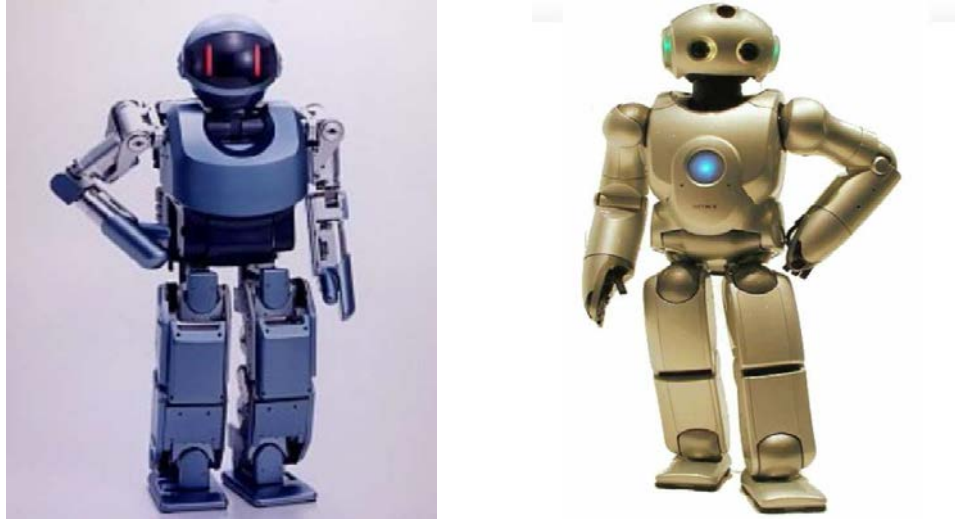


Figure 2.10 SDR-3X (left) [124] and QRIO (right).

performances including dance steps synchronized to music and stable biped walking.

NAO

Widely used by worldwide universities as an educational tool and research platform, NAO with 58 cm tall (shown in Figure 2.11) is an open source programmable bipedal robot developed by Aldebaran Robotics in France [125]. Since his birth in 2006, NAO has been constantly evolving to be a friendly, engaging, interactive companion and partner around the house. The robot has a total of 25 DoF whose key elements are MaxonTM coreless brush DC motors for precision and reliability, spur and planetary gears for a fairly good back drivability, and actuators consisting of grouping two rotary joints together to make a Universal joint module for cost. Besides, cameras, microphones, tactile and pressure sensors were placed in the sensor network, along with various communication devices including voice synthesizer and speakers.

NAO used a linear inverse pendulum model [126] and quadratic programming combined with feedback from joint sensors to achieve omnidirectionally stable walking [21]. NAO could walk on a variety of floor surfaces, such as carpeted, tiled, and wooden floors with robustness and disturbance rejection. Besides, a fall manager was designed to protect NAO from falling down. Moreover, the whole-body motion module based on generalized inverse kinematics handling Cartesian coordinates, joint control, balance, redundancy, and task priority, was adopted to perform various complex tasks such as catching small object, navigation [127, 128], dancing and making cognitive decision [129].



Figure 2.11 NAO [125].

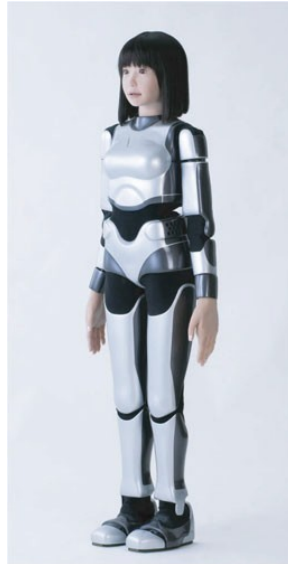


Figure 2.12 HRP-4C [130].

Recently, NAO could generate some emotional postures including anger, sadness and happiness [131].

HRP-4C

Developed by AIST in 2009 to realize human-like motions, HRP-4C (also referred to cybernetic humanoid robot) [130, 132-134] as shown in Figure 2.12 is the latest bipedal robot in the HRP series with a young Japanese female appearance that is 43 *kg* in weight and 158 *cm* tall, containing servo motors and harmonic drive gears in most of the joints. Successfully, 8 joints concretely linked and driven by two separate servomotors were



Figure 2.13 PETMAN (left) [135] and Atlas (right) [136].

adopted into the face to create basic facial motions. A distributed control system in which extremely tiny distributed motor drivers were placed close to the motors, combined with the ZMP criterion, was designed to enable the robot to achieve daily tasks.

In addition to human-like facial expressions such as blink, HRP-4C can walk, conduct 90-degree turn, make a bow and recently perform an impressive dancing and singing act with a group of professional dancers from Japan at the Digital Content Expo 2010. Therefore, it has moved one step closer to interact with human beings.

PETMAN and Atlas

PETMAN is an anthropomorphic robot designed by Boston Dynamics in 2011 aiming at studying the feasibility of chemical testing using a fully articulated robotic mannequin for the US military [137]. Indeed, natural agile movement is absolutely essential for the robot to simulate how a soldier stresses protective clothing under realistic conditions. PETMAN stands about 175 cm tall, weighs 80 kg and uses hydraulic actuators to achieve high power output and provide a degree of compliance absorbing the ground impacts. Regarding the control system there is not enough information to get, but it can be realized from the online videos that PETMAN has also used an algorithm based on foot placement as it has the ability to recover balance from pushing by adapting its foot on the right location. As the fastest walking robot in the world, PETMAN can perform a human like walking at the speed of 5.1 km/h. Moreover, the robot is able not only to crawl, kneel, go up the stairs, but also to conduct jumping jacks, squat thrusts, press-ups and a variety of suit-stressing

calisthenics during exposure to chemical warfare agents, all without losing his balance.

In 2013, an advanced version of PETMAN called Atlas [136] (all shown in Figure 2.13) was developed by Boston Dynamics, including a torso two hands, arms, legs, feet and a total of 28 hydraulically-actuated degrees of freedom. As a bipedal robot with high mobility, Atlas was designed to negotiate with outdoor and rough terrain environments. Equipped with an off-board, electric power supply via a flexible tether, the robot can walk bipedally leaving the upper limbs free to carry, lift, and manipulate stuff in the environment. In addition, Atlas is coordinated and strong enough to pick its way through congested spaces and climb using hands and feet in some extremely challenging terrain.

Others

With the more deep development of humanoid robotics, a large amount of bipedal robots aiming at whole-body activities has emerged in the world as shown in Figure 2.14, including REEM-C developed by PAL Technology [138], KHR-1 [139] from Kondo, RoboNova [140] from Hitec, a series robots of HOAP [141, 142] developed by Fujitsu Laboratories, a compact-size humanoid robot morph3 [143, 144] and PINO [145, 146] from ZMP Inc., etc.

From the above, these bipedal robots use multiple high-torque actuators and precise control scheme to carefully control all joints at any given time to emulate human behaviours and accomplish complex tasks. Generally, their design principles are based on serial kinematic chains of stiff joints and links with fully actuated and feedback/feedforward-controlled joints. Driven by stiff actuators and based on either single-joint or multi-joint models, the joints are controlled to get complex and accurate trajectories by using independent joint space controller.

Although these robots can reliably perform not only bipedal locomotion such as walking/running but also whole-body activities such as dance, their motion performance is still not comparable to real human movement in terms of stability, flexibility and agility which can easily be observed from human gaits. Such robots cannot exploit natural dynamics and self-stability of compliant and elastic, dynamic human locomotion. Besides, from an energy point of view, these robots are highly inefficient because they require actuation at each joint to perform any motion and the actuation is usually obtained from electric (QRIO from Sony), hydraulic (Atlas from Boston Dynamics) or pneumatic high-torque motors.

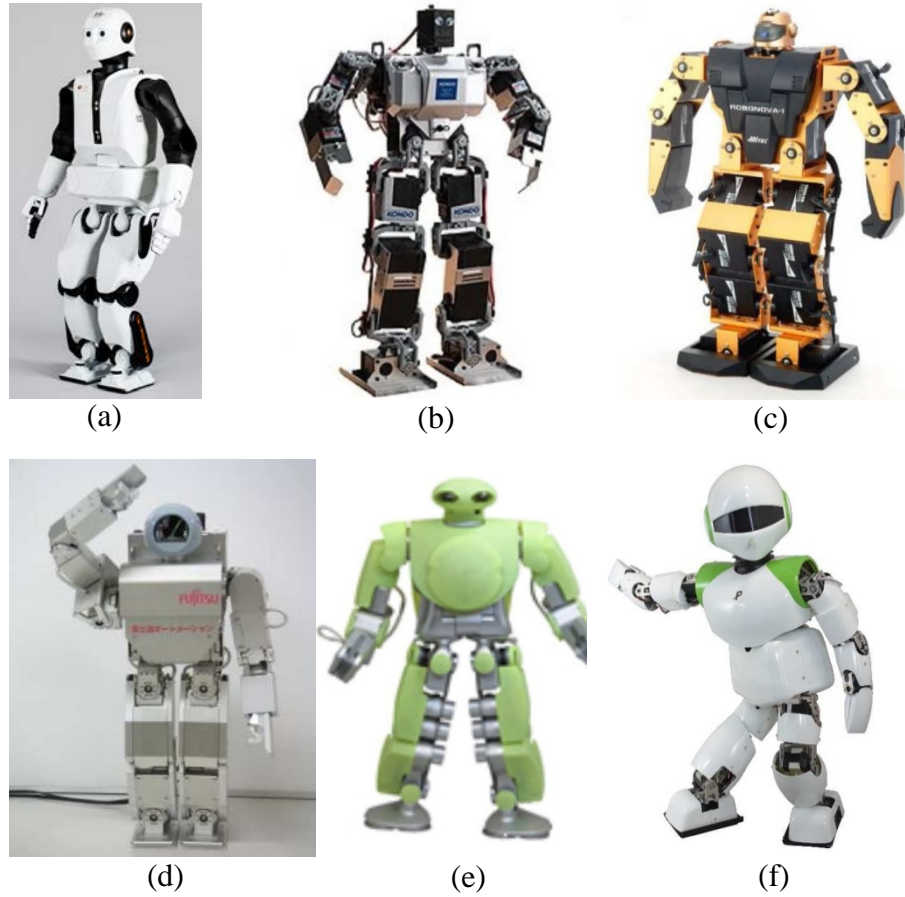


Figure 2.14 (a) REEM-C [138], (b) KHR-1 [139], (c) RoboNova [140], (d) HOAP [141, 142], (e) morph3 [143, 144], (f) PINO [145].

2.3 Bipedal Robots to Investigate Human Biology

Not only being used to emulate the agile and graceful movements of human, biologically inspired bipedal robots can also be used as physical models to make a contribution to hypothesis testing in such fields as biomechanics, human body functions and properties, neuroscience, etc. In this section, the bipedal robots that are used as scientific tools to investigate scientific theories of human biology will be discussed.

2.3.1 Using Bipedal Robots to Study Biomechanics

Most researchers study biomechanics by observing people as they walk, measuring joint angles and ground reaction forces [147], however, there is another approach, which is designing and testing bipedal robots that can be compared to humans in terms of control, gait appearance and energy use [148], to study biomechanics (such as passive dynamics in human bipedal walking and human limit cycle walking).

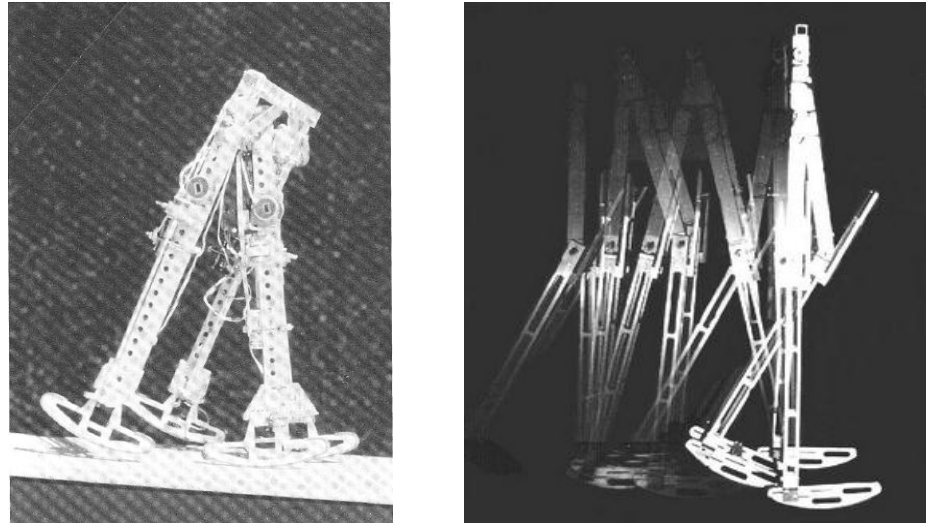


Figure 2.15 McGeer kneeless (left) and kneed (right) passive dynamic walking robot [149, 150].

2.3.1.1 Passive Dynamic Walking Robots

The bipedal robots that can achieve agile movements are mostly based on the mainstream control scheme (i.e., precise joint-angle control). However, for the study of biomechanics, this control scheme is unsatisfactory, as it requires highly precise actuators with high frequency response, and more energy. To address these issues, passive dynamic walking robots were proposed as a new design and control scheme. In contrast to the mainstream robots, which actively control every joint at any time, passive dynamic walking robots, which base their locomotion on natural dynamics solely, do not control any joint angle at any time. In this section, some bipedal robots that are used as scientific tools to study biomechanics, especially passive dynamics in human walking, will be discussed.

Bipedal Robots Developed by McGeer

Passive dynamic walking robot was invented and initially developed by Tad McGeer in late 1980s. Inspired by simpler calculations from Tom McMahon and Simon Mochon at Harvard [151], in 1989, McGeer built a kneeless bipedal robot (as shown in Figure 2.15a) for experiments on two-dimensional gravity-powered walking [6]. This robot stands 50 *cm* tall and weighs 3.5 *kg*, with the outer legs connected by a crossbar and alternate like crutches with the central leg, and semi-circular feet. Toe-stubbing was prevented by small motors that folded the feet sideways during the swing phase. Finally, this robot can walk in a naturally stable limit cycle without any active control.



Figure 2.16 Imitation of McGeer developed by Nagoya Institute of Technology [152].

Successfully in 1990, a kneed passive dynamic walking robot [150] as shown in Figure 2.15b was developed by McGeer to show that human-like bipedal locomotion can be achieved without the use of any controller. This robot consists of 4 legs in which each two legs are connected to each other (2 outside and 2 inside) to generate more stable walking, with the knee connected by pin joints with mechanical stop to avoid knee bouncing and hyper-extension. In addition, curved feet that resemble human feet were used in this prototype that has a total of 5 DoF to achieve more stable gaits.

In contrast to kneeless robot, this kneed passive dynamic walking robot offers a better solution for the problem of foot clearance during the recovery phase and generates more stable gaits. In terms of energy consumption, they are equally efficient. However, this kneed robot had an extra mechanism to increase energy consumption due to the collision when the swing knees were locked. Moreover, the foot design required improvements to achieve a more positive locking torque assisting bipedal locomotion.

Imitation of McGeer Biped

After the success of McGeer, there are various imitating versions for four legged passive dynamic walking robots inspired from McGeer. Among them, there is an impressive model designed by Yoshito Ikemata *et al.* of Nagoya Institute of Technology in 2006 [152] as shown in Figure 2.16, which was able to complete over 100,000 steps, walk for more than 13 hours, and travel for more than 15 km. The robot weighs 1.5 kg and each leg is 42 cm in length, consisting of four legs with the knees in which the inner one and the outer

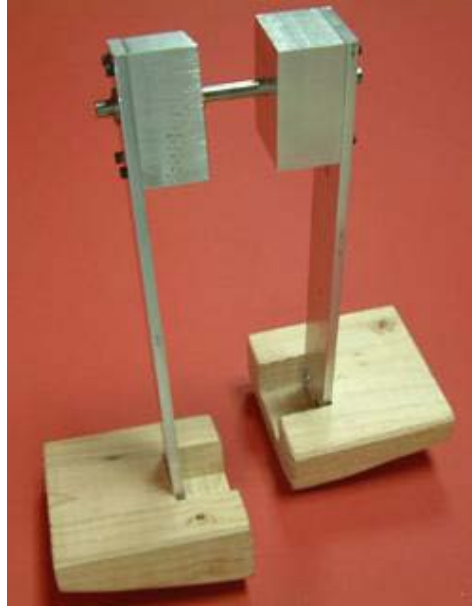


Figure 2.17 Passive dynamic walking robot developed by MIT [153].

one is mechanically linked in the sagittal plane. With each leg connected over a revolute joint at the hip and same mechanism for knee lock compared to McGeer, the curved shape of the feet has been improved in this imitation model. Moreover, this passive dynamic walking robot has an extra circular stopper to maintain constant inter-leg-angle at heel strike.

Generally, the McGeer and the imitation both have a human-like bipedal locomotion being viewed from the side. Nevertheless, there are extremely unnatural walking gaits being viewed from the front, as they are all designed to only have planar motions.

Bipedal Robots Developed by MIT

In 2004, a simple passive dynamic walking robot with arc-shaped feet was developed by Tedrake *et al.* at MIT [153] with the goal of achieving 3-Dimension (3D) dynamically stable walking as shown in Figure 2.17. This robot has two legs that are connected by a hinge joint, and large curved feet, with the only passive joint located at the hip. When being placed at the top of a small ramp and given a small push sideways, the robot will stand on a single stance leg, while the opposite swing leg leaving the ground and swing forward on the ramp. After the swing leg strikes on the ground and becomes the stance leg, this cycle continues resulting in stable 3D walking through a ramp. The curvature of the feet was a challenging design parameter in this robot, consisting of two curvatures, one of which enabled the stance leg to rock on one side while the other leg swinging forward.



Figure 2.18 Passive dynamic walking robot developed by Cornell University [148].

Nevertheless, the motions generated by this 3D passive walking robot were significantly not similar to the human walking gaits, but similar to the gates of a penguin, due to extensive rocking motion of the curved feet.

Bipedal Robots Developed by Cornell University

A much more improved passive dynamic walking robot was presented in 2001 by Steven Collins at Cornell University [154] as shown in Figure 2.18. This robot stands 85 *cm* tall, weighs 4.8 *kg* and is composed of widely curved feet, legs, knees and arms, each of which is mechanically linked to the opposite leg (left arm to right leg and vice versa). Being considered to achieve one of the best naturally human-like walking gaits, the robot used counter-swing arms to reduce angular momentum effects of the vertical axis, soft heels to reduce the instability caused from the collision of contact with the ground, wide feet to guide the bipedal locomotion, and swinging the arms side to side at appropriate time to reduce rocking. Compared to the McGeer robot, the use of upper body, especially counter-swing arms, were designed to improve walking stability. In addition, knees were added to solve foot scuffing issue and obtain foot clearance.

Being able to walk stably at the speed of 0.51 *m/s*, this robot has successfully implicated passive dynamics in human walking and may help point the right way toward

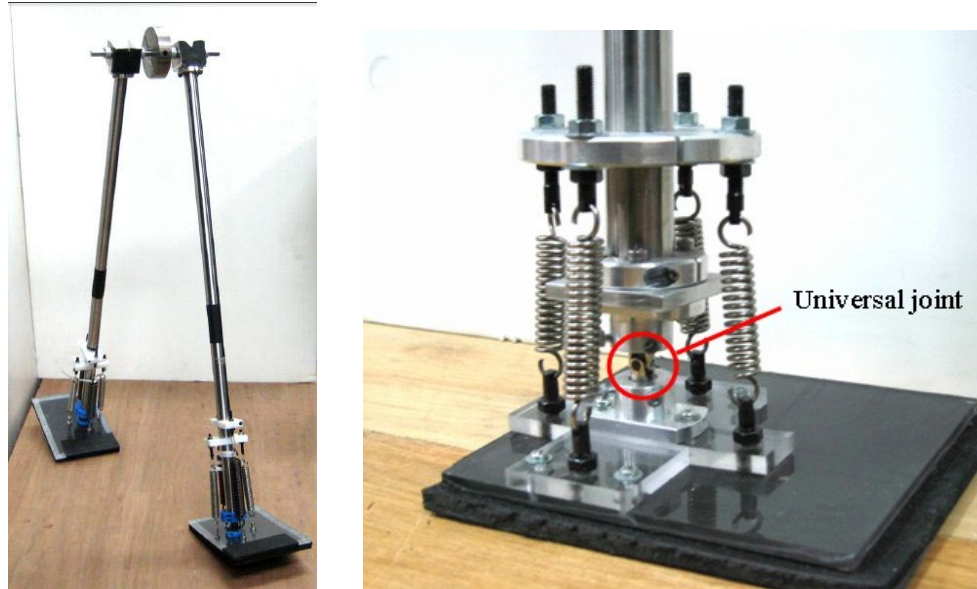


Figure 2.19 Passive dynamic walking robot (left) and ankle details (right) developed by Keio University [155].

simple and efficient bipedal robots with human-like walking motions.

Bipedal Robots Developed by Keio University

Although the curved feet model would be a reasonable solution to achieve walking stability, it has been recently realized that using flat feet model combined with ankle springs is also an alternative method [155-157], leading to a passive dynamic walking robot developed by Narukawa *et al.* of Keio University in 2009 as shown in Figure 2.19.

This robot weighs 2.3 kg and has two symmetrically straight legs (no knee) that are about 80 cm long based human legs and connected by a hinge joint. Each flat foot and each leg were linked by a universal joint with four extension springs and two DoF (each DoF is restrictedly, mechanically controlled by two springs) as shown in Figure 2.19. In addition, sponge sheets were attached to the feet to increase friction, and the extension springs allowed the stance leg rocking on one side and the other leg swing forward.

Experimental results have shown that this flat feet robot can complete longer steps and walk faster than those using curved feet model, and it can also generate stable walking gaits by providing sufficient friction torque [156]. In addition, it can reduce the oscillations by using springs with appropriate torsional spring constant, making the motion more stable and smooth.

2.3.1.2 Passive Dynamic Walking Robots with Simple Actuation

To demonstrate that the human-like properties of passive dynamic walking robots are not dependent on gravitational power, but rather extend to level-ground walking, a minimal actuation is required. Subsequently, passive dynamic walking robots that use less control and energy, yet walk more naturally than the robots based on precise joint control, further suggesting the significance of passive dynamics in human bipedal locomotion, will be discussed in this part.

TU Delft Biped

The Delft Biorobotics Laboratory in Delft University of Technology, which has long history of developing walking bipeds based on the principles of passive dynamic walking, started their research in 1995 with the development of a 3D walking robot without controls called Stappo [158]. Subsequently, an impressive row of prototypes has been built as shown in Figure 2.20.

Among them, Bob based on fully 3D dynamic simulation and stability analysis, and actuated by soleus stretch-reflex was designed in 2000 [158]; Baps based on phasic actuation and stiffness control was designed in 2001 [158-161] using McKibben Muscles as pneumatic actuation; Mike with hip and knee joints was designed in 2002 to study how hip actuation can be used to enhance the stability of human walking [158, 161-163]; Max with knees and an upper body was designed in 2003, using McKibben muscles to provide minimal actuation to walk on a flat floor [158, 161, 164, 165].

As one of the most impressive passive dynamic walking robot with simple actuation, Denise was developed by Wisse *et al.* in 2004 [158, 161, 166-169], consisting of two legs with knees, hip, upper body and two counter-swinging arms. It stands 1.5 m tall, weighs 8 kg and has a maximum speed of 0.4 m/s with five internal degrees of freedom (two at the ankles, two at the knees, and one at the hip). The two legs were linked together by the bisecting mechanism of the hip, resulting in that as one leg moves forward, the other moves the same amount backward. The knees (that contained mechanical stops to avoid hyperextension and could be locked with a controllable latch) and the ankles were all passive without any actuator. However, two antagonist pairs of McKibben muscles were used to provide power across the hip joint to drive the walking motion and to decrease the chance of a fall forward [169]. Besides, two sensors were placed beneath each foot to provide the contact switch signals, allowing the right knee to be released when the left

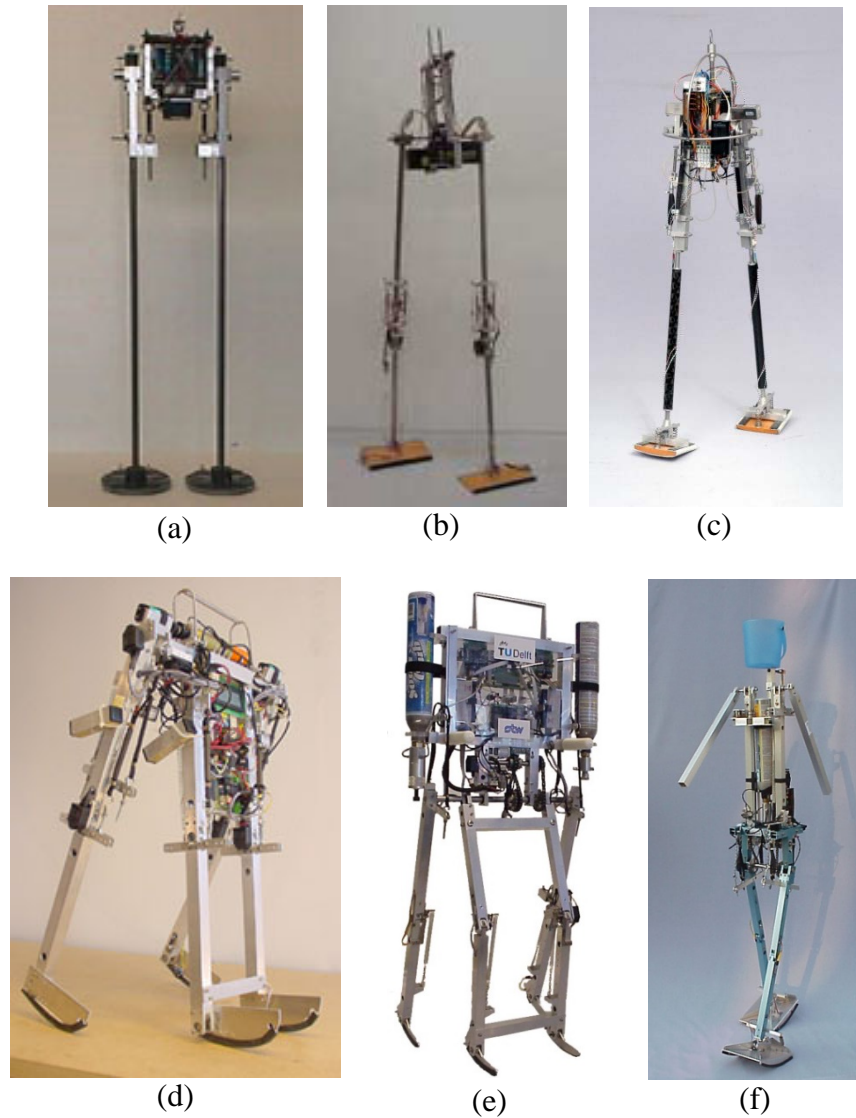


Figure 2.20 (a) Stappo, (b) Bob, (c) Baps, (d) Mike, (e) Max, (f) Denise. [158, 161, 169]

foot hits the ground and the hip muscles to pull the right leg forward, and vice versa.

Cornell Biped

The Cornell biped based on the passive dynamic walking principles and powered by electric motors with springs that drive ankle push off [148, 170], was designed by Andy Ruina of Cornell University *et al.* in 2005 to minimize energy loss that happens both in human walking when the feet hit the ground and robot bipedal walking when actuators actively brake movements causing negative work. As shown in Figure 2.21, it has five internal degrees of freedom (one at the hip, two at the knees and two at the ankles), with each arm mechanically linked to the opposite leg, and the small body is kinematically

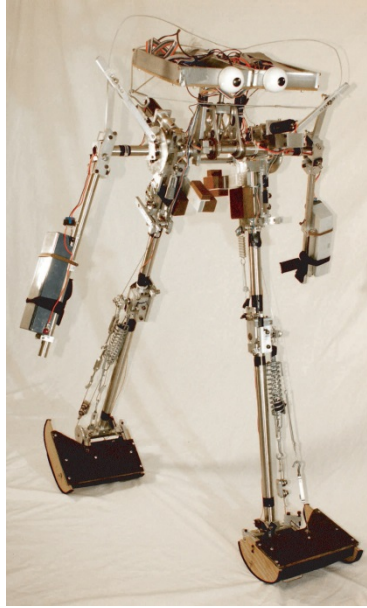


Figure 2.21 The Cornell biped [170].

constrained so that its midline bisects the hip angle. It weighs 12.7 kg and can walk with the speed of 0.44 m/s .

As widely known, the primary energy losses for humans and robots during constantly walking are caused by dissipation when a foot hits the ground and by active braking by the actuators. Therefore, the Cornell biped has demonstrated that it is completely possible to avoid the energy loss due to this negative work, and in fact, the only work done by the actuators is positive in the process of the right ankle actively extending when the left foot hits the ground, and vice versa. This has led to low energetic cost (c_{et} of ~ 0.2), which is equivalent to real human walking (c_{et} of 0.2) and is an order of magnitude lower than the robot Asimo (estimated c_{et} of 3.2) [170]. Furthermore, the average mechanical power of the two ankle joints was about 3 W , and the Cornell biped totally consumed 11 W including microcontroller, electronics and actuators.

MIT Biped Toddler

Based on the simple passive dynamic walking robot shown on the left in Figure 2.22, Toddler was design by MIT Russ Tedrake *et al.* from MIT [153, 171, 172] with the goal to optimize a control policy during bipedal locomotion by using online reinforcement learning algorithms. As shown on the right in Figure 2.22, it is 43 cm tall, weighs 2.75 kg and has six internal DoF (two passive hips and two motors in each ankle) with each arm mechanically linked to the opposite leg to obtain stability and restrain the effects of

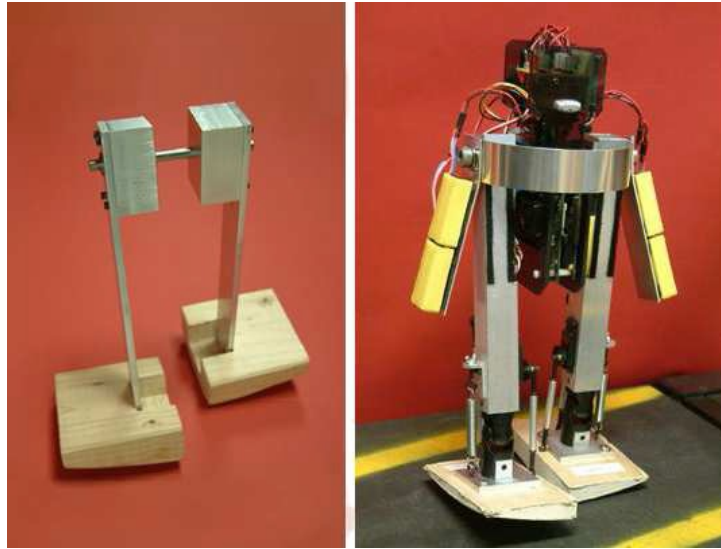


Figure 2.22 A simple passive dynamic robot (left) and Toddler (right) [171].

angular momentum.

Successfully, by making small and random changes to the parameters and measuring the change in walking performance, a statistical gradient following algorithm which combined measurements from previous steps with the measurement from the current step was presented to improve the stability of the step-to-step dynamics. Since the learning problem was simplified by the intrinsic mechanical stability, the robot could continuously adapt to the terrain during walking due to the sufficiently rapid learning. Experimental results revealed that with the right mechanisms based on biomechanics, human bipedal locomotion is energy-efficient and possibly less difficult to control than originally thought [171].

Cornell Ranger

To approach the high reliability and the low power usage of human walking on flat ground, Ranger [173-176] was developed by Bhounsule, Ruina *et al.* between 2006 and 2012. As shown in Figure 2.23, the Cornell Ranger (stands about 1 m tall and has a total mass of 9.9 kg including batteries) is a knee-less four-legged bipedal robot which is computationally and energetically autonomous, except that it need to be started manually and steering is done based on a hobby-type radio control. The inner pair of legs, same as the outer pair, move together acting as one leg. And each leg has an ankle and a foot without knee joint, with the outer feet moving in union due to long cables through the box and the inner feet connected to move together through a horizontal shaft. Ranger has three internal degrees

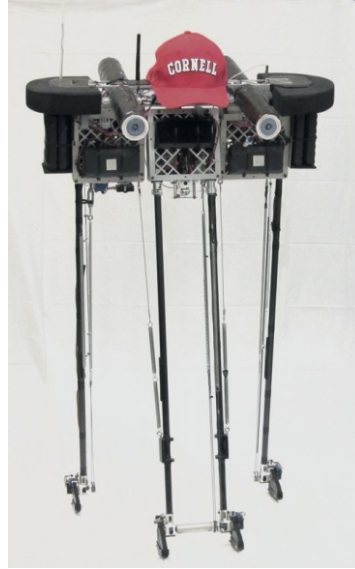


Figure 2.23 Cornell Ranger [176].

of freedom including one hip and two ankles that are all powered by brushed DC motors. A hip spring tending to align the legs was in parallel with the hip motor, and two ankle motors were near the hip axis to actuate the ankles via one-way (toe-off) cable drives [176]. For ground clearance, a return spring on each ankle was used to power foot lifting. Besides, a small force motor was implemented to steer the robot by twisting the inner legs about a vertical axis.

Without being touched by a person, Ranger could walk 65.2 *km* in 186,076 steps and about 31 *h* with low energetic cost of transport (c_{et} of 0.28, comparable to human walking), which was achieved by the development of an intuitively tuned nominal trajectory based on simple bipedal locomotion models, an accurate bench-test-based simulation, and the offline design of a simple reflex-based feedback stabilizing controller. The robot consumed 11.5 *W* including positive mechanical work (~21%), motor dissipation (~34%), sensors, processors and communications (45%) [176]. Therefore, the high reliability and low energy use of Cornell Ranger suggests that simplified implementation of offline trajectory optimization, stabilized by a low-bandwidth reflex-based controller, could be reasonably adopted to investigate the energy-effective reliable human bipedal locomotion.

2.3.1.3 Other Bipedal Robots Based on Precise Control Scheme

Lucy

To explore the role of compliance in walking and running, a bipedal robot called Lucy

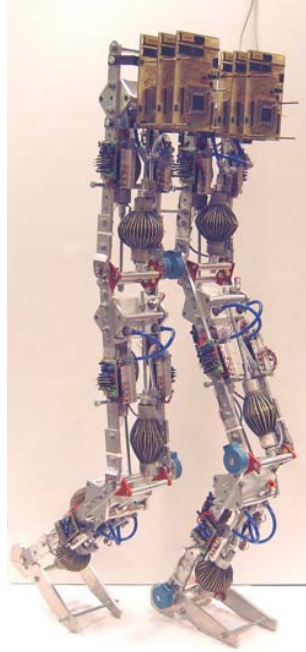


Figure 2.24 Lucy [177].

[177] was developed in 2005 at Vrije University of Brussel in Belgium, using pleated pneumatic artificial muscles, the torque and the compliance of which were controllable. Figure 2.24 shows the complete robot Lucy that is 150 *cm* tall weighs less than 30 *kg*. The structure was made of aluminium alloy (AlSiMg1) and was composed of an upper body and two legs (each of which had an upper leg, a lower leg and a foot). One-dimensional pin joints were used to connect the ankle, knee and hip. Besides, a vertical and horizontal sliding mechanism by means of a seventh pin joint was connected to the hip to avoid turning over in the frontal plane, and Lucy could move restrictedly in the sagittal plane to avoid unnecessary design and control complexity.

Inverse dynamics combined with an addition of PID control were used in the tracking-joint control system, with ZMP criterion used to generate the walking trajectories [177-184]. The strategy based on a single pendulum structure was developed to reduce energy consumption, combining actively trajectory control with the exploitation of the natural dynamics. However, the robot was only able to walk at the maximum speed of 0.15 *m/s* due to flat feet and the slow dynamics of the muscle-controlled valves. Since the muscles have a high power to weight ratio and their compliant behaviour helps in absorbing impact shocks, storing and releasing of energy [177, 180, 185], Lucy could be successfully used as a tool to investigate the role of compliance in human bipedal locomotion such as energy efficient walking and running.

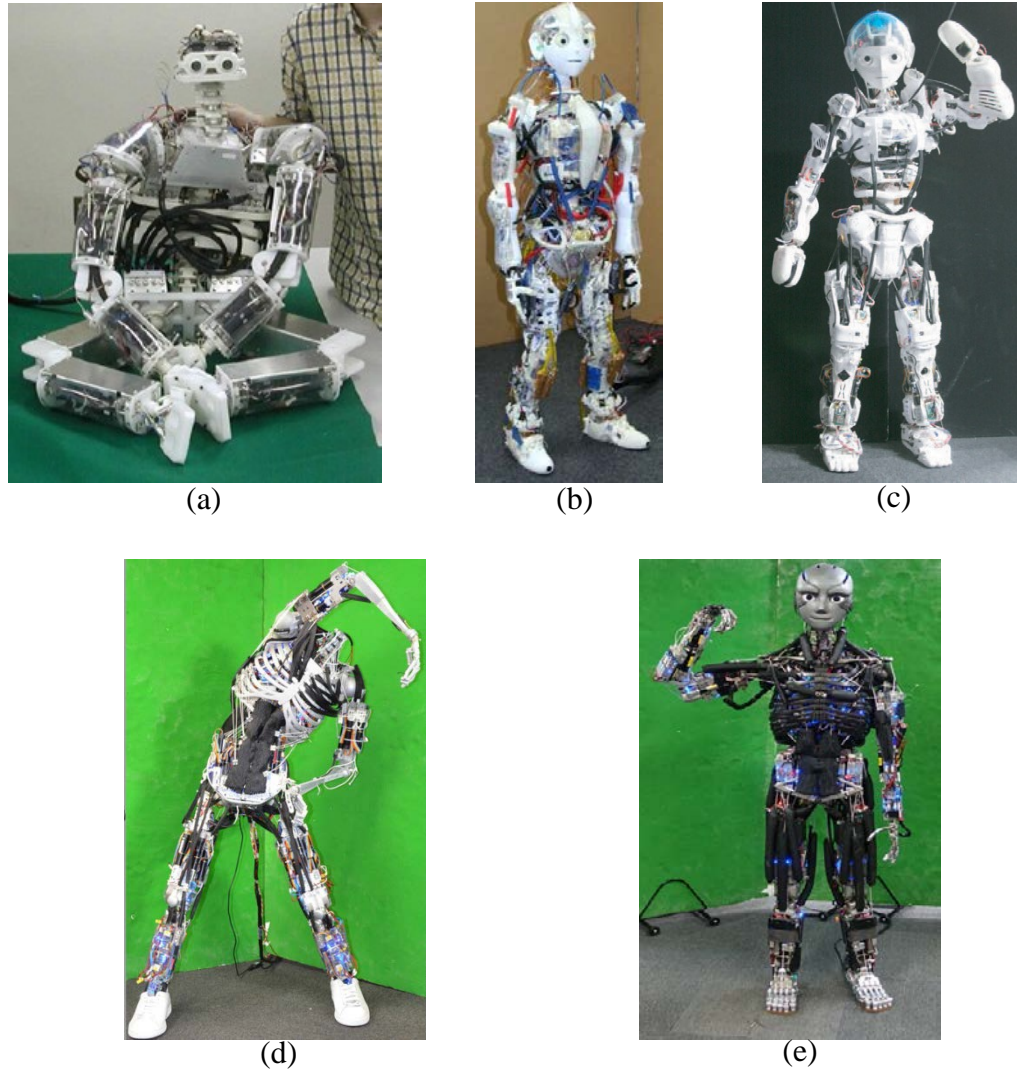


Figure 2.25 (a) Kenta, (b) Kotaro, (c) Kojiro, (d) Kenshiro, (e) Kengoro [186, 187].

Kenta, Kotaro, Kojiro, Kenshiro and Kengoro

Form 2000, the JSK Laboratory at the University of Tokyo started their study on whole-body musculoskeletal humanoids as shown in Figure 2.25, with the aim of learning human musculoskeletal structure and function, and understanding how to manage its complex body. Kenta [186, 188, 189] was unveiled in 2002 as the first life-size prototype, the characteristics of which was a complicated trunk structure with vertebrae (imitating human vertebrae structure with a lock mechanism designed to prevent excessive movement), which was made of moulded plastic resin by Selective Laser Sintering (SLS) method (used in all this series of musculoskeletal robots). However, Kenta could not achieve any low limb motions. Improving the actuation power, Kotaro [186, 190] was developed in 2006 with the ability of standing to some degree which Kenta never could do.

In addition, it has a compound shoulder structures consisting of a collarbone and a scapula [191], resulting in human-like upper body natural movement. In order to solve lack of joint power in Kenta and Kotaro, Kojiro with high-power actuation system [186, 192] was designed in 2007 with the leg embedding enough actuators to conduct stepping, and walking with the support by human [193]. Besides, Kojiro adopted new spherical chest shoulder joint mechanism [194, 195] to move more smoothly with less friction.

All the robots mentioned above were designed by changing and simplifying the tendon arrangements and bone shapes as compared to human body, however, due to the limitation of implementation technology (i.e., bone materials and actuators), they were all inadequate as an agile and complex human body in the real world. Therefore, Kenshiro [186, 196-198] and Kengoro [187, 199] were developed to imitate human body with great accuracy, such as weight ratios and sizes of each bones/limbs, muscle arrangements and joint arrangements and muscle output power. Kenshiro stands 158 *cm* tall and weighs approximately 50 *kg* corresponding to almost Japanese 12 years aged boy with a total of 64 joint DoF. The joint structures of Kenshiro especially the spines and knee joints were different from conventional musculoskeletal robots. According to human anatomical data, in the spine structure, lumbar vertebrae was designed as a five-series articular joint structure, each joint of which could rotate in roll and pitch axis but not in yaw axis. Also, the chest was designed as a solid construction with no movable parts, in which 30 actuators were embedded to drive cervical vertebrae (neck), lumbar vertebrae (spine) and arms. In each knee of Kenshiro, a parallel linkage structure (as human cruciate ligaments) combined with a floating bone (as a patella) were designed to achieve a screw home movement (typical movement of human knee). Besides, the muscle arrangement imitated human main muscle arrangements (especially the geometric positions of muscle insertion points in bones), while sophisticated bone was designed to imitate human-like bone shapes. With these special structures, Kenshiro could perform some human-like motions including twisting, squatting, and one-step walking (falling down after that motion) [200].

The idea of multifunctional skeletal structures was adopted in the design of Kengoro to achieve both humanoid performance and human-like proportions and devised sensor-driver-integrated muscle modules for improved muscle control. It was equipped with human mimetic five-fingered hands and feet. Multi-DOFs and multi-sensors were implemented in the foot to facilitate natural adaptation to the ground. The toe is actuated by a muscle connected to a 90-W motor placed on the lower leg link to perform tip-toe

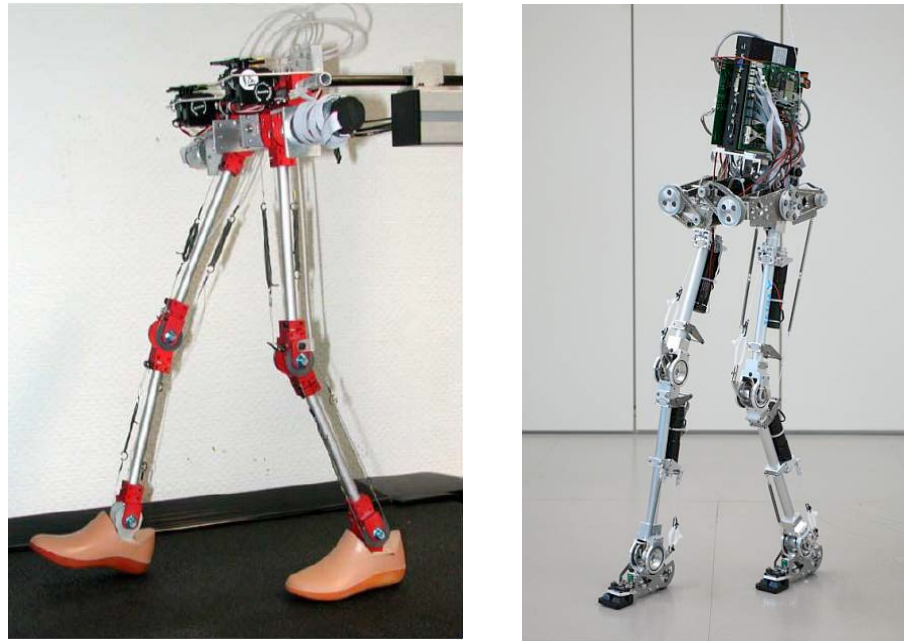


Figure 2.26 JenaWalker II (left) and BioBiped (right) [201].

standing with support by hands for balancing. The skeletal structure is composed of a combination of extra super duralumin (A7075) and carbon fibre-reinforced plastic for more strength and lightness. Several body parts, such as the outer cover, were 3D printed, same with Kenshiro. Two types of sensor-driver-integrated muscle modules were used to control the muscle force. Antagonist inhibition control was designed to contributing to arm movement in a wide range of motions.

Although, all this series of musculoskeletal robots were equipped with conventional DC motors and sensors, they could not achieve any dynamically stable bipedal locomotion, even just walking.

BioBiped1

In 2010, BioBiped1 [201, 202] was presented as the first of a planned series of musculoskeletal robotic platforms (BioBiped project) being developed by TU Darmstadt for the purpose of long-term investigating and evaluating hypotheses and theories from biomechanics of human locomotion (3D stable walking, running, and standing) in real robots. Based on the previously developed JenaWalker II (Figure 2.26a), an elastic and biologically inspired bipedal walking robot attached at the trunk to a lateral guide [203-205], BioBiped1 (Figure 2.26b) stands approximately 97 *cm* and weighs 9.5 *kg*. It consists of a trunk, a hip and two legs, each of which is composed of three segments (foot, shank

and thigh) corresponding to the human anatomy. It has six DoF, one DoF in each knee and ankle for the pitch movement, and two DoF in the hip for the roll and pitch movement.

The movement of the elastic leg was enabled by the integration of muscle-tendon-like structures: mono-articular muscles spanning only one joint were placed in the hip, knee and ankle joints for power generation, while bi-articular muscles that could span two joints and extend and flex the coupled joints in coordination were placed in thigh and shank for transfer of energy and coordination of joint synchronization. Extensors of the knee and ankle joints were integrated by unilateral structures, each consisting of a cable including an extension spring in series with a geared rotary electric direct-current motor. Also, DC motors were incorporated for the mono-articular extensors of each knee and ankle muscle pair as actuators, while a bidirectional series elastic actuator was attached to the muscle pair in the hip [206-209]. For monitoring, analysing and evaluating motions, an analogue device inertial measurement unit was mounted on the hip, while position sensors were placed in the joint and force sensors in the feet.

A bio-inspired approach for joint position control based on a learning inverse dynamics [206], combining a basic feedback control (i.e., conventional PD-control) with a feedforward control, was designed to generate hopping motions. Although BioBiped1 could only perform hopping motion not any running and walking, it showed that by using compliant mono- and bi-articular structures based on human-like segmentation and actuation of the legs to mimic main human leg muscle groups, typical human functionality in running and walking could be achieved.

Athlete Robot

To understand the role of the musculoskeletal body and investigate how humans control their complex body in dynamic locomotion, especially sprinting as it requires maximizing the potential resources of a musculoskeletal structure, Athlete Robot based on the anatomical structure of a human being was developed by Niyama *et al.* in 2010 [210, 211].

As shown in Figure 2.27, it stands 1.2 m tall with the legs extended and weighs about 10 kg. Similar to the human body that is comprised of unique mechanisms such as elastic tendons, bi-articular muscles and antagonistic drive, the Athlete Robot has an artificial musculoskeletal system mimicking the anatomical structure of a real person, i.e., corresponding to the major muscles distribution of the lower extremity of human body, the

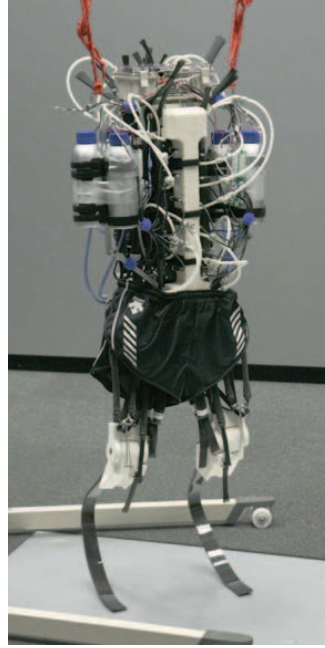


Figure 2.27 Athlete Robot [210].

robot has mono- and bi-articular muscle groups with each muscle group composed of several muscles. Besides, an elastic blade was implemented simply as the tendons around the ankle joint to store energy and absorb impact from the ground. The pneumatic muscle actuators were used for the system allowing compliant and agile movements. Force/torque control could be easily achieved by using pressure control, while custom-made proportional control valves were employed to control the inner pressure of the muscles [211, 212]. Pressure sensors in the muscles, contact sensors in the feet, and an inertia measurement unit (IMU) were placed for measurement.

The Athlete Robot, based on activation patterns for the pneumatic actuators derived from human EMG data and controlled by feedforward motor command, has successfully achieved five running steps and travelled approximately 4 m with an average velocity of 2.42 m/s (i.e., 8.7 km/h) [213]. The experimental results revealed the significant contribution made by a lower limb musculoskeletal bipedal robot and feedforward motor command in agile human-like legged locomotion. However, the motion information measured by the sensors was not used to supplement the motor commands, and running at various speeds and steering control should be explored in future study.

2.3.2 Using Bipedal Robots to Study Neuroscience

Human body is able to move with elegance and efficiency combining appropriate

biomechanics in musculoskeletal system with neural control. As a prominent example of this, human walking is a dynamic, partly self-stabilizing process relying on the interaction of the biomechanical design with its neural control. It has been suggested that these agile motor movements involve a hierarchy of levels, where higher level control (e.g., cortical) arises only pointwise, and where the lower ones (e.g., interactions between muscles and the spinal cord) are largely autonomous, as needed. Apart from studying this process from observing and measuring human activities, bio-inspired bipedal robot is another feasible tool to investigate the scientific theory in neuroscience of human body, which will be discussed next.

DB and CB

With ERATO Kawato Dynamic Brain Project, in collaboration with the SARCOS Research Corporation in USA, ATR Laboratories in Japan developed an anthropomorphic bipedal robot called Dynamic Brain (DB) between 1996 and 2001 [214] with the aim of studying how human brain generates behaviours.

As shown in Figure 2.28a, DB stands approximately 1.85 m tall and weighs 80 kg with legs, arms (with palms but no fingers), a jointed torso, and a head equipped with an artificial vestibular organ (gyro sensor). Containing 25 linear hydraulic actuators and five rotary hydraulic actuators, it has 30 degrees of freedom (three in the neck, two in each eye, seven in each arm, three in each leg, and three in the trunk), each DoF has a position sensor and a load sensor except for the eyes. By using the algorithms based roughly on principles of information processing in the brain containing some or all of three learning elements (supervised learning, imitation learning, and reinforcement learning), the robot DB could perform 30 different tasks [215-220] including Okinawan folk dance “Katya-shi” [221], three-ball juggling [214], devil-sticking [222, 223], air-hockey pole balancing, sticky-hands interaction with a human [224], tumbling a box [225], tennis swing [226], playing air hockey against a human opponent [222, 223] (Figure 2.29), visually-guided arm reaching toward a target, adaptation of smooth pursuit eye movement and the vestibulo-ocular reflex [227], drumming, and paddling a ball. However, DB could not work autonomously as it needs to be powered by an external hydraulic pump through oil hoses arranged around the mount and a computer system connected to by wires.

Subsequently, following the ERATO Dynamic Brain Project, Gordon Cheng *et al.* started the ICORP Computational Brain Project (2004-2009) in collaboration with

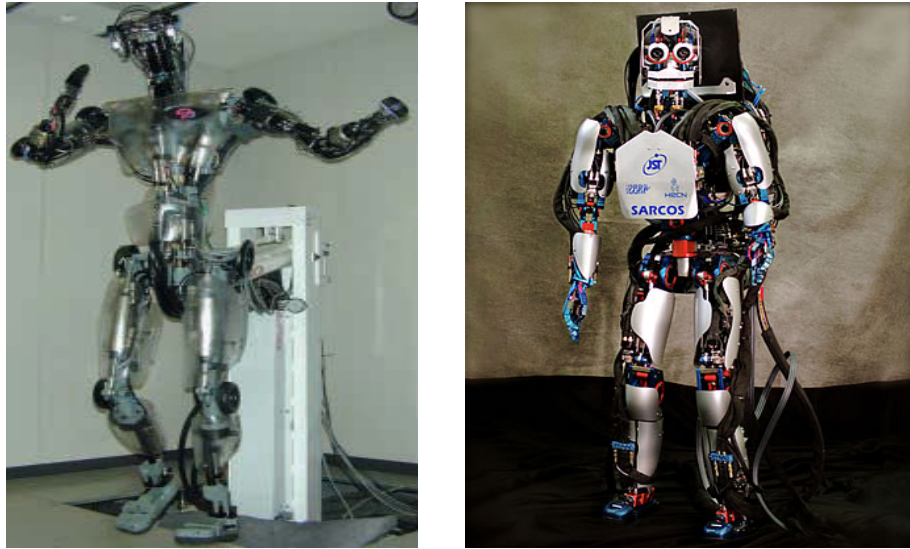


Figure 2.28 DB (left) [214] and CB (right) [228].



Figure 2.29 DB playing air hockey against a human opponent [222, 223].

SARCOS, leading to development of another bipedal robot called CB [228-230] with the goal of investigating human-like information processing and exploring the underlying mechanisms of the human brain while dealing with the environment in real world. In contrast to DB, CB was designed for full-body autonomous interaction, specifically for walking and simple manipulations. It stands 157.5 *cm* tall, weighs 92 *kg* as shown on the right in Figure 2.28b and has a total of 51 degrees-of-freedom (14 in the legs, 14 in the arms, 4 in the eyes, 3 in the neck, 1 in the mouth, 3 in the torso, and 12 in the hands). Successfully, CB was presented experimentally with three main abilities: human-like locomotion (walking) [231-234], full-body compliant control (3D balancing and physical

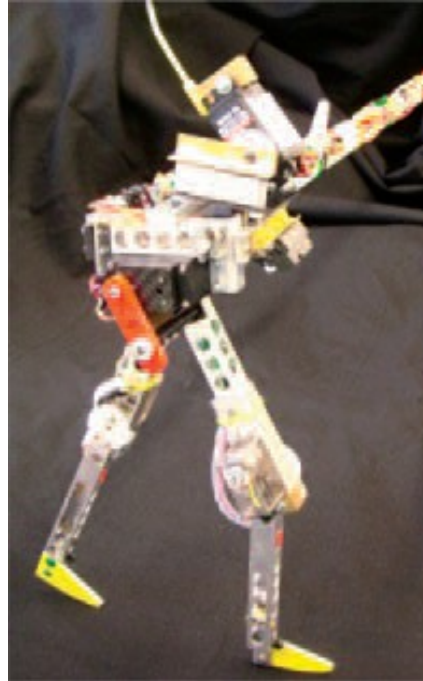


Figure 2.30 RunBot [7].

interactions) [29, 235-237], and perception (visual processing and ocular-motor responses) [228, 238, 239].

RunBot

In 2006, Manoonpong from University of Göttingen *et al.* developed RunBot based on passive dynamic walking principles and neuronal control with simulated synaptic plasticity [7], aiming at better understanding the interaction of different components in human walking as well as in other complex movements.

As shown in Figure 2.30, RunBot stands 23 *cm* and has four active joints (right and left hips and knees) driven by modified RC servo motors. It has curved feet allowing for rolling action and a lightweight structure with proper distribution of mass at the limbs. A hard-mechanical stop was installed on the knee joints, preventing it from going into hyperextension, similar to the function of knee caps in human. The RunBot can walk at the speed of up to 3.5 leg-length/s which so far has not been achieved by other dynamic walking robots, using three levels of control that are biomechanical level (biomechanical design inspired from passive walking robots to assure stability), spinal reflex level (low-level neuronal structure creating dynamically stable gaits with some degree of selfstabilization to assure basic robustness), and postural reflex level (higher levels of

neuronal control using peripheral sensing to assure flexibility of the robot in different terrains).

Nonetheless, it is a passive dynamic walking robot, as it does not use any explicit gait generation or precise tracking joint control, but instead fully relies on two neuronal control levels. In addition, the network could learn to use mechanisms of simulated synaptic plasticity at the postural reflex level, emulating the idea of learning to avoid a long-loop body-reflex. Successfully, RunBot is the first to use a similar hybrid and adaptive, mechano–neuronal design strategy to design and control a small, fast biped walking robot and to make it learn to adapt to different terrains to some extent [7, 240, 241]. Finally, it was shown that the tight coupling of biomechanical design with neuronal control, guided by sensory feedback from the walking pattern, combined with synaptic learning may be a reasonable way to better understand and investigate the scientific theories in human locomotion.

iCub

Through five-year RobotCub Project (2005-2010) [242, 243], a child-size bipedal robot iCub [244-247] was developed by Italian Institute of Technology (IIT) as an open humanoid platform for cognitive and neuroscience research, with the aim of advancing the neural understanding of cognitive systems, i.e., how a human child learns the basic motor skills as well as learning and recognizing different objects.

The robot iCub is a whole-body robot consisting of a head, a trunk, two arms, two hands, a waist, and two legs with totally 53 degrees of freedom as shown in Figure 2.31. It stands approximate 1 *m* tall and weighs 22 *kg* comparable to the size of a 3.5-year-old child with a mechatronic, modular, and compact architecture. The robot was equipped with two digital cameras, microphones, gyroscopes, accelerators, and force/torque sensors in all the actuated joints. The local DSP joint controllers (that were used to process the low-level control loop in real-time) communicated with each other via CAN bus which connected to the central PC104 computer (in the head of the robot). Besides, an Ethernet Protocol connection was adopted to connect the PC104 computer to an external PC cluster [246, 247].

Based on different sensorimotor coordination models, a layered controller system was designed to make iCub perform various tasks, e.g., drumming, crawling, reaching sitting,



Figure 2.31 iCub [248].

squatting, wearing hats, grasping the usual ball, and even assembling LEGO bricks [244-246, 249-252]. However, the robot iCub could not achieve stable walking influenced by both the mechanical design of the legs (that lacked robustness enough due to the cable drive system connecting the motors to the ankle joints) and communication network delays (limitation of the CAN network).

Infant Robot

In 2009, an infant-sized musculoskeletal robot Pneuborn-7II [253] driven by McKibben pneumatic actuators, based on a previous pneumatic musculoskeletal system [254-256], was designed by Narioka *et al.* of Osaka University with the goal of clarifying the role of embodiment (especially the musculoskeletal system of human body) in the early stage of the development in the real world. It stands 0.8 m and weighs 5.44 kg as shown in Figure 2.32, with 26 degrees of freedom (ten in the arms, ten in the legs, two in the neck, and four in the trunk). Ball and socket joints were used in shoulder and hip joints that were attached to the trunk with certain angles, according to the anatomical structure of a real human infant. Besides, a spinal structure was implemented by three pitch and three yaw joints to make the trunk rotate, flex, and extend. The pneumatic muscles were placed in the shoulder, hip, knee, neck, and trunk joints (the other joints were passive), with a bi-articular muscle implemented over the hip joint and the knee joint corresponding to a human hamstring.

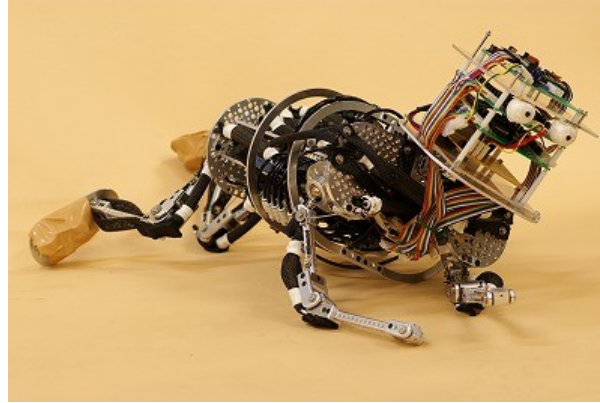


Figure 2.32 Pneuborn-7II [253].

CPGs and Powell's optimization method were applied to acquire locomotion especially crawling motion with the maximum speed of 0.82 m/min . The infant robot has the ability to move around for at least several hours without breakdown and overheating, for an extended period in contact with the environment [257]. However, there are some issues existing in the robot such as the much lower crawling velocity compared to the real infant human that are caused by both hardware and software design, and small parameter search space.

2.4 Conclusion

As mentioned above, studying bio-inspired bipedal robots is an enormous endeavour with two main objectives which are taking inspiration from biological principles to emulate human agile behaviours (e.g., walking, running, climbing, crawling and dancing), and using these robots as scientific tools to investigate hypotheses and scientific theories of human anatomy (e.g., biomechanics, neuroscience, and human body functions and properties). Although there are many common aspects and methods between the two objectives during the construction of the physical models (i.e., the robots), some subtle but important points also exist. Most importantly, the ultimate purpose of the research is different. The first objective can contribute to robotics research such as providing a feasible method that is simpler (low complexity of implementation) or better (such as energy consumption, motion velocity, and agile movements) than other methods to achieve human-like motions in the robot. The second objective can contribute to the investigation of human biology such as proposing new experimental methods, validating experiments against human data, or providing new hypotheses and theories to

biomechanics, neuroscience, or understanding of human structures and properties, etc.

Therefore, a study in this field should start with properly defining the ultimate goal (one or both). Otherwise, it is completely risky if the results of this study contribute neither to robotics (no meaningful method) nor to human biology (not in accordance with the well-established theories, methods, and experiments).

The last 50-year human history, especially after ZMP criterion and its relation to human walking stability being proposed in 1969, has seen great progress and advance in the bipedal robots that aim at contributing to robotics (the first objective). However, most of them use multiple high-torque actuators and sophisticated control schemes (e.g., ASIMO [50, 51], HRP Project [60], QRIO [121, 122], and Atlas [136]) to carefully control all joints at any given time. Running, climbing, jumping, swimming and rapidly catching moving objects appear as natural and quite easy activities for a healthy human, yet big challenges exist for these impressive robots. This is mainly caused by the difficulty of motor interaction of complex multi-joint movements which requires appropriate biomechanics, neuronal control system, and adaptivity with the environment. Unlike robots, a human, however, is able to perform agile motor behaviours with elegance and efficiency. Generally, these mainstream robots are far from human-like because they require actuation in the joints to perform any motion, as opposed to human locomotion (e.g., walking) that extensively relies on natural dynamics of the neuro-musculo-skeletal system (such as pendulum-like swinging movements of the limb). Therefore, such robots are highly inefficient from an energy point of view, and are extremely stiff so that they can not perform flexible behaviours. Due to the limitation of the physical model, one of the most recent solution is developing more bio-inspired control algorithms, e.g., CPGs [16] and learning approaches [17], to achieve more human-like movements.

Along with the explosive development of humanoid robotics, bio-inspired bipedal robots designed as scientific tools are increasingly contributing back to human biology. The most conventional methods of studying human biology are observing people as they move [147, 258], measuring desired data by electrical devices during experiments on a real person, and numerical simulation [259] in computer. As the new and impressive methods to investigate human biology, bio-inspired bipedal robots can become important component of the scientific cycle of producing hypotheses, conceptions and assumptions, testing them in experiments and adjusting them properly towards new theories. Repeatable,

parameterized experiments can be conducted in the robot model by programming. Relevant variables and parameters difficultly measured on human can be monitored by implementing multiple sensors (e.g., internal forces) in them. The morphology of robots can be changed in systematic ways to perform different tasks [201]. They can perform movements that would be dangerous or even unreasonable for human, exploring the optimization of human movements (e.g., motions, exercises or sports that are helpful for human health). Thanks to the more advanced communication and computer technologies, the robots can be controlled by numerical models (controllers) that replicate some parts of the neuronal control system inspired from human nervous system [7, 240, 241]. Using the right type of actuators and materials (e.g., muscle-like actuators [177, 184]), and human-like body structure (e.g., series elastic cable-spring structure inspired from human muscle-tendon groups [201]), compliance of the musculoskeletal system can be properly mimicked. Moreover, they can be a testbed for experimenting new active exoskeletons and prostheses, which could reduce the risks on human body caused by inappropriate design. In a word, bio-inspired bipedal robots can be used to conduct some experiments that would be harmful or even impossible for human to do. In the future, they might even reduce the necessity of human involving in the experiments.

The above-mentioned robots have made valuable contributions to understanding the musculoskeletal system of human body. Yet, the biomechanics including kinematic (e.g., joint axis of rotation) and kinetic (e.g., mechanics of body segment and 3D musculoskeletal geometry) characteristics of these robots has not been thoroughly related to human musculoskeletal characteristics. In fact, human movement is a process of morphological computation based on the physical body during interaction with the environment, and depends heavily on the mechanical properties, joint parameters, and arrangement of perceptual, motor, and processing units. It is important to choose the appropriate features and functional parts to replicate in the robot so that it has compatible structure and function interplay of the human body whilst complying strictly with physical rules for further research on human MSK. This is often the case with the biomechanics of human MSK which governs biped locomotion, including the body segment properties, joint parameters and 3D musculoskeletal paths.

Since understanding agile movements requires a systematic approach that explores the interaction of all involved components (the musculoskeletal system, the nervous system, and the environment), a more elaborate model that takes into account more aspects of the

human neuro-musculo-skeletal system (e.g., with anthropathic skeletal body structures, multiple muscles, and multi-layered neural control levels) is a key research aspect to make a contribution to robotics or human biology. It is important to choose the appropriate features and functional parts of human biology to replicate in the robot. As not all structures and features during human locomotion are dispensable for robot locomotion, only replicating the key relevant features to design a bio-inspired bipedal robot is required.

Chapter 3

Biomechanics of Human

Musculoskeletal System

This chapter studies the biomechanics of human musculoskeletal system (MSK), which gives humans the ability to move with elegance and efficiency using the skeletal system and the muscular system. As million-year selection and evolution, the human MSK evolves to be a highly ideal mechanical mechanism to support and transport the human body, which could inspire engineers to develop robots as effective and economic as humans using innovative technology and methodology.

Human musculoskeletal system, composed of bones, cartilages, skeletal muscles, tendons, ligaments and other connective tissues, provides form, support, behaviour and stability for the human body. The skeletal system provides the fundamental framework for body shape and load bearing, and also protects human body from external impacts, where joints connect all the bones. The muscular system is the prime mover of human movements, where skeletal muscles are arranged in layers over the bones and normally attached to bones through tendons so that the energy generated from the contractile elements of the muscle fibres can drive body motions [260].

Since each individual has different characteristics in terms of body structure, mechanical properties and muscle arrangements, we cannot explore human MSK from anatomy books or any commercial human model which are generalised and scaled from millions of human data. For example, the body shape of a 100-kilogramme male is obviously incomparable with a 50-kilogramme male leading to completely different mechanical properties, but in commercial model or anatomy books there is a scaled factor

to generalize and unify them to the same standard. Even if the body structure and the mechanical properties of two individuals are equivalent, their muscle arrangements may vary a lot which affects the moment arm of muscle contraction during human movements. Muscle origin, insertion and volume depend both on inborn and postnatal exercise. A person who takes regular exercise could lift much heavier stuff than a physically inactive one with similar body properties. Thus, a more systemic method should be applied to study human MSK for better developing bioinspired bipedal robots or bio-robots.

We study and investigate human MSK using the same subject. A three-dimensional (3D) whole-body musculoskeletal model of a healthy male subject constructed from the Visible Human Project database was used as the biological counterpart to inspire the design of the robot. Results in the analysis of the biomechanics of human body will be presented, mainly showing the segmentation, body segment properties (mass centre, mass ratio, and moment of inertia), joint parameters (joint centre and axis of rotation), and muscle path of the whole body, etc. The work in this chapter was conducted mainly in the University of Manchester and partly in Jilin University.

3.1 Data Source

Unlike learned from human anatomy books or some commercial software which only give the general concept and functions of the muscles and the bones, computer-generated phantoms are a more suitable tool to study the biomechanics of human MSK where I can directly or indirectly obtain the morphological, anthropometric, kinematic and kinetic data of each body segment and joint. Image processing such as Computed Tomography (CT), Magnetic Resonance Imaging (MRI), ultrasound and cryosection images can be used to correctly examine the anatomy, structure and geometry of human MSK with high accuracy. Reverse engineering such as Mimics, Rhino and Amira software can be applied to rebuild the 3D musculoskeletal model.

The Visible Human Project (VHP) from U.S. National Library of Medicine (NLM) has created publicly-available complete, anatomically detailed, 3D representations of a human male body, which provides a public library of cross-sectional cryosection, CT, and MRI images obtained from one male cadaver [261-263]. Based on the datasets, a whole-body computational phantom called XCAT [264-266] has been created in Rhino software by Duke University, of which the anatomy is defined using non-uniform rational b-splines

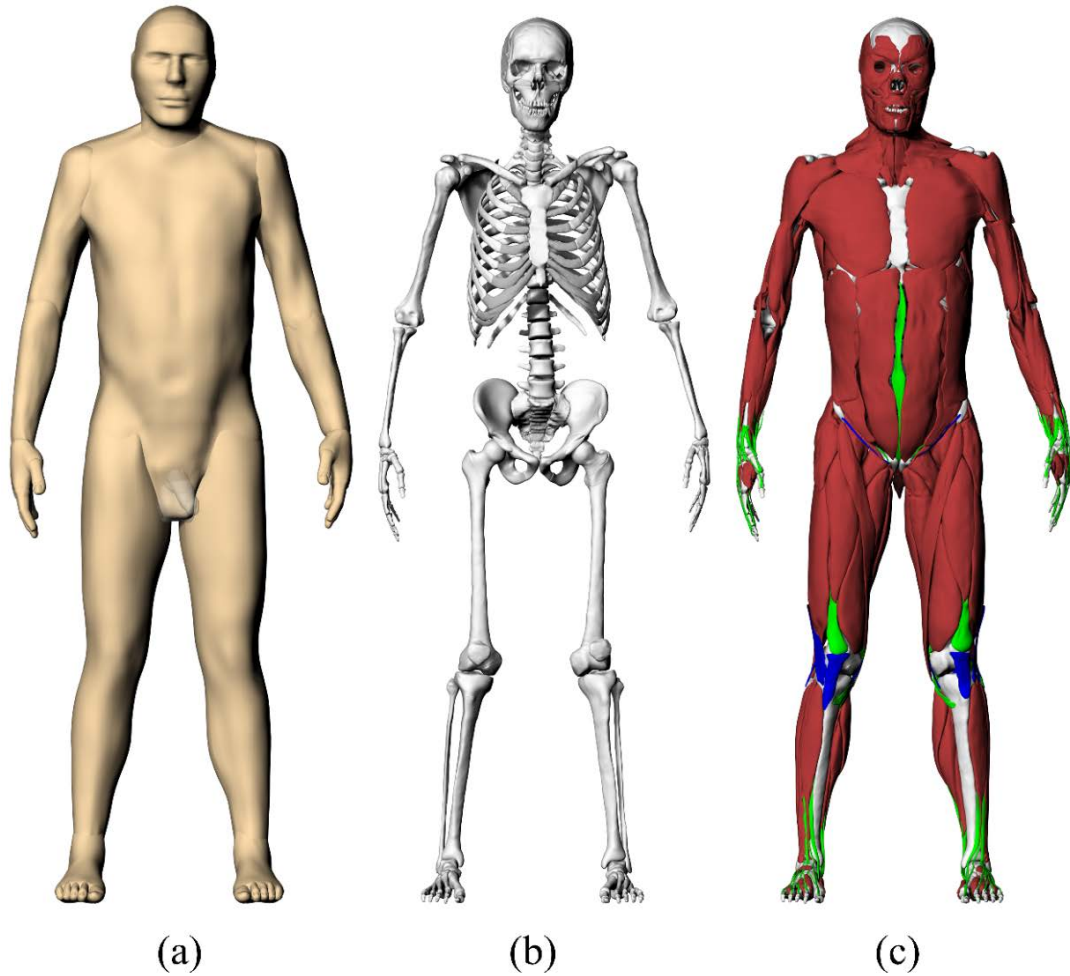


Figure 3.1 Whole body model based on VHP, including (a) skin, (b) skeleton and (c) muscle.

(NURBS) and includes thousands of defined structures.

By converting surface-based model to solid-based model, a 3D whole-body musculoskeletal model consisting of skin, skeleton, and muscles was successfully reconstructed in NX (Siemens, Germany) (see Figure 3.1). For example, the skeleton of human subject is imported to NX by using Step214 file which is exported from Rhino, and all the bones are displayed in the Part Navigator (see Figure 3.2). With the model, the details of the skeletal and the muscular system were quantified and modified. The anthropometric data, the mechanical properties and muscle arrangements were analysed.

3.2 Terminology and Kinematics

Specific terms are used to describe the relationship of one body part/segment/region to

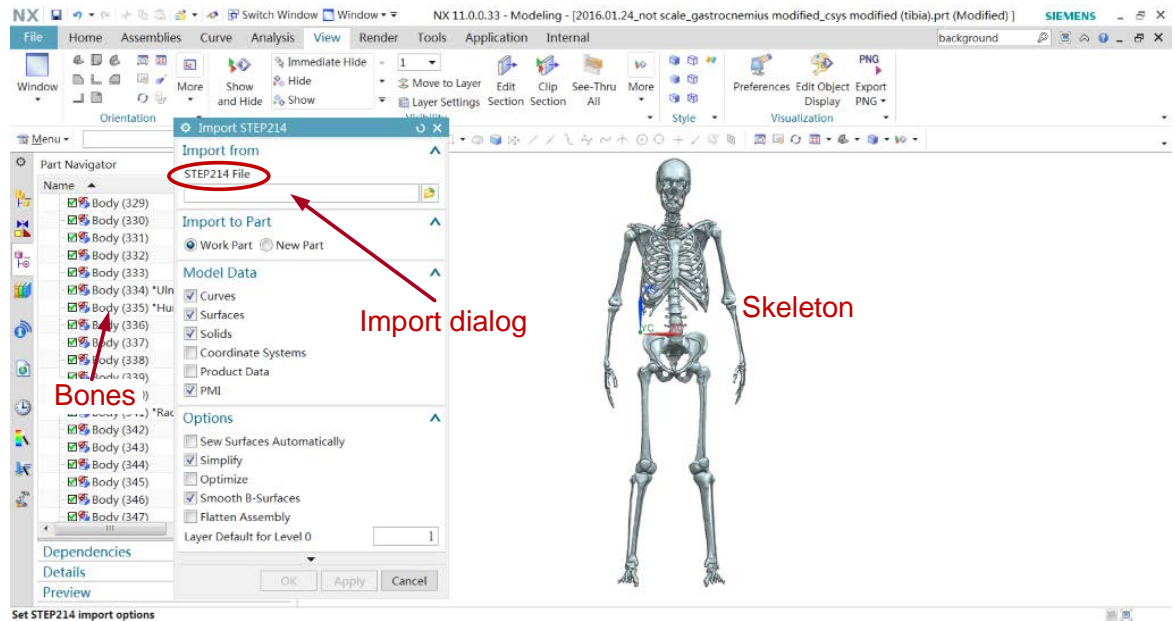


Figure 3.2 Skeleton model in NX imported from Rhino.

another and are considered in relation to the anatomical position of the body. To facilitate the understanding of the relation of structures one to another and the movement of one segment with respect to another, imaginary reference planes pass through the body in such a way that they are mutually perpendicular to each other (Figure 3.3). Passing through the body from front to back and dividing it into two symmetrical right and left halves is the sagittal plane. Any plane parallel to this is also known as a parasagittal plane. A plane passing through the body from top to bottom and lying at right angles to the sagittal plane is the frontal (coronal) plane. This divides the body into anterior and posterior parts. All planes that divide the body in this way are known as (frontal) coronal planes. Finally, a plane passing through the body at right angles to both the sagittal and frontal planes dividing it into upper and lower parts is known as a transverse (horizontal) plane. A whole family of parallel transverse planes exist; it is therefore usual when presenting a particular transverse section to specify the level at which it is taken.

Within each plane a single axis can be identified, usually in association with a particular joint, about which movement takes place. An anterior-posterior directed axis in the sagittal (or a parasagittal) plane allows movement in a frontal plane. Similarly, a longitudinal axis in a frontal plane allows movement in a transverse plane. Lastly a medial-lateral axis in a frontal plane provides movement in a paramedian plane.

By arranging that these various axes intersect at the centre of joints, the movements

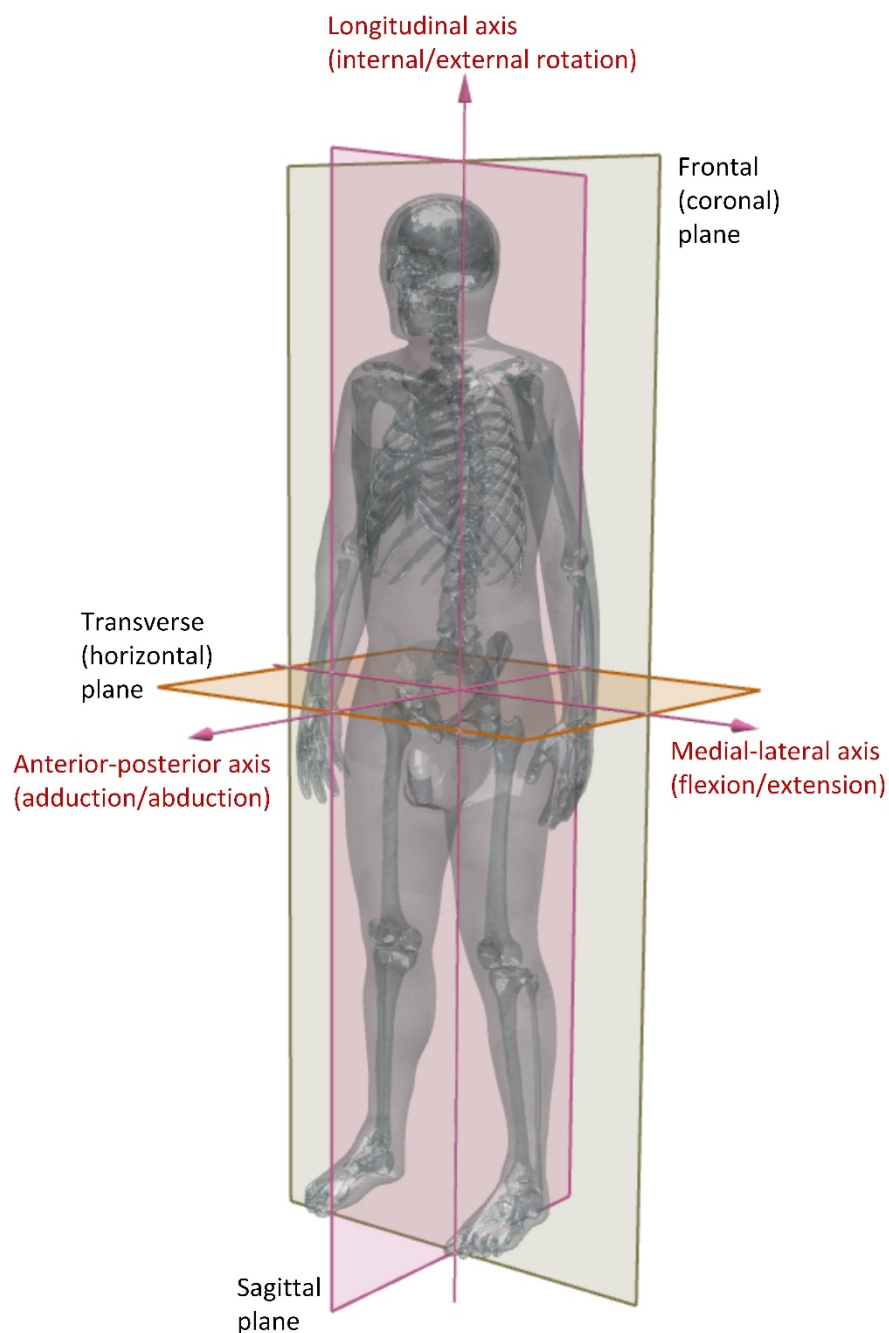


Figure 3.3 Frontal (Coronal), sagittal, and transverse (horizontal) planes in the human body.

possible at the joint can be broken down into simple components. It also becomes easier to understand how specific muscle groups produce particular movements, as well as to determine the resultant movement of combined muscle actions.

Anterior (ventral) means to the front or in front, e.g. the patella lies anterior to the knee joint.

Posterior (dorsal) means to the rear or behind, e.g. gluteus maximus lies posterior to the hip joint. (Ventral and dorsal are used more commonly in quadrupeds.)

Superior (cephalic) means above, e.g. the head is superior to the trunk;

Inferior (caudal) means below, e.g. the knee is inferior to the hip.

Medial means towards the median plane or midline, e.g. the index finger lies medial to the thumb.

Lateral means away from the median plane or midline, e.g. the thumb lies lateral to the index finger.

Kinematics describes the motion of a joint in three planes: frontal, sagittal, and transverse. Rarely do movements of one body segment with respect to another take place in a single plane. They almost invariably occur in two or three planes simultaneously, producing a complex pattern of movement. However, it is convenient to consider movements about each of the three defined axes separately. Movement about a medial-lateral axis occurring in the parasagittal plane is referred to as flexion and extension; that about an anterior-posterior axis in a frontal plane is termed abduction and adduction; and that about a longitudinal axis in a transverse plane is termed internal and external rotation.

All movements are described, unless otherwise stated, with respect to the anatomical position, this being the position of reference. In this position joints are often referred to as being in a 'neutral position'.

Flexion is the bending of adjacent body segments in a parasagittal plane so that their two anterior/posterior surfaces are brought together, e.g. bending the elbow so that the anterior surfaces of the forearm and arm move towards each other (for flexion of the knee joint the posterior surfaces of the leg and thigh move towards each other).

Extension is the moving apart of two opposing surfaces in a parasagittal plane, e.g. the straightening of the flexed knee or elbow. Extension also refers to movement beyond the neutral position in a direction opposite to flexion, e.g. extension at the wrist occurs when the posterior surfaces of the hand and forearm move towards each other. Flexion and extension of the foot at the ankle joint may be referred to as plantarflexion and dorsiflexion respectively.

Plantarflexion is moving the top (dorsum) of the foot away from the anterior surface of the leg.

Dorsiflexion is bringing the dorsum of the foot towards the anterior surface of the leg.

Abduction is the movement of a body segment in a frontal plane such that it moves away from the midline of the body, e.g. movement of the upper limb away from the side of the trunk.

Adduction is the movement of a body segment in a frontal plane such that it moves towards the midline of the body, e.g. movement of the upper limb back towards the side of the trunk.

Internal Rotation is the rotation of a limb segment about its longitudinal axis such that the anterior surface comes to face towards the midline of the body, e.g. turning the lower limb inwards so that the toes point towards the midline.

External Rotation is the rotation of a limb segment about its longitudinal axis so that its anterior surface faces away from the midline plane, e.g. turning the lower limb so that the toes point away from the midline.

Supination is used in conjunction with the movements of the forearm and foot. In the forearm, it is the movement that the palm of the hand faces forwards. In the foot it is the movement whereby the forefoot is turned so that the sole faces medially, and always accompanied by adduction of the forefoot.

Pronation is used in conjunction with the movements of the forearm and foot. In the forearm, it is the movement that makes the palm of the hand face backwards. In the foot it is a movement of the forefoot which causes the sole to face laterally, and always accompanied by abduction of the forefoot.

Inversion is used to describe composite movements of the foot, which is the movement of the whole foot to make the sole face medially. It consists of supination and adduction of the forefoot.

Eversion is used to describe composite movements of the foot, which is the movement of the whole foot so that the sole comes to face laterally. It consists of pronation and abduction of the forefoot.

3.3 Segmentation

Quantitative biomechanical analyses of human movement typically require the estimate of

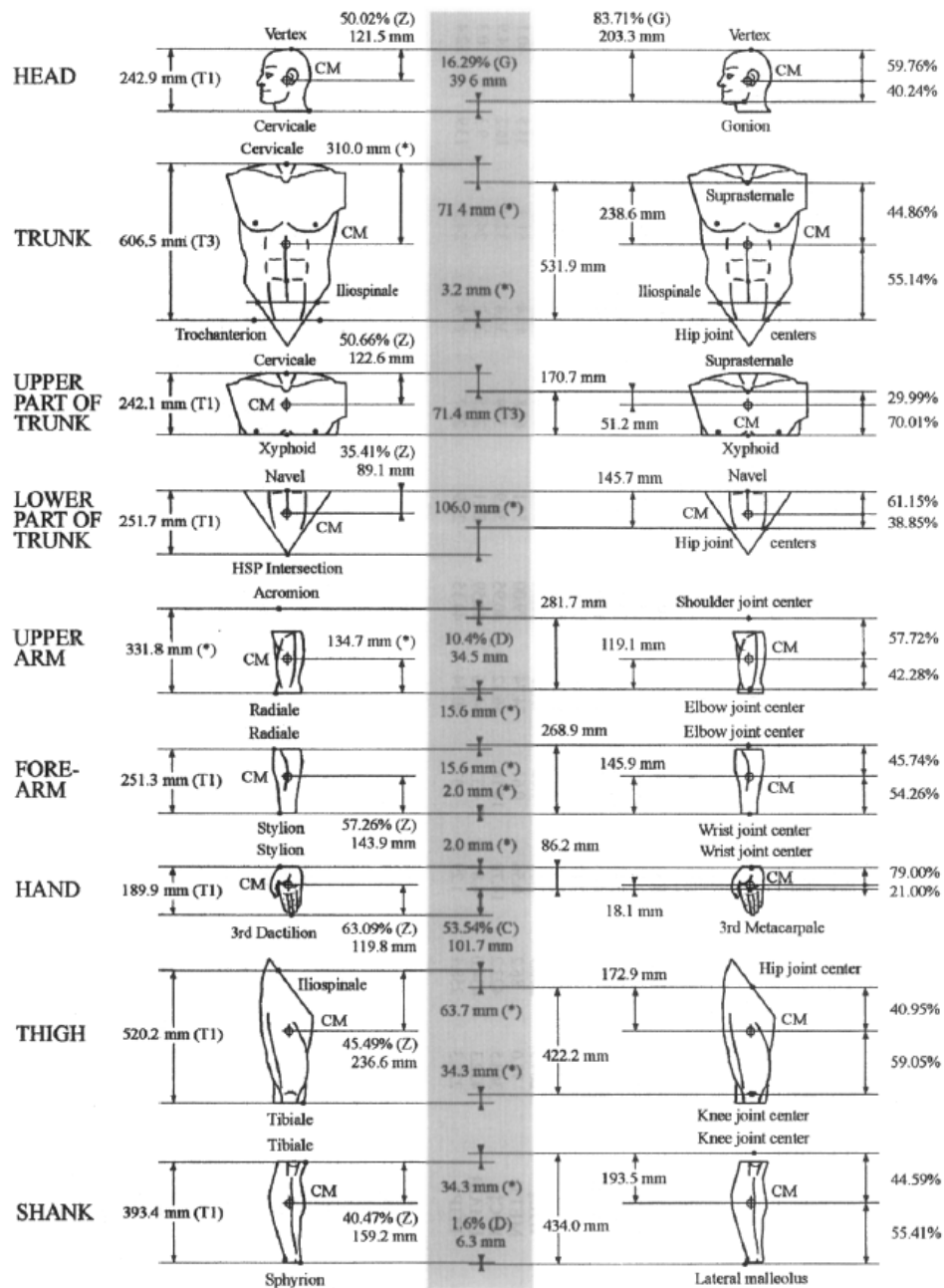


Figure 3.4 Adjustments to Zatsiorsky-Seluyanov's segment inertia parameters. The adjusted distances are shown on the right of the shaded area [267].

the body segment inertia parameters (mass, position of the centre of mass, principal axes and moments of inertia).

Instead of using bony landmarks as reference points for defining segments, joint centres and other commonly used landmarks were adopted to segment the human body based on a number of carefully selected sources of anthropometric data [267] as shown in . In the 3D whole-body model constructed, human body was segmented to

Table 3.1 Estimated segments defined between the respective start points and end points.

Segment	Start point	End point
Head and neck	Vertex	Cervicale
Upper trunk	Cervicale	Xyphion
Middle trunk	Xyphion	Omphalion
Lower trunk (pelvis)	Omphalion	Hip joint centre, HSPs
Upper arm	Acromion	Radiale
Forearm	Radiale	3rd dactylion
Thigh	Hip joint centre, HSPs	Tibiale
Shank	Tibiale	Sphyrion
foot	Sphyrion	Heel

acquire the major functional parts according to the body segment definitions as the adjustments to original Zatsiorsky Seluyanov's dataset [267]. The main landmarks used for segmentation are as follows:

3rd dactylion The tip of the 3rd digit. gonion-the most lateral point on the posterior angle of the mandible.

Acromion The most lateral point on the lateral margin of the acromial process of the scapula.

Cervicale The superior palpable point of the spine of the seventh cervical vertebra.

Heel The posterior point of the heel.

Hip joint centre The joint centre of hip.

Hip Segmentation Planes (HSPs) The boundaries between thighs and trunk, defined as planes passing through the respective hip joint centre, parallel to the trunk sagittal axis, and forming a 37° angle with the sagittal plane.

Omphalion The centre of the navel.

Radiale The most proximal point on the lateral edge of the radius.

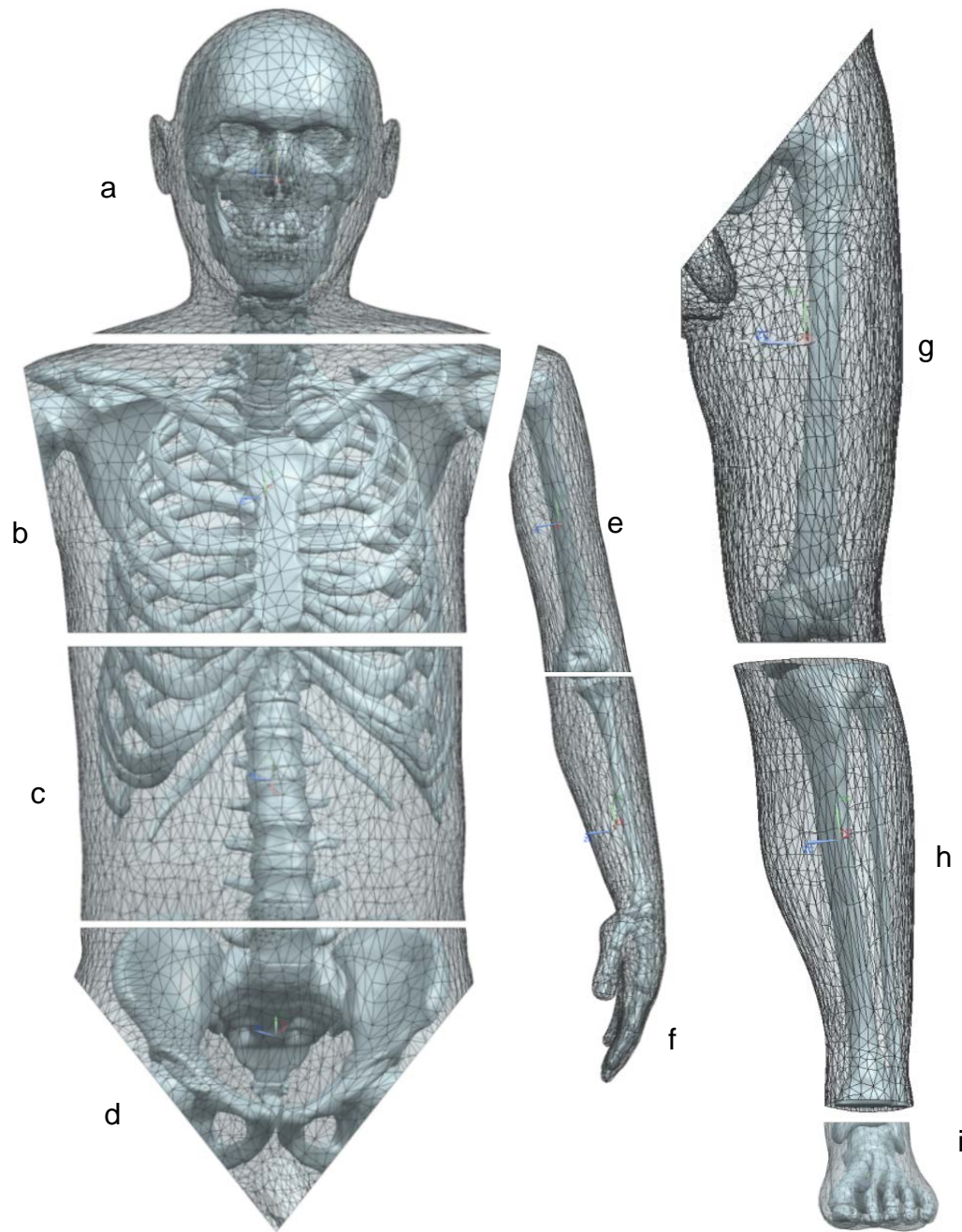


Figure 3.5 Various body segments in NX including (a) head and neck, (b) upper, (c) middle and (d) lower trunk, (e) upper arm, (f) forearm, (g) thigh, (h) shank, (i) foot.

Sphyrion The distal tip of the tibia.

Tibiale The most proximal point on the medial margin of the head of the tibia.

Vertex The most cranial point of the head, when the head is oriented in the Frankfort plane.

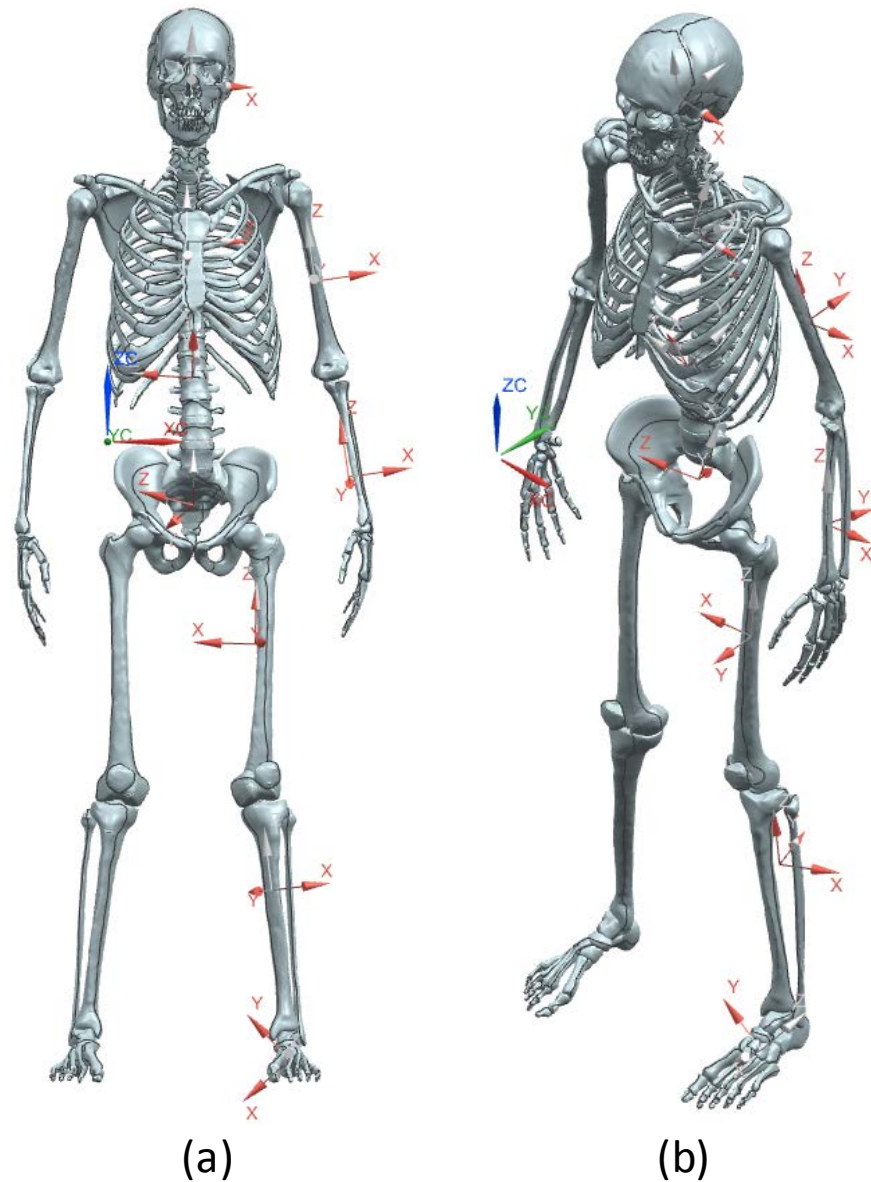


Figure 3.6 (a) Front and (b) Trimetric view of the coordinate system. Skin is hidden. XC, YC, and ZC represented the global coordinate system; and the red colour X, Y, Z represented local coordinate system.

Xyphion (Substernale) The midpoint of the sulcus between the body of the sternum (breastbone) and the xyphoid process.

From a biological point of view, the real human body is asymmetric, such as segment origin, joint centre and axis, muscular origin and insertion, etc. However, from a robotic point of view, to simplify the modelling and design process of the robot, it is reasonable to assume that the model being analysed should be symmetric with the sagittal plane. The

Table 3.2 Local coordinate system of each segment relative to global coordinate system.

Body segment	Origin (Mass centre) (mm)			Direction vectors (Principal axes)	$\begin{bmatrix} I_{xx} & I_{xy} & I_{xz} \\ I_{yx} & I_{yy} & I_{yz} \\ I_{zx} & I_{zy} & I_{zz} \end{bmatrix}$		
	x	y	z				
Head and neck	132.588	226.582	566.469	$\begin{bmatrix} 0.999528598 & -0.019593377 & -0.023636424 \\ 0.023438723 & 0.984238654 & 0.175285193 \\ 0.019829453 & -0.175756571 & 0.984233926 \end{bmatrix}$			
Upper trunk	126.292	260.291	318.401	$\begin{bmatrix} 0.014335854 & 0.924642361 & -0.380566667 \\ -0.002270266 & 0.380634898 & 0.924722618 \\ 0.999894659 & -0.012392701 & 0.007555911 \end{bmatrix}$			
Middle trunk	134.509	242.532	101.386	$\begin{bmatrix} 0.027905366 & 0.490634266 & 0.870918657 \\ 0.100885608 & 0.868191683 & 0.485865512 \\ -0.994506604 & 0.074304904 & 0.073725143 \end{bmatrix}$			
Lower trunk	136.717	261.140	-100.528	$\begin{bmatrix} -0.004045456 & 0.463379957 & 0.886150467 \\ -0.477304215 & 0.777803927 & -0.408903090 \\ -0.878728809 & -0.424617553 & 0.218026635 \end{bmatrix}$			
Left upper arm	329.574	279.836	255.382	$\begin{bmatrix} 0.988947926 & 0.014909009 & 0.147511766 \\ -0.025387928 & 0.997264964 & 0.069412131 \\ -0.146073450 & -0.072390001 & 0.986621627 \end{bmatrix}$			
Left forearm	382.838	266.126	-56.011	$\begin{bmatrix} 0.989683582 & -0.018333791 & 0.142092504 \\ 0.044666116 & 0.981832175 & -0.184419408 \\ -0.136129886 & 0.188863581 & 0.972522083 \end{bmatrix}$			
Left thigh	29.470	392.556	-9.830	$\begin{bmatrix} -0.229767239 & 0.149361648 & 0.961716234 \\ 0.973241288 & 0.038206162 & 0.226587033 \\ -0.002900073 & 0.988044223 & -0.154143447 \end{bmatrix}$			
Left shank	260.781	296.549	-713.876	$\begin{bmatrix} 0.917774933 & 0.380185186 & 0.114666457 \\ -0.379228541 & 0.924786778 & -0.030905147 \\ -0.117791703 & -0.015120824 & 0.992923197 \end{bmatrix}$			
Left foot	289.080	232.157	-984.445	$\begin{bmatrix} -0.742979475 & 0.122817833 & -0.657949299 \\ -0.669001830 & -0.166301041 & 0.724417362 \\ -0.020446283 & 0.978396517 & 0.205723615 \end{bmatrix}$			

following analysis only considered the left part of the arm, leg and foot. The right part could be obtained by “mirror” command and careful modification in NX. In the end, the subject has been segmented into 14 parts (Table 3.2 and Figure 3.5), which included head and neck, 2 upper arms, 2 forearms, 3 trunks, 2 thighs, 2 shanks, and 2 feet.

3.4 Body Segment Properties

In order to obtain the mass centre, mass ratio and moment of inertia of each body part in its local coordinate system, body segment properties have been measured in NX. The

Table 3.3 Body segment properties of each major body segment.

Body segment	Mass (kg)	Mass ratio (%)	Moment of inertia relative to the principal axes of each segment $\times 10^3$ (kg \cdot mm ²)		
			I_x	I_y	I_z
Head and neck	5.701	7.229	38.553	33.207	22.333
Upper trunk	14.318	18.156	176.337	158.461	106.902
Middle trunk	14.162	17.958	145.220	141.609	118.854
Lower trunk	9.678	12.272	80.547	70.292	69.400
Left upper arm	2.138	2.711	18.104	17.186	2.579
Left forearm	1.443	1.830	17.982	17.714	1.258
Left thigh	10.004	12.685	169.649	158.658	42.041
Left shank	2.918	3.700	30.118	29.552	4.653
Left foot	0.999	1.267	3.546	3.474	0.802

density of human body was simplified to two values: the bone density was set to 1.3 g/cm³ [268], and the density of other parts of the body was set to 0.987 g/cm³. Thus, the average density of whole body was 1.015 g/cm³, which is reasonable according to measurements on various subjects [269]. The subject was 36 years old, 78.836 kg in weight, and 171.5 cm tall.

To simplify the design process of the robot, each segment should have its own local coordinate system. In this case, the mass centre was the origin and the principal axes were corresponding to its x, y, and z axis. The local coordinate systems were connected together in the global coordinate system which was inherited from the model in Rhino, as shown in Table 3.2 and Figure 3.6. Thus, body segment properties including mass, mass ratio and moment of inertia were analysed in the local coordinate system as shown in Table 3.3.

3.5 Joint Parameters

Joints are the connections made between bones in the human body which links the skeletal system into a functional whole. Their prime functions are to allow for different degrees

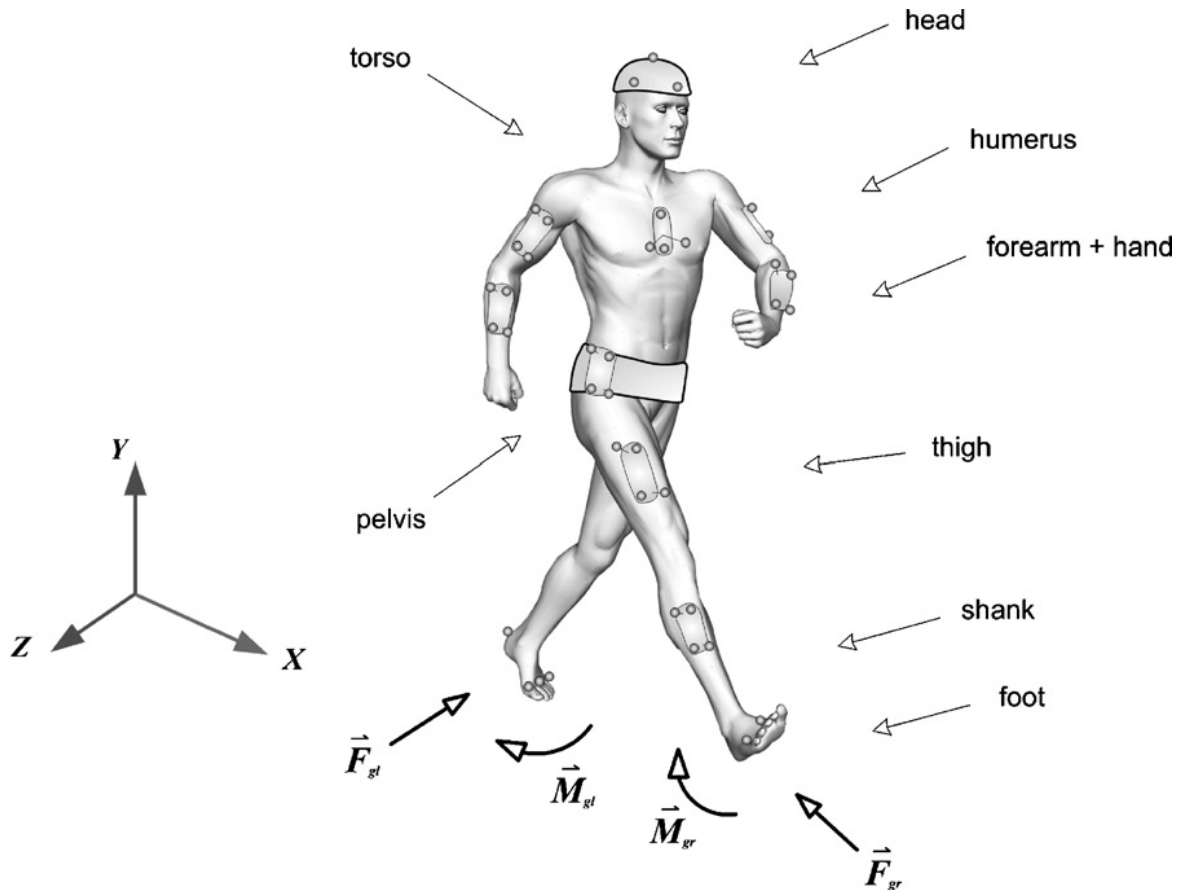


Figure 3.7 The 3D whole-body model with 13 segments and 12 connecting joints used for calculating joint parameters. A marker cluster mounted on a plastic plate was attached to each body segment (52 markers in total). The global X-axis is the direction of progression, the Y-axis is vertical, and the Z-axis is to the right [270].

and types of movement. According to the type and degree of movement they allow, joints can be classified functionally: synarthrosis that permits little or no mobility, amphiarthrosis that permits slight mobility, and synovial joint that is freely movable. Most joints related to human locomotion are hinge joint or ball and socket joint distinguished with one, two and three degrees of freedom. In our study, the hip joint, as with the shoulder, the neck and the waist joint, is considered as ball and socket joint. The ankle joint is a combination of two hinge joints, named as the talocrural joint in the medial-lateral direction and the subtalar joint in the anterior-posterior direction. Other joints including the elbow and the knee joint are simplified as one hinge joint.

Joint centre and joint axis of rotation are crucial to human motion. This part explained how to create them in the model and analyse them in NX.

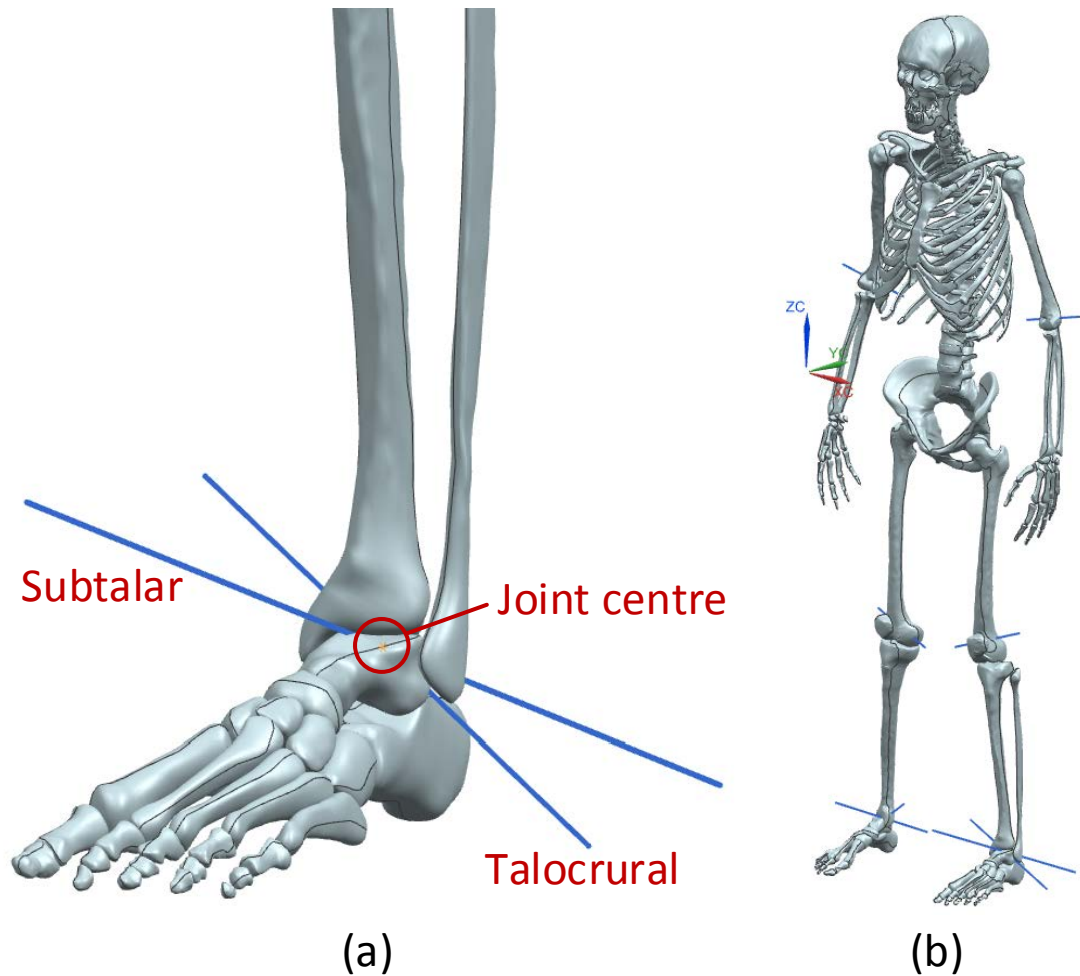


Figure 3.8 Joint parameters (a) in the ankle and (b) in the whole body including joint centres (hidden in the bones) and joint axes of rotation (blue lines).

Motion capture technique has been widely used in recording the 3D human motion, which is characterised by the time histories of segmental or joint angles. Generally, optoelectronic motion analysis systems are employed by using infrared camera arrays to track the positions of passive or active markers attached on the body segments of the subject [270].

The original kinematic data of the landmarks of human body were measured from 3D human gait experiments using VICON 3D motion capturing system (see section 6.2.1), and then simplified and modified later. The human body was represented as an articulated multi-segment system (Figure 3.7) with 13 rigid segments (head, torso, pelvis, thighs, shanks, feet, upper arms and forearms). 3D whole-body gait measurements (walking along an indoor walkway) were conducted in a healthy male subject to provide kinematic inputs

Table 3.4 Position and orientation of each joint relative to the local coordinate system. Elbow, shoulder, hip, knee, ankle joint and all the limbs are the left of the body. 1st of the joint axis of ankle joint was subtalar axis and 2nd was talocrural.

Joint	Type	Local coordinate system	Position (mm)			Orientation (x, y, z)
			x	y	z	
Elbow	One hinge	Forearm	-5.603	3.934	182.192	(0.996, -0.041, 0.084)
		Upper arm	3.183	14.590	-139.071	(0.995, -0.051, 0.089)
Shoulder	Ball and socket	Upper arm	-9.191	-20.871	143.340	
		Upper trunk	-37.174	65.028	174.483	
Neck	Ball and socket	Head and neck	-1.409	3.262	-126.569	
		Upper trunk	-54.798	111.621	3.495	
Waist	Ball and socket	Middle trunk	-108.308	-38.962	-15.303	
		Lower trunk	77.340	-39.021	13.931	
Hip	Ball and socket	Thigh	23.802	21.725	172.814	
		Lower trunk	-47.440	-28.515	-77.679	
Knee	One hinge	Shank	-17.945	-26.364	182.564	(0.943, -0.259, 0.211)
		Thigh	-3.940	-4.753	-211.754	(-0.934, 0.046, 0.353)
Ankle	Two hinges	Shank	-10.651	-18.904	-231.856	1 st : (-0.486, -0.783, -0.389) 2 nd : (-0.753, 0.108, 0.649)
		Foot	-17.767	23.465	53.609	1 st : (-0.201, 0.540, -0.818) 2 nd : (0.212, 0.975, -0.061)

(i.e., the trajectory of the markers) for the gait model. Each experimental condition was measured five times. Motion data were recorded at 100Hz by the Vicon system. A set of specially designed thermoplastic plates, each carrying a cluster of four reflective markers, were attached to the 13 body segments. The head marker cluster was carried by a helmet. The plastic plate carrying the pelvis marker cluster was located by an elastic hip belt. The plastic plates and the helmet can increase the accuracy of the recorded kinematic data by eliminating the relative motion between the markers and the segment.

The anatomical landmarks were located through a set of static calibration procedures using a calibration wand and four reflective markers placed in the capture zone. Before the walking trials, the calibration markers were removed according to the calibrated anatomical system technique. The centre positions of the joints were based on anatomical

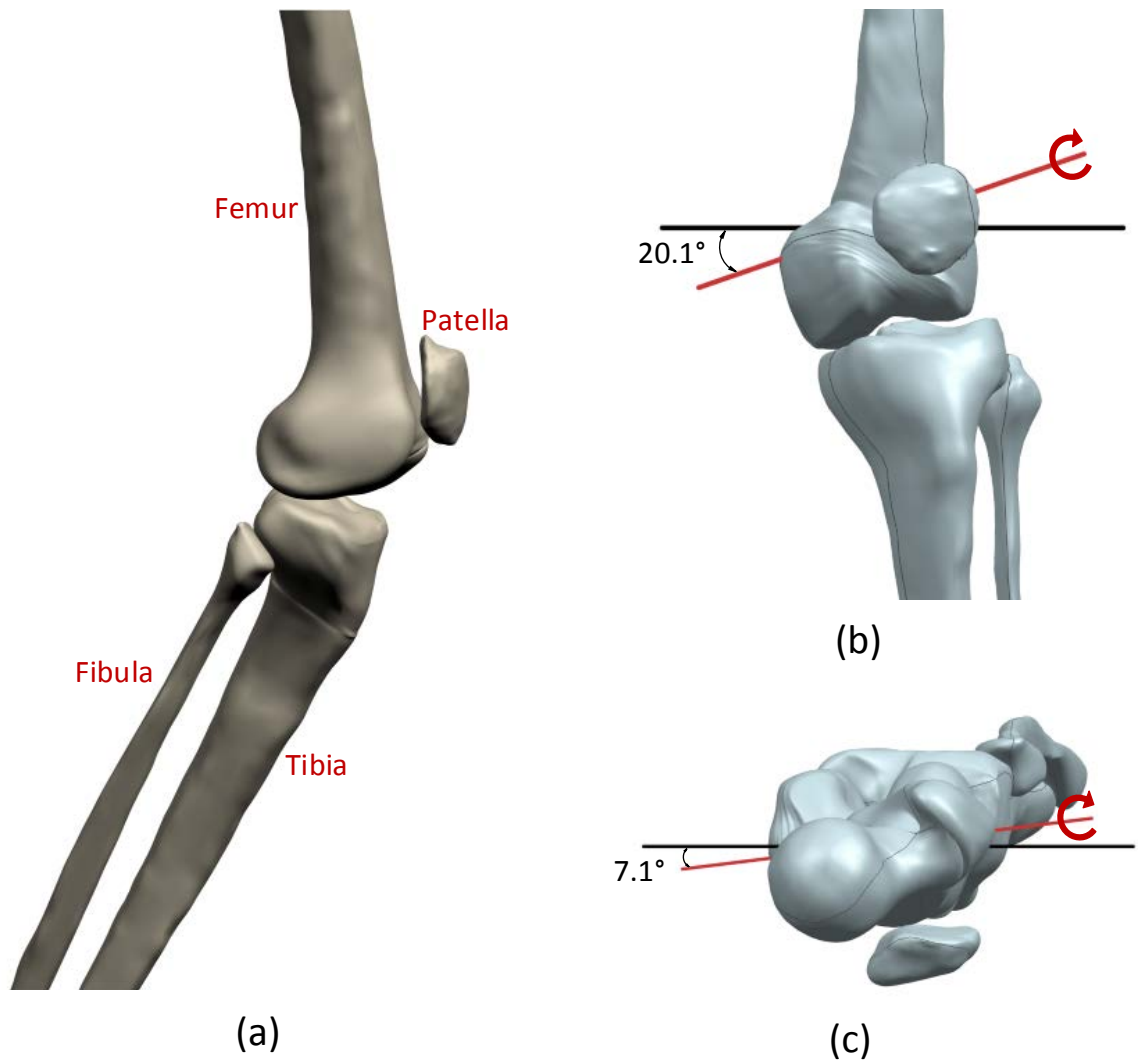


Figure 3.9 Knee joint. (a) Two-joint structure. (b) Joint axis in coronal plane (front view). The axis rises up at a 20.1° angle from the horizontal medial-lateral axis in the frontal plane. (c) Joint axis in transverse plane (top view). The axis is oriented 7.1° with the horizontal medial-lateral axis of the thigh.

landmarks of human body. All reflective marker should be captured by at least three cameras during a walking gait. All trials with more than 10 consecutive missing frames were discarded. After fill-gap processing, the trajectory data of each marker were filtered using a low pass zero lag fourth-order Butterworth digital filter with a cut-off frequency of 6 Hz .

Using the coordinates of the landmarks as reference, the joint centre was simplified to a single point and the joint axis of rotation was simplified to a straight line in the model. As shown in Figure 3.8, the joint centre was hidden in the bone and the blue lines

represented the joint axes of rotation (such as the elbow, knee, and ankle). The position of each joint centre and the orientation of each joint axis of rotation were determined in the local coordinate system (the body segment), as shown in Table 3.4.

3.5.1 Knee joint

The knee joint transmits loads, facilitates positions and movements of the body, aids in the conservation of momentum, and provides the necessary moments for activities involving the leg. The human knee, the largest and perhaps most complex joint in the body, is principally a two-joint structure composed of the tibiofemoral joint and the patellofemoral joint (Figure 3.9(a)). The tibiofibular joint has a valuable role but does not participate in motion. The knee sustains high forces and moments and is situated between the body's two longest lever arms, the femur and the tibia, making it particularly susceptible to injury.

Although knee motion occurs simultaneously in three planes, the motion in the sagittal plane (flexion/extension) dominates during human locomotion rather than in the frontal plane (adduction/abduction or valgus/varus) and the transverse plane (internal/external rotation), so that it accounts for nearly all of the motion. Also, although many muscles produce forces on the knee, at any particular instant the quadriceps muscle group (Vastus and Rectus femoris) predominates, generating a force that accounts for most of the muscle force acting on the knee. Basic biomechanical analyses can be limited to motion in one plane and to the force produced by a single muscle group and still give an understanding of knee motion and an estimation of the principal forces and moments on the knee.

Indeed, there are three instantaneous axes of rotation in human knee motion, including the tibiofemoral, patellofemoral, and patellotibial axis. The range of motion is greatest in the tibiofemoral axis, so the knee joint can be simplified to one hinge joint instead of three hinge joints and the axis of rotation is set at an oblique angle that is oriented upward at an angle 20.1° from the horizontal medial-lateral axis in the frontal plane and approximately 7.1° with the horizontal medial-lateral axis in the transverse plane (Figure 3.9(b) and (c)).

3.5.2 Ankle joint

The primary task of the ankle is to provide a stable, adaptable, and efficient interface between the body and ground for locomotion. This task requires the ankle to be sufficiently pliable during early stance phase to conform to varying surface terrain, to absorb and translate forces while maintaining superincumbent whole-body stability, and to

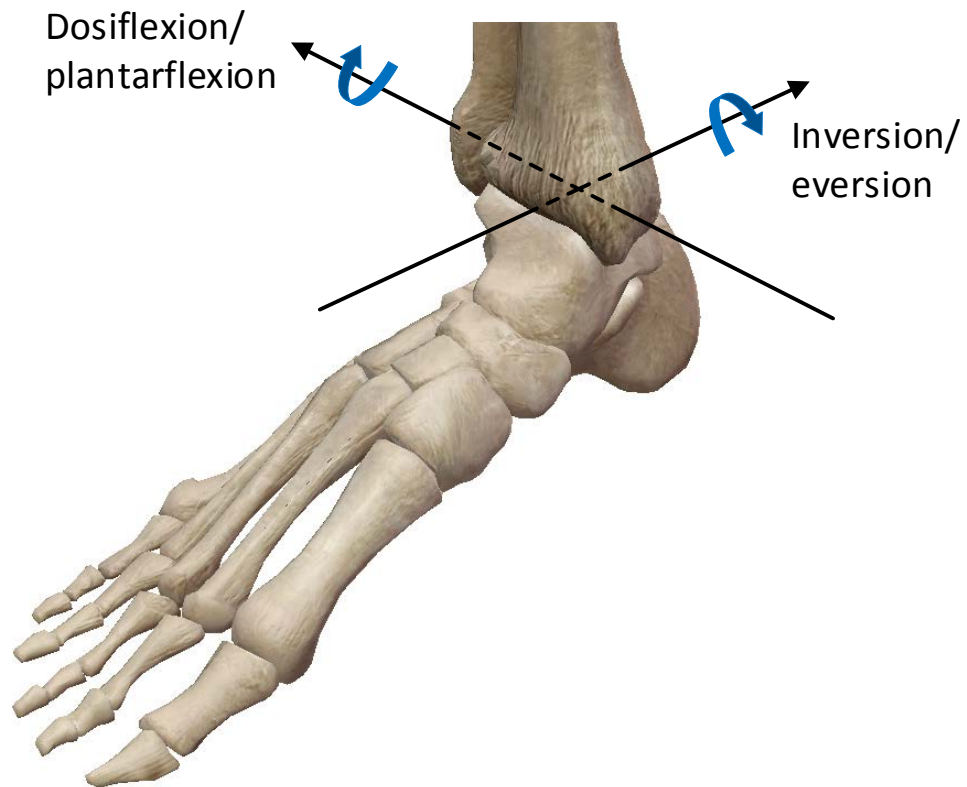


Figure 3.10 Typical motions in the ankle.

rapidly achieve sufficient rigidity during the late stance phase to propel the body forward using the rigid lever of the longitudinal arch.

Due to the projection of the foot anteriorly from the coronal plane of the body, the terminology describing motion of the ankle differs in several important ways from standard descriptions of motion in other areas of the body. Flexion/extension of the foot is termed dorsiflexion and plantarflexion respectively and occurs around a medial/-lateral axis in the sagittal plane. This motion occurs primarily at the talocrural joint. Inversion and eversion represent motion in the coronal plane about an anterior-posterior axis (this motion is termed abduction/adduction elsewhere in the body). Inversion/eversion occurs primarily at the subtalar joint and can be demonstrated by moving the plantar surface of the foot to face medially (inversion) or laterally (eversion) (Figure 3.10).

Talocrural joint

The axis of talocrural joint is set at a slightly oblique angle such that the lateral portion (lateral malleolus) is posterior and inferior to the medial portion (medial malleolus) (Inman, 1976). The axis forms an approximately 34.4° angle with the horizontal medial-

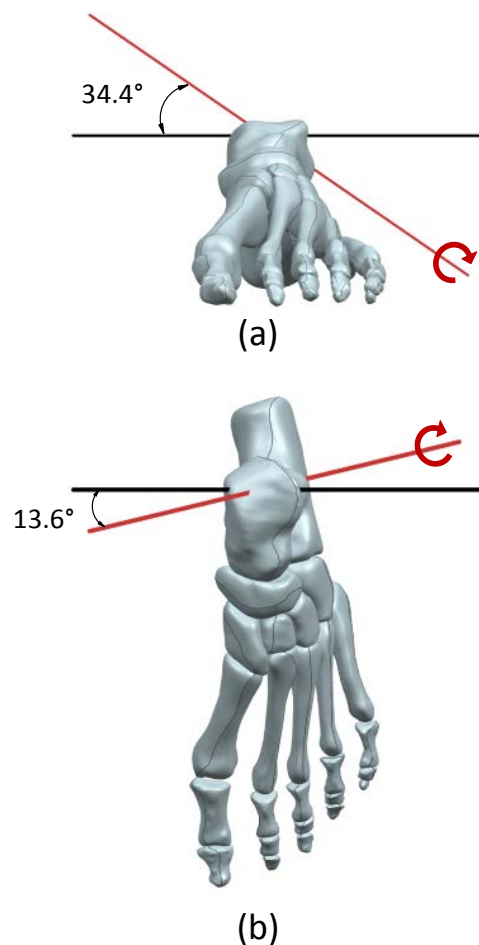


Figure 3.11 Talocrural joint axis. (a) Coronal plane (front view). The axis rises up at a 34.4° angle from the horizontal medial-lateral axis in the frontal plane. (b) Transverse plane (top view). The axis is oriented 13.6° with the horizontal medial-lateral axis of the foot.

lateral axis in the frontal plane and approximately a 13.6° angle with the horizontal medial-lateral axis in the transverse plane (Figure 3.11). Technically, this obliquity to the standard axes requires the terminology of pronation and supination be applied to the ankle joint. However, the obliquity of the axis cannot change the vast majority of the motion consisting of dorsiflexion and plantarflexion. Consequently, in most clinical situations the components of the other two planes are ignored and the talocrural joint is suggested to function in the sagittal plane alone.

Subtalar joint

The subtalar joint axis has one degree of freedom and is set at an oblique angle that is

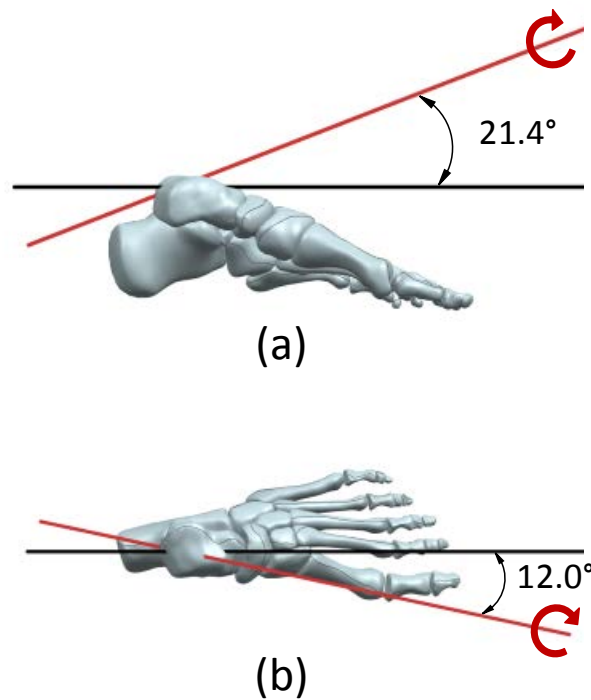


Figure 3.12 Subtalar joint axis. (a) Sagittal plane (medial view). The axis rises up at a 21.4° angle from the horizontal anterior-posterior axis. (b) Transverse plane (top view). The axis is oriented 12.0° medial to the midline of the foot.

oriented upward at an angle 21.4° from the horizontal and medially 12.0° from the midline (Figure 3.12). This almost even split between the anterior-posterior axis and the vertical axis creates almost equal amounts of the component motions of inversion/eversion and abduction/adduction. The small amount of obliquity toward the medial-lateral axis suggests that the subtalar joint has very little motion component of plantarflexion/dorsiflexion. Similar to the talocrural joint in which the small amounts of inversion/eversion and abduction/adduction were not considered clinically meaningful, the plantarflexion/dorsiflexion component of the subtalar joint is considered negligible.

3.6 Muscle Path

One of the important parts of the robot is the actuation system, which in this case is the muscular system. Functional muscle groups power human locomotion and support our body at the same time. Muscles coordinate human movement because the forces generated by them develop mechanical energy and mechanisms for energy exchange among the segments.

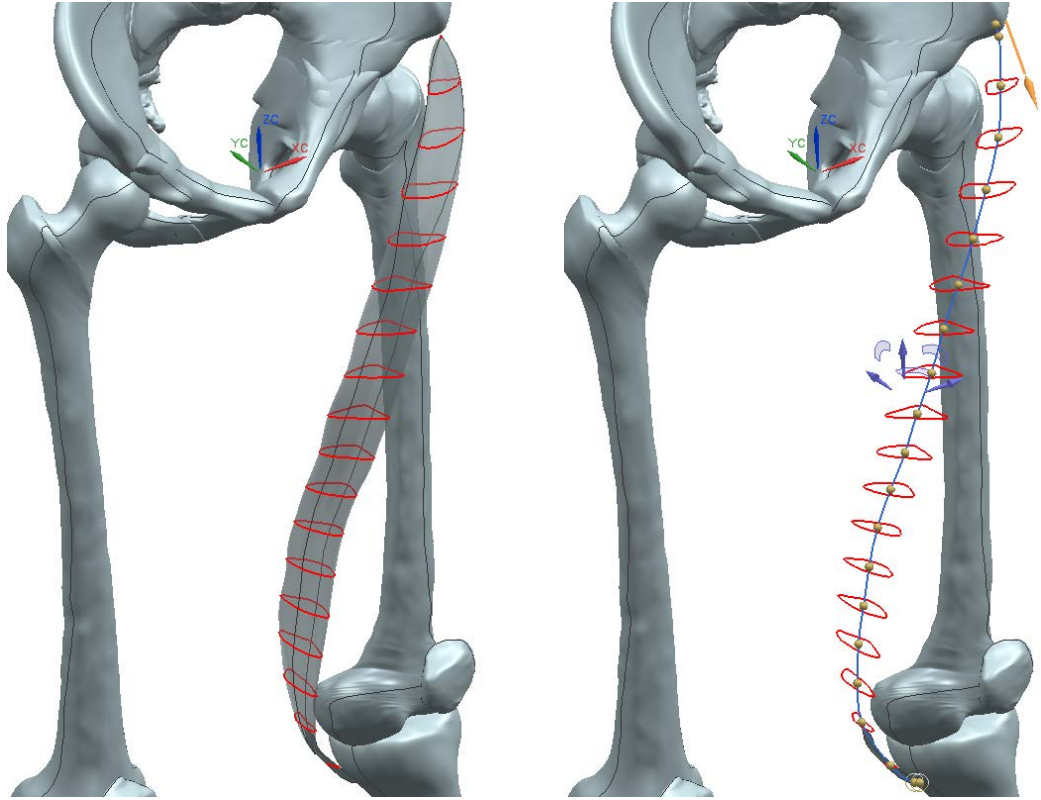


Figure 3.13 The process of generating muscle path. Red lines were the surface profile of the cross-section and blue curve was the muscle path.

Since artificial muscles will be used as the actuation in the future, the musculoskeletal geometry was also quantified in this study. The 3D muscle paths of all major muscles were represented as smooth curves. The centroid line of each muscle was created by connecting several points (including the origin and the insertion) in the muscle volume using a spline with each point being the centroid of the muscular cross section. The process of generating the 3D muscle path (Figure 3.13) was as follows: firstly, the surface profiles (red curves) of several cross-sections were created, then the centroids of the cross-sections were connected using a spline to define the muscle path (blue curve). The centroid lines of the muscles were considered as a simplified representation of the muscular system, which may play important in the robot design to drive segment motions and maintain joint stability. Since it is unnecessary to consider all the muscles in the human body, in this study, I mainly considered 68 major functional muscle groups, the details of which were shown in Table 3.5. The insertion, the origin and the path of each muscle are the same as corresponding human muscle, resulting in same moment arm as real human muscle when the artificial muscle unit performs muscle contracting behaviour.

Table 3.5 68 main functional muscle groups including 6 in the head and neck, 20 in the trunk, 10 in two arms, 18 in two thighs and 14 in two shanks. Triceps muscle, as well as Hamstrings and Gastrocnemius muscles was considered as two muscle volumes respectively.

Body segment	Muscle name	Number
Head and neck	Sternocleidomastoid	2
	Splenius capitis	2
	Semispinalis capitis	2
Trunk	Rectus abdominis	2
	Pectoralis major	2
	Pectoralis minor	2
	Erector Spinae	2
	Trapezius	2
	Rotator cuff	2
	Rhomboids	2
	Latissimus dorsi	2
	Psoas and Iliacus	2
	Intercostals and obiques	2
Arm (left and right)	Biceps	2
	Brachialis	2
	Triceps	4
	Deltoid	2
Thigh (left and right)	Rectus femoris	2
	Vastus	2
	Hamstrings	4
	Iliotibial tract and Gluteus	2
	Gluteus maximus	2
	Sartorius	2
	Gracilis	2
	Adductor longus	2
Shank (left and right)	Tibialis anterior	2
	Tibialis posterior	2
	Gastrocnemius	4
	Soleus	2
	Fibularis (Peroneus) longus	2
	Extensor digitorum longus	2

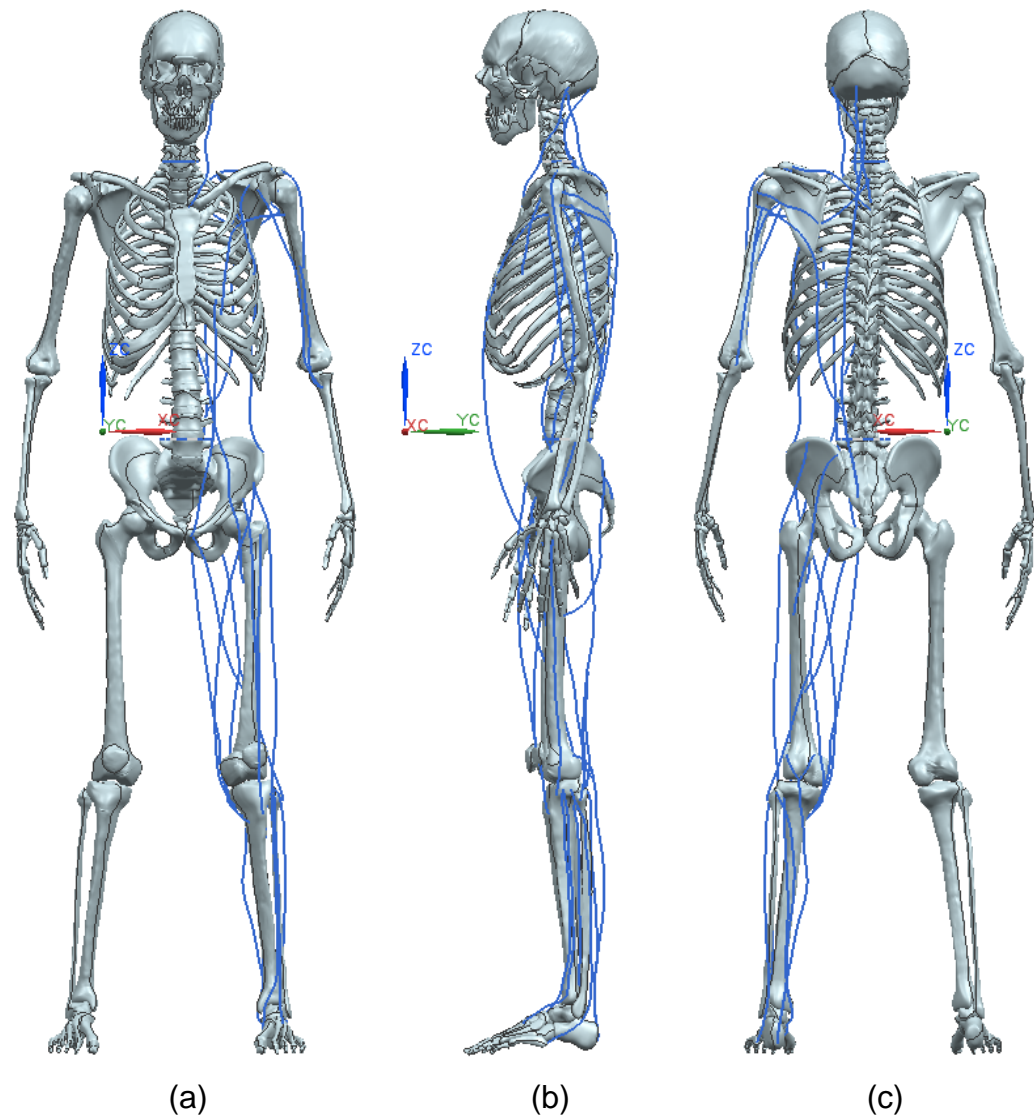


Figure 3.14 (a) Front, (b) Right and (c) Back view of the left part of simplified whole-body muscular system, blue curves representing the muscle paths.

Figure 3.14 showed the left part of simplified whole-body muscular system of the subject, and the blue curves represented the muscle paths. As we know, the leg is the major part that affects human locomotion. Thus, the muscle paths in the leg should be carefully modified after generating from the centroids. The muscle paths in the left shank were shown in Figure 3.15, including 6 muscle groups Tibialis anterior, Tibialis posterior, Gastrocnemius, Soleus, Extensor digitorum longus and Peroneus longus. The muscle paths in the left thigh were shown in Figure 3.16, including 8 muscle groups Rectus femoris, Vastus, Hamstring, Iliotibial tract and Gluteus, Gluteus maximus, Sartorius, Gracilis, Adductor longus.

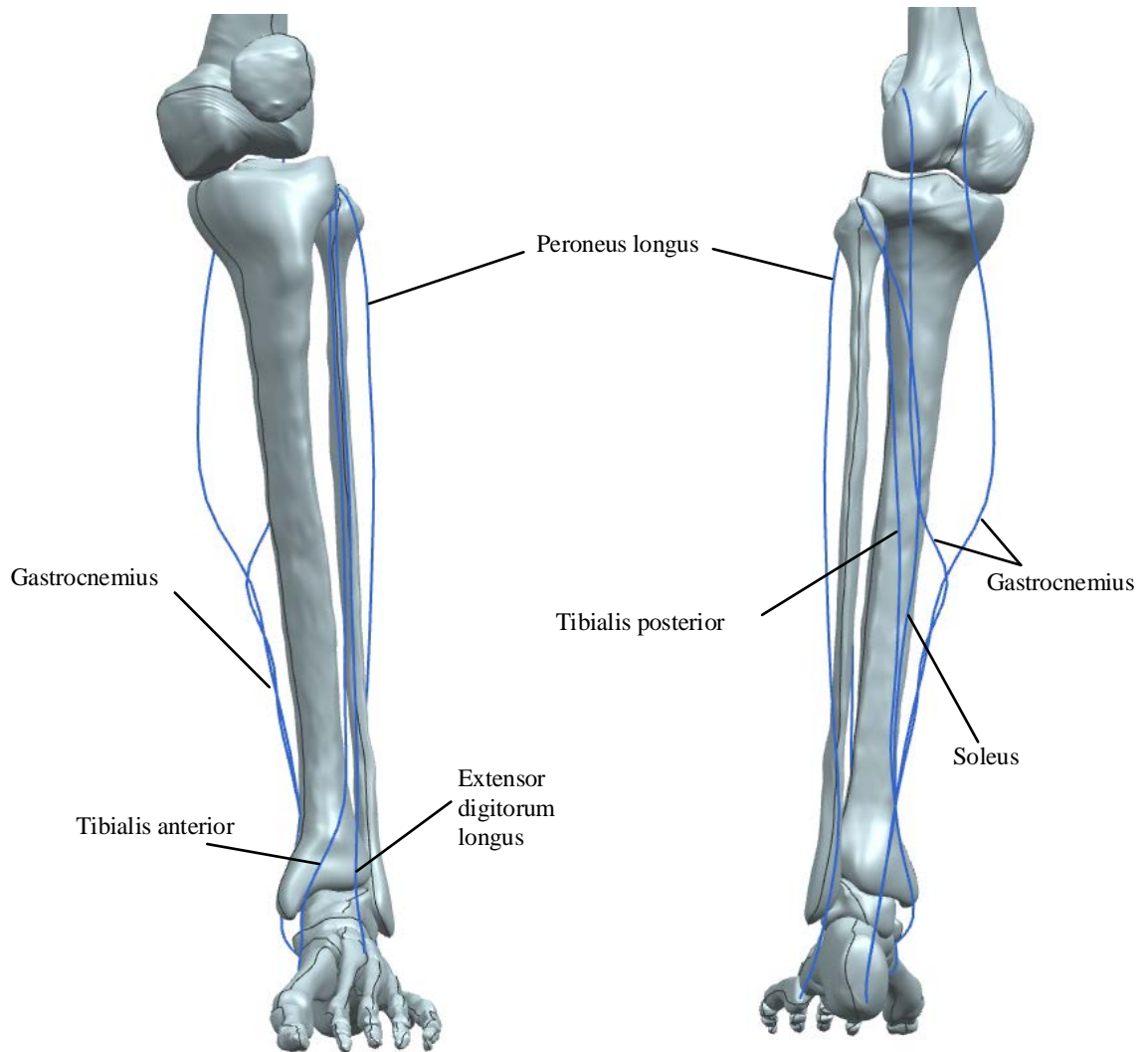


Figure 3.15 Front (left) and back (right) view of the muscle paths in the left shank.

3.7 Conclusions

In this chapter, the biomechanics of human MSK were analysed. A 3D whole-body musculoskeletal model of a healthy male constructed from the Visible Human Project database was rebuilt in NX software. Skin, skeletal and muscle model were reconstructed to segment the main functional part of human body and measure the body properties.

Anthropometric data, key kinematic parameters and musculoskeletal geometry were measured and analysed to provide key design parameters for the bio-robot. The human body was considered as 14 segments including the head and neck, the upper, middle and lower (pelvis) trunk, two upper arms, two forearms, two thighs, two shanks and two feet.

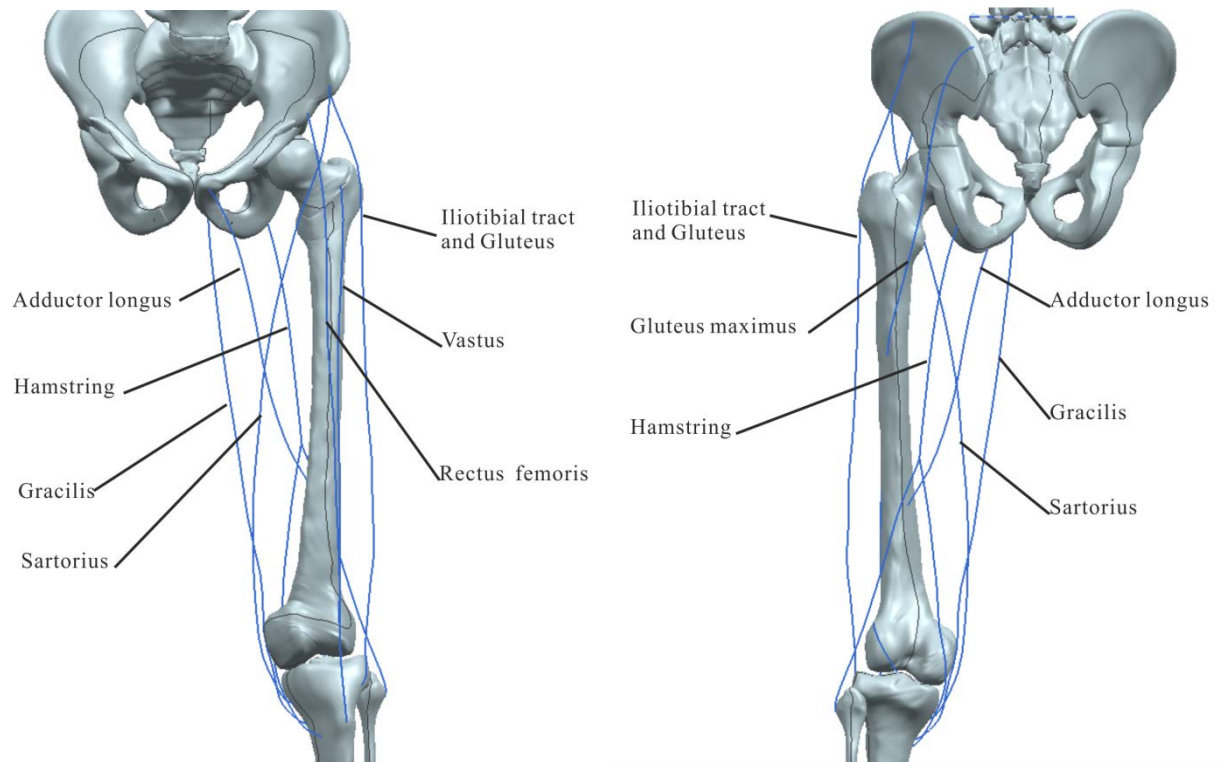


Figure 3.16 Front (left) and back (right) view of the muscle paths in the left thigh.

All the anthropometric data for each major body segment was determined in its local coordinate system (where the coordinate axes are the principal axes of the body) by analysing the 3D whole-body model using computer aided design software. Those would provide key design parameters for each part of the bio-robot.

In vivo 3D whole-body gait measurements were conducted on a healthy male subject with a very similar body configuration. The key kinematic parameters obtained for each major anatomical joint (e.g., the ankle, knee, hip, spine, shoulder and elbow) were used to inform the joint design of the bio-robot. The joint centre of the rotating axis of each joint were obtained in which the knee and ankle were discussed in detail as they play a key role in biped locomotion.

In addition, the musculoskeletal geometry (including the insertion, origin and muscle path) for each major muscle group was carefully determined based on the 3D whole-body musculoskeletal model. 68 main functional muscle groups including 6 in the head and neck, 20 in the trunk, 10 in two arms, 18 in two thighs and 14 in two shanks were considered. Those information will be used for the design of artificial tendon groups of the bio-robot simulating the mechanical functions of major musculotendon units.

The contributions to knowledge in this chapter include the following:

- Built a 3D whole body solid model of the human subject;
- Analysed the biomechanics of human musculoskeletal system using the same human subject including segment properties and joint parameters;
- Determined 3D musculotendon paths of major muscle groups using the same human subject.

Chapter 4

Development of the Physical Prototype

Computer-aided design (CAD) involves the use of computers to create design drawings and product models, which is usually associated with interactive computer graphics (known as a CAD system) to aid in the creation, modification, analysis, or optimization of a design [271]. They are powerful tools and are widely used in the mechanical design and geometric modelling of robotics.

Computer-aided manufacturing (CAM) involves the uses of computers and computer technology to assist in all the phases of manufacturing a product, including process and production planning, machining, scheduling, management, and quality control. Computer-aided design and computer-aided manufacturing are often combined into CAD/CAM systems. This combination allows the transfer of information from the design stage into the stage of planning for the manufacture of the robot, without the need to reenter the data on part geometry manually. The database developed during CAD is stored; then it is processed further, by CAM, into the necessary data and instructions for operating and controlling production machinery, material-handling equipment, and automated testing and inspection or product quality.

NX is an advanced high-end CAD/CAM/CAE software package, which has been owned since 2007 by Siemens PLM Software [272, 273]. Considering the mathematical and physical accuracy, friendly user interface and the integration of design and manufacturing process, 3D model of the robot was designed in NX software based on the biomechanics of human MSK that are analysed in chapter 3, and then exported as STL files to 3D print.

3D printing is a form of additive manufacturing technology where a 3D object is created by laying down or build from successive layers of material. It is a great way to

create objects without having complex expensive moulds created or having the objects made with multiple parts. Objects can be of almost any shape or geometry and typically are produced directly from 3D CAD model data. Due to the complexity of the skeletal part designed for the robot, 3D printing is selected as the manufacturing technique.

In this chapter, mechanical design of the skeletal body of the robot is described in section 4.1, including the functional parts (e.g., arms, trunks, legs and feet) and connecting joints (e.g., ankles, knees, hips, spine, shoulders and elbows). As controlling a robot with the same size as a human is too difficult, the robot has been scaled to half of the real human and then 3D printed in section 4.2. In section 4.3, a whole-body muscular system consisting of various coiled fishing lines with different material properties (stiffness and preload) are designed. Finally, the skeletal body and muscular body are integrated in section 4.4. The work in this chapter was conducted mainly in Jilin University, China.

4.1 Mechanical Design of the Skeletal Structure

As mentioned in the last section, a 3D whole-body musculoskeletal model was used as the biological counterpart to inspire the design of the robot. Anthropometric data, key kinematic parameters and musculoskeletal geometry were measured and analysed to provide key design parameters for the bio-robot. The robot was designed according to individual parts based on its own local coordinate system, including foot, leg, trunk, and arm along with their connections (i.e., joints). The biomechanical properties of each part have high similarity compared with the real human subject in terms of dimensions, mass properties (e.g., mass centre, mass distribution, and moment of inertia) kinematic parameters (joint centre and joint axis of rotation).

From a biological point of view, the real human body is asymmetric, such as segment origin, joint centre and axis of rotation, muscular origin and insertion, etc. However, from a robotic point of view, to simplify the modelling and design process of the robot, it is reasonable to assume that the model being analysed should be symmetric with the sagittal plane. The following design process only considered the left part, and the right part could be obtained by “mirror” command and careful modification in NX.

4.1.1 Foot

Foot is the only element which contacts ground during human walking, supporting whole

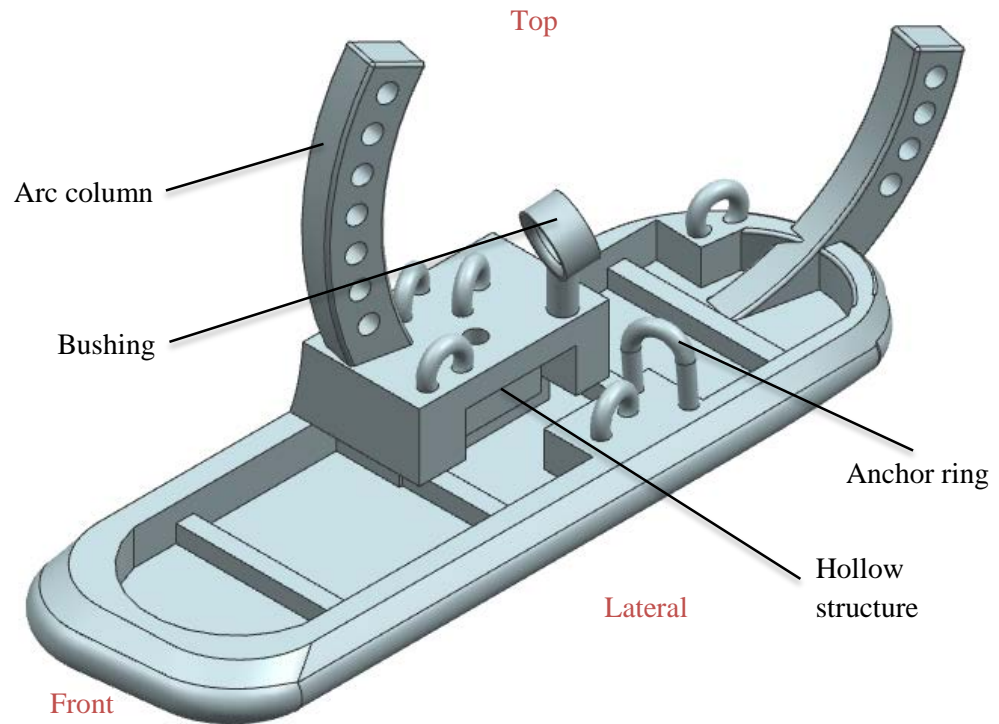


Figure 4.1 Left foot design in NX.

weight of the body. As shown in Figure 4.1, the left foot has a flat bottom and hollow structure that is designed to reduce weight and balance the mass properties, along with rings as muscle insertions and origins, bushing as the guide of muscle path, and two arc columns as connections of the ankle joint. It is 2.017 kg in weight, 25.50 cm long, 8.35 cm wide, and 12.57 cm high.

4.1.2 Leg

From a biomechanical point of view, the leg consists of the shank which links foot through ankle joint and the thigh that links pelvis through hip joint. Accordingly, the thigh and shank part were designed separately in their own local coordinate system.

Thigh is most “powerful” segment in the lower limbs of human body, which can generate a large amount of energy in human motion especially in sports field thanks to several main functional muscle groups. The main part of robotic thigh was designed based on human femur with some grooves and holes in it to assemble other components (Figure 4.2a). Besides, five extra parts were designed to balance the mass properties using solid volume and guide the artificial muscle groups using bushings (Figure 4.2b). Furthermore,

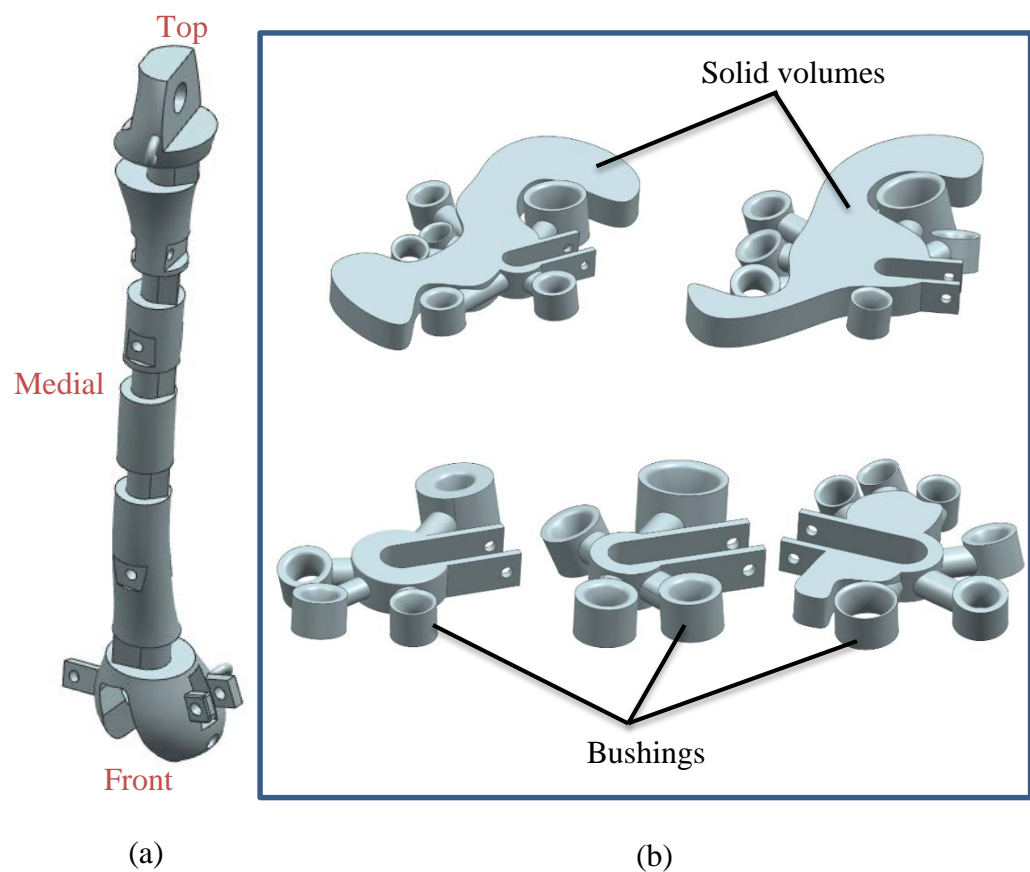


Figure 4.2 Left thigh design in NX including (a) main and (b) extra components.

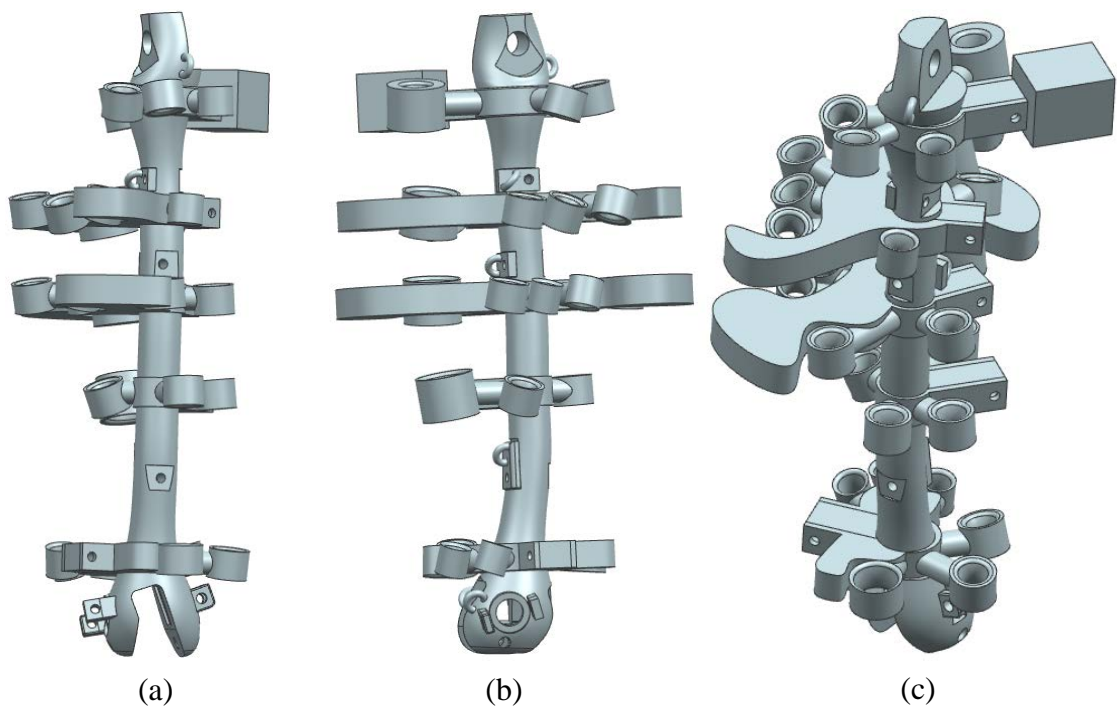


Figure 4.3 (a) Front, (b) Left and (c) Isometric view of the assembly of left thigh.

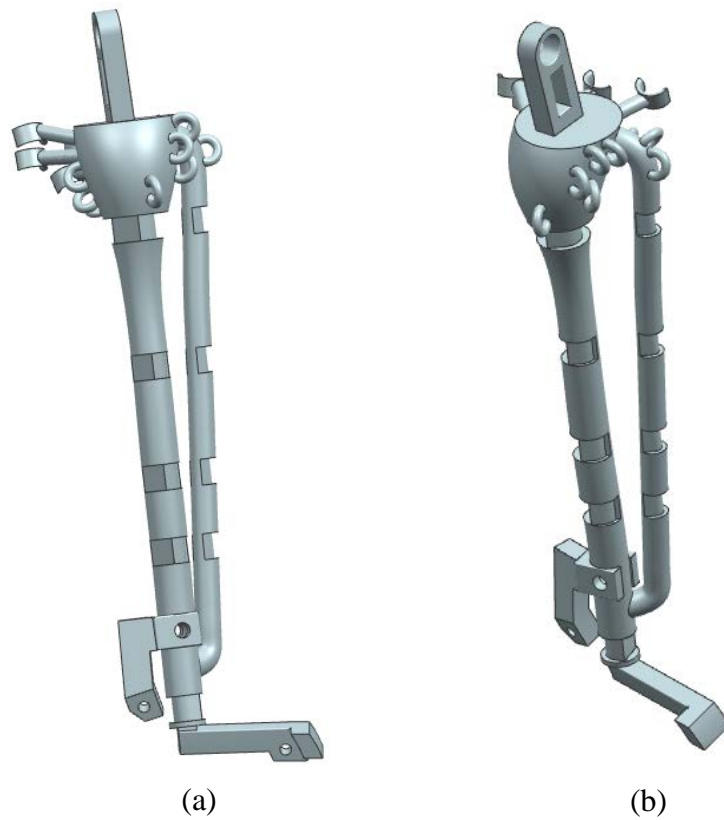


Figure 4.4 (a) Front and (b) Isometric view of left shank.

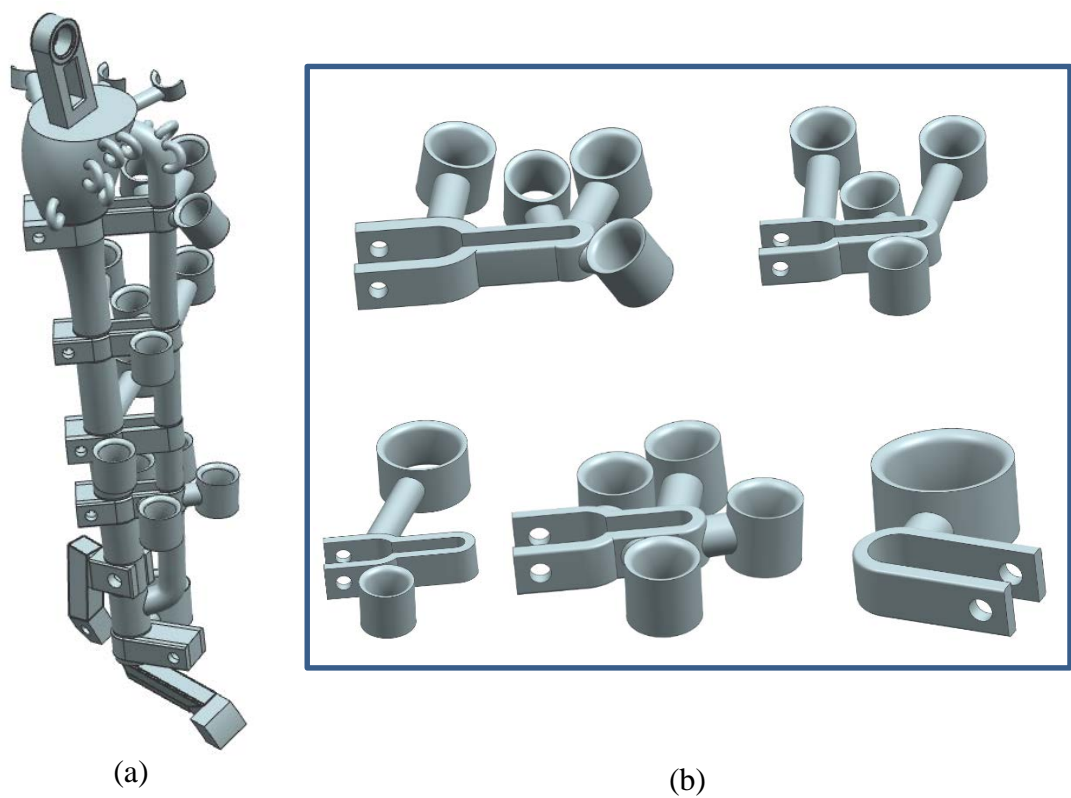


Figure 4.5 Assembly of (a) left shank and (b) extra components.

metal anchor rings were designed as muscle insertions and origins which connect the musculotendon units and the skeleton (see Figure 4.2 and Figure 4.3). The robotic thigh is 11.102 kg in weight, and 43.906 cm high.

Shank is another key segment in human lower limbs for achieving stable and flexible locomotion, since it connects two of the most sophisticated functional joints in human body, i.e., ankle and knee. Inspired from tibia and fibula structure, the main robotic shank was designed based on two cylinders along with some rings, bushings and two cuboids (Figure 4.4) as connections to the muscles and ankle joints. Besides, five extra components were used to balance the mass properties (using solid volumes) of shank and to limit the directions (using bushings) of muscles. As shown in Figure 4.5a, left shank is 3.455 kg in weight, 40.300 cm high.

4.1.3 Trunk

According to different function in human body, the trunk of the robot is divided to three parts: lower trunk, middle trunk and upper trunk. The head has not been included as it contributes few in robot walking.

Lower Trunk, also considered as Pelvis, is the part connecting upper and lower body with the function to bear the weight of the upper body when standing and sitting, transferring that weight from the axial skeleton to the lower appendicular skeleton when standing and walking, and providing attachments for and withstanding the forces of the powerful muscles (especially mono- and bi-articular muscle groups for bipedal movements) of locomotion and posture. Inspired from human pelvis, the robotic lower trunk is 10.199 kg in weight, 20 cm high, 28 cm in length, and 23 cm in width, consisting of a main solid similar to human pelvis, rings, bushings, and a hexagonal groove that is used to insert and stable hip joint (Figure 4.6).

Middle trunk, where most of human internal organs locate, is one of the largest part in human body, providing attachments for organs, associated muscle, membranes, and other soft tissues. Accordingly, the robotic middle trunk is comprised of a rectangular shell, external and internal of which are designed to direct muscle paths, and several weights that balance the mass properties and link artificial muscles (Figure 4.7). It is 14.863 kg in weight, 17.8 cm in height, 27 cm in length, and 25.176 cm in width.

Upper trunk, containing head in this case, is the body which links the arms (through

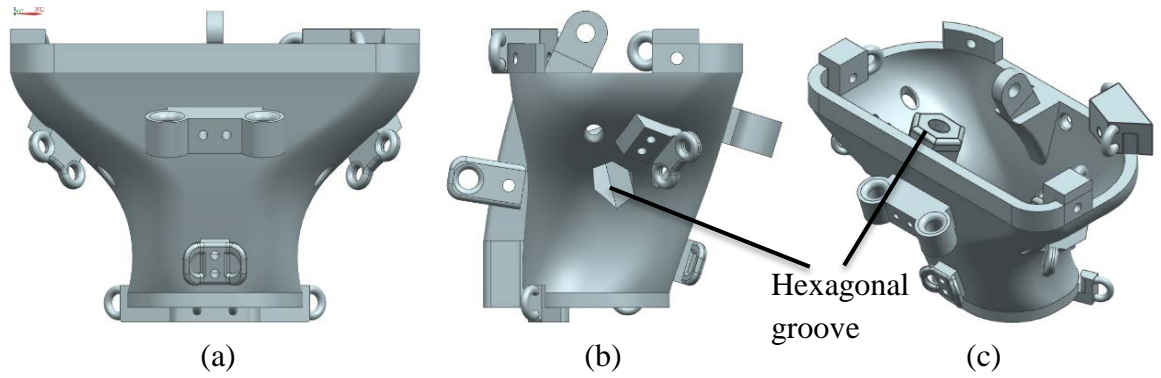


Figure 4.6 (a) Front, (b) Left and (c) Isometric view of lower trunk.

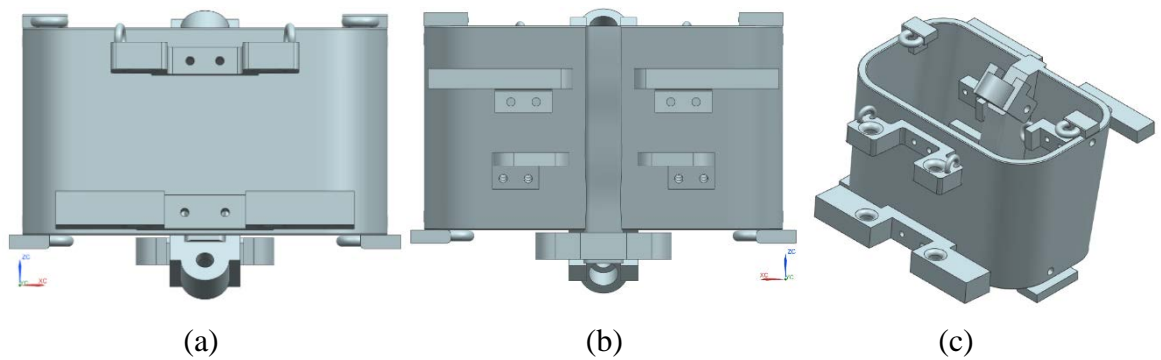


Figure 4.7 (a) Front, (b) Back and (c) Isometric view of middle trunk.

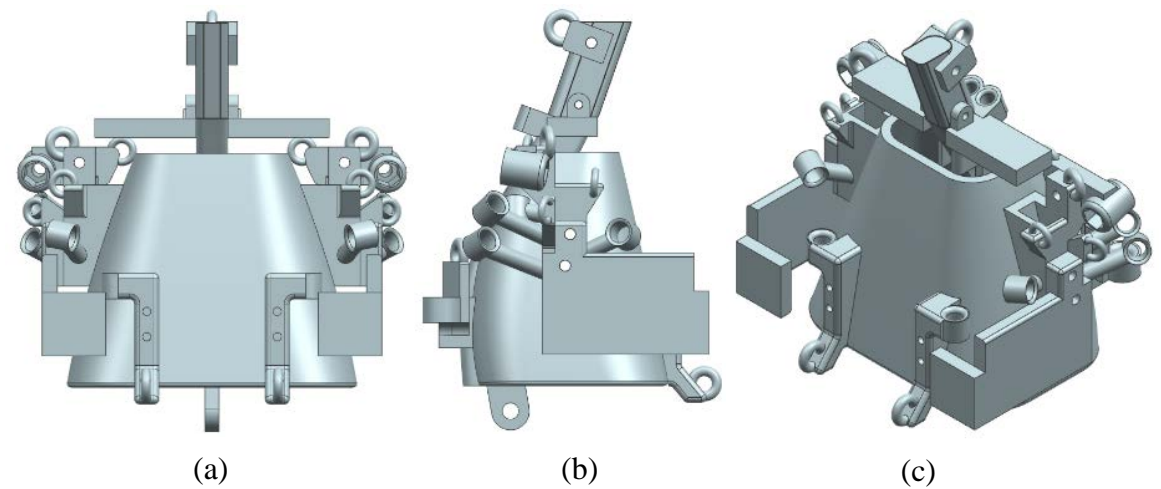


Figure 4.8 (a) Front, (b) Left and (c) Isometric view of upper trunk.

shoulder joints) and head (through cervical vertebra) to humans. Its main functions are to provide origins and insertions for muscles, and coordinate lower limbs and arms in bipedal locomotion, especially walking and running. The robotic upper trunk, consisting of a trapezoidal shell, several extra weights for attaching muscles and balancing the mass properties, and a cuboid representing head (Figure 4.8), is 14.999 kg in weight excluding



Figure 4.9 Left forearm in NX.

the cuboid, 21.25 *cm* in height, 26.8 *cm* in length, 23.7 *cm* in width.

4.1.4 Arm

Forearm, one of the most flexible component in human body, is simplified to a cylinder in the robot (Figure 4.9) as the research is mainly focused on bipedal locomotion. The robotic forearm weighs 1.411 *kg*, and is 43 *cm* long.

Upper arm which extends from the shoulder to the elbow, can move through a remarkable range of motion (e.g., abduction, adduction, rotation, raise in front of and behind the trunk and full 360° move in the sagittal plane) as one of the most mobile parts in human body. Inspired from human humerus, the robotic upper arm consists of a main cylindrical body (Figure 4.10a) and three extra weights (Figure 4.10b). As shown in Figure 4.10c, the upper arm is 1.998 *kg* in weight, and 31.812 *cm* in length.

4.1.5 Joints

Joints, connections between bones in human body, are constructed to allow stable, flexible

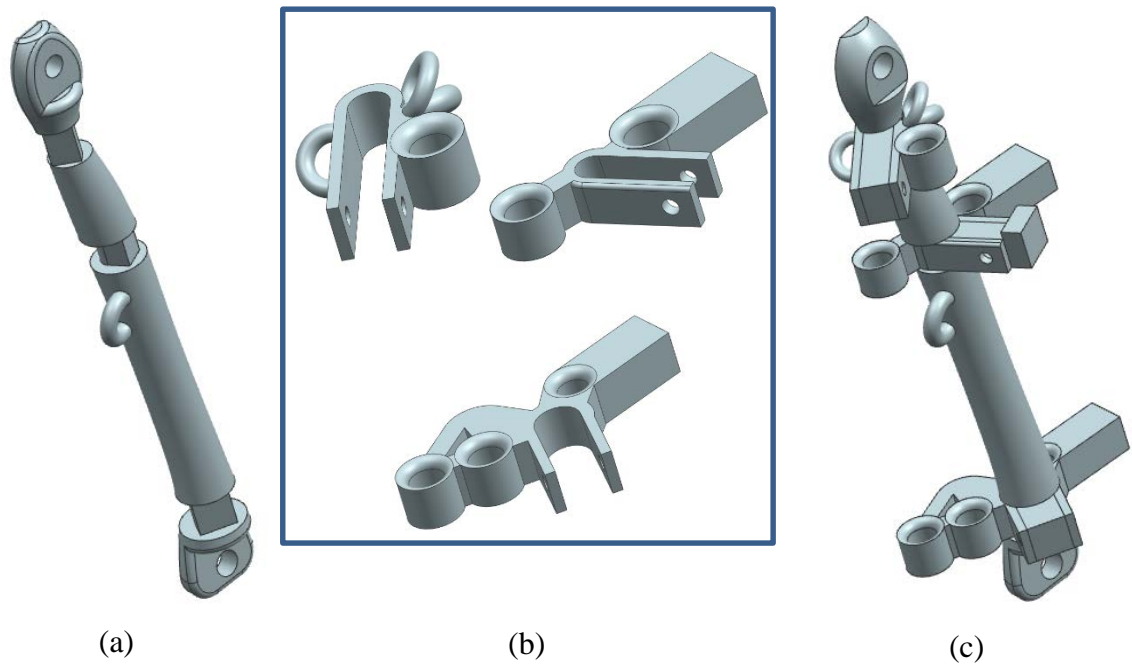


Figure 4.10 (a) Main body, (b) Extra weights and (c) Assembly of left upper arm.

and efficient motions with different degree of freedom (DoF). In human, most of the joints have 6 DoFs, however, it is impossible to physically imitate the joints structure in robot. The translations in the joint are so small that they can be excluded when developing joints in the robot. In fact, it is reasonable to design the robotic joints with similar functions to human joints using commercial bearings such as ball and socket joint and clevis joint. For instance, the main motions in human ankle during locomotion include rotations along the talocrural joint and subtalar joint, so the robotic ankle can be designed as 2 DoFs mechanism.

Ankle, mainly consisting of the talocrural joint and subtalar joint which allow dorsiflexion and plantarflexion, inversion and eversion of the foot respectively, support most of the body weight and dampen vibration during bipedal locomotion, e.g., walking and running. Inspired from that, the ankle joint of the robot is designed with two DoFs, along the subtalar axis and talocrural axis (Figure 4.11c), implemented with two types of plastic bearings KSTM-05 (Figure 4.11a) and KGLM-05 (Figure 4.11b) from IGUS to connect shank and foot (Figure 4.11d) which can compensate misalignment.

As we all know, the joint axes in human ankle are tilted to the ground and the oblique angle varies for different individuals, in contrast to conventional humanoids of which the joint axis is parallel to the ground.

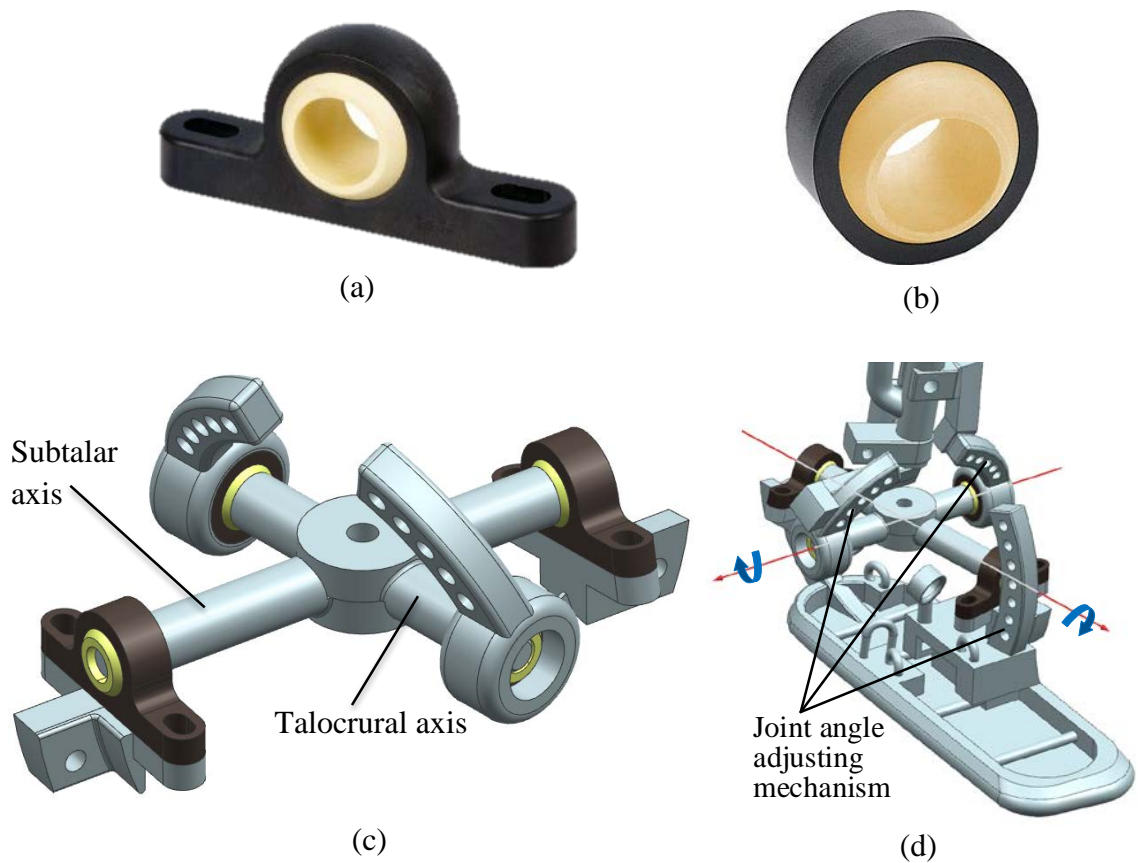


Figure 4.11 Configuration of the robot's left ankle. (a) KSTM-05; (b) KGLM-05; (c) The subtalar axis and talocrural axis; (d) Joint angle adjusting mechanism. Various angles of rotating axis can be obtained through four arc columns and the angle between the subtalar and talocrural axis.

In the robot, joint angle adjusting mechanism (Figure 4.11d) of the ankle using linked spherical bearings is developed to change the axis orientation of the talocrural and subtalar joint. The oblique angle of the talocrural joint axis can be altered every 9 degrees with 5 levels from 0° to 36° (Table 4.1), where the datum axis is the horizontal medial-lateral axis. Also, the oblique angle of the subtalar joint axis can be altered every 7 degrees with 7 levels from 0° to 42° (Table 4.2), where the datum axis is an axis in the transverse plane oriented 12.0° medial to the midline of the foot. The interval of the levels in the talocrural joint of 9° and the interval of the levels in the subtalar joint of 6° were specified to reduce the combinations of the physical tests of the robot.

There are several joints in the forefoot of humans such as intertarsal and tarsometatarsal joints which can facilitate ankle push off during walking, however, it is too

Table 4.1 The oblique angle of the talocrural joint axis.

Axis level	Angle with the datum axis (°)	Angle with the horizontal medial-lateral axis in the frontal plane (°)	Angle with the horizontal medial-lateral axis in the transverse plane (°)
Level 1	0	0.0	0.0
Level 2	9	8.5	3.0
Level 3	18	17.0	6.2
Level 4	27	25.7	9.7
Level 5	36	34.4	13.6

Table 4.2 The oblique angle of the subtalar joint axis.

Axis level	Angle with the datum axis (°)	Angle with the horizontal anterior-posterior axis in the sagittal plane (°)	Angle with the horizontal anterior-posterior axis in the transverse plane (°)
Level 1	0	0.0	12.0
Level 2	7	7.2	12.0
Level 3	14	14.3	12.0
Level 4	21	21.4	12.0
Level 5	28	28.5	12.0
Level 6	35	35.6	12.0
Level 7	42	42.6	12.0

sophisticated to consider them in a real robot as it will cause instability and the control of them are uneasy to solve.

Knee, among all the joints involved in locomotion, performs the highest range of motion (approx. 70°). Knee motion in the sagittal plane is essential for achieving the major bipedal functions (including forward propulsion and weight support), representing a crucial site of action of most biarticular leg muscles and playing a central role for the energy transfer between the knee, hip and ankle, whilst transversal and frontal knee movements have a minor role in locomotion. Therefore, one DoF plastic plain bearing WFM-0608-04 is adopted to simplify knee joint in the robot, and spherical bearing IGUS_EGLM-05 (Figure 4.12a) to adjust different angles of knee axis of rotation.

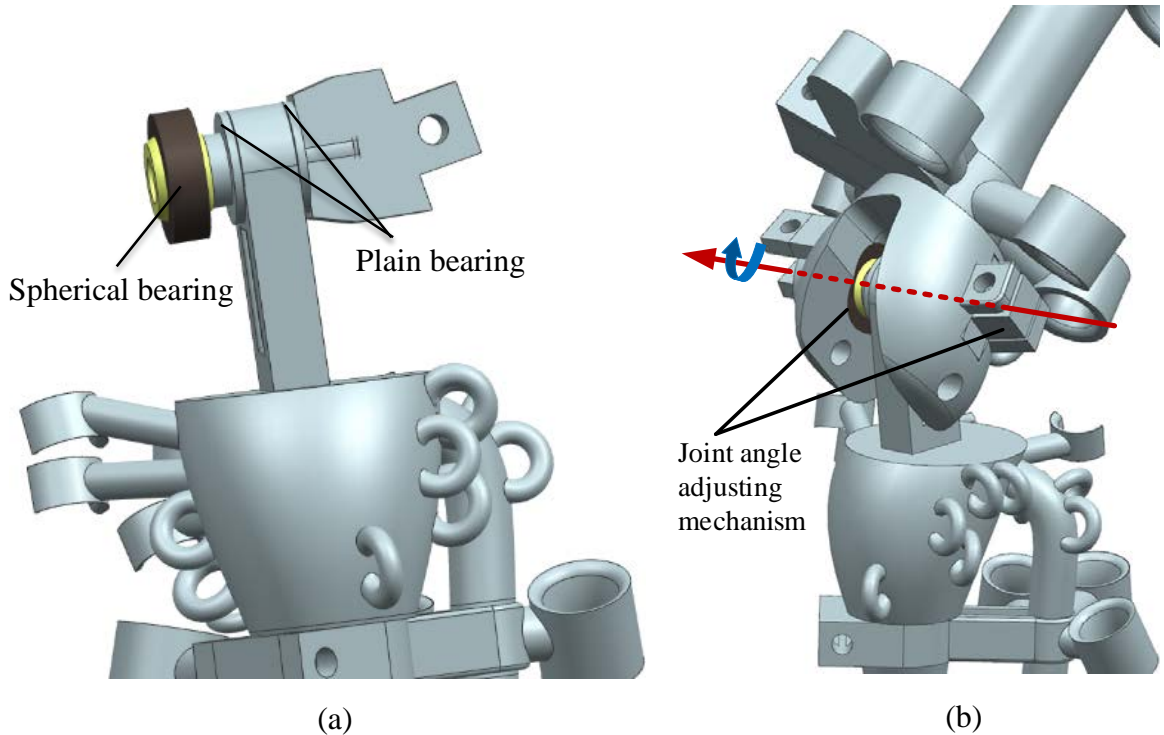


Figure 4.12 Configuration of the robotic left knee. (a) Plain and spherical bearing in knee joint. (b) Joint angle adjusting mechanism.

Similar to the ankle joint in which the axes of rotation are tilted to the ground, the joint axis of human knee is also not parallel to the transverse plane unlike traditional robots. In the robot, joint angle adjusting mechanism (Figure 4.12b) using spherical bearing is designed to change the angle. The oblique angle of the knee joint axis can be altered every 5 degrees with 7 levels from -5° to 25° (Table 4.3) in which the datum axis is an axis in the transverse plane oriented 6.5° anterior to the horizontal medial-lateral axis of the knee.

Hip, the most important part in retaining balance, has two main functions which are to support the weight of the body in both static (e.g. standing) and dynamic (e.g. walking or running) postures, and assure the movement of the lower limbs for body progression. Generally, all the hip muscles pass through the centre of the femoral head, resulting in three DoFs and three pair of principal directions: flexion and extension in the sagittal plane (forward-backward); abduction and adduction in the frontal plane (left-right); lateral rotation and medial rotation around a longitudinal axis (along the thigh); and a combination of these movements (i.e. circumduction, a compound movement in which the leg describes the surface of an irregular cone). Inspired from that, the robotic hip joint

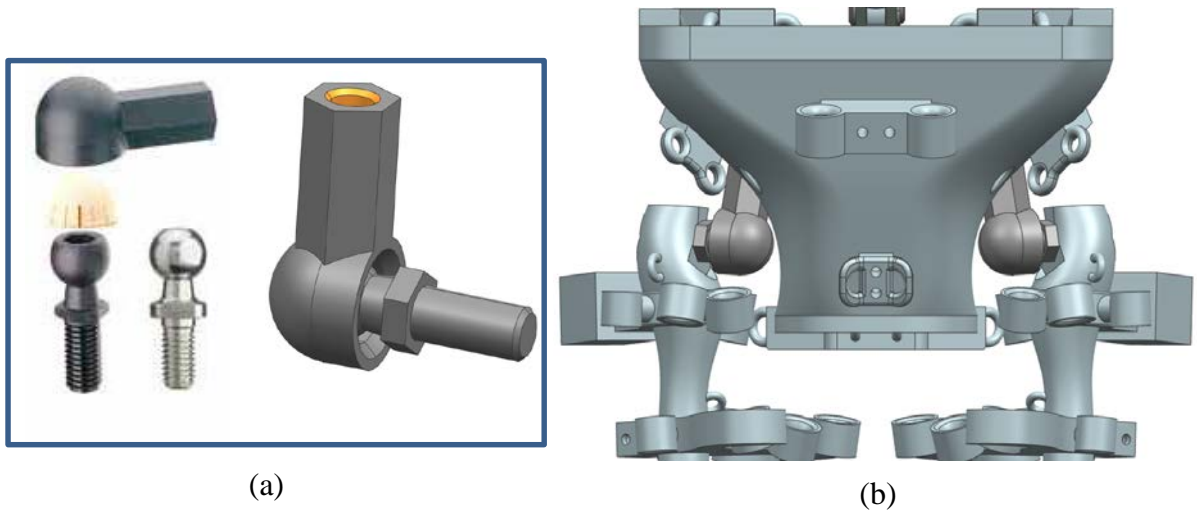


Figure 4.13 Configuration of the left hip. (a) angle joint; (b) connection between pelvis and thigh.

Table 4.3 The oblique angle of the knee joint axis.

Axis level	Angle with the datum axis (°)	Angle with the horizontal medial-lateral axis in the frontal plane (°)	Angle with the horizontal medial-lateral axis in the transverse plane (°)
Level 1	-5	-5.0	6.3
Level 2	0	0.0	6.5
Level 3	5	5.0	6.6
Level 4	10	10.1	6.8
Level 5	15	15.1	6.9
Level 6	20	20.1	7.1
Level 7	25	25.2	7.3

(see Figure 4.13b) is achieved by using angle joint (IGUS WGRM-08 MS shown in Figure 4.13a) for rotating and pivoting motions.

Shoulder similar to the hip joint, can be considered as a ball and socket joint with 3 DoFs, the structure of which allows it to move through a tremendous range of motion. As shown in Figure 4.14, angle joint IGUS WGRM-06 MS is used to connect upper trunk and upper arm of the robot as shoulder joint.

Elbow is the synovial hinge joint between the upper arm and the forearm, which

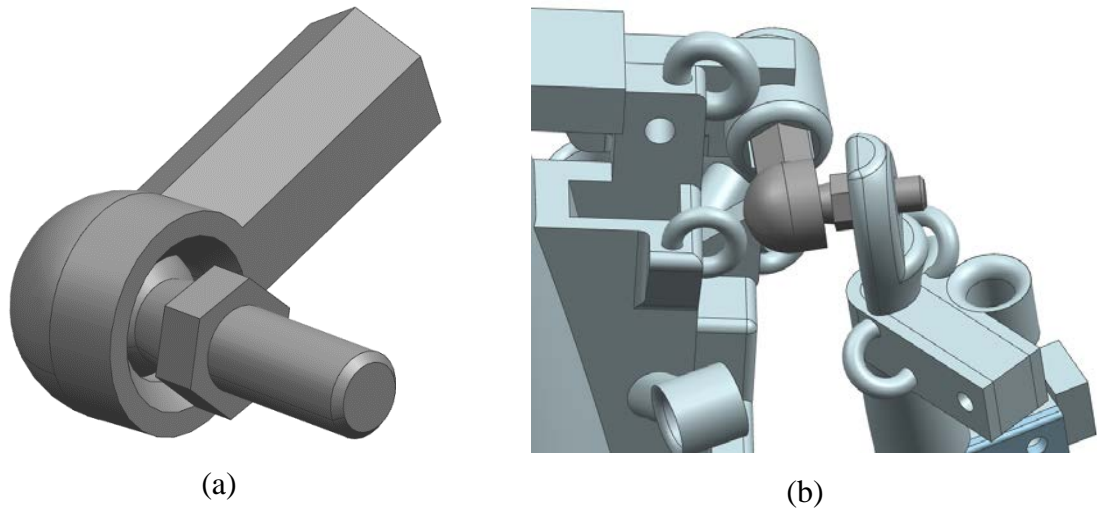


Figure 4.14 Configuration of the left shoulder. (a) angle joint; (b) connections of shoulder joint.

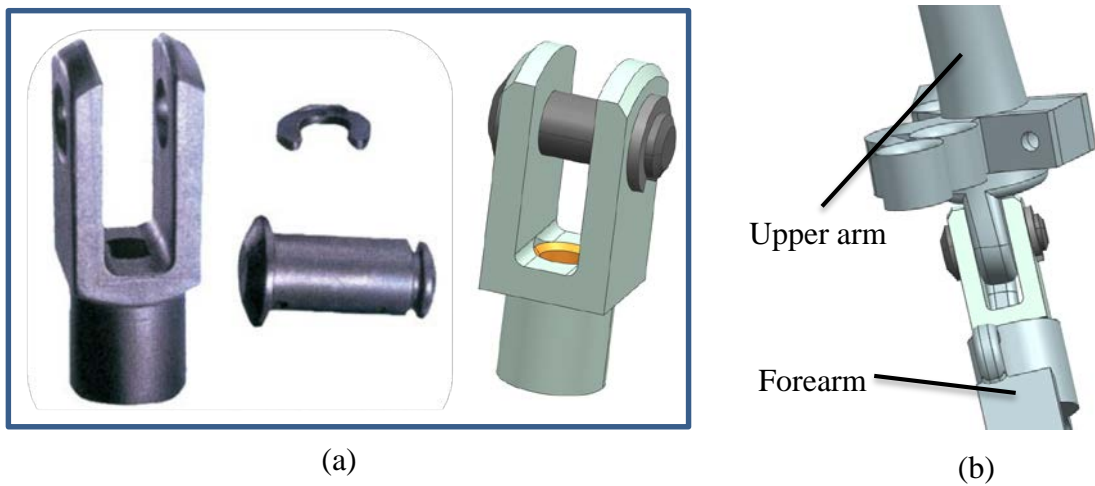


Figure 4.15 Configuration of the left elbow. (a) clevis joint; (b) connections of elbow.

allows flexion and tension. It can be simplified to a clevis joint, resulting in one DoF; accordingly, IGUS GERMK-06 is implemented to represent elbow joint in the robotic arm (Figure 4.15).

Spine, also called vertebral column in human anatomy, contains spinal cord which is part of the central nervous system supplying nerves and receiving information from the peripheral nervous system within the body. Since bipedal locomotion is the priority in this research, the robotic spine can be represented by several clevis joints (IGUS GERMK-06), connecting the lower, middle and upper trunk (Figure 4.16).

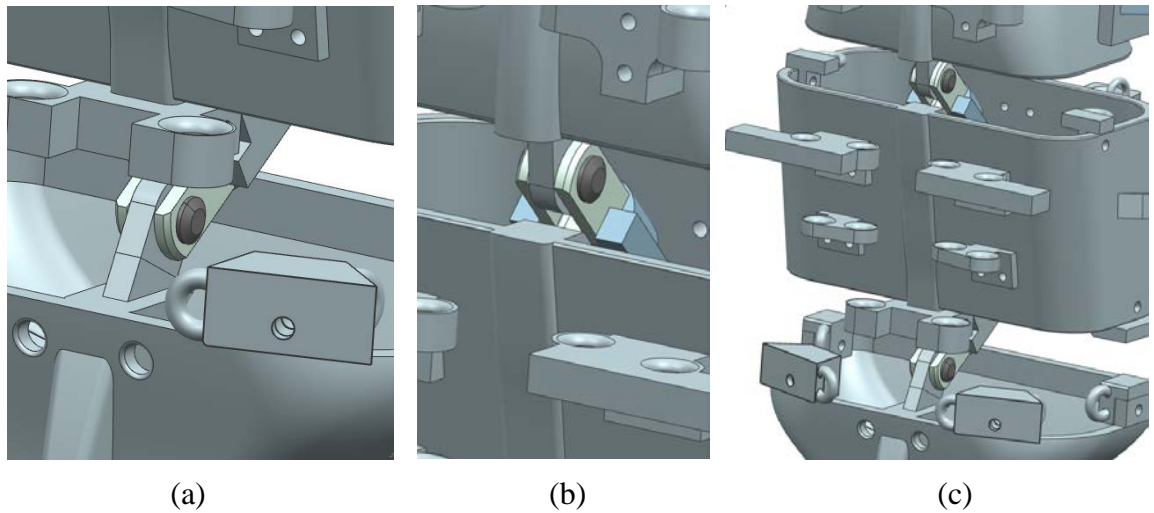


Figure 4.16 Configuration of the robotic spine. (a) connections between the lower and the middle trunk; (b) connections between the upper and the middle trunk (c) simplified robotic spine.

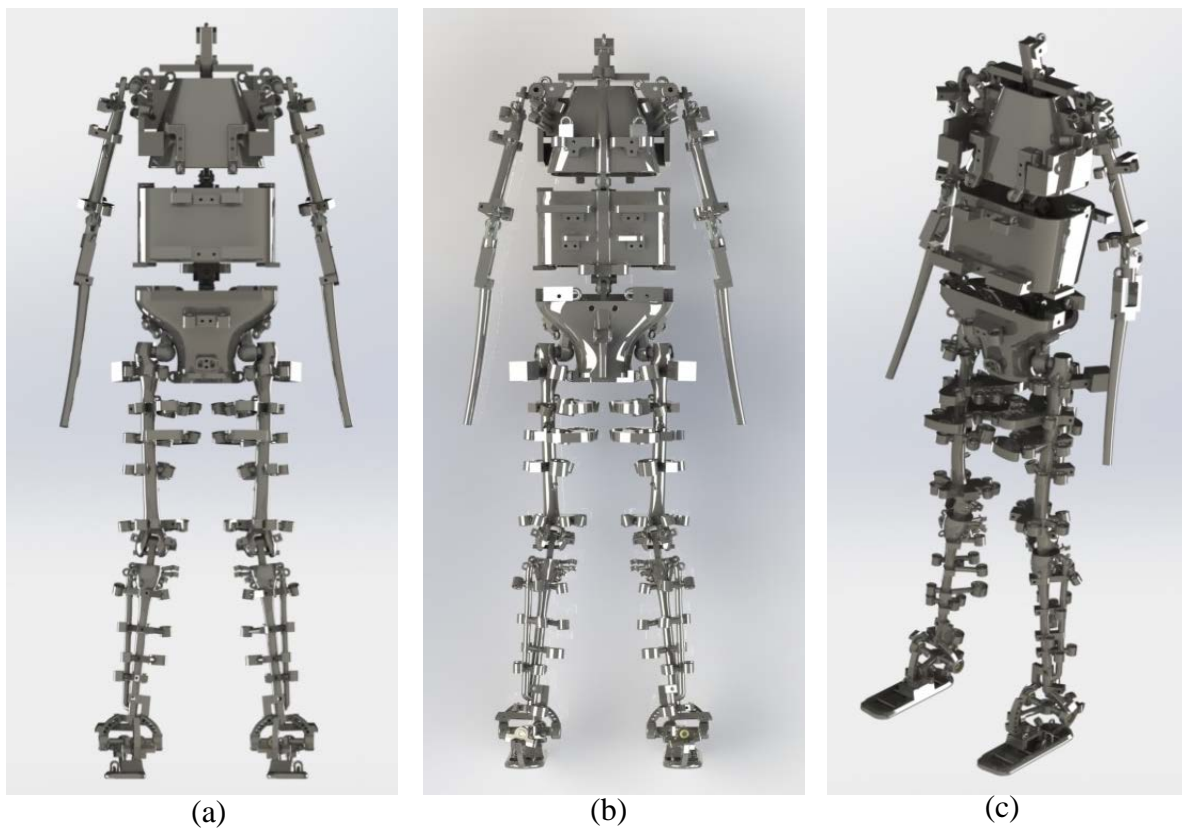


Figure 4.17 (a) Front, (b) Back and (c) Isometric view of the assembled robot in NX.

4.1.6 Assembly

As this research is mainly focused on bipedal locomotion, head and neck is not considered

Table 4.4 Body segment properties of the original robot in the local coordinate system.

Body segment	Mass (kg)	Mass ratio (%)	Moment of inertia in the local coordinate system $\times 10^3$ (kg \cdot mm 2)		
			I_x	I_y	I_z
Upper trunk	14.999	18.742	160.591	148.833	95.769
Middle trunk	14.863	18.572	161.230	129.399	105.537
Lower trunk	10.199	12.744	82.512	71.218	65.182
Left upper arm	1.998	2.497	16.966	15.893	1.716
Left forearm	1.411	1.763	18.349	18.188	0.329
Left thigh	11.102	13.873	168.426	154.339	37.817
Left shank	3.455	4.317	46.923	45.892	4.301
Left foot	2.017	2.520	11.742	10.957	2.627

Table 4.5 Body segment properties of the scaled robot in the local coordinate system.

Body segment	Mass (kg)	Mass ratio (%)	Moment of inertia in the local coordinate system $\times 10^3$ (kg \cdot mm 2)		
			I_x	I_y	I_z
Upper trunk	1.875	18.742	5.018	4.651	2.993
Middle trunk	1.858	18.572	5.038	4.044	3.298
Lower trunk	1.275	12.744	2.579	2.226	2.037
Left upper arm	0.250	2.497	0.530	0.497	0.054
Left forearm	0.176	1.763	0.573	0.568	0.010
Left thigh	1.388	13.873	5.263	4.823	1.182
Left shank	0.432	4.317	1.466	1.434	0.134
Left foot	0.252	2.520	0.367	0.342	0.082

in the design of the robot. Thus, the assembly of robot is shown in Figure 4.17, which is 80.027 kg in weight, and 154.792 cm tall excluding the head. All connections in the robot used plastic commercial bearings, hexagon socket bolts and nuts. Body segment properties of each major segment are in Table 4.4.

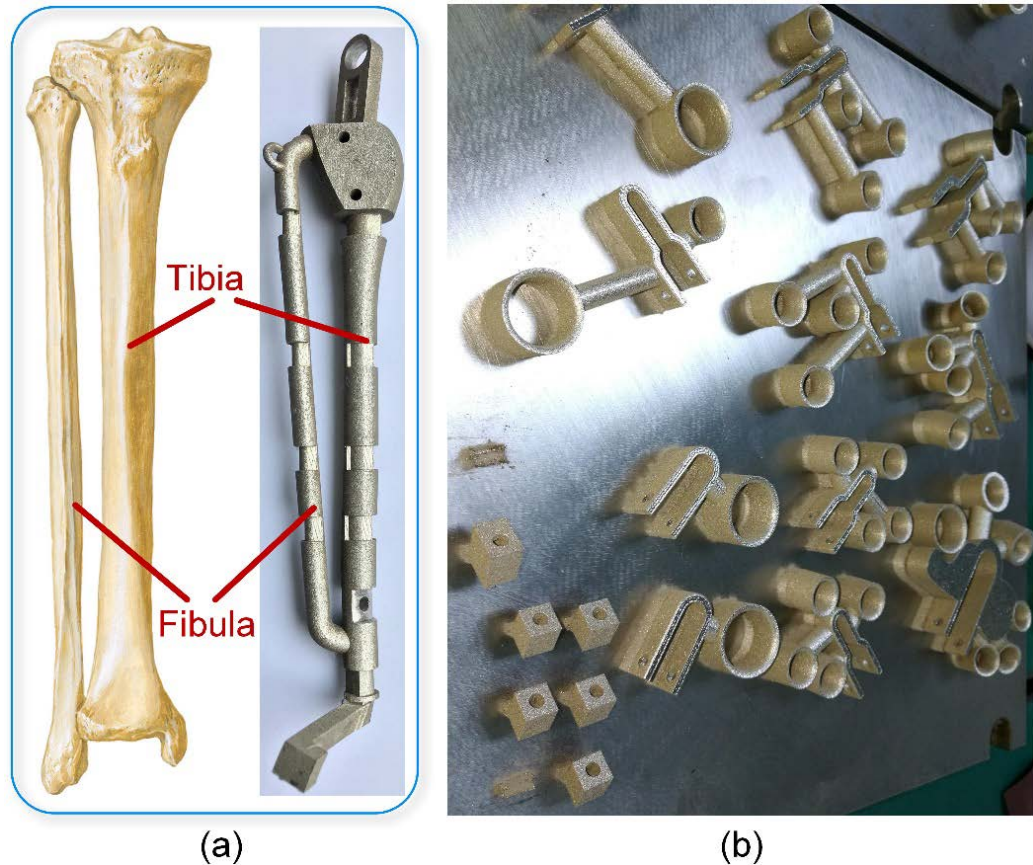


Figure 4.18 3D printed (a) skeleton-like shank and (b) muscle guide of the robot.

4.1.7 Scale

In order to obtain the analysed biomechanics data in terms of mass properties, joint centre and axis of rotation and muscle paths, 3D metal printing technique, also known as Additive Manufacturing, is adopted to assure the anticipated shape of each designed segment. As controlling a bipedal robot with the same size to human body is too difficult, and 3D metal printing a whole-body robot that has same size as human is too expensive, the robot has been scaled to half of human subject in dimensions which leads one eighth in weight and one thirty-second in moment of inertia compared to human body (Table 4.5).

4.2 3D Printing of the skeletal structure

4.2.1 3D Metal Printing

As a leading-edge system for Additive Manufacturing, EOS M280 is the perfect solution for direct, cost-efficient manufacturing of high-quality metal tool inserts, prototypes and end products, particularly for those that have special requirements in terms of surface,

Table 4.6 Technical data of M280.

Name	Value
Building volume (including building platform)	250 mm x 250 mm x 325 mm
Laser type	Yb-fibre laser, 200 W or 400 W (optional)
Precision optics	F-theta-lens, high-speed scanner
Scan speed	up to 7.0 m/s
Variable focus diameter	100 - 500 μm
Power supply	32 A
Power consumption	maximum 8.5 kW / typical 3.2 kW
Nitrogen generator	integrated
Compressed air supply	7,000 hPa; 20 m ³ /h
Argon supply	4,000 hPa; 100 l/min

shape, and structure. Its high level of productivity and ergonomic periphery make the system ideal for the economical and batch-size optimized additive manufacturing of components throughout all phases of the product lifecycle. It is based on the innovative Direct Metal Laser Sintering (DMLS) system by EOS, which can produce components by means of Additive Manufacturing – fully automatically, without tools and based directly on 3D CAD design data. For this purpose, it is equipped with a 200 W or 400 W fibre laser which melts fine metal powder and builds up the product layer by layer. Constant monitoring of the process ensures that all components are produced in excellent, reproducible quality. The technical details are illustrated in Table 4.6. This method allows us to create products with extremely complex geometries including skeleton-like shape (Figure 4.18a), muscle guide (Figure 4.18b) and joint of the robot. Metal printed parts are also fully dense and can include precision internal features that cannot be created using traditional machining.

Direct metal laser sintering involves spreading a very thin layer of metal powder across the surface that is to be printed. A laser is slowly and steadily moved across the surface to sinter this powder, which means that the particles inside the metal are fused together, even though the metal is not heated enough to allow it to melt completely. Additional layers of powder are then applied and sintered, thus “printing” the object one

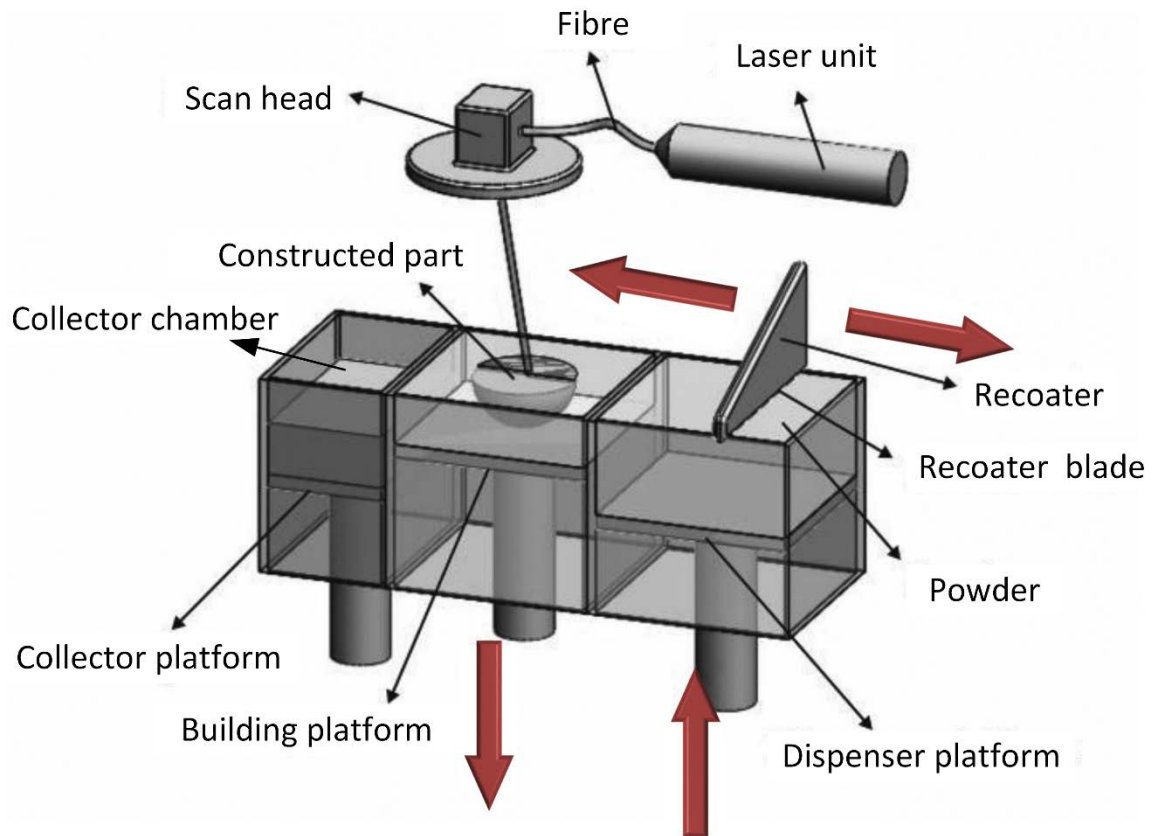


Figure 4.19 Schematic diagram of the EOS M280 system.

cross-section at a time. In this way, DMLS gradually builds up a 3D object through a series of very thin layers.

A schematic diagram of the DMLS system in EOS M280 is shown in Figure 4.19. For construction of any part the machine performs the steps as following. The building and dispenser platforms are lowered by one-layer thickness so that the recoater blade can move without collision. When the recoater stands in right position, the dispenser platform driven by a piston rises to supply the amount of powder for the next layer. Then the recoater moves from the right to the left position, in this way the metal powder is spread from dispenser to the building area and the excess metal powder falls into collector chamber. Then the head scan moves the laser beam through 2D (X-Y) cross section and is precisely switched on and off during exposure of designated areas. The energy absorbed by metal powder will cure and sinter the already solidified areas. This process proceeds layer-by-layer until all parts in a job are completed (see Supplementary Video 1). Thus, in few hours the machine can produce 3D parts with high complexity and accuracy. In addition, during the building process, sintered parts do not attain more or less their final

properties, so depending on the application of part, a post-processing treatment is necessary.

Unlike technologies such as Fused Deposition Modelling (FDM), parts cannot be removed straight after printing with DMLS. There are a number of compulsory steps to do before the print can be finished. Also, there are a number of optional steps to take for better finish quality. These post processing mainly includes the following:

Heat Treatment. Before removing the object from the build platform, heat treatments are required with Direct Metal Laser Sintering. This involves heating and cooling the object at regulated temperatures to help the part solidify and become stronger. This also helps decrease the porosity of the metal.

Support Removal. Supports help with metal part quality in a variety of ways. Firstly, they act as a heat sink, deflecting heat from the part and minimizing distortion due to heat and printing stresses. Unlike with Stereolithography or FDM, removing supports with DMLS is not as easy as just breaking off the plastic supports. With DMLS, the metal supports need to be broken off with machines, which can lead to problems with surface finish on these areas. These areas need to be filed afterwards.

Excess Powder Removal. As with Selective Laser Sintering, parts are surrounded with the material powder in the build chamber. Therefore, any excess unsintered powder needs to be removed from the build chamber to the collector chamber for reusing in future prints.

Optional Extras. Machining to improve surface finish, polishing to shinier surface finish or metal plating.

4.2.2 General Guidelines of Designing 3D Metal Printed Parts

With metal printing, there is a fair amount of trial and error that goes into perfecting a design. However, there are some common design pitfalls that can be avoided to streamline the process. It is important to have the process in mind when creating CAD models. There are some general guidelines that should be followed when designing parts for metal printing:

Wall Thicknesses. Walls that are too thin will begin to collapse under their own weight. Walls should be no thinner than 0.5 mm.

Holes and Gaps. The limitations for gaps and holes may vary widely based on the printer being used, the metals being used, and part geometry. The general rule of thumb is to not design a gap or hole under 0.5 mm. Smaller gaps run the risk of the sides merging together and filling the empty space. On the other hand, supports need to be added for holes greater than 8 mm.

Overhangs: 0.5 mm is the maximum length that should be used for an overhang, and all downward facing structures need to be designed to a chamfer (more than a 45° angle to the horizontal), with a concave or convex shape so the part can support itself. Support structures need to be included in the part's design to exceed these guidelines.

Support Generation. Supports are needed for two reasons. The first is to hold parts to the substrate plate. The second is for heat dissipation. Any areas below 45° from horizontal need supports added. This applies to most of the metals. However, there are exceptions. Ti64 (an alpha-beta titanium alloy) parts can have walls angled to be as low as 30° without supports.

Part Orientation. Unlike other manufacturing processes, 3D printing creates parts with anisotropic properties, which means that they have different mechanical properties in different build directions. In the X and Y directions, for example, parts have higher tensile strength than they do in the Z direction. Hence, part orientation needs to be considered prior to printing. This is especially true if parts are for mechanical/structural purposes where a certain area will sustain some degree of pressure and stress. As any surface below 45° from horizontal need extra supports, suitable orientation of the part can reduce the number of the supports during printing.

There is also an aesthetic element to part orientation. Downfacing surface areas of printed parts will have a poorer surface finish compared to the top-facing surfaces. If certain areas of a part need better surface finishes, they should be taken into consideration during part orientation. For complex parts, it is important that part orientation is such that if there are supports that may affect part function, they can be removed.

Although it may take a few attempts to find the best parameters, design, and orientation for building a part, once discovered (and documented), the process is tremendously consistent. It will result in the same part every time, build after build. Although this may be assumed as a given for any manufacturing process, the predictability and efficiency of metal printing should never be overlooked.

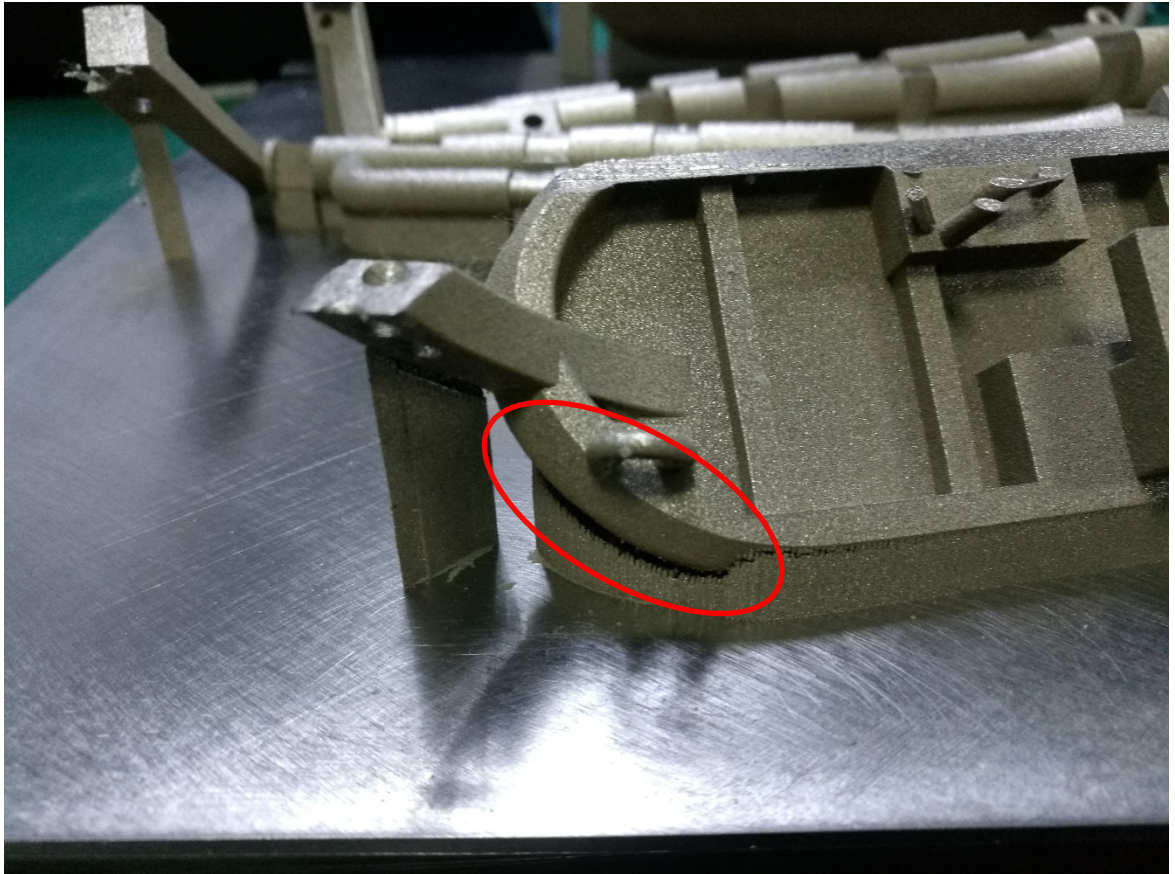


Figure 4.20 Fracture (red circle) between the part and the support during printing.

4.2.3 Limitations

Build times for 3D metal printing are much longer compared to most traditional manufacturing methods. It also typically requires several builds to fine tune a part's design for mass production through 3D metal printing.

It may seem obvious, but the size limitation is another problem. Parts cannot be larger than the machine's build platform, which varies from printer to printer. In this case, the dimensions are around $250 \times 250 \times 325$ mm, which means that the part being printed cannot exceed this size. The orientation of the part located in the build platform has to be determined reasonably for space limitation.

4.2.4 Problems Occurred in the Printing Process

The longer it takes to print a metal part, the higher the chances it will fail. There will be a great deal of internal stress created during the repeated heating and cooling that must take place. The more time it takes to build the part, the more likely the part is to distort during

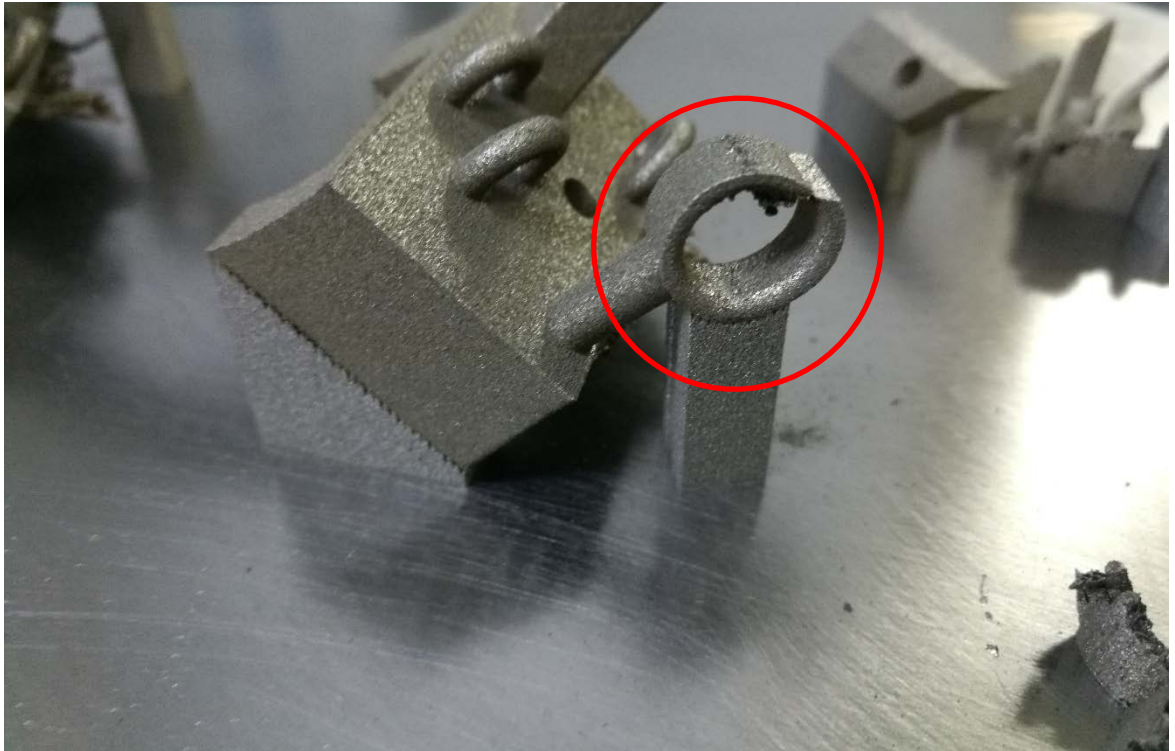


Figure 4.21 Distortion and fracture in the part during printing.

the printing process due to its large volume, and those internal stresses will increase up over the build time; stresses cannot be relieved during metal printing. When the internal stress is great enough, the part will distort, and the build will fail.

One typical failure is the fracture between the support and the part printed (see Figure 4.20). When the internal stress in the connecting region exceed the maximum value that the support could provide, the edge of the part will tear off from the support. The top layer of the part is then not even, which will resist the moving of the recoater during the spreading of the powder for next layer printing.

Another failure that occurred is the distortion and fracture of the part which has holes (see Figure 4.21). Theoretically, holes above 8 mm should be added with support. However, some structures with critical value in hole dimension, such as 7.5 mm, could also fail to print due to the internal stress concentration.

One of the most common failure is caused by the high frictions or collision between the recoater and the top layer of the part when the recoater moves from the dispenser platform through the build platform for spreading the powder. If a distortion of the part has already occurred or a small bump on the build surface of the part exists (due to the previous improper sintering process), the sintered part will get struck with the recoater

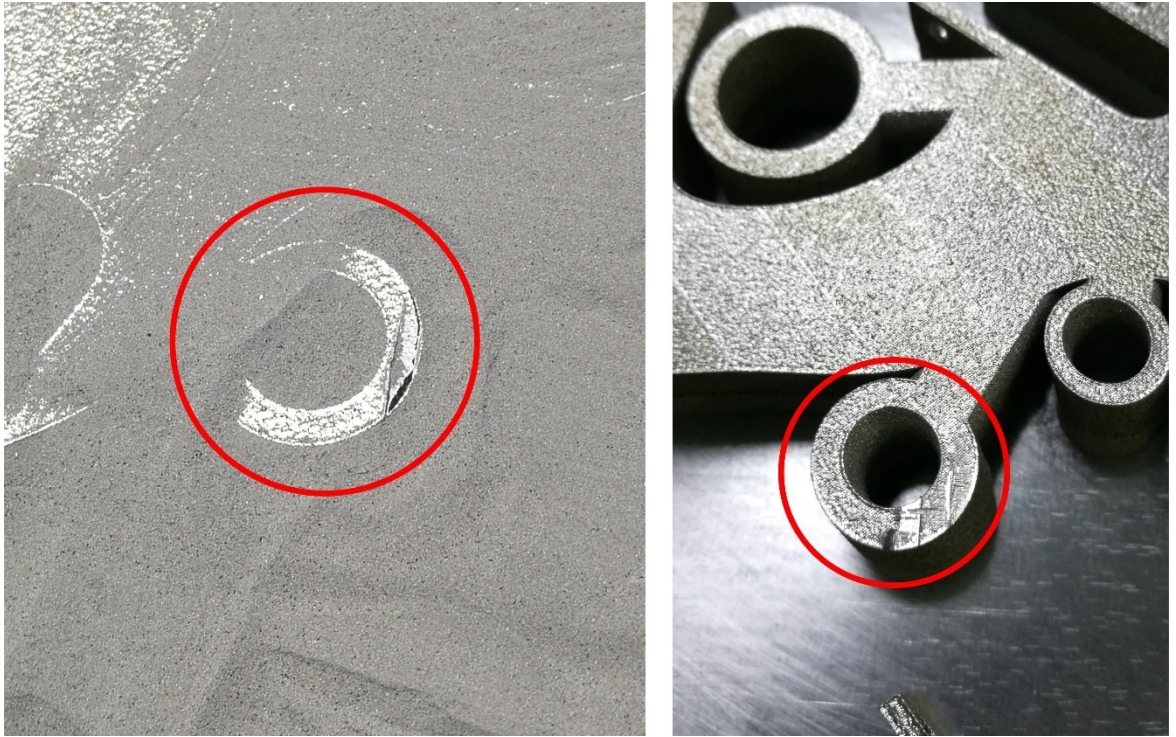


Figure 4.22 Failure caused by collision between the recoater and the parts.

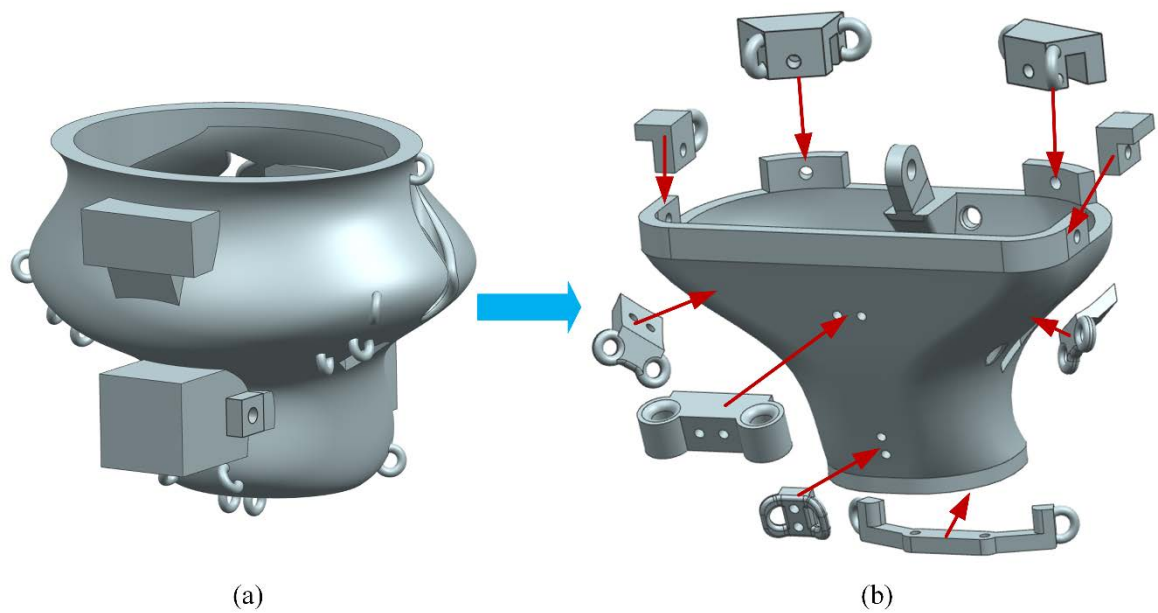


Figure 4.23 Adjustment of the lower trunk. (a) original design and (b) final design.

blade. This could damage the sintered surface of the part (see red circles in Figure 4.22) and induce oscillation between the recoater and the build platform. The powder will randomly spatter in the build chamber which will lead to incorrect sintering or even break the recoater blade in the next spread move.

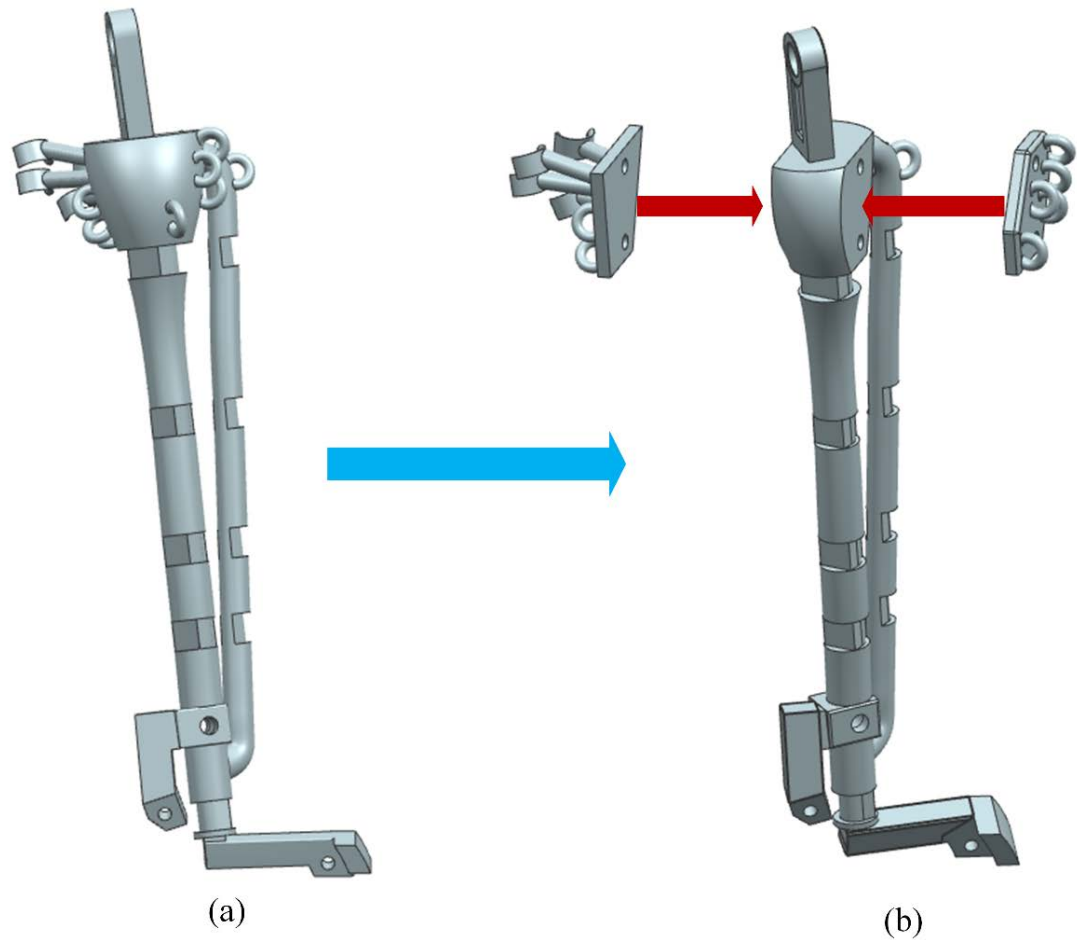


Figure 4.24 Adjustment of the left shank. (a) original design and (b) final design.

4.2.5 Redesign of the Model

Supports need to be added and other factors (excess heat and post-processing) need to be taken into account, which oftentimes would significantly alter the original design.

The original design of the lower trunk (pelvis) (see Figure 4.23a) is a whole entity that consists of a solid with complex curved surface, several weight balance volumes, and a number of rings considered as insertion and origins of the artificial muscle-tendon units (introduced in section 4.3). There are too many supports that need to be added during the printing, as the number of the areas with 45° from horizontal plane does not reduce to reasonable level no matter the orientation of the pelvis. Thus, some segments need to be redesigned to reduce supports and prevent failures from occurring in the printing process. The pelvis was redesigned to a multiple-part assembly (see Figure 4.23b) in which the guide of the muscles, the connecting point of muscles, and the balance weight were integrated in the main body by bolts and nuts.

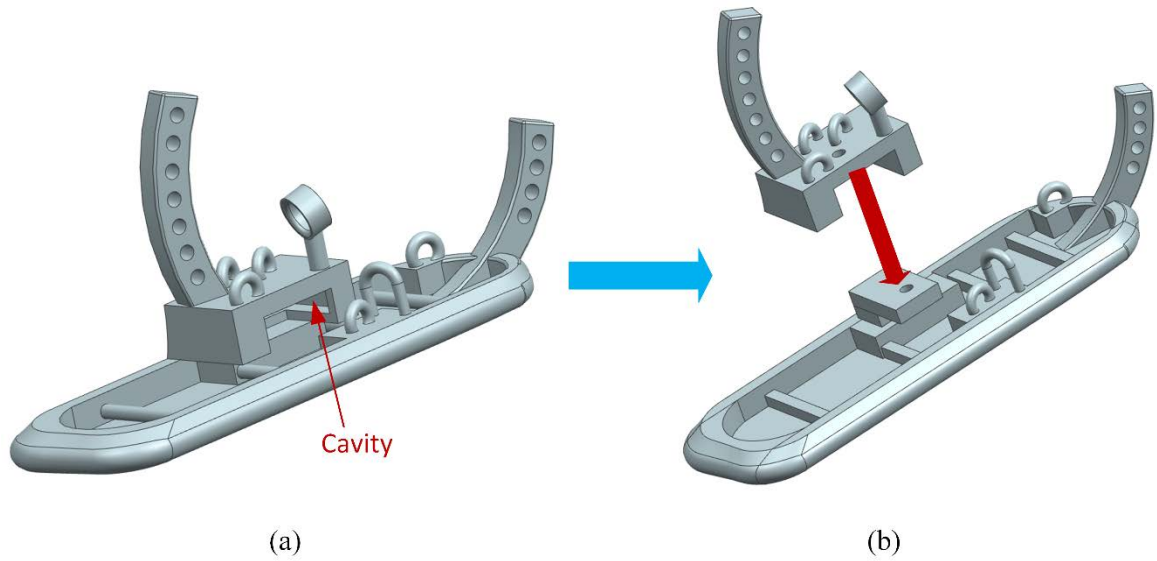


Figure 4.25 Adjustment of the left foot. (a) original design and (b) final design.

The shank has two cylinder-like volumes (mimics the tibia and fibula), and several rings and supporting guides for the muscles same in the pelvis. It must be horizontally placed on the build platform during 3D printing to reduce cost and time. The rings and the muscle guides are in the same zone which is located in the proximal of the shank (see Figure 4.24a). This may lead to fracture or distortion discussed above during the sintering process. So, the main body was simplified to a component without the rings and muscle guides which could be added using bolts and nuts after printing (see Figure 4.24b).

Unlike the pelvis and the shank, the foot was redesigned due to the complex cavity structure (see Figure 4.25a). It is uneasy to remove the supports as working space is limited. Finally, the foot was adjusted to two parts (see Figure 4.25b) that could be assembled by bolts and nuts.

4.2.6 Material and the Printed Skeleton

Some of the most common and reliable metals for 3D printing include stainless steel, aluminium, titanium, cobalt chrome and Inconel alloy. Choosing the best material is vital for ensuring the robot will perform the same biomechanics as need.

Stainless steel powder is used as 3D printing material to assure that the biomechanical properties of the segment is similar to real human body and the strength of the robot is high enough during walking tests. It has high hardness and toughness, and is highly machinable and can be highly polished. Stainless steel is commonly used for pressure



Figure 4.26 3D printed components of the bipedal robot. (top left) and (top right) showed the assembly of the lower body, (bottom left) and (bottom right) showed the assembly of the upper body.

die casting molds, surgical tools, and general engineering parts. The lower and upper body of the 3D printed components were shown in Figure 4.26, in which commercial



Figure 4.27 The design of shoes. (a) isometric view and (b) functional surfaces at bottom.

plastic bearings (see in section 4.1.5) were implemented in the joints.

4.2.7 Shoes

As most tests are on a ramp and the friction between the robot and the surface affects the motion performance, a pair of shoes (see Figure 4.27a) was designed for the robot to wear so that the friction can be adjusted to fit the terrain. Functional surfaces including well-arranged hexagonal protuberances (see Figure 4.27b) were added in the bottom of the shoes for skid resistance. A curved surface at the bottom mimics the commercial shoes that may benefit foot clearance during walking. The hexagonal protuberances in the heel were bigger than those in other regions which could absorb shock during heel strike of the foot.

ProJet 5500X (3D Systems, U.S.A) is a multi-material composite printer that generates stunningly realistic, functional prototypes and patterns for a variety of applications. It can produce over-molded parts, multi-material assemblies, rubber-like components, jigs and fixtures, dies and more. This 3D printer simultaneously prints and blends both flexible and rigid photopolymers within the VisiJet family of materials, layer-by-layer at the pixel level in a variety of colours and shades (including opaque, clear, black or white and numerous shades of grey), to achieve superior mechanical properties and custom performance characteristics. Also, VisiJet rigid plastic, elastomeric and composite materials are engineered for performance with varying degrees of flexibility,



Figure 4.28 Top (left) and bottom (right) view of the 3D printed shoes.

material transparency and differentiated shades in one part.

The printer can mix any two base materials together pixel-by-pixel to achieve various properties, in up to twelve different composite ratios. An entire object can be printed in any of these composites, or a specific region of a part can be easily selected to be printed with any number of different material combinations. In this case, I used the combination of VisiJet CR-WT and VisiJet CE-BK as the mixed materials. The material properties of these two-mixed composites are described in Table 4.7. Among them, RWT-EBK 500 is a slightly flexible material with good tensile strength ($1.7\text{--}3.7\text{ MPa}$), hardness (Shore A 80) and tear resistance ($25\text{--}32\text{ kN/m}$).

A pair of rubber-like shoes (see Figure 4.28) were 3D printed using RWT-EBK 500 material. Unlike other single material 3D printer, ProJet 5500X uses photopolymers as the build material and wax as the support material. Post-processing was needed as wax must be removed using oil, which would add a layer of grease into the surface of the shoes. Thus, it was polished using a file after wax removal to increase friction of the surface.

4.3 Design of a Whole-Body Muscular System

4.3.1 Background

Artificial muscle groups, i.e., muscle-tendon units were designed to simulate the mechanical functions of major musculotendon units. Several types of material are considered. Electrothermally driven shape-memory metal wires can contract fast and deliver large strokes under heavy loads, but are difficult to control due to hysteresis and

Table 4.7 Material properties of multi-material composites (VisiJet CR-WT + VisiJet CE-BK)

Material Name	Description	Tensile Strength (MPa)	Flexural Strength (MPa)	Flexural Modulus (MPa)	Impact Strength (Notched Izod) (J/m)	Shore A Hardness, Scale A	Shore D Hardness, Scale D	Tear Resistance (kN/m)
		ASTM D-638	ASTM D-790	ASTM D-790	ASTM D-256	ASTM D-2240	ASTM D-2240	ASTM D-624
RWT-EBK 100	Very Rigid	18-27	18-21	450-750	18-25	N/A	75	N/A
RWT-EBK 150	Slightly Rigid	14-19	12-13	350-550	22-30	N/A	70	N/A
RWT-EBK 200	Rigid	11-14	7-7.4	150-250	32-52	N/A	65	N/A
RWT-EBK 250	Rigid	8-11	3.9-4.2	70-180	29-42	N/A	60	N/A
RWT-EBK 300	Slightly rigid	5-9	1.6-1.9	30-80	74-114	N/A	55	N/A
RWT-EBK 350	Slightly Rigid	4.5-8.5	N/A	N/A	N/A	N/A	50	N/A
RWT-EBK 450	Slightly flexible	3-6.6	N/A	N/A	N/A	90	N/A	44-62
RWT-EBK 500	Slightly flexible	1.7-3.7	N/A	N/A	N/A	80	N/A	25-32
RWT-EBK 550	Flexible	1-3	N/A	N/A	N/A	70	N/A	18-23
RWT-EBK 600	Flexible	0.7-2	N/A	N/A	N/A	60	N/A	11-17
RWT-EBK 650	More Flexible	0.6-1.8	N/A	N/A	N/A	50	N/A	6.6-9.3
RWT-EBK 700	Very flexible	0.3-1	N/A	N/A	N/A	40	N/A	6.5-8.5

are expensive [274]. Electrochemically driven fibres of organic conducting polymers can perform large strokes, but they require an extra containment system and have limited cyclicality and cycle rate, adding to system cost and weight [275]. Thermally powered shape-memory polymers have low work capacity unless they are fibre-reinforced [276], but polymer/carbon nanotube (CNT) composite fibres with high work capacity must be redrawn between cycles [277]. Polymeric electric field-driven electrostrictive rubbers and relaxor ferroelectrics are fascinating because of their large strokes and high efficiencies but due to the high electric fields they are difficult to allocate as artificial muscle fibres [278]. High-performance hybrid CNT muscles [279] can provide fast, high-force, large-stroke torsional and tensile actuation, but are expensive because of the high cost of CNT yarn.

Recently, Haines et al [280, 281] found that inexpensive high-strength polymer fibres used for fishing line and sewing thread such as nylon and polyethylene can be easily transformed by twist insertion under load to provide fast, scalable, nonhysteretic, long-life tensile and torsional muscles. After considering the power, stroke, hysteresis, life cycle and efficiency, nylon monofilament is chosen as the raw material to deploy as the muscle-tendon unit of the robot.

4.3.2 Fabrication

A fabricating system for the muscle-tendon units that consists of a DC motor, a motor controller, and a DC power source, is set up as shown in Figure 4.29(a). The original fishing line twists to coiled fishing lines (see Figure 4.29b) driven by the rotation of the motor, with load hanging on the end of it. During twist, the load must not rotate with the fishing line. Several circles should be allowed at the end of twist in case of the resilience of the fibre. The number of circles which are needed to form a coiled fishing line in a test with same length, diameter fishing line and same weight, is constant.

With different diameters and load during twist, the stiffness of these artificial muscle-tendon units could be altered easily. The weight applied during coiling is important and is adjustable over a narrow range for a given fibre: too little weight and the fibre snarls during twist insertion; too much weight and the fibre breaks [280]. Coils formed by twist insertion obtain some twist liveliness, meaning that they can untwist, especially when external loads add on. This problem can be avoided by thermal annealing to set the

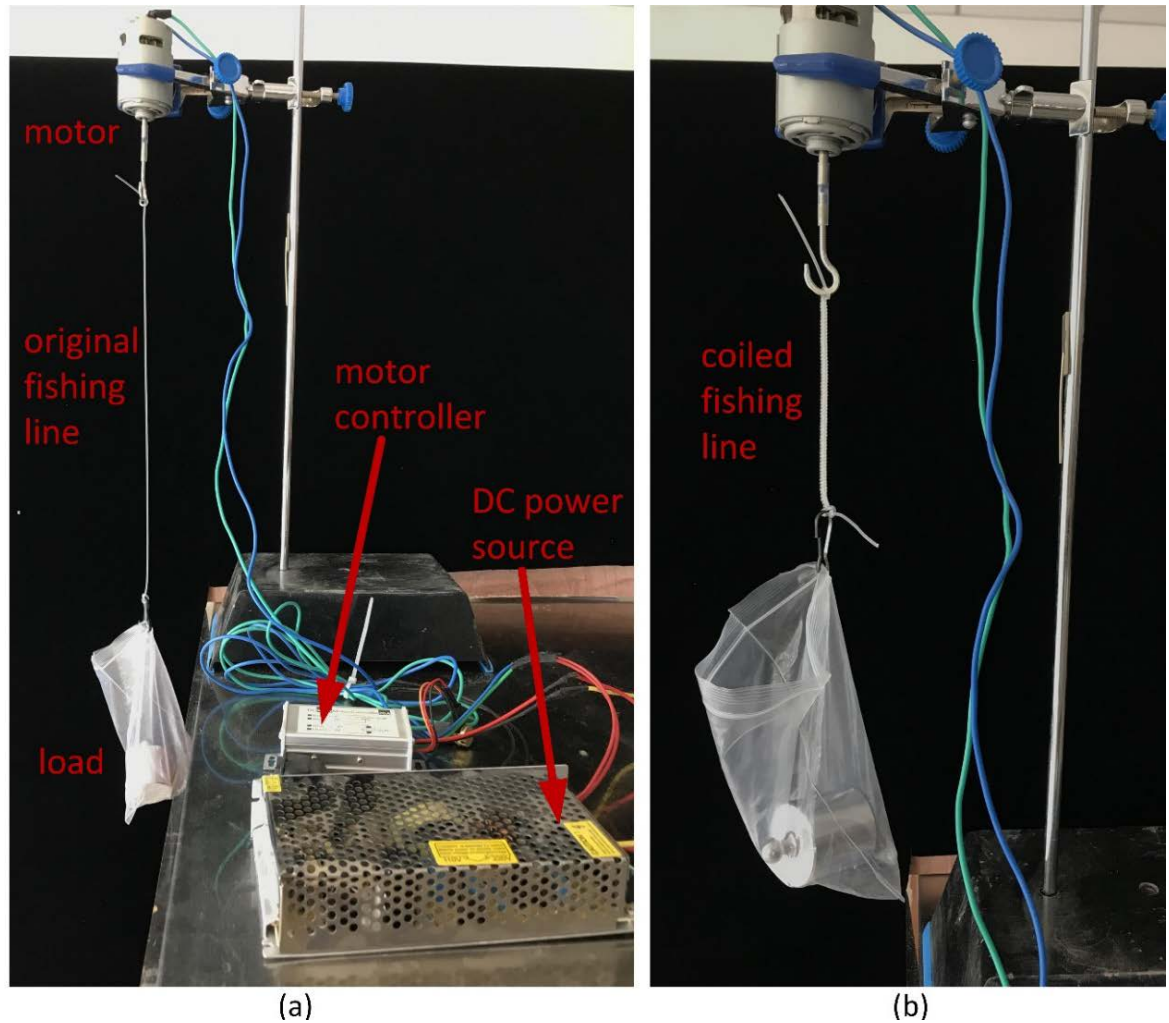


Figure 4.29 (a) Fabricating system for muscle-tendon unit and (b) coiled fishing line.

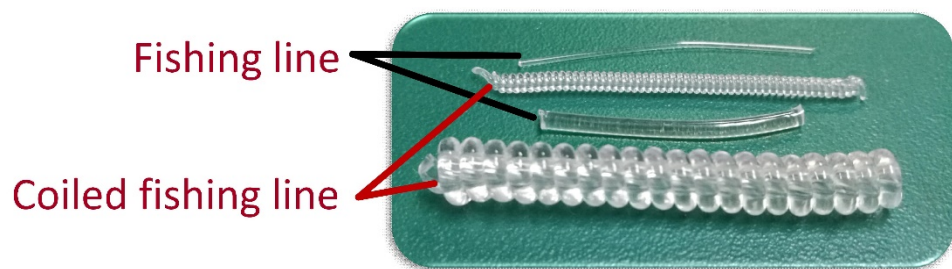


Figure 4.30 Artificial muscle tendon units using nylon 6 monofilament fishing line. From top to bottom are a non-twist 0.47-mm-diameter fibre, coiled fibre of 0.47-mm-diameter fibre, a non-twist 1.5-mm-diameter fibre and coiled fibre of 1.5-mm-diameter fibre.

structure [280]. A series of nylon 6 fishing lines were twisted or coiled to form elastic units with spring properties, as shown in Figure 4.30.

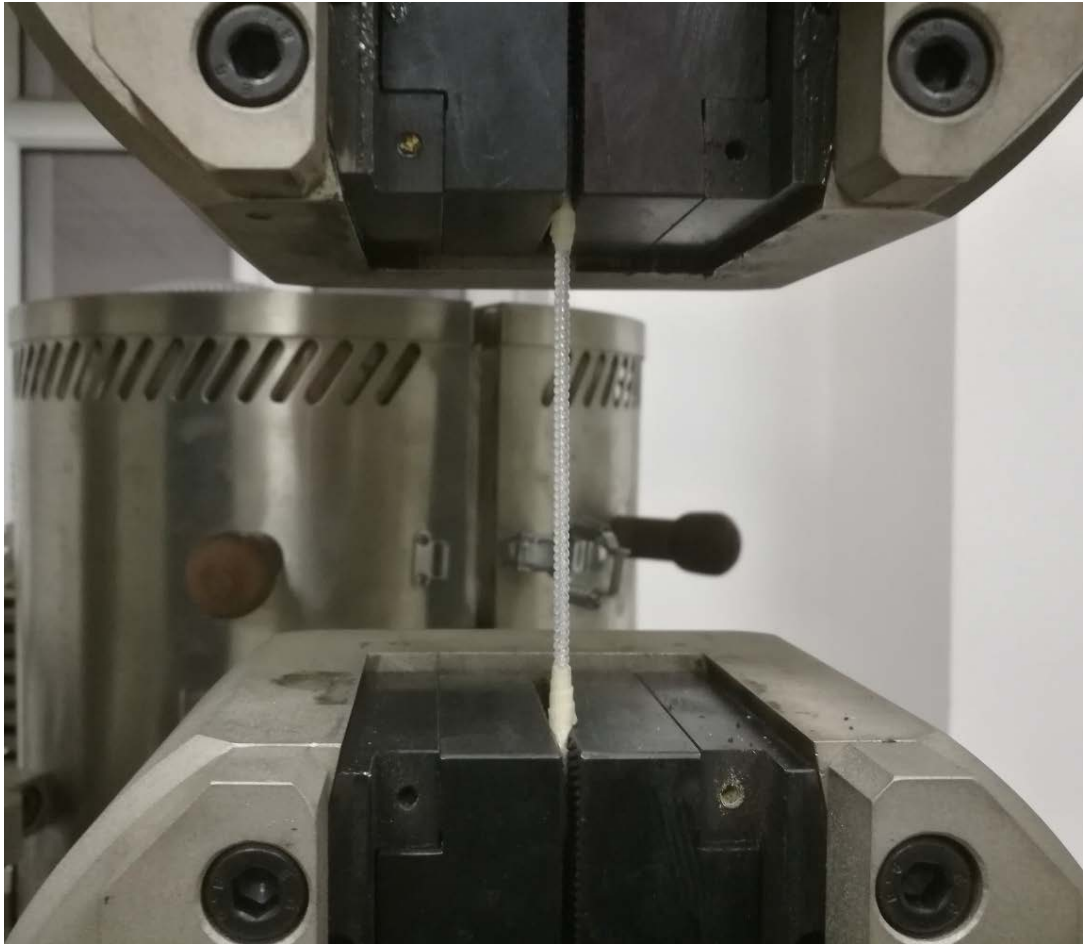


Figure 4.31 Material property testing of a coiled fibre using a tensile/compression testing machine.

4.3.3 Material properties of the muscle-tendon unit

The material properties of coiled fishing lines have been tested. Since the results will change according to different original length, normalised values are adopted as reference which is defined as the values per 100 *mm* length converted from the real experimental values. The material properties of various coiled fishing lines (Table 4.8-Table 4.10) are tested using a tensile/compression testing machine (see Figure 4.31). Length is the original fibre length before tensile test, elongation is the difference between the elongated fibre length and the original fibre length, elongation percentage is defined as elongation divided by original fibre length, maximum load is the critical load value before fracture, stiffness is defined as force divided by elongation, and normalised stiffness is defined as stiffness per 100 *mm* fibre length.

Generally, the coiled fibres become stiffer when the diameter or load during twist

Table 4.8 Material properties of non-annealing coiled fibres twisted from 1.2-mm-diameter fibre under different loads.

Original diameter (mm)	Load during twist (kg)	Stiffness ($N\cdot mm^{-1}$)	Length (mm)	Elongation (mm)	Elongation percentage (%)	Maximum load (N)	Normalised stiffness (per 100mm) ($N\cdot mm^{-1}$)
1.2	1.0	0.57995	42	136.4600	324.90	76.70	0.24358
1.2	1.2	0.46752	67	136.6310	203.93	64.10	0.31324
1.2	1.4	0.33685	88	213.5480	242.67	68.80	0.29643
1.2	1.6	0.38670	76	218.4600	287.45	79.90	0.29389
1.2	1.8	0.42787	85	196.7930	231.52	79.90	0.36369
1.2	2.1	0.42236	110	134.8810	122.62	60.80	0.46460
1.2	2.3	0.52841	96	99.4600	103.60	56.90	0.50727

Table 4.9 Material properties of non-annealing coiled fibres twisted from 1.5-mm-diameter fibre under different loads.

Original diameter (mm)	Load during twist (kg)	Stiffness ($N\cdot mm^{-1}$)	Length (mm)	Elongation (mm)	Elongation percentage (%)	Maximum load (N)	Normalised stiffness (per 100mm) ($N\cdot mm^{-1}$)
1.5	2.1	0.62431	96	199.3810	207.69	112.40	0.59934
1.5	2.3	0.65033	94	178.4640	189.86	111.70	0.61131
1.5	2.5	0.54559	135	200.0480	148.18	107.10	0.73655
1.5	2.7	0.69010	105	178.7100	170.20	120.90	0.72461
1.5	3.1	0.97241	70	136.0480	194.35	130.30	0.68069
1.5	3.3	0.66849	113	163.7100	144.88	114.40	0.75539

increases, meaning that thicker untwisted fibre and heavier weight in twist insertion will augment the normalised stiffness and reduce the elongation percentage of the coiled fibre.

The non-annealed and annealed coiled fibre have different properties while the coiled fibre stabilised by thermally annealing is much stronger, i.e., larger value of normalised stiffness. The normalised stiffness of non-annealed and annealed coiled fibre formed by twisting 1.5-mm-diameter fibre under 2.5 kg load are $0.73655 N\cdot mm^{-1}$ and $1.83326 N\cdot mm^{-1}$, the latter is almost 2.5 times than the former.

Table 4.10 Material properties of annealing coiled fibres twisted from 1.2-mm-diameter and 1.5-mm-diameter fibres under different loads.

Original diameter (mm)	Load during twist (kg)	Stiffness ($N \cdot mm^{-1}$)	Length (mm)	Elongation (mm)	Elongation percentage (%)	Maximum load (N)	Normalised stiffness (per 100mm) ($N \cdot mm^{-1}$)
1.2	1.5	0.70926	100	167.8770	167.88	95.10	0.70926
1.2	1.7	0.76231	167	92.7980	55.57	70.70	1.27306
1.2	2.0	1.34588	90	56.9640	63.29	75.40	1.21129
1.2	2.2	0.78656	158	95.9600	60.73	75.30	1.24276
1.5	2.5	1.60812	114	96.4640	84.62	142.10	1.83326

4.3.4 Selecting principle

Functional muscle groups power human locomotion and support our body at the same time. Muscles coordinate human movement because the forces generated by them develop mechanical energy and mechanisms for energy exchange among the segments. In this case, muscle force and joint motion were used as reference to choose proper muscle tendon unit. The elongation of some muscles in the lower limbs of human body during walking (Table 4.11) are calculated in NX software. The lower limb muscle forces (normalised to body weight and gait cycle duration) are determined by the data of Alexander et al [282] who computed muscle force using a musculoskeletal model where kinetic data were recorded with two force plates imbedded into the ramp.

I assume that the elongation and the force generated by muscle are linear. Thus, the stiffness of the muscle can be defined as,

$$Stiffness = \frac{force}{elongation_{max}} \quad (4.1)$$

where $elongation_{max}$ is the maximum elongation of the muscle, e.g., the $elongation_{max}$ of Hamstrings is the difference value between flexion and extension, $force$ is the muscle force. The elongation of main muscle groups in lower limbs are shown in Table 4.11. Comparing the stiffness with the material properties of the coiled fibres (Table 4.8-Table 4.10), the appropriate stiffness of corresponding musculotendon units are selected.

Table 4.11 Muscle changes during human walking.

Muscle name	Motion	Elongation /mm
Gluteus maximus (GMAX)	Flexion	44.43160
	Extension	-17.64450
Hamstrings	Flexion	50.01940
	Extension	-6.28540
Rectus femoris (RF)	Flexion	3.38150
	Extension	-41.18350
Vastus (VAS)	Flexion	26.77980
Gluteus medius (GMED)	Flexion	15.14900
	Extension	-4.88440
Adductor longus	Flexion	-35.42680
	Extension	7.25390
Soleus	Dorsiflexion	5.70950
	Plantarflexion	-10.57440
Gastrocnemius (head)	Flexion	-15.27530
Extensor longus	Dorsiflexion	10.00410
	Plantarflexion	-7.72110
Tibialis anterior	Dorsiflexion	10.01680
	Plantarflexion	-7.40500

4.4 Integration

In the end, based on the measured and analysed anthropometric data, key kinematic parameters and musculoskeletal geometry of a real human subject, the 3D printed skeletal structure and artificial muscle tendon units were designed, manufactured and then integrated together comprising the bio-inspired bipedal robot (see Figure 4.32) in which the mass properties, joint centre and joint axis of rotation and muscle paths are extremely similar to a real human body.

4.5 Conclusions

In this chapter, the physical prototype of the robot was developed based on human musculoskeletal biomechanics that were analysed in chapter 3. Functional parts of the

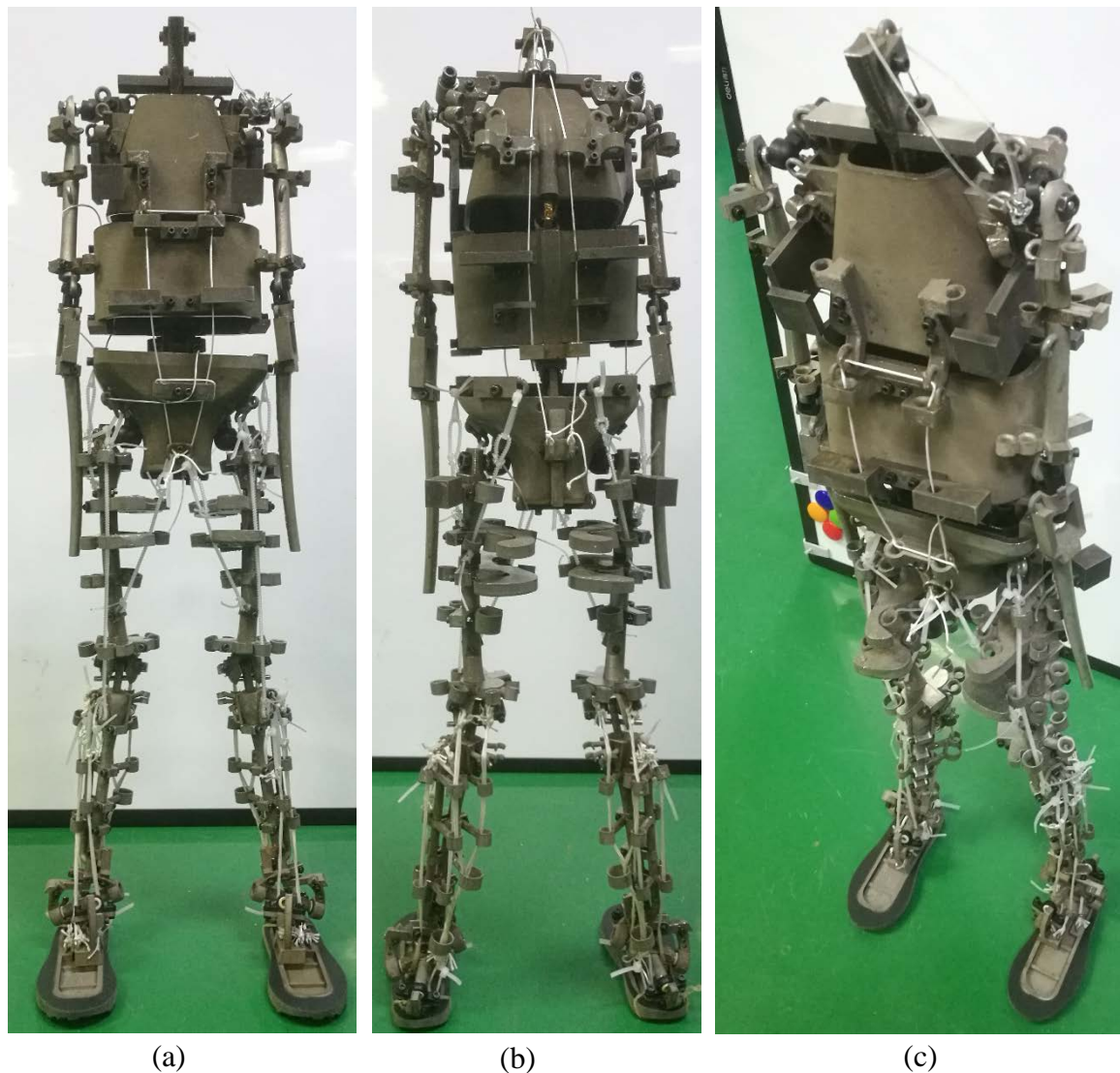


Figure 4.32 (a) Front, (b) Back and (c) Isometric view of the assembled bio-inspired bipedal robot. Grey solid was the skeletal structure, and white lines represented the artificial muscle tendon units.

robot were designed in NX software including the arm (forearm and upper arm), leg (thigh and shank), trunk (upper, middle and lower trunk), and foot. Each body segment shares similar mechanics with a human subject in terms of anthropometry, mass distribution and mass moment inertia.

Also, major joints that dominate the whole-body motion were designed. Elbow, joints in the trunks, knee joint was simplified as one degree of freedom (DoF) hinge joint. The ankle was considered as a combination of two hinge joints with two DoFs, one in the talocrural and the other in the subtalar joint. The shoulder and hip joint were designed based on spherical joints that have three DoFs. All joints used commercial plastic bearing

to limit motion range. Furthermore, angle adjusting mechanism was added in the knee and ankle to study how the joint angle affects normal walking. Thus, the solid model of each body part was designed and assembled in NX software, and STL files were exported for 3D printing.

The robot was scaled to half of the real human subject in dimensions which leads to one eighth in weight and one thirty-second in moment of inertia compared to human subject. 3D metal printing technique based on the innovative Direct Metal Laser Sintering (DMLS) system by EOS (EOSINT M 280) was adopted to manufacture the skeletal body of the robot which will preserve the anticipated shape of each designed segment, e.g., the shank of the robot mimics human tibia and fibula. Due to low strength, small density and weak impact resistance of plastic-like material, stainless steel was used as 3D printing material to assure that the weight is similar to real human body and the strength of the robot is strong enough during walking tests.

The artificial muscle-tendon unit twisted from nylon 6 monofilament fishing line was fabricated to form the whole-body muscular system of the robot. The material properties of various units that depend on the diameter of the uncoiled monofilament fibre and the weight in the twist insertion were measured by a tensile/compression testing machine. Normalised stiffness was introduced as the reference to select proper unit replacing corresponding human muscle.

Finally, the 3D printed skeletal body (including 13 segments and 12 joints) and the fabricated muscular system containing different artificial muscle-tendon units were integrated together, composing the physical prototype of the robot.

The contributions to knowledge in this chapter include the following:

- Designed a bipedal robot with the same musculoskeletal biomechanics as the human subject;
- Designed a whole body anthropomorphic skeletal structure with the same body segment mechanics as the human subject including mass distribution, centre mass position and moment of inertia;
- Designed anthropomorphic robotic joints with the same kinematic parameters as the human subject including joint centre position and axis of rotation;
- Designed angle adjusting mechanisms where the joint axis of rotation in the ankle

and knee can be altered;

- Designed a whole body artificial muscular system with the same musculotendon paths as the human subject;
- 3D metal printed a whole body humanoid robot.

Chapter 5

Simulations in Adams

There are numerous general multi-body simulation packages available commercially and academically for general robotic simulation. A number of software packages have been developed to provide dynamic simulation capabilities for multibody systems, and in particular, robotic systems. Several have been written in MATLAB for ease of integration with other analysis, control, and simulation programs. Many packages are open source, and some are offered at a relatively low cost to the user. They differ in their capabilities in a variety of ways including: speed, topologies and joint models supported, accuracy, underlying dynamic formulation and associated order of complexity, user interface, graphics support, numerical integration routines, integration with other code, application support, and cost. Among those commonly cited are: Adams, Autole, Bullet, DART, DynaMechs, Gazebo, Open Dynamics Engine, Robotics Studio, Robotics Toolbox, Robotran, SD/FAS, Simbod, SimMechanics, SYMORO and Webots.

Adams (MSC, U.S.A.) multibody dynamics software is a commercial professional software which incorporates precise physics by simultaneously solving equations for kinematics, statics, quasi-statics and dynamics. This software has an integrated numerical analysis and finite element analysis tools. Thus, it has been selected as the tool to carry out dynamic simulation of the robot.

In this chapter, all aspects that relate to computer simulation in Adams are presented. The work in this chapter was conducted mainly in Jilin University, China. In section 5.1, the computational model was developed in Adams. Joints, ground contact, material properties of the body part, simplified artificial muscle were described. In section 5.2, passive walking of the robot on a ramp was successfully simulated. Kinematic and kinetic data were measured during walking. In section 5.3, the design of experiment was used to



Figure 5.1 Mechanical body of the lower part in Adams.

study the influence of the orientation of joint axis in the ankle on normal passive walking. Best configuration of the talocrural and subtalar joint has been confirmed that can propel the robot to walk the most distance on the ramp.

5.1 Development of the Model in Adams

The model in Adams is slightly different with the solid model designed in chapter 4. The term of joints in human body and the robot are called connectors in Adams. They are metaphysical motion pair such as revolute (only rotating motion along a determined axis) and translational joint (only translating motion along a specific trajectory), not real solid joints. Ground contact between the foot of the robot and the ramp should be created properly to mimic the environment as real as possible. There is no unit in the software that can mimics the muscle of human body or the artificial muscle-tendon units of the robot. Reasonable simplification should be adopted.

5.1.1 Mechanical Body

The mechanical body in Adams is directly inherited from the 3D musculoskeletal model

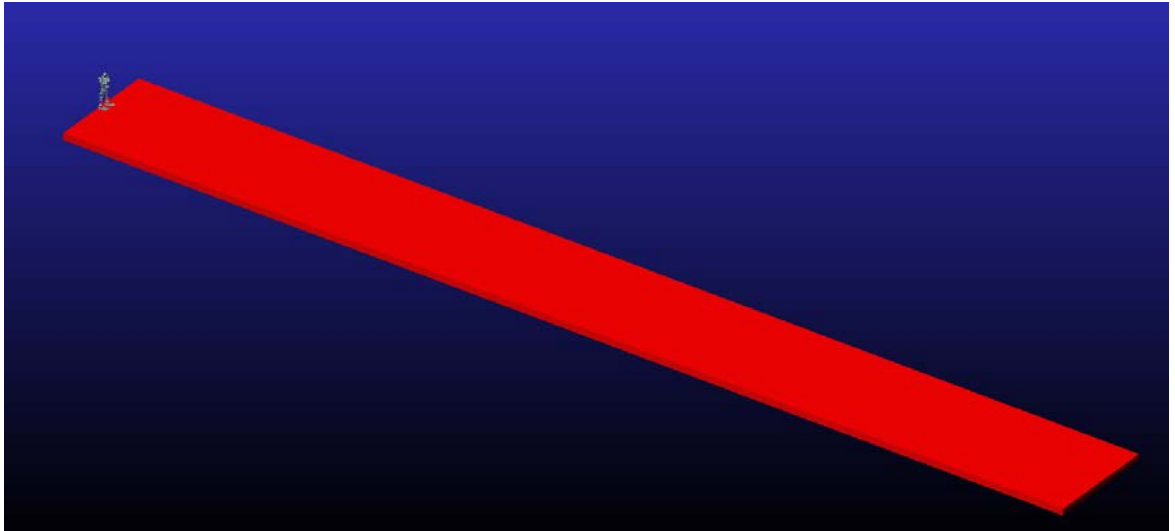


Figure 5.2 The ramp in Adams.

that is built in chapter 4. The lower limbs of the robot (Figure 5.1) are rebuilt containing the pelvis, thigh, shank, and foot, talocrural joint and subtalar joint, where the pelvis is replaced by a straight cylinder with same mass properties as the CAD model in NX.

5.1.2 Joints

The knee joint is fixed, and the hip joint is simplified as a 1-DoF hinge joint, because 3 DoF ball and socket joint leads to instability during walking. The ankle joint is set up to two revolute joints instead of a universal joint, as the angle between the axes of rotation of the talocrural joint and the subtalar joint varies according to different settings of the ankle joint. A function variable is used to change the coupled orientation of the two rotating axes, so the simulation model of the ankle joint has same modality as the physical model when the angle of the talocrural joint or subtalar joint changes.

5.1.3 Ground Contact

A rectangular solid (Figure 5.2) with 15 *m* in length, 2 *m* in width, and 0.1 *m* in height is fixed in the ground as the ramp. The angle between the ramp and the ground can be easily adjusted using a function variable.

A contact force is created between each foot and the ramp. Contact parameters are selected from the recommended value Table 5.1 in Adams. In the physical tests, a pair of rubber insoles is implemented in the foot of the robot, and the ramp is made of wood.

Table 5.1 Recommended value of contact parameters in Adams in which k is stiffness, c is the damping, e is exponent, d is penetration depth, vs and vd are static and dynamic friction velocity respectively. The unit is System International (SI) except that the unit of length is millimetre.

Material 1	Material 2	k	c	e	d	vs	vd
Steel (Dry)	Steel (Dry)	100000.000	50.000	1.5	0.1	0.1	10
Steel (Greasy)	Steel (Greasy)	100000.000	50.000	1.5	0.1	0.1	10
Steel (Greasy)	Steel (Dry)	100000.000	50.000	1.5	0.1	0.1	10
Aluminium (Dry)	Aluminium (Dry)	35000.000	28.000	1.5	0.1	0.1	10
Aluminium (Dry)	Steel (Dry)	35000.000	28.000	1.5	0.1	0.1	10
Aluminium (Dry)	Steel (Greasy)	35000.000	28.000	1.5	0.1	0.1	10
Aluminium (Greasy)	Aluminium (Greasy)	35000.000	28.000	1.5	0.1	0.1	10
Aluminium (Greasy)	Steel (Dry)	35000.000	28.000	1.5	0.1	0.1	10
Aluminium (Greasy)	Steel (Greasy)	35000.000	28.000	1.5	0.1	0.1	10
Aluminium (Greasy)	Aluminium (Dry)	35000.000	28.000	1.5	0.1	0.1	10
Acrylic	Acrylic	1150.000	0.680	2.0	0.1	0.1	10
Acrylic	Steel (Dry)	1150.000	0.680	2.0	0.1	0.1	10
Acrylic	Steel (Greasy)	1150.000	0.680	2.0	0.1	0.1	10
Acrylic	Aluminium (Dry)	1150.000	0.680	2.0	0.1	0.1	10
Acrylic	Aluminium (Greasy)	1150.000	0.680	2.0	0.1	0.1	10
Nylon	Nylon	3800.000	1.520	2.0	0.1	0.1	10
Nylon	Steel (Dry)	3807.762	1.520	2.0	0.1	0.1	10
Nylon	Steel (Greasy)	3800.000	1.520	2.0	0.1	0.1	10
Nylon	Aluminium (Dry)	3800.000	1.520	2.0	0.1	0.1	10
Nylon	Aluminium (Greasy)	3800.000	1.520	2.0	0.1	0.1	10
Nylon	Acrylic	3800.000	1.520	2.0	0.1	0.1	10
Rubber (Dry)	Rubber (Dry)	2855.000	0.570	1.1	0.1	0.1	10
Rubber (Dry)	Steel (Dry)	2855.000	0.570	1.1	0.1	0.1	10
Rubber (Dry)	Steel (Greasy)	2855.000	0.570	1.1	0.1	0.1	10
Rubber (Dry)	Aluminium (Dry)	2855.000	0.570	1.1	0.1	0.1	10
Rubber (Dry)	Aluminium (Greasy)	2855.000	0.570	1.1	0.1	0.1	10
Rubber (Dry)	Acrylic	2855.000	0.570	1.1	0.1	0.1	10
Rubber (Dry)	Nylon	2855.000	0.570	1.1	0.1	0.1	10
Rubber (Greasy)	Rubber (Greasy)	2855.000	0.570	1.1	0.1	0.1	10
Rubber (Greasy)	Steel (Dry)	2855.000	0.570	1.1	0.1	0.1	10
Rubber (Greasy)	Steel (Greasy)	2855.000	0.570	1.1	0.1	0.1	10
Rubber (Greasy)	Aluminium (Dry)	2855.000	0.570	1.1	0.1	0.1	10
Rubber (Greasy)	Aluminium (Greasy)	2855.000	0.570	1.1	0.1	0.1	10
Rubber (Greasy)	Acrylic	2855.000	0.570	1.1	0.1	0.1	10
Rubber (Greasy)	Nylon	2855.000	0.570	1.1	0.1	0.1	10
Rubber (Greasy)	Rubber (Dry)	2855.000	0.570	1.1	0.1	0.1	10

Thus, the stiffness is set to 2855 N/mm , damping to 0.57 $N\cdot s/mm$, exponent to 1.1, penetration depth to 0.1 mm , static and dynamic friction velocity to 0.1 mm/s and 10 mm/s respectively.

5.1.4 Material Properties

The robot was adopted using stainless steel in which the density is $7.83 \times 10^{-6} \text{ kg/mm}^3$, and the mass properties along with moment of inertia is calculated automatically in Adams. Wood was used as the material of the ramp same in the physical test, where the density is $4.38 \times 10^{-7} \text{ kg/mm}^3$ and other parameters are computed by the software.

5.1.5 Artificial Muscle

In the physical model of the robot, coiled fishing lines are used as the muscle-tendon unit to replace human muscles, where the acting path is curved. As there are not corresponding muscle units in the Adams model, several possible solutions (Figure 5.3) were tried to simulate the muscle-tendon unit, such as force vector, pulley systems, flexible volumes and springs. Force vector is not suitable because the accurate value of the coiled fishing lines during walking in the physical test cannot be quantified easily. Pulley systems require the pulleys being coplanar in the start of the simulation. However, the muscle-tendon unit is a 3D curve which makes the supporting points, in this case, the pulleys, not being in the same plane. This will cause some errors during the simulation. Flexible volumes may be the appropriate way to solve this problem, but it need enormous remodelling of the muscle-tendon unit and extra work to determine the material properties using some Finite Element Analysis (FEA) software. Also, adding hundreds of flexible elements in Adams will tremendously increase simulation period.

In the end, springs are chosen as the simplified artificial muscular units. Four springs are implemented in each ankle joint, two in the sagittal plane to allow forward-backward motion and two in the frontal plane to allow medial-lateral motion. The insertion and origin of each muscle-tendon unit are considered as reference for the start and end points of the spring, so it can imitate real muscles as much as possible. The anterior spring corresponds to the Extensor Digitorum Longus, the posterior to the combination of the Gastrocnemius and Soleus, the medial to the Tibialis Anterior, and the lateral to the Fibularis (Peroneus) Longus. The only values that need to be confirmed are the stiffness

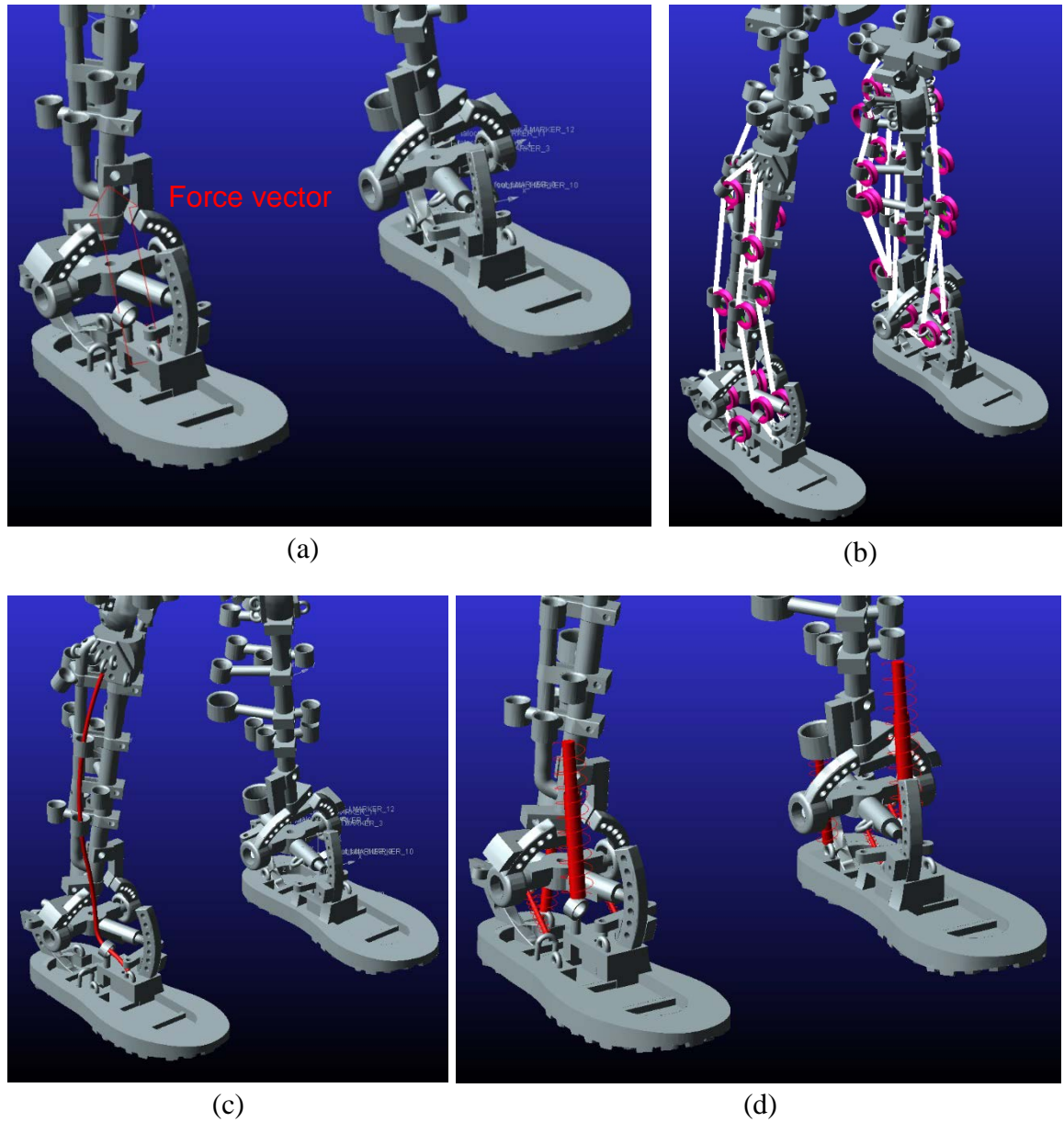


Figure 5.3 Four solutions replacing muscle-tendon unit. (a) Force vector located in the origin and insertion of Tibialis Anterior muscle. (b) Pulley systems. (c) Flexible volumes such as one corresponding to Tibialis Anterior muscle. (d) Springs implemented in the ankle joint.

and the preload.

5.1.6 Variables

Slope Angle. It affects greatly the walking motion by changing the step length, velocity, roll and pitch angle, etc. If the slope has a large angle, the robot would tend to

fall forward easily, and if the slope has a small angle it would tend to stop walking as the energy transmission is slower than large angle. Theoretically, for each different slope angle, proper springs with corresponding material properties (mainly including stiffness and preload) can be selected to drive the robot to achieve stable walking.

Slope Friction. Slope friction is a key factor that causes stopping, slipping and yaw motion along the transverse plane. If the friction is too large, the robot would stop walking, and if it is too small the robot might slip on the surface or fall down, especially when the roll and pitch motions are larger which increases the torques and forces in the foot. Static and dynamic coefficient should be chosen reasonably.

Spring Properties. Four tensile springs are applied in each ankle joint. Stiffness and preload of the springs dominate the material properties that affect walking motion. Also, damping is another factor which should be considered because the simulation results varies a lot even if small changes occurred in damping.

Initial Conditions. The robot has to be launched in determined initial conditions setting initial position, angles, accelerations and velocities that could lead to stable passive walking. Very high accelerations or large angles would lead to an immediate falling.

Talocrural Angle. The angle of the talocrural joint axis can be altered every one degree from 0° to 36° . The datum axis is the horizontal medial-lateral axis. All the settings are strictly following the joint parameters illustrated in section 4.1.2.

Subtalar Angle. The angle of the subtalar joint axis can be altered every one degree from 0° to 42° . The datum axis is an axis in the transverse plane oriented 12.0401° medial to the midline of the foot. All the settings are strictly following the joint parameters illustrated in section 4.1.2.

5.2 Simulation

5.2.1 Model Validation

In Adams the results are approximations through a process of numerical analysis. The solver solution is firstly to Taylor expand input data according to the step size that we set such as force and moment which are input as complex functions of time, and then to conduct numerical calculation. If the step size is too large (i.e., total steps is not enough in a set time) which means the Taylor series

Table 5.2 Parameters of initial conditions for simulation.

Initial conditions		Value
Slope angle ($^{\circ}$)		9.0
Initial roll angle ¹ ($^{\circ}$)		9.5
Initial yaw angle ² ($^{\circ}$)		9.0
Talocrural angle ($^{\circ}$)		0
Subtalar angle ($^{\circ}$)		0
Slope friction		0.8
Spring damping		0.372
Stiffness of the springs in the ankle (N/mm)	Anterior	30.0
	Posterior	8.0
	Medial	4.0
	Lateral	30.0
Preload of the springs in the ankle ³ (N)	Anterior	-30.0
	Posterior	-180.0
	Medial	-20.0
	Lateral	-60.0

¹ Positive value means tilting laterally.

² Positive value means tilting backwards.

³ Negative value means tension.

expansion is too small, the computational errors will increase, or the results will even diverge. If the step size is too small, the computing accuracy will increase but the time consumed is too long. Thus, the step size is set to 0.01 s.

Also, initial conditions including internal parameters (e.g., spring properties and initial angle in the ankle joint) and external parameters (e.g., slope angle and friction) are set according to Table 5.2. To validate the simulation model, the talocrural and subtalar angle are applied with 0° that means they are parallel to the ground while standing. The robot is launched as following which is slightly different in the physical test (see section 6.3.1):

Tilt: Tilt the support leg by bending the ankle joint and holding the support foot in full contact with the ramp, which means rotating the robot a determined angle along the subtalar joint of the support leg.

Move: Move the pelvis a bit backwards in order to set the robot leg perpendicular to the ground, i.e., rotate the robot a determined angle along the talocrural joint of the support leg.

Release: Release the robot.

The robot can walk 3547.5 mm in 43.2 s, and the mean velocity is 153.25 mm/s. It fell in the end as the roll angle was too large to retain stable walking see in Supplementary Video 2. The global coordinate system is defined as follows: the X-axis is to the right, the Y-axis is in the direction of progression and the Z-axis is vertical.

5.2.2 Kinematics

5.2.2.1 Centre of Mass (CoM)

The position of the CoM of the robot during passive walking on the ramp were predicted. For a steady walk, the projections of the CoM along three axes are shown in Figure 5.4. The CoM made sideways excursions of ± 50 mm in medial-lateral direction which is 0.105 times the leg length, forwarded 3547.5 mm in progression and declined 558.5 mm in vertical direction before falling. It can be seen that the trajectories of CoM in the sagittal plane, especially along the Z axis, had certain fluctuation during walking. These oscillations were caused by the completely passive walking of the robot. The knee joints have been locked and only the hip and ankle joints facilitate the motion, meaning that the changing of the CoM profits from the tilting of the stance leg and swing of the free leg caused by the inertia and gravity. In a gait cycle, the CoM will increase in the Z axis at the starting point in the stance phase and then decrease when the robot starts moving the CoM from the stance leg to the swing leg.

5.2.2.2 Velocity

The velocity of CoM in three axes (Figure 5.5) were derived from the data in Figure 5.4. The spikes of the medial-lateral velocity around the peaks and valleys were caused by the ground impacts of the swing leg. When the robot was entering to the heel strike phase, the landing foot collided with the ramp and rapidly reduced the velocity. If the collisions were inelastic, it would cause the velocity loss thus the robot would stop walking. However, due to the elasticity of the springs in both ankle joints of the legs, the collision caused an oscillatory motion and the weight transfer between two legs. The

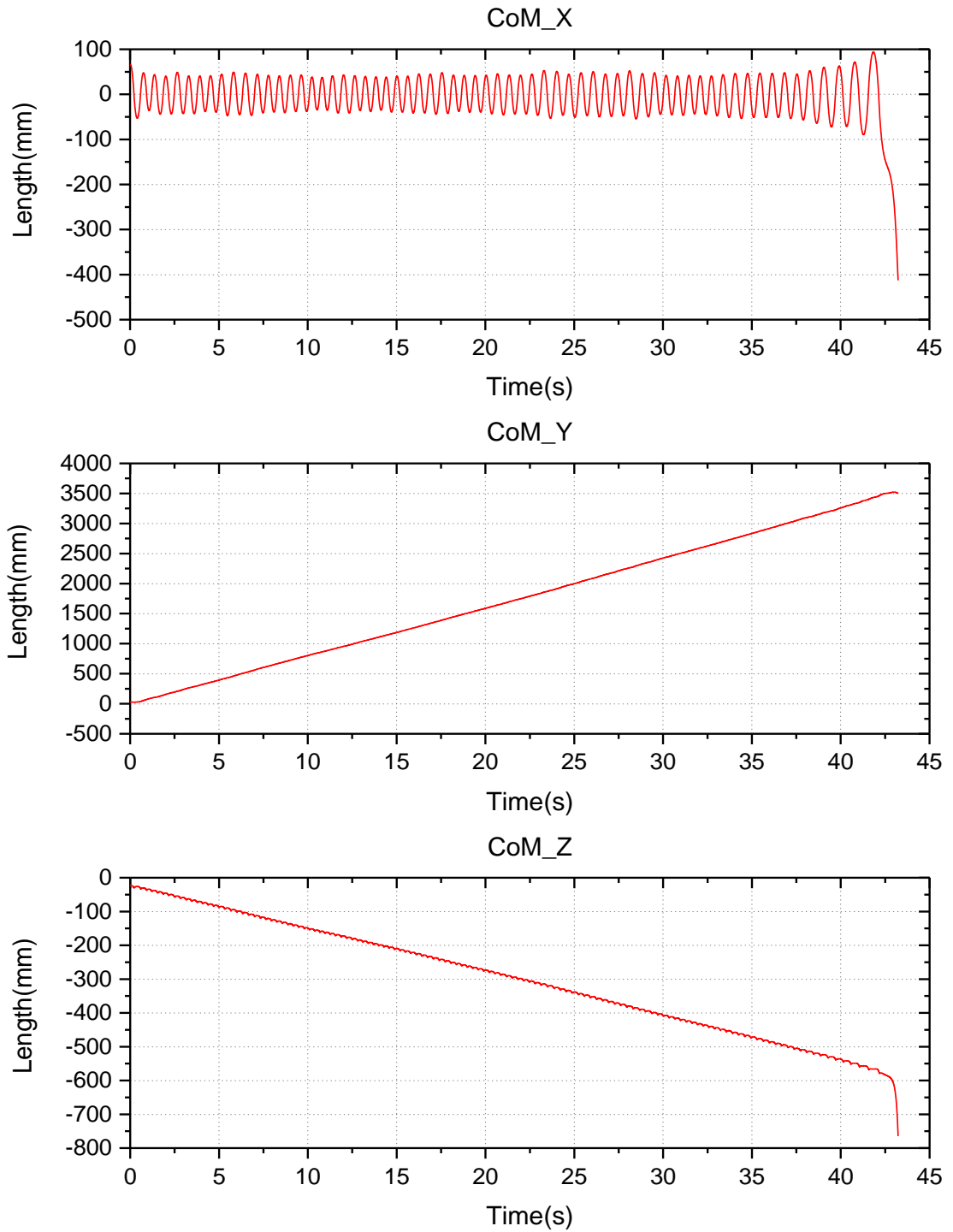


Figure 5.4 CoM of the robot during passive walking in Adams simulation. The global X-axis is to the right (top), the Y-axis is in the direction of progression (middle) and the Z-axis is vertical (bottom).

energy stored in the springs (mainly the medial one) of the support leg was released in the post-collision phase (i.e., after the maximum tilting or roll motion of the leg), hence there was a fast boost-up after the velocity reduction. This is also caused by the gravity and

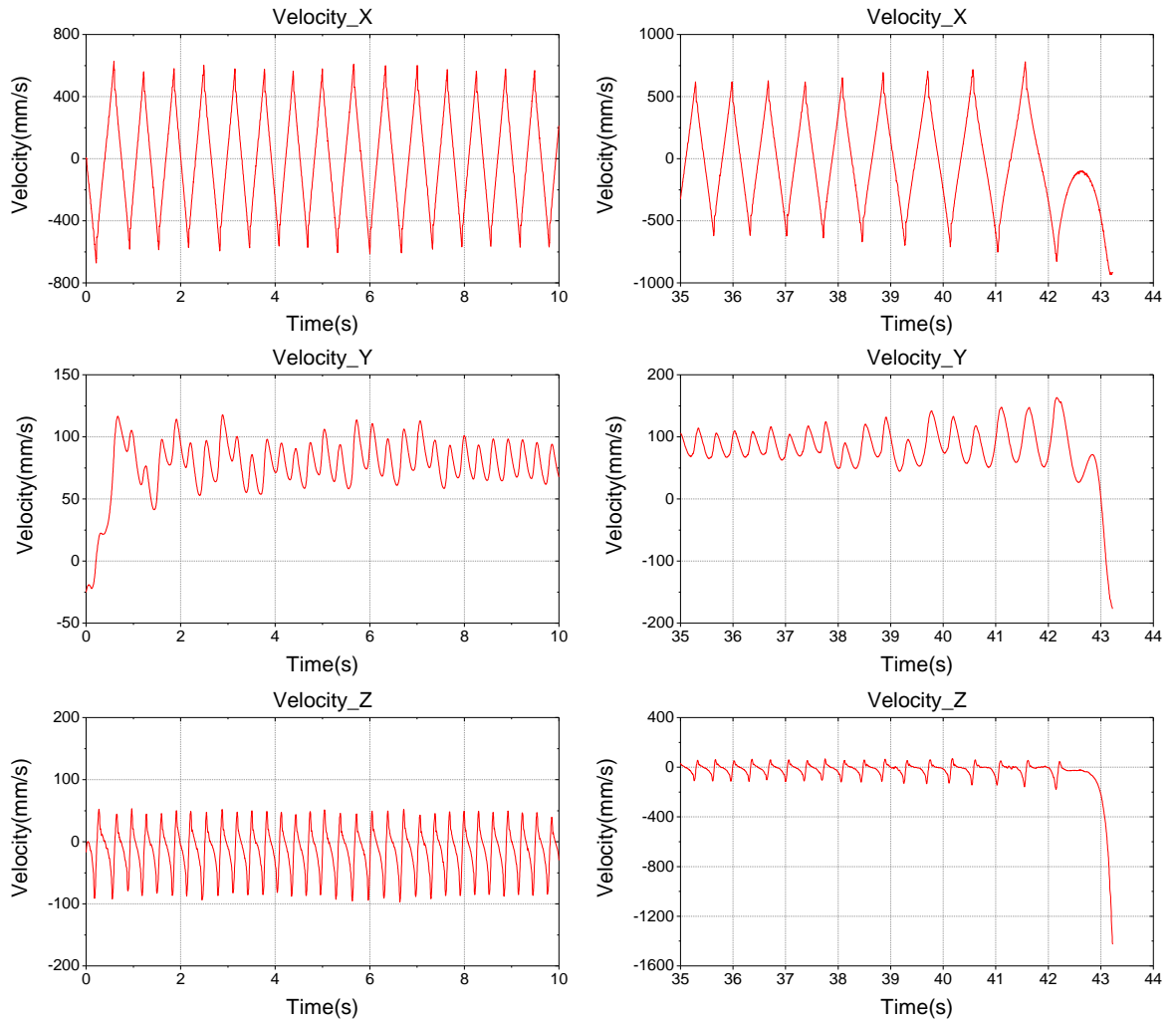


Figure 5.5 Velocity of the robot during passive walking in Adams simulation. Left part is the velocity of stable walking from launching to 10 s and right part is the velocity of last few seconds before falling.

inertia. The same feature also occurred in the vertical direction.

The y-axis velocity was around 75 mm/s with $\pm 32\%$ fluctuations, and no negative value showed that the robot would not fall backward during stable walking. The fact that the absolute value of the negative velocity in z-axis was higher than that of the positive velocity showed that the robot descended more rapidly than ascended in a walking gait which complied with the trajectory of the z-axis CoM (Figure 5.4, bottom).

5.2.2.3 Ankle Motion

Comparing the walking motion of the robot with humans could lead to error. The fact

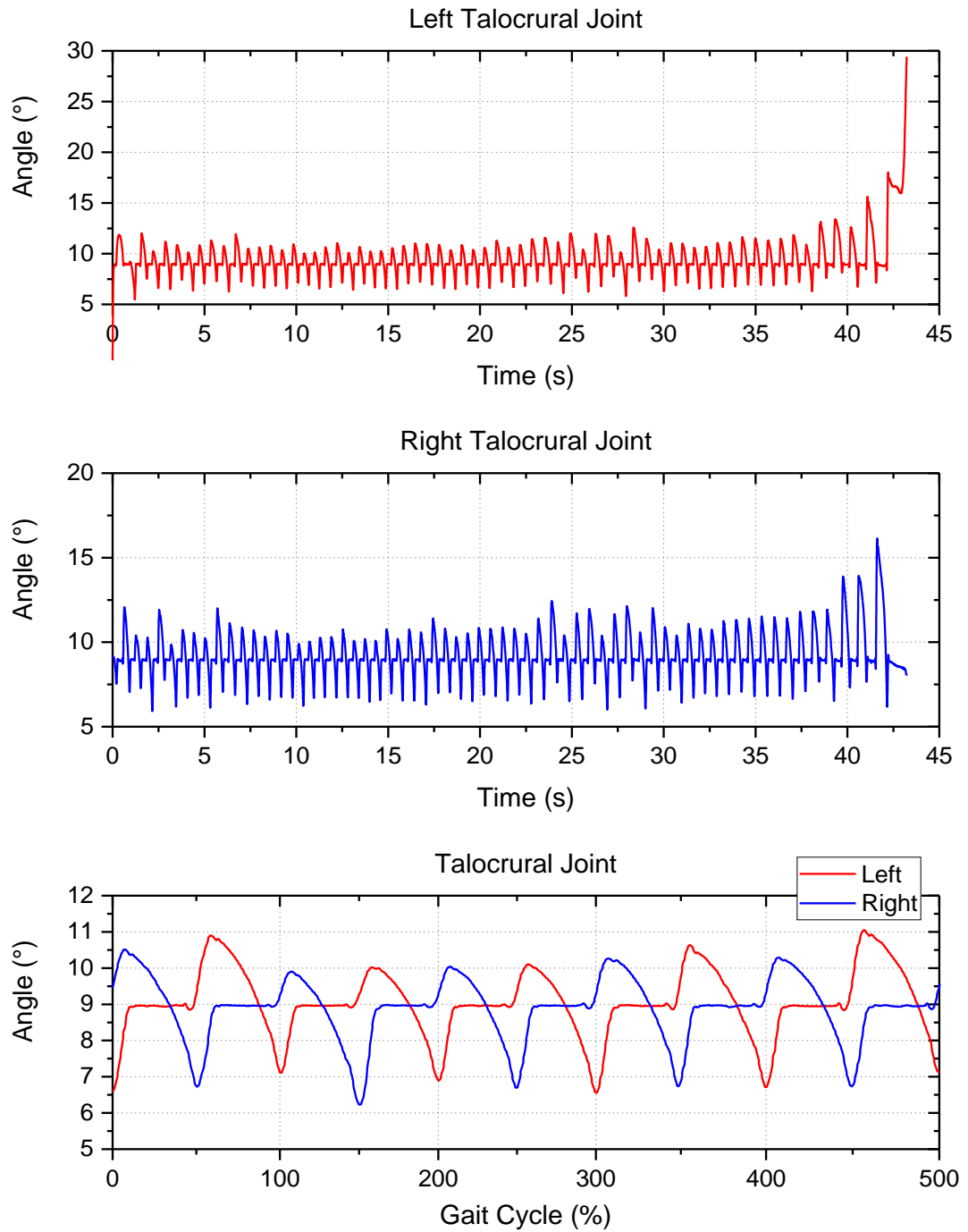


Figure 5.6 The angle motion of the left (top) and right (middle) talocrural joint during walking in simulation. The bottom is the angle of two joints in 5 gait cycles starting from heel strike of the right foot. Zero value in the talocrural joint means that the robot is in upright position. Positive value means Dorsiflexion.

humans have knees makes their walking motion very different. The robot needs roll motion to create clearance that allows the leg to swing forward without collision between its foot and the ramp, while humans do not need such a roll motion as they create

clearance by bending the knee joint. The motion of the foot is different, the robot lands and raises almost parallel to the ramp while humans land and raise with a relative angle with the ground and also bend the toes about their joint (i.e., push off) during the raising.

The angle motion in the talocrural joint and subtalar joint during passive walking were recorded in Figure 5.6 and Figure 5.7. From initial foot contact through foot flat, the talocrural joint plantarflexes, the subtalar joint everts, and the foot pronates. In a walking gait, the motion pattern of the talocrural joint and subtalar joint are similar, just with approximately 50% phase difference. When the angle of the right talocrural joint decreases from the peak to the valley point, the angle of the contralateral joint is almost constant (Figure 5.6, bottom). This phenomenon also occurs in the subtalar joint that the left subtalar joint would keep unchanged when the right one first increases and then decreases (Figure 5.7, bottom). In the last several gaits before falling, the maximum angle in both talocrural and subtalar joint rose slowly and had a sudden augment in the end.

From initial foot contact, the talocrural joint is in a 9° plantarflexion which increased until foot flat, but it rapidly dorsiflexes (still in plantarflexion) during the latter part of stance as the body passes over the foot. The motion then returns to plantarflexion during swing until the next initial contact. The term of motion and biological definition is different, such as that the motion from large plantarflexion to small plantarflexion can be named as dorsiflex. Rotation of talocrural joint during passive walking on the ramp averages $6^\circ\sim 10^\circ$ plantarflexion, with a total motion of 4° . Maximum plantarflexion occurs at foot flat, and maximum dorsiflexion occurs at the end of the stance phase. At initial contact, the talocrural joint is almost 9° (see Figure 5.8). From initial contact to foot flat, the ankle plantarflexes (i.e., extends) to a maximum of 10° as the foot is lowered to the ramp surface. At the end of stance, the ankle dorsiflexes (i.e., flexes) a maximum of 4° to 6° in plantarflexion as the leg rotates anteriorly and medially over the supporting foot. During the early stage of swing, the ankle rapidly plantarflexes to neutral position as the robot weight is transferred onto the contralateral leg to attain foot clearance. The talocrural joint is in neutral position (9° in plantarflexion) during the rest of swing.

The subtalar joint rotates in stance, which affects the weight-bearing alignment of the entire robot. Unlike human walking, the motion at the subtalar joint is bigger than the talocrural joint as it provides foot clearance that is performed by knee flexion and extension in humans. And subtalar rotation is the motion which permits the foot to adapt

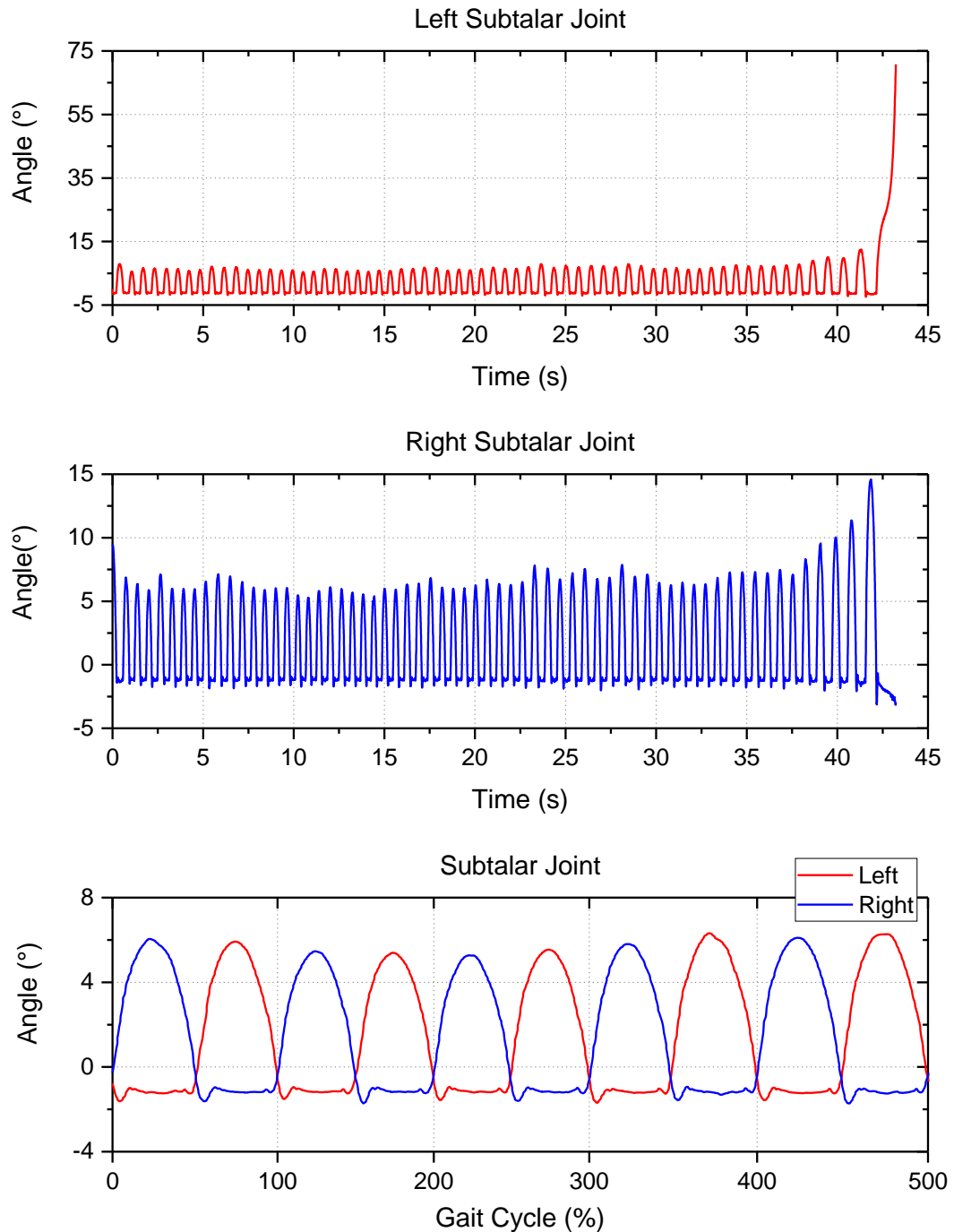


Figure 5.7 The angle motion of the left (top) and right (middle) subtalar joint during walking in simulation. The bottom is the angle of two joints in 5 gait cycles starting from heel strike of the right foot. Zero value in the talocrural joint means that the robot is in upright position. Positive value means Eversion.

to various surfaces. During initial contact, the subtalar joint begins everting until peak eversion is reached by the middle of stance (see Figure 5.8) which averages 5.7° . This rapid eversion is followed by gradual inversion, with peak inversion achieved by early of

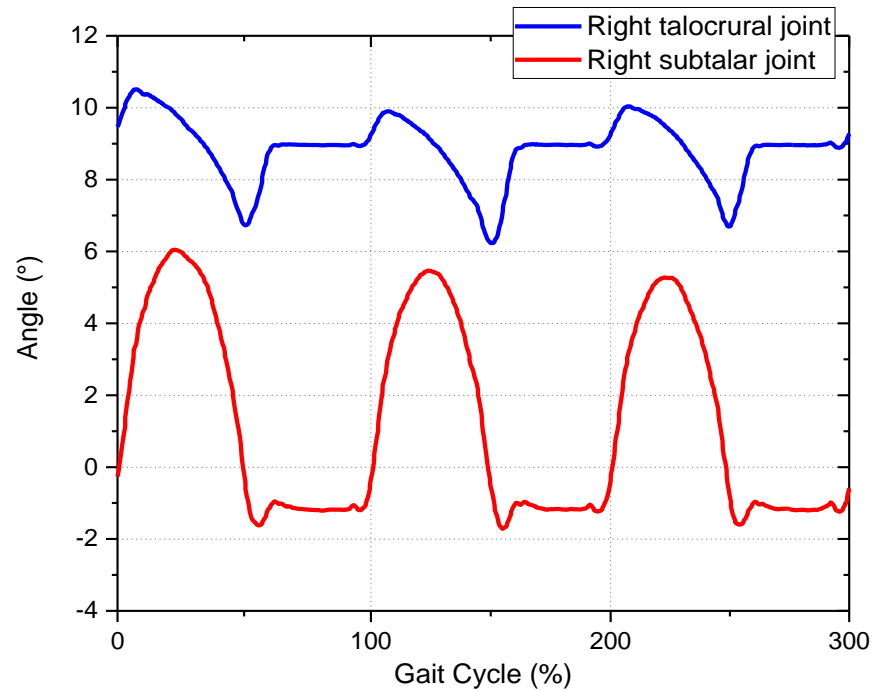


Figure 5.8 The angle motion of the right talocrural and subtalar joint during 3 walking gaits starting from heel strike of right foot in simulation. Zero value in the talocrural joint means that the robot is in upright position. Positive value means Eversion and Dorsiflexion.

swing. The foot drifts back to neutral position (1° in inversion) during swing. Rotation of subtalar joint during passive walking on the ramp averages 5.7° eversion and 1.8° inversion, with a total motion of 7.5° . Similar to the talocrural joint, the term of motion and biological definition is different, such as that the motion from large eversion to small eversion can be named as invert. Subtalar inversion helps to bring about stability of the foot and propel the transfer of CoM to the other leg.

5.2.3 Kinetics

5.2.3.1 Ground Reaction Forces (GRFs)

GRFs and the related biomechanical events during passive walking on the ramp are illustrated in Figure 5.9. The following events were determined from the horizontal shear forces: braking peak, propulsive peak, and braking and propulsive impulses. Medial and lateral impulses were determined from the medial-lateral shear forces. Passive peak, active peak, minimum between peaks, and impulse were calculated from the vertical GRF. The

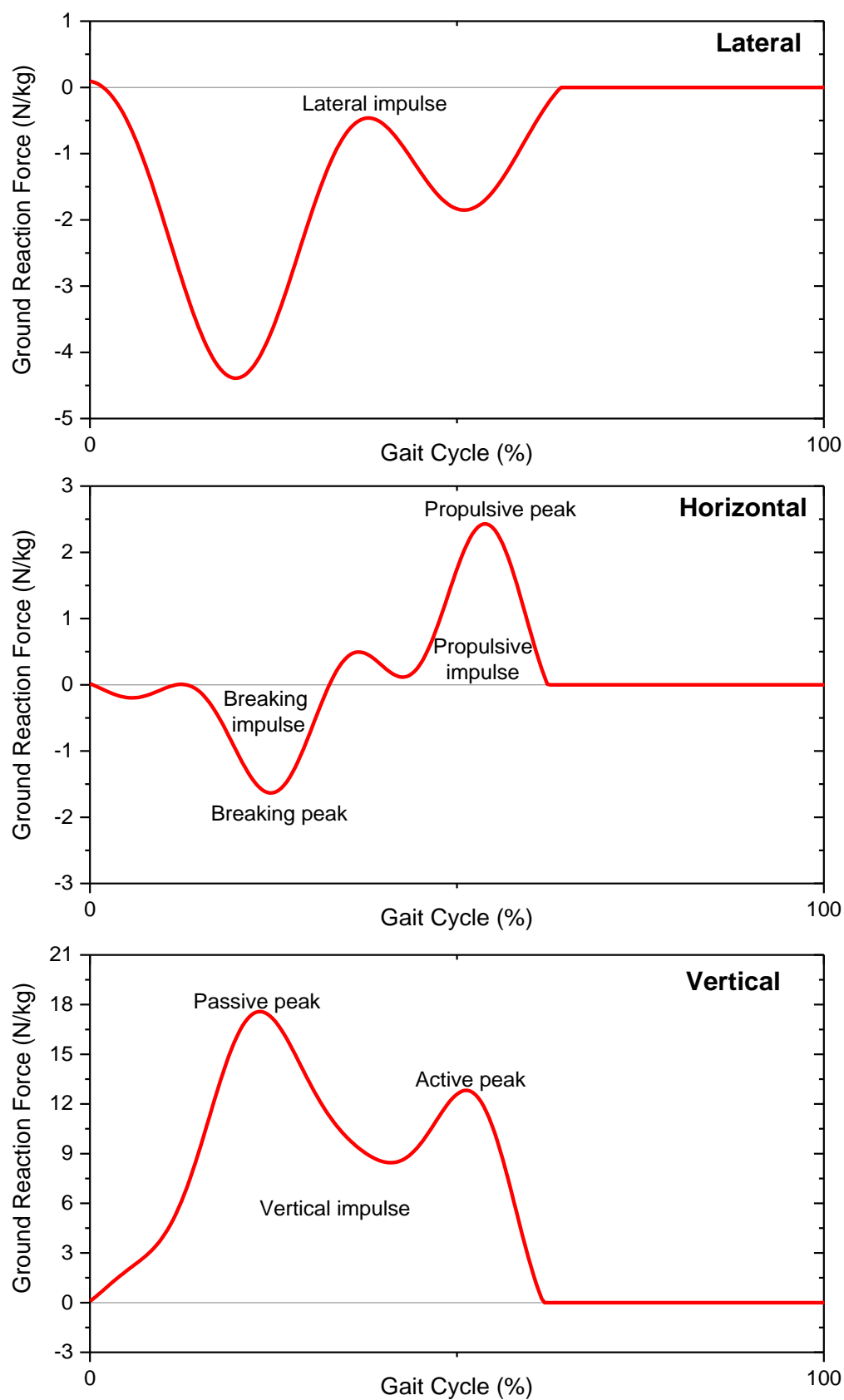


Figure 5.9 Ground reaction forces including medial-lateral (top), horizontal (middle), and vertical (bottom) forces in simulation. Key impulses and peaks are labelled.

general pattern of GRFs are similar to humans, but the peak values vary in all three components. The passive peak of vertical GRF in simulation is about 18 N/kg , which is 12 N/kg in humans. Breaking peak of horizontal component is -1.8 N/kg and propulsive peak is 2.5 N/kg , and they are -2.2 and 2.2 N/kg respectively in humans. The peak value in lateral impulse of medial-lateral GRF is -4.4 N/kg , compared to -0.6 N/kg in humans. In a word, the peak values of the main biomechanical events in GRFs during the robot walking are all higher than that in humans except the breaking peak. This might be caused by the different walking pattern of the robot that no knee flexion exists and the range of roll motion are much larger than humans.

5.2.3.2 Spring Forces

Spring forces in the anterior, posterior, medial and lateral position were predicted in Adams and plotted in Figure 5.10. It can be notice that the forces in the anterior-posterior springs are much higher than that in the medial-lateral springs. It is intuitive thinking that the anterior-posterior springs greatly impact biped walking by holding the robot in upright position, as they try to recover to free lengths and produce a torque about the talocrural joint which will protect the robot from falling down during walking. This feature can also be compared in nature with humans where Tibialis Anterior, Soleus and Gastrocnemius muscles are much stronger than other muscles around the ankle. The fact that the posterior spring has the maximum tension force also indicates the Achilles tendon plays a main role in providing stability to human walking motion.

There is transverse relationship between springs in the anterior-posterior and medial-lateral position. For example, if the robot gets tilted backward, the medial-lateral springs also produce forces that generate torques about the talocrural joint. The same occurs when the robot is tilted sideward and the anterior-posterior springs also affect the torques generated about the subtalar joint. When the robot's CoM is translated more laterally as stance progresses, the tension of the springs in the medial side of the ankle increases and drives the foot to invert. Theoretically, the tension force in the medial spring should reach the maximum value when the lateral spring force is in minimum. However, the results are different that when the lateral force is in peak value with -5 N , the medial one is beyond -30 N higher than the valley value. This is because the posterior spring has influence around the subtalar joint when the robot tilted laterally.

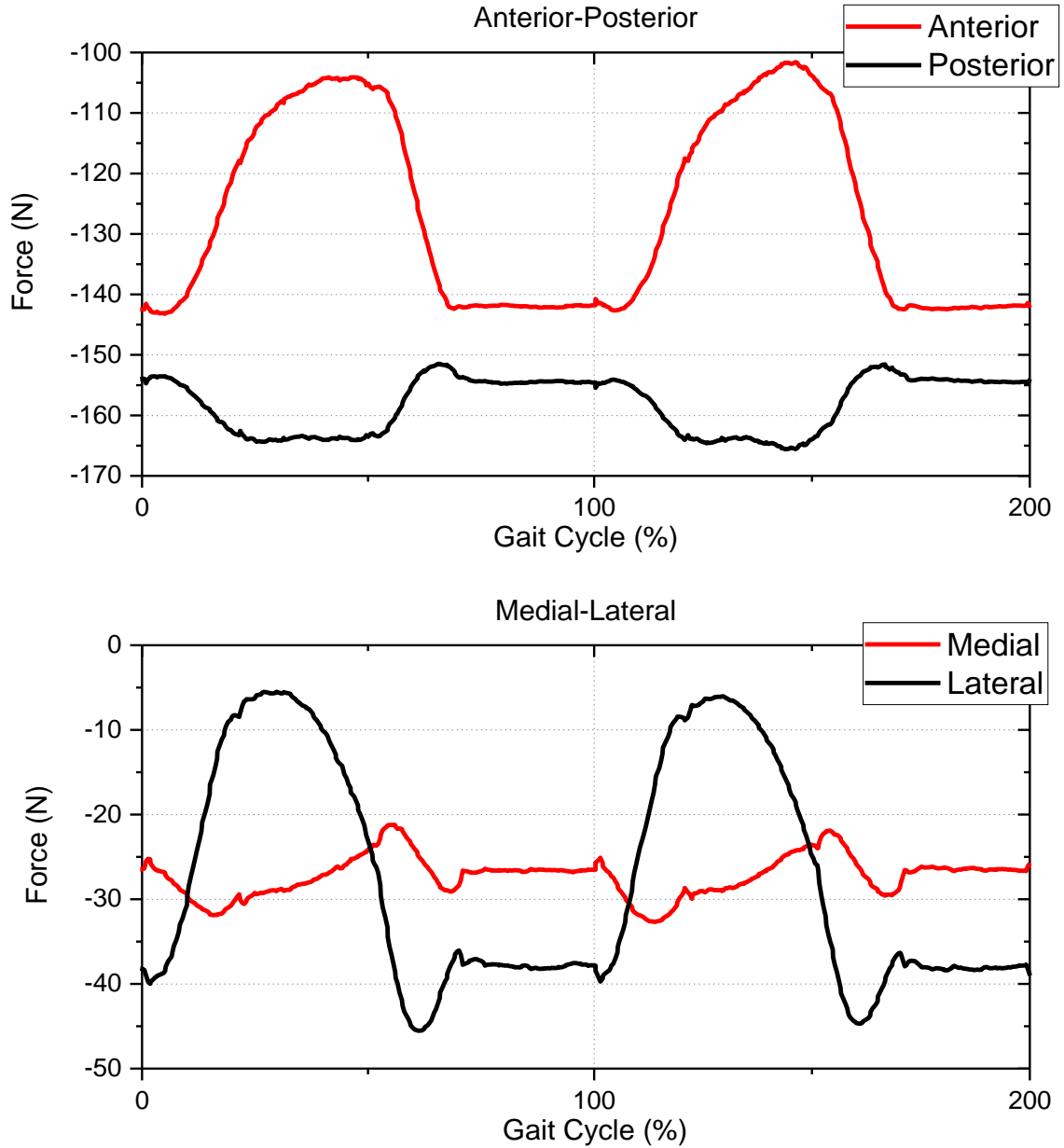


Figure 5.10 Spring forces in the ankle during 2 stable walking gaits including the anterior-posterior (top) and the medial-lateral (bottom) in simulation. Negative value means tension.

5.2.4 Cost of Transportation (CoT)

To compare efficiency between humans and robots of different sizes, it is convenient to use the dimensionless specific cost of transport as follows,

$$CoT = \frac{\text{energy consumed}}{\text{distance} \cdot \text{weight}} \quad (5-1)$$

CoT of the robot walking is 0.21 similar to CoT 0.2 of human walking, estimated by the

volume of oxygen they consume. The robot is similarly energy effective as humans.

5.3 Design of Experiment (DOE)

5.3.1 Background

Design of experiments (also called experimental design) is a collection of procedures and statistical tools for planning experiments and analysing the results. In general, the experiments may measure the performance of a physical prototype, the yield of a manufacturing process, or the quality of a finished product.

Although DOE techniques were developed around physical experiments, they work just as well with virtual experiments in Adams. In this case, the experiments help better understand and refine the performance of the mechanical system. DOE techniques can improve understanding of the design, increase the reliability of the conclusions, and often get an answer faster than trial-and-error experimentation.

For simple design problems, it is often possible to explore and optimize the behaviour of the system using a combination of intuition, trial-and-error, and brute force. As the number of design options increases, however, it becomes more and more difficult to do this quickly and systematically. Varying just one parameter at a time does not tell you a lot about the interactions between parameters. Trying many different parameter combinations can require many simulations, therefore leaving a great deal of output data to sift through and understand.

DOE methods provide planning and analysis tools for running a series of experiments. The basic process is to first determine the purpose of the experiments. For example, the variations that have the biggest effect on your system can be identified. Then, a set of investigated parameters (called factors) for the system should be chosen and the way to measure the appropriate system response should be developed. Then a set of values for each parameter (called levels) would be selected and a set of experiments (called runs, trials, or treatments) would be planned in which the parameter values are varied from one experiment to another. The combination of actual runs to perform is called the design.

An experiment set up in this way is called a designed experiment, or matrix experiment. The runs are described by the design matrix that has a column for each factor and a row for each run. The matrix entries are the level for each factor for each run.

After execution, the performance of the system at each run are record and the changes in performance across the runs can be analysed. The type of analysis depends on the purpose of the experiment. Common analyses are analysis of variance (ANOVA) that determines the relative importance of the factors, and linear regression, which fits an assumed mathematical model to the results.

Experiments with two or three factors may only require five or ten runs. As the number of factors and levels grows, however, the number of runs can quickly escalate to dozens, even hundreds. As a result, a good design is critical to the success of the experiment. It should contain as few runs as possible, yet give enough information to accurately depict the behaviour of the system. The best design depends on the number of factors and levels, the nature of the factors, assumptions about the behaviour of the product or process, and the overall purpose of the experiment.

DOE methods allow to combine all of these requirements into an efficient, effective design for your problem, and couple it with the appropriate analysis of the results. In this study, DOE was used to explore how the ankle axis of rotation affects biped locomotion.

5.3.2 Parameters and Objective

In the robot test, parameters that can be investigated on normal walking are enormous. The main terms that I focused are kinematics in the joint, in this case, the angle of the talocrural and the subtalar joint axis. The objective of each combination (trial) is the distance travelled on the ramp.

There are 37 levels from 0° to 36° for the talocrural joint and 43 levels from 0° to 42° for the subtalar joint, resulting in 1591 trails. Each combination has same initial conditions, slope angle and friction, and spring properties. Only difference is the angle of the talocrural and subtalar joint axis of rotation. I assume the robot can achieve stable walking if it can travel more than 1100 *mm*. Full details of the results are illustrated in the Supplementary Table S1.

5.3.3 Subtalar Angle

The talocrural angle was set to a constant value to study the subtalar joint. For a determined talocrural angle (no more than 24°), the robot can walk stably in a certain region (see Figure 5.11, top). There are two situations occurred when the subtalar angle is

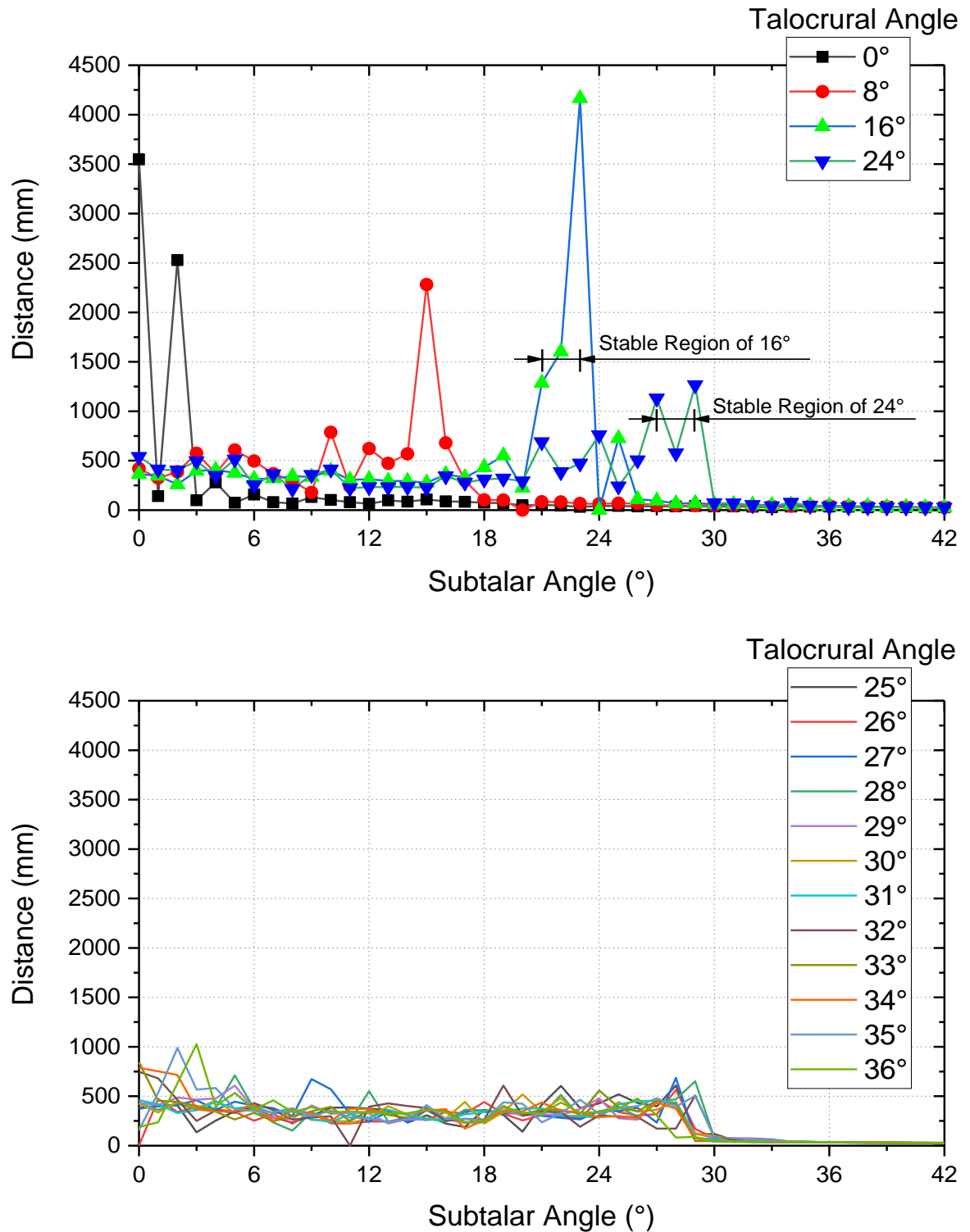


Figure 5.11 Typical plots of the distance travelled as a function of the subtalar angle for passive walking of the robot in simulation.

out of the stable range: the robot ends in falling when the subtalar angle is less than the stable angle; the robot ends in stopping when the subtalar angle is greater than the stable

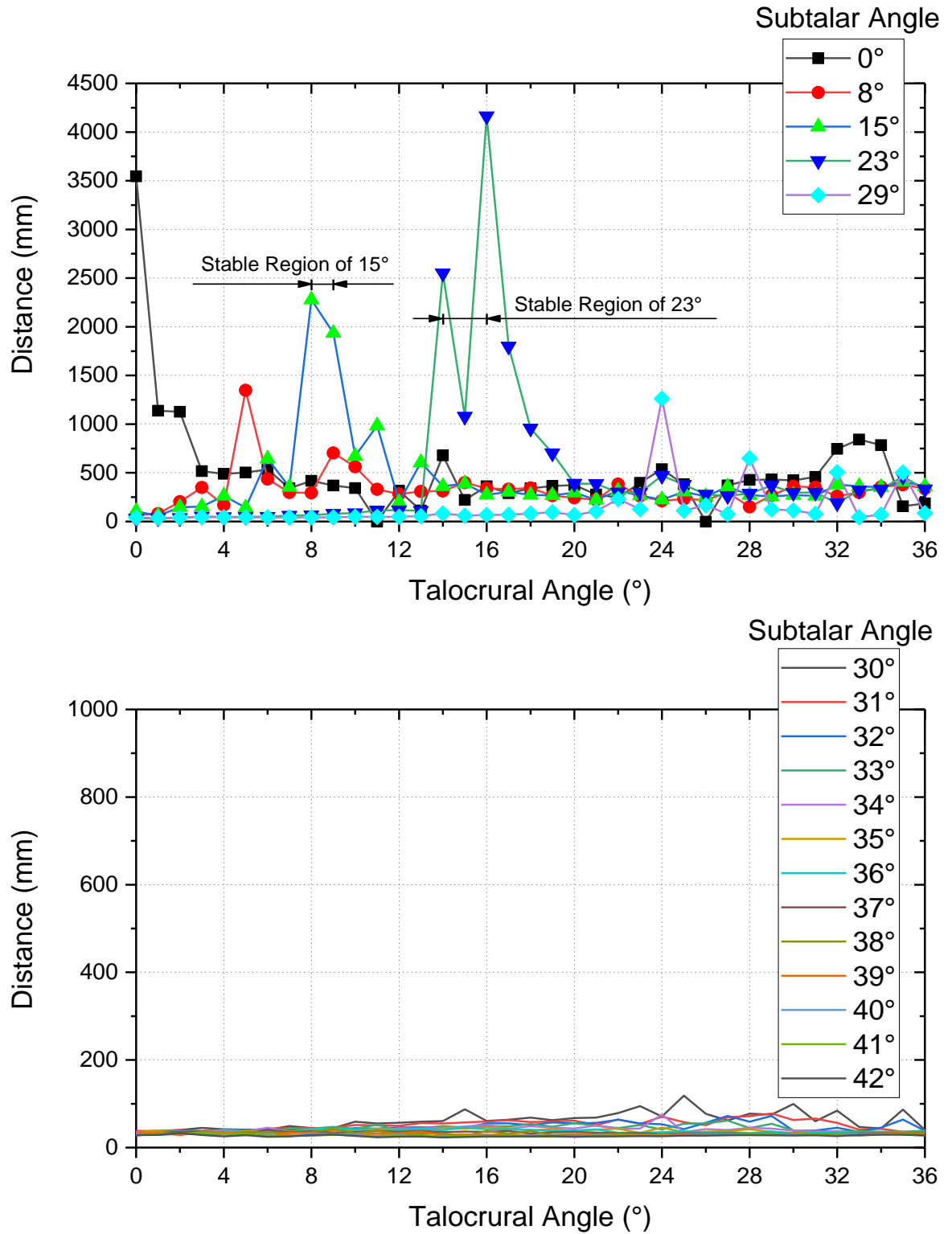


Figure 5.12 Typical plots of the distance travelled as a function of the talocrural angle for passive walking of the robot in simulation.

angle. When the talocrural angle $> 24^\circ$, the robot cannot walk stably. In this case, there are two endings occurred, falling when the subtalar angle is less than 30° and stopping when

the angle is greater than or equal 30° (see Figure 5.11, bottom).

The stable region of the subtalar angle grows along the talocrural angle increasing. The stable regions of 0° and 8° talocrural angle are $0^\circ\sim3^\circ$ and 15° in subtalar angles, respectively. When the talocrural angle increases to 16° and 24° , the stable angles in the subtalar joint change to $21^\circ\sim23^\circ$, and $27^\circ\sim29^\circ$, respectively.

5.3.4 Talocrural Angle

The subtalar angle was set to a constant value to study the talocrural joint. For a determined subtalar angle (no more than 29°), the robot can walk stably in a certain region (see Figure 5.12, top). Same to the subtalar joint, there are two situations occurred when the talocrural angle is out of the stable range: the robot ends in stopping when the talocrural angle is less than the stable angle; the robot ends in falling when the talocrural angle is greater than the stable angle. When the subtalar angle $>29^\circ$, the robot cannot walk stably. Unlike the subtalar angle, there is only one ending occurred which is stopping after launching (see Figure 5.12, bottom).

Similar to the subtalar joint, the stable region of the talocrural angle grows along the subtalar angle increasing. The stable regions of 0° and 8° subtalar angle are $0^\circ\sim3^\circ$ and 5° in talocrural angles, respectively. When the subtalar angle increases to 15° , 23° and 29° , the stable angles in the talocrural joint alter to $8^\circ\sim9^\circ$, $14^\circ\sim16^\circ$, and 24° , respectively.

5.3.5 Correlation for Stable Walking

A graph of the travelled distance as a function of both the angle of the talocrural and subtalar joint axis is sketched in Figure 5.13. The sketch is based on a number of cross-sections in the parameter space of the talocrural angle (Figure 5.12) and subtalar angle (Figure 5.11). The stable region for the talocrural angle rises up with an increasing subtalar angle up to 29° , beyond which no stable solutions were found for any talocrural angle. A search up to subtalar angle equals to 42° provided ever increasing talocrural angle, so I extrapolate the result to conclude that no stable passive walking motions exist for a subtalar angle of more than 29° . Similarly, no stable walking motions occur for a talocrural angle of more than 24° . The distance travelled of stable passive walking firstly decreases with the increase of the stable angle. After reaching a valley value, it increases sharply to the peak with 16° talocrural angle and 23° subtalar angle. Beyond this peak

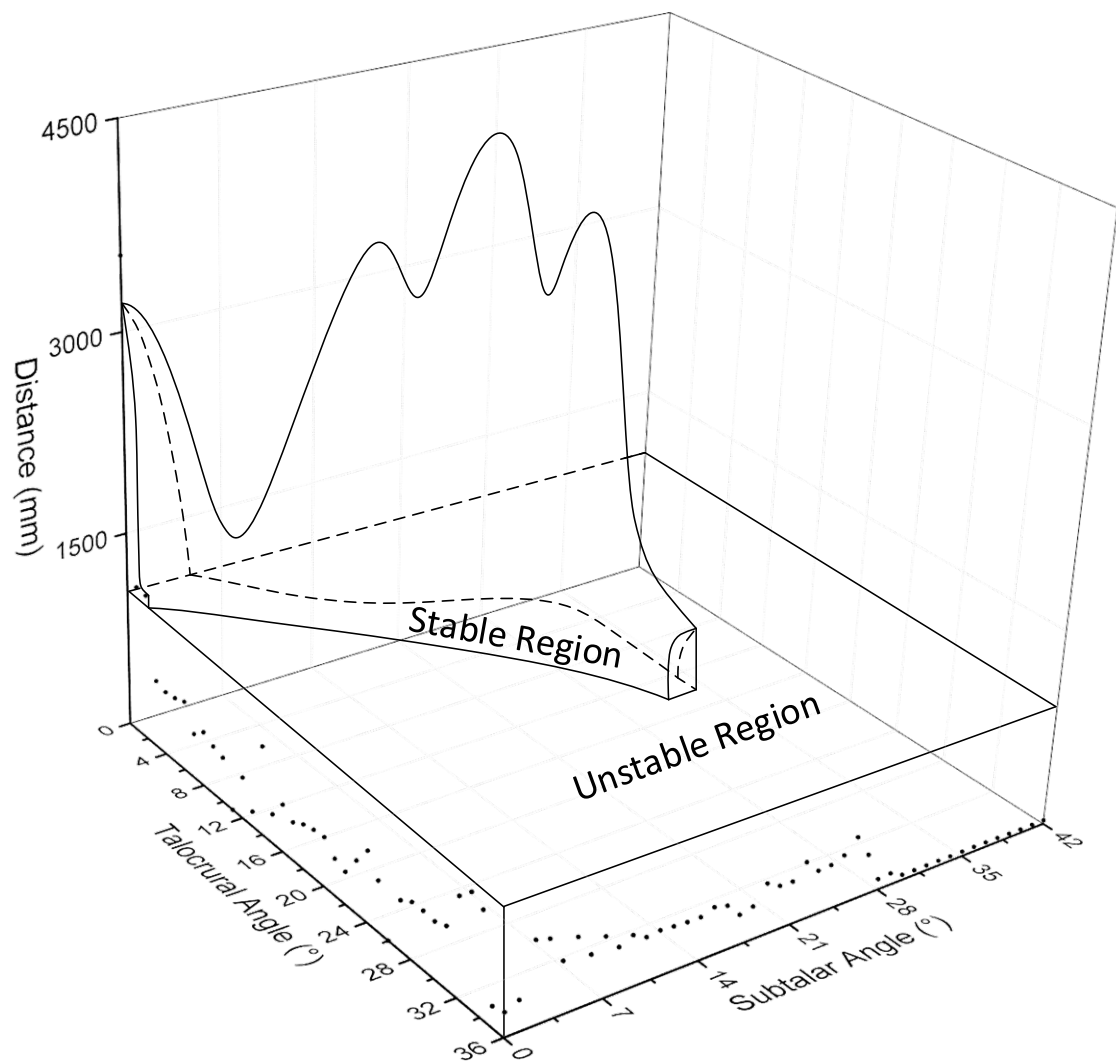


Figure 5.13 A sketch of the dependency of the distance travelled as a function of ankle joint orientation including the talocrural and subtalar angle for passive walking of the robot in simulation. The left and right face of the figure are equal to Figure 5.12 and Figure 5.11, respectively.

value, the distance declines along with the increase of the stable angle until the edge of the stable region.

A more detailed graph of the travelled distance is illustrated in Figure 5.14. The stable region located in the narrow strip from the combination of 0° - 0° to 24° - 29° where the former is the talocrural angle and the latter is the subtalar angle. When the angle of the subtalar joint axis of rotation is beyond the stable region, the robot is unable to walk, and it would stop walking just after launching. However, the robot can perform few steps of unstable gait after launching and end in falling down when the angle is lower than the

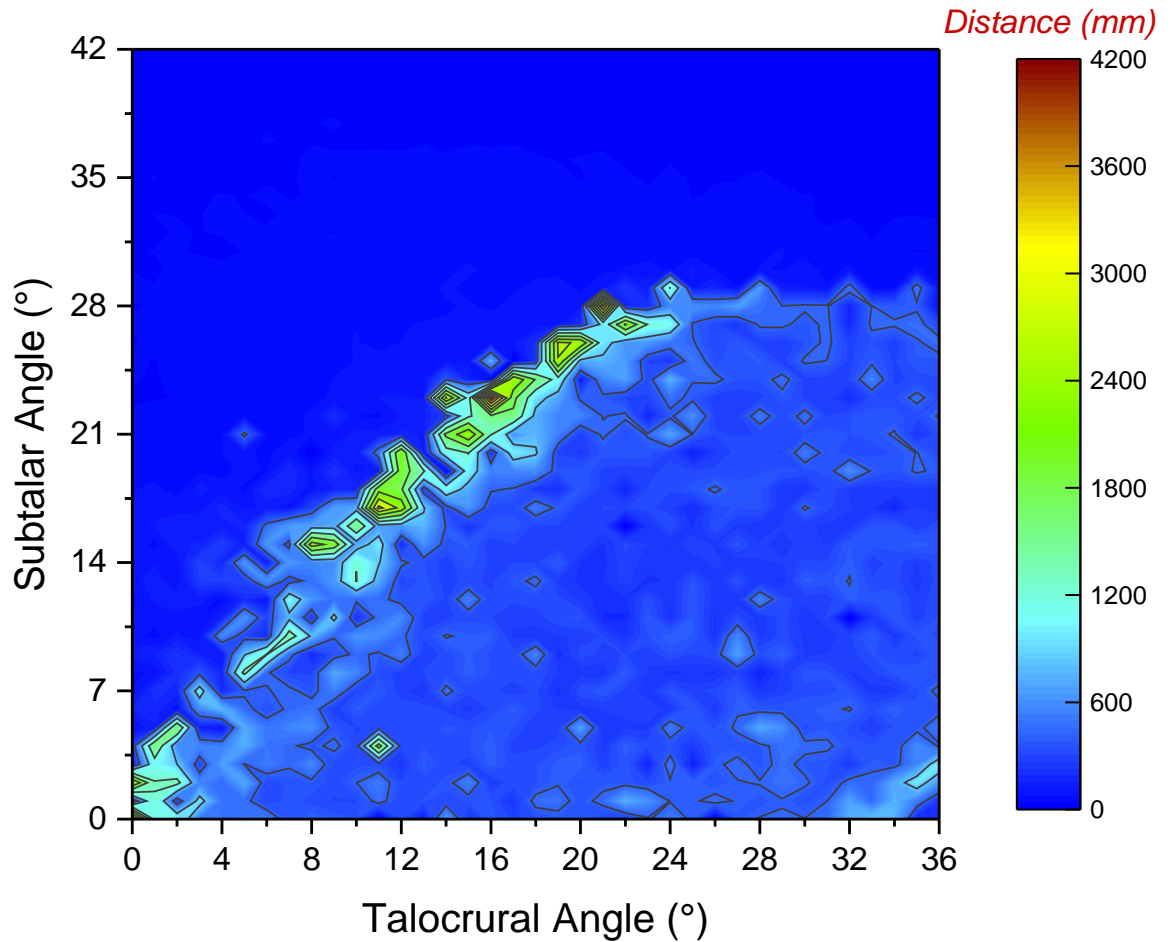


Figure 5.14 Distance travelled as a function of the talocrural and subtalar angle for passive walking of the robot in simulation. The best configuration is 16° in the talocrural joint and 23° in the subtalar joint.

stable range. The reason is that no roll motion could be obtained to create clearance between the foot and the ramp when the subtalar angle is too large (bigger the angle is, more vertical the subtalar joint axis is). The completely opposite characteristic happens in the talocrural joint that the robot cannot walk (stop walking just after launching) if the angle of the talocrural joint axis of rotation is too small, and it can perform unstable walk (falling after a few steps) if the angle is beyond the stable region.

The best combination of the ankle joint orientation is 16° talocrural angle and 23° subtalar angle, where the robot can walk stably to 4166.2 mm 17.4% longer than the distance travelled under the setting of 0° in the talocrural and subtalar angle (the axes are parallel to the ground when standing). There are several circles located around the peak point in which the robot can travel more distance than the other region. They include the

configurations of 10° ~ 20° talocrural angles and 16° ~ 26° subtalar angles.

5.3.6 Best combination

The CoM and spring forces of the robot with 16° talocrural angle and 23° subtalar angle were predicted and plotted in Figure 5.15 and Figure 5.16, respectively. The robot walked 150 mm sideways in medial-lateral direction (see Figure 5.15, top). The minimum tension force in the anterior and lateral spring (see Figure 5.16) are less than that when the robot walks with straight ankle axes paralleled to the ground (see Figure 5.10). The posterior and medial spring share similar pattern in terms of force range and variation trend. The balanced tension forces in the anterior (130 N) and lateral (20 N) spring during swing phase are lower than that in straight ankle axes (142 N and 26 N respectively). Thus, the oblique axis in the ankle may benefit turning ability during walking and reduce force in the muscles around the ankle joint. These could be studied in the future.

5.4 Conclusions

A computational model was designed to simulate passive walking on the ramp in Adams. Parameters related to the simulation were defined including the joints, ground contact, artificial muscle and the variables which affects walking pattern.

The model has been validated to achieve stable walking after launching with a determined initial condition. It could walk 3547.5 mm long. The centre of mass and velocity were predicted during walking. The ankle motions mainly in the talocrural joint and subtalar joint were also predicted. Roll motion in the subtalar joint is larger than human walking as it need to create foot clearance by tilting the robot laterally rather than knee bending. Ground reaction forces in a walking gait were predicted. The general patterns in all three axes are comparable to humans, but the peak values are different, i.e., the peak values of main biomechanical events in GRFs during the robot walking are all higher than that in humans except the breaking peak. This might be caused by the different walking pattern of the robot that no knee flexion exists and the range of roll motion are much larger than humans. Spring forces in the anterior, posterior, medial and lateral position in the ankle were analysed. The fact that the forces in the anterior-posterior springs are much higher than that in the medial-lateral springs complies with humans where Tibialis Anterior, Soleus and Gastrocnemius muscles are much stronger than other

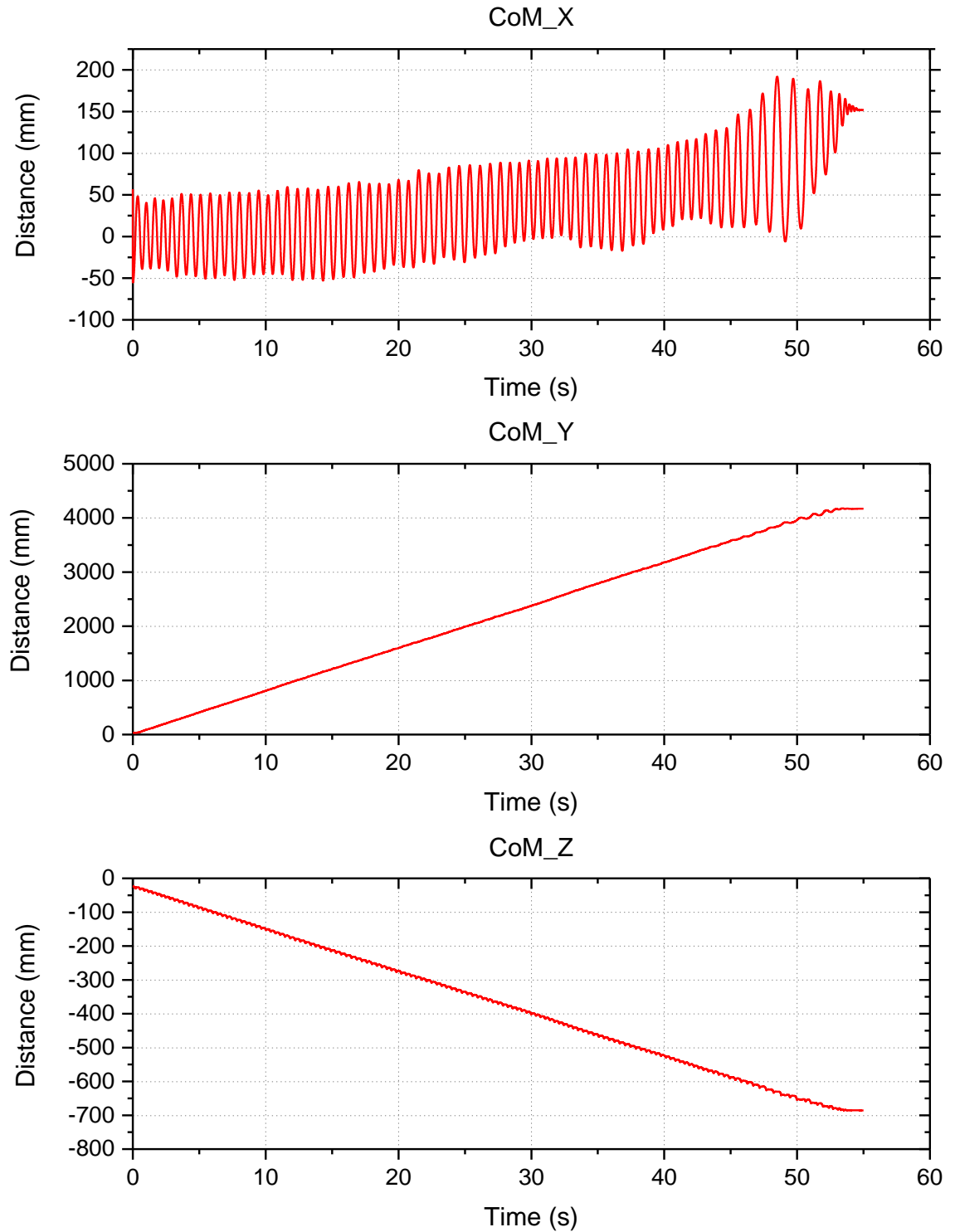


Figure 5.15 CoM of the robot during passive walking with 16° talocrural angle and 23° subtalar angle.

muscles around the ankle. The *CoT* of the robot for passive walking calculated was 0.21 in which humans walk with *CoT* 0.2. The robot is energy effective.

The design of experiment was conducted by changing the angles of the talocrural

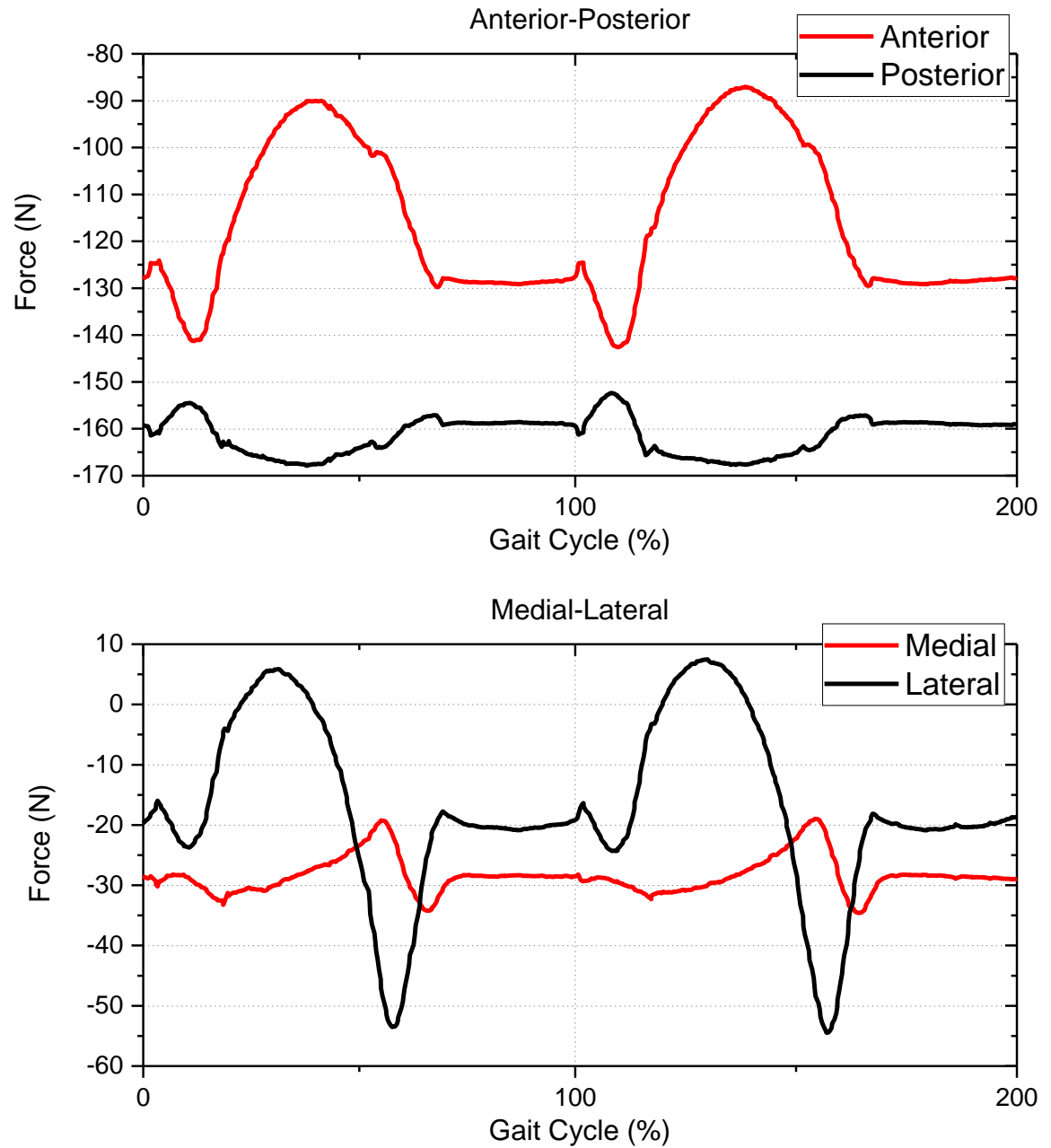


Figure 5.16 Spring forces in the ankle during 2 stable walking gaits including the anterior-posterior (top) and the medial-lateral (bottom). The talocrural angle is 16° and subtalar angle is 23° . Negative value means tension.

(from 0° to 36°) and subtalar (from 0° to 42°) joint axis. Only one angle in one joint was altered with one degree in a combination, resulting in 1591 trials. Distance travelled and the ending status (falling or stopping) of each trial were recorded. The results showed that no stable walking can be performed by the robot for a subtalar angle of more than 29° or a talocrural angle of more than 24° . The best configuration in the ankle is 16° talocrural angle and 23° subtalar angle, where the robot can travel on the ramp up to 4166.2 mm,

17.4 % longer than 0° in the talocrural and subtalar angle (parallel to the ground when standing). The most stable regions for passive walking are $10^\circ\sim 20^\circ$ talocrural angles and $16^\circ\sim 26^\circ$ subtalar angles. Thus, the oblique axis of rotation in the ankle may facilitate normal walking for biped robots.

The contributions to knowledge in this chapter include the following:

- Built a computational robotic model in Adams including the skeleton and the musculotendon units;
- Predict the stable region for biped walking with various ankle configurations: no stable walking can be performed for a subtalar angle of more than 29° or a talocrural angle of more than 24° , and the most stable angle for the talocrural joint is $10\text{-}20^\circ$ and for the subtalar joint is $16\text{-}26^\circ$;
- Predict the best combination of the orientation of ankle axis which could travel the longest distance on the ramp.

Chapter 6

Physical Tests

Although the simulation results have revealed the ankle joint function during walking gait in a way, it is indispensable to conduct walking tests for the physical robot. 3D passive-dynamic simulation has abnormally high yaw in periodic motion, because there are many uncertain effects in 3D analysis, e.g., collision, rolling, friction and scrubbing torque, that are difficult to characterise and to determine the importance [283]. Simulation sometimes leads to different results in physical tests of the robot, such as the Delft robot whose swift swing-leg motion cannot increase lateral stability as showed in simulations [148]. The number of variables that affect the results is too large. Therefore, the configuration in the simulation is only considered as reference but will be changed if needed in the real experiment. The upper body was ignored during test except for the pelvis as the lower body governs bipedal locomotion especially in normal walking and adding the upper body could increase instability.

In this chapter, all the aspects related to the testing of the robot are discussed. Section 6.1 presents the main variables that affect the robot walking on the ramp, where the slope angle, surface frictions, muscle settings (stiffness and preload), initial conditions and ankle joint settings are dominant parameters. Section 6.2 illustrates the experimental installation used for testing, mainly containing a Motion Capture System, a force-plate array consisting of three Kistler force plates, and a ramp with the ability to adjust slope angle. Preliminary tests are conducted and discussed in section 6.3. Results including the repeated passive walking motion, gait cycle, characteristics of the ankle joint, and measurements of GRFs are discussed in section 6.4. Functional analysis has been tested in Section 6.5 to demonstrate the potentials of using this robot platform to examine the underlying mechanisms of human musculoskeletal biomechanics, mainly for the internal

functions of human MSK and its interactions with the environment. The work in this chapter was conducted mainly in Jilin University, China.

6.1 Variables

Since the walking motion is influenced by various variables that change its motions, velocity, stability, and ultimately its success, the 3D printed robot was developed to be implemented various configurations which can adapt itself to different walking conditions. The walking motion of the robot can be assumed as a problem to be solved for each set of determined variables. They can be grouped in 3 sets: external, internal and related to the walking motion. External variables are derived from outer elements, e.g., the slope, friction or damping of the ramp. Internal variables are derived from the robot settings, e.g., the material properties of musculotendon units, the axis of rotation of the talocrural and subtalar joint. Variables related to the walking motion such as initial conditions are also important as they change the walking pattern. Main variables are explained as follows:

Slope Angle. Similar to the simulation, the slope angle plays a major role in the walking motion especially in passive walking by influencing the step length and velocity. In fact, for a determined angle, the robot can achieve stable walking by adjusting the material properties (stiffness and preload) of the artificial muscle- tendon units in the muscular system. However, the slope angle should be confirmed and remain unchanged to investigate the factors that affect walking.

Friction. It is the key factor leading to slipping, rotating in the transverse plane or even stopping. If the friction between the foot and the ramp is too small, the robot would spin along the longitudinal axis or slip on the surface. Contrarily, it may stop walking if the friction is too large. Damping of the ramp may have negative effect on walking stability by creating oscillations between the stance leg and the ramp especially in the heel strike. This problem has been avoided in the design of the ramp (see section 6.2.3).

Muscle Settings. Artificial muscle-tendon units representing the corresponding human muscles are applied in the robot. Stiffness and preload of the unit are the determinant factors for passive walking as they stabilised the robot by generating torques in the joints, driving the robot to upright position and making it enter to the next gait cycle.

Talocrural Angle. The angle of the talocrural joint axis can be altered every 9 degrees from 0° to 36° (i.e., 5 levels in total). The datum axis is the horizontal medial-

lateral axis. All the settings are strictly following the joint parameters in section 4.1.2.

Subtalar Angle. The angle of the subtalar joint axis can be altered every 7 degrees from 0° to 42° (i.e., 7 levels in total). The datum axis is an axis in the transverse plane oriented 12.0° medial to the midline of the foot. All the settings are strictly following the joint parameters illustrated in section 4.1.2.

Initial Conditions. They should be determined before the physical tests and remain as same as possible in each test. Initial roll angle of the supporting leg, initial pitch angle of the swing leg, and release velocity of the robot (i.e., initial kinetic energy given by human) compose the main initial conditions that must be considered. Too large roll angle or velocity may lead to an immediate falling.

6.2 Experimental Installation

6.2.1 Motion Capture System

Motion capture is the process of recording the movement of objects or people. The technology originated in the life science market for gait analysis but is now used widely by VFX studios, military, entertainment, sports, neuroscientists, and for validation and control of computer vision [284] and robotics [285].

Generally, optoelectronic motion analysis systems are employed by using infrared camera arrays to track the positions of active or passive markers placed on the measured objective of interest [260]. Among them, Vicon Motion System (Oxford Metrics Limited, UK) is one of the key players in optoelectronic motion capture systems based on markers. Passive optical system uses markers coated with a retroreflective material to reflect light that is generated near the cameras lens. The camera's threshold can be adjusted so only the bright reflective markers will be sampled, ignoring skin and fabric. The centroid of the marker is estimated as a position within the two-dimensional image that is captured. The grayscale value of each pixel can be used to provide sub-pixel accuracy by finding the centroid of the Gaussian. An object with markers attached at known positions is used to calibrate the cameras and obtain their positions and the lens distortion of each camera is measured. If two calibrated cameras see a marker, a three-dimensional fix can be obtained.

In our study, the Vicon System containing 7 MX-40 cameras fixed indoor on the triangle bracket (Figure 6.1) is used to capture and record the 3D motion of the biped



Figure 6.1 The Vicon System used to record 3D motion of the robot.

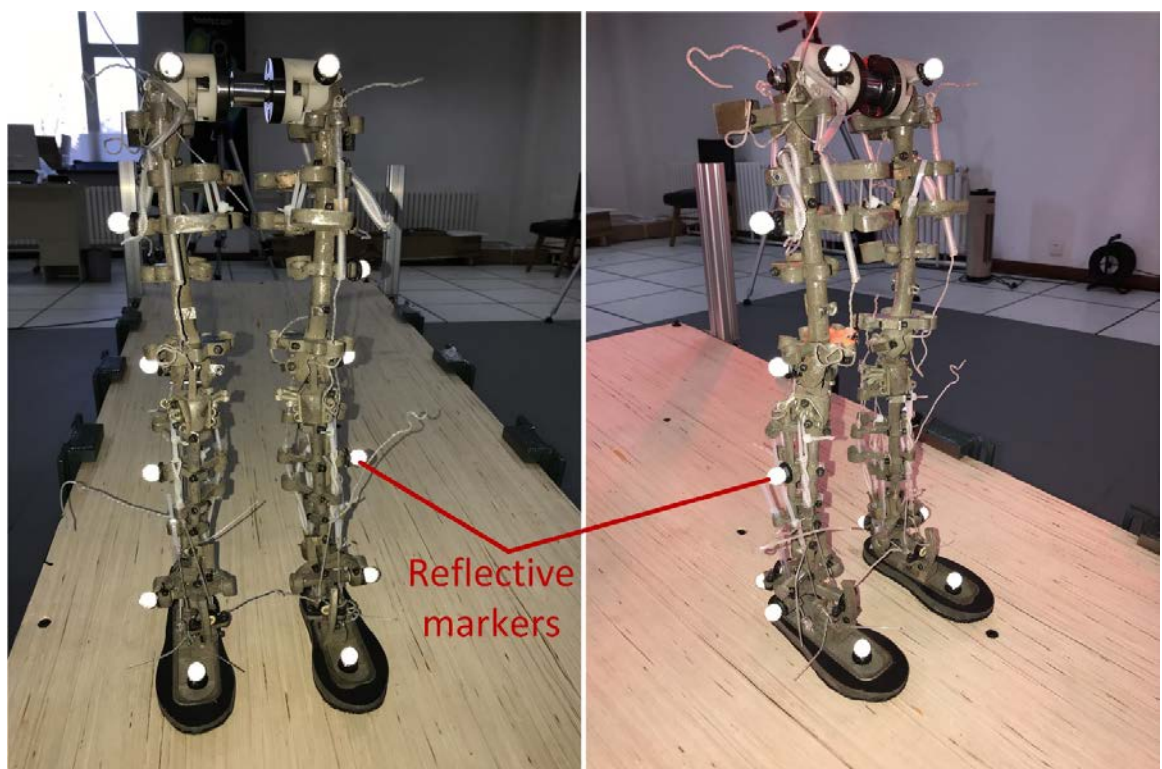


Figure 6.2 The biped robot attached with reflective markers on the landmark.

Table 6.1 Definition and position of the markers placed on the robot.

Marker Label	Definition	Position
LASI/RASI	Anterior superior iliac spine	Posterior side of the pelvis
LPSI/RPSI	Posterior superior iliac spine	Anterior side of the pelvis
LTHI/RTHI	Thigh	Placed on the lateral side of the thigh
LKNE/RKNE	Lateral knee	Placed on the lateral edge of the knee joint
LKNEM/RKNEM	Medial knee	Placed on the medial edge of the knee joint
LTIB/RTIB	Shank	Placed on the lateral side of the shank
LANK/RANK	Lateral talocrural	Placed on the lateral edge of the talocrural joint
LANKM/RANKM	Medial talocrural	Placed on the medial edge of the talocrural joint
LHEE/RHEE	Posterior subtalar	Placed on the posterior edge of the subtalar joint
LHEEA/RHEEA	Anterior subtalar	Placed on the anterior edge of the subtalar joint
LTOE/RTOE	Toe	Placed on the top of the forefoot

robot. Special wallpapers are stuck on the test zone of the ground to avoid reflexion of the infrared light. Dozens of rubber balls are attached with reflective tape, which needs to be replaced periodically. The markers are attached directly to the landmarks of the robot shown in Figure 6.2. Four markers located at the pelvis were used to compute the hip joint motion and global position of the robot. Two markers were placed on each left and right knee, talocrural joint, and subtalar joint. One marker was attached in each thigh, shank and foot. There are 22 markers in total used to capture the 3D motion of the robot, the details

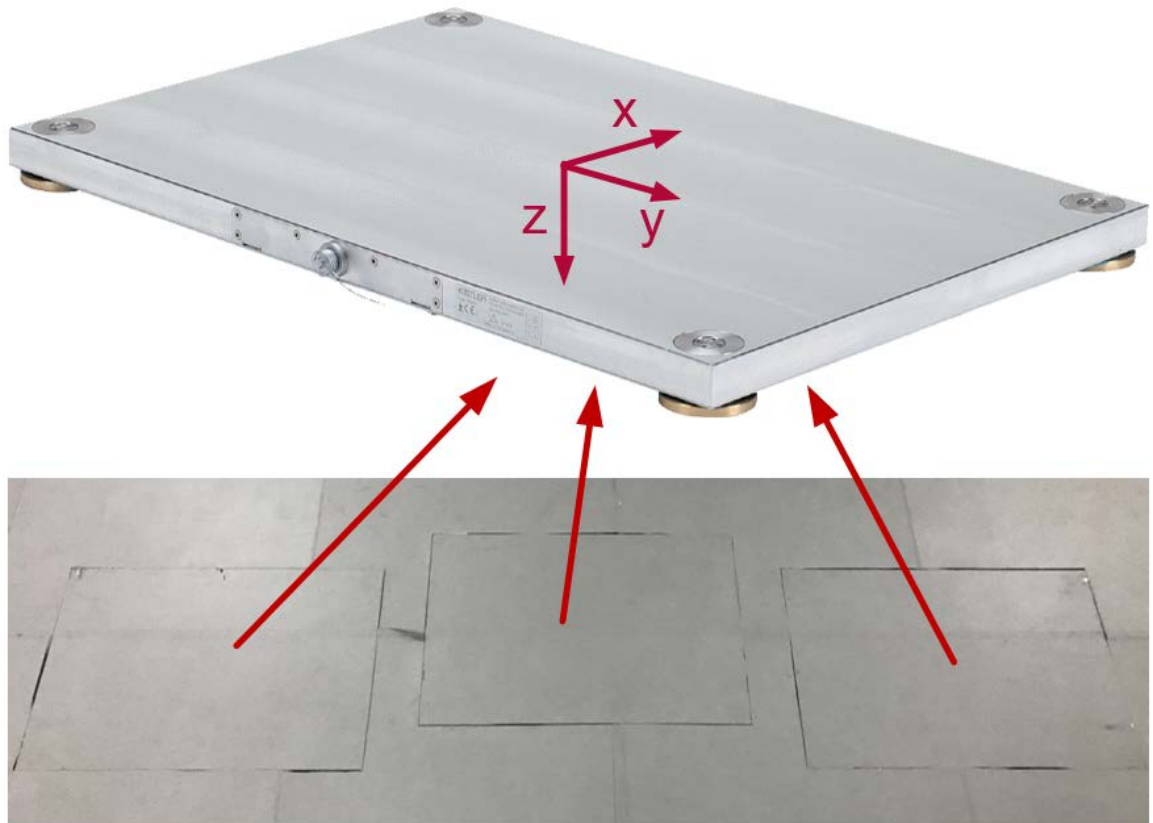


Figure 6.3 A force-plate array containing three Kistler force plates mounted on the ground.

are introduced in Table 6.1. The sampling frequency of the Vicon System is set to 100 Hz. With this system, kinematic data including position, velocity and acceleration of the markers can be directly measured, and kinematic data of the body segments and joints of the robot can be further calculated.

6.2.2 Force Plates

Force plates are measuring instruments that measure the ground reaction forces (GRFs) generated by a body standing on or moving across them, normally to quantify balance, gait and other parameters of biomechanics. In universities, clinics and rehabilitation centres, force plates are indispensable tools for clinical research, sports and performance diagnostics, motion analysis and occupational safety of which the objects are humans.

Rather than conventional frame mounted force plates, Kistler multicomponent force plates from Switzerland that can simply be used on any flat surface are used for testing. The plate's low overall height of just 35 mm and weight of under 18 kg allows flexible, portable use. The piezoelectric 3-component force sensors have very low crosstalk values

Table 6.2 Technical data of Kistler force plate.

Name		Unit	Value
Measuring range	F_x, F_y	kN	$-2.5 \dots 2.5$
	F_z	kN	$0 \dots 10$
Overload	F_x, F_y	kN	$-3/3$
	F_z	kN	$0/12$
Linearity		%FSO	$<\pm 0.2$
Hysteresis		%FSO	<0.3
Crosstalk	$F_x \leftrightarrow F_y$	%	$<\pm 1.5$
	$F_x, F_y \rightarrow F_z$	%	$<\pm 2.0$
	$F_z \rightarrow F_x, F_y$	%	$<\pm 0.51$
Rigidity	x-axis ($a_y = 0$)	$N/\mu m$	≈ 12
	y-axis ($a_x = 0$)	$N/\mu m$	≈ 12
	z-axis ($a_x = a_y = 0$)	$N/\mu m$	≈ 8
Natural frequency	$f_n(x, y)$	Hz	≈ 350
	$f_n(z)$	Hz	≈ 200
Operating temperature range		$^{\circ}C$	$0 \dots 60$
Sensitivity range	F_x, F_y	mV/N	≈ 40
	F_z	mV/N	≈ 18
Threshold		mN	<250
Drift		mN/s	$<\pm 0.10$

and in conjunction with the special design principle ensure excellent accuracy of the centre of pressure (CoP). This force plate is designed specifically for use in gait and balance analyses. It has a built-in charge amplifier compatible with all of the common motion analysis systems. Despite the very wide measuring range ($0 \dots 10 \text{ kN}$), this force plate offers excellent accuracy and linearity over the entire spectrum of applications (4 measuring ranges) and guarantees overload protection up to 12 kN . The detailed technical data is shown in Table 6.2. Kistler force plate has a high compatibility with 3D motion capture system such as Vicon system introduced in section 6.2.1.

Three Kistler force plates (Figure 6.3) are well-arranged and mounted on the test zone to record the 6-component force and moment during robot walking on the ramp. They can collect data simultaneously or independently. When they work together, in this case the ramp is placed on three force plates, kinetic data of the moving object including GRFs and CoP can be directly measured or indirectly computed by combining all the data of three



Figure 6.4 NordicTrack T22.5 treadmill for testing (top) and swing caused by the gap between the belt and the base of the treadmill (bottom).

force plates. The contact area between the ramp and the ground should be completely in the surface of the three force plates, otherwise the measured data is incomplete. This requires a special design of the ramp which will be presented in section 6.2.3. The sampling frequency of the force plate is 1000 Hz . Integrated with the Vicon system, kinematic and kinetic data can be obtained synchronously with no delay.

6.2.3 The Ramp

A treadmill (NordicTrack T22.5, USA), of which the footprint is 1540 mm in length and 510 mm in width, was firstly used as the platform for testing (Figure 6.4, top). It can

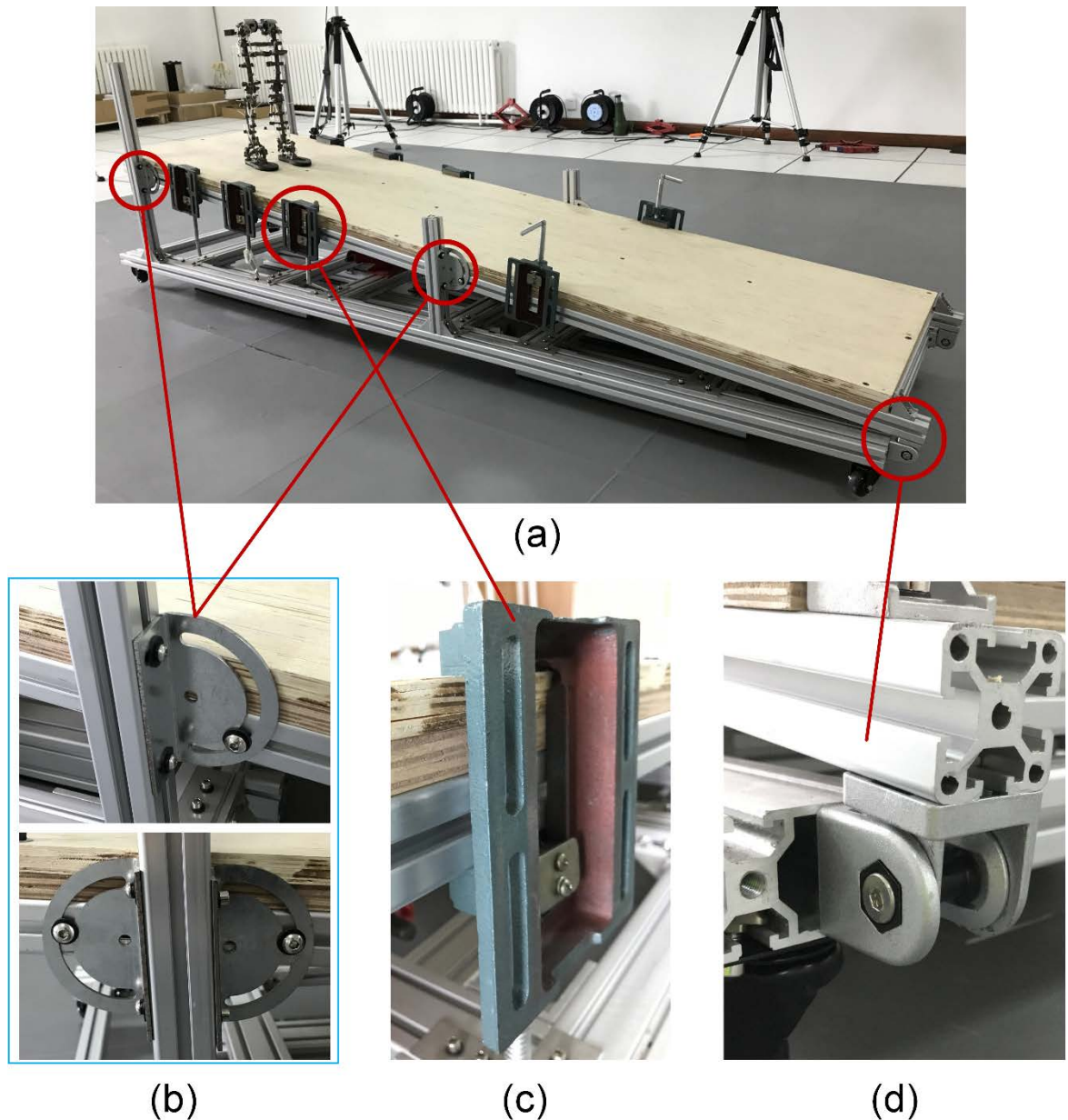


Figure 6.5 (a) New design of the ramp including (b) angle adjustment plates, (c) vices and (d) hinges.

easily incline to 15 degrees and decline to -3 degrees with 0.5-degree interval by a hydraulic system. Although it has the ability to conveniently change the slope angle, the fact that there is a gap between the belt and the base of the treadmill will severely affect the walking motion during the test. The closer to the motor in the ends it is, the bigger the gap is (Figure 6.4, bottom). This phenomenon has a negative effect on the walking and leading to failure due to damping and decelerating or even stopping the robot depending on the synchronization between the swinging of the belt and the heelstrike impacts of the robot. When the robot is released in the invalid zone of the terrain (i.e., the big gap zone),

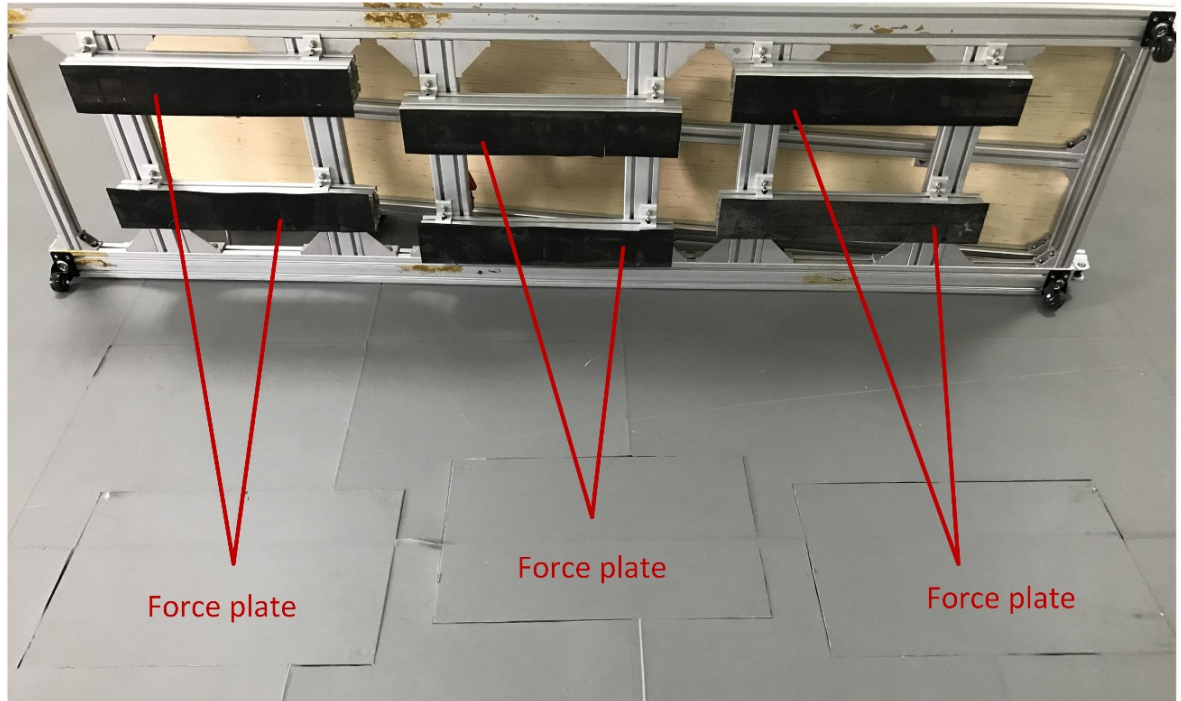


Figure 6.6 Special design of the ramp for measuring GRFs.

it cannot walk because the kinetic energy transferred from the gravity is absorbed by the vibration of the belt. Similarly, when the robot successfully launches and walks to the invalid zone in the end of the terrain, it will decelerate and stop walking because of the vibration of the belt. In a word, the energy loss caused by the vibration will have a negative influence on the test. Thus, a new platform (Figure 6.5a) was developed to resist this defect.

The main body is a 40-mm thick board that is fixed in the aluminium alloy extrusion profiles using bolts and nuts. The upper (parallel to the board) and the lower (parallel to the ground) lay of the frame are connected by two hinges (Figure 6.5d) to alter the slope angle between the board and the ground. Three angle adjustment plates (Figure 6.5b) are deployed in the middle and the top of each side of the frame to fasten the board and the profiles. There are 8 extra vices (Figure 6.5c) placed on the edges of the frame, cooperated with the bolts to avoid vibration between the board and the frame during robot walking.

As the ramp will be placed on the force plates to record GRFs data, special design is considered to assure that the contact area between the ramp and the ground is completely in the surface of the three force plates. Six profiles (two correspond to one force plate) pasted with rubbers (Figure 6.6) are fixed on the bottom of the ramp, where the length is a

bit less than that of the force plate. To avoid the influence of the ramp's weight, the force plate should be reset to zero level before each test. Thus, the measurements of the three force plates are the GRFs that are reacted on the robot during walking by transferring from the ramp.

6.3 Preliminary Test

Preliminaries test is developed to confirm the best possible conditions to be used in the real test. In this initial test, the robot was taken to its limits by changing the configurations of the artificial muscle-tendon units, the launching procedure and the initial conditions of launching to figure out positive or negative effects of them. Roll motion of the stance leg is discussed as it severely changes the walking pattern. Failing state if stable walking cannot be performed has been explained.

6.3.1 Launching

The launching has a main influence in the success of the walking motion. The robot is taken to a position as though it was already walking when it gets on the ramp. Therefore, one of the legs is raised by tilting the support leg from its ankle. Furthermore, in some cases the hip joint of the swing leg is rotated forward so that the robot body is displaced forward in order to induce the robot walking down the slope. However, specific initial conditions for the launching cannot be stated; the walking motion depends on many variables as mentioned before, thereby the perfect launching must be found out for each different configuration. For instance, successful initial conditions for a determined configuration of slope angle, muscle-tendon units, etc. may not work for a slightly different robot setting. Therefore, the perfect launch should be studied and adjusted for each robot configuration and walking motion desired. The steps to follow for most of the cases are defined below.

Tilt: Tilt the support leg by bending the ankle joint and holding the support foot in full contact with the ramp, which means rotating the robot along the subtalar joint of the support leg.

Move: Move the pelvis a bit forward in order to increase the displacement that induces the robot to walk down the slope, i.e., rotate the robot along the talocrural joint of the support leg.

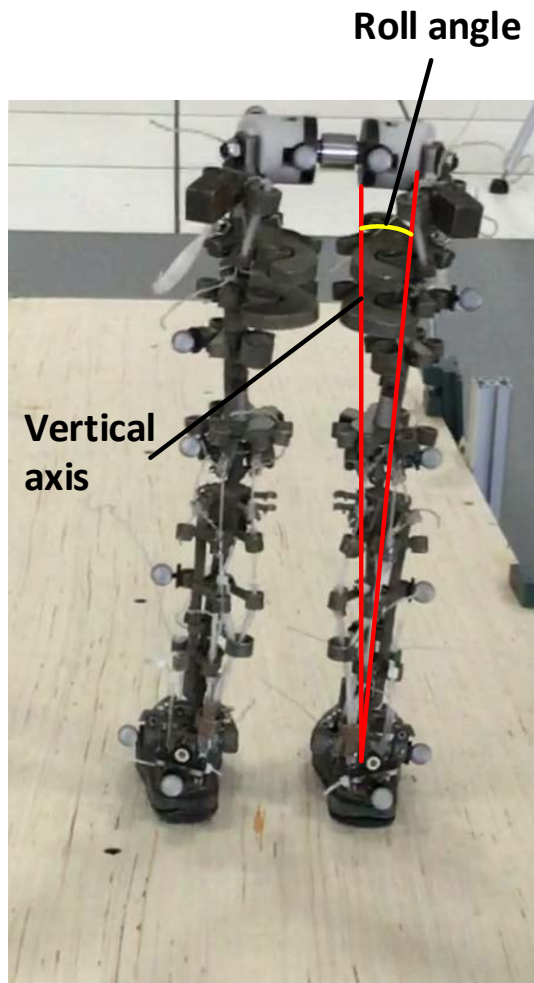


Figure 6.7 Roll motion of the robot during passive walking on the ramp.

Rotate: Rotate the hip joint of the swing leg from the pelvis in order to place its foot slightly ahead to the support foot, only if the natural motion of the swing leg caused by the gravity is insufficient to drive the robot walk down.

Release: Release the robot.

6.3.2 Roll Motion

Roll motion (see Figure 6.7) is the swinging movement that the robot performs within the coronal plane and about its longitudinal axis (mainly around the subtalar axis in the ankle). The maximum roll angle is one of the keys to perform stable passive walking, as the knee joints are locked and it is main factor to create sufficient clearance between the swinging leg and the ramp which permit swinging forward motion without collision. The roll angle is defined as 0° when the robot is statically placed at the top of the ramp. A roll motion

cycle, for instance may be within the range $\pm 12^\circ$, is obtained after launching of the robot in which the initial conditions determine the range of roll motion. This cycle should be repetitive and constant at every step to perform stable walking on the ramp.

Roll motion should be controlled to produce sufficient clearance to allow the leg to swing forward without colliding with the ground. The roll motion of the stance leg should be synchronized with the desired swinging of the other leg. It starts at the same time as the swinging of the other leg and they should finish their cycle simultaneously. In other words, the roll angle starts from 0° at the heel strike of the foot and rises up to maximum tilting the robot about the supporting leg, while the contralateral leg swings forward. Once the maximum roll angle is reached, the robots is propelled to return to its upright position making the roll angle decrease toward 0° in which the swing leg should terminate its cycle and start to enter heel strike phase. Asynchronization of the two cycles leads to failure. If the roll angle returns to zero point while the swinging of the contralateral leg is in the middle or out of its cycle, the robot would impact the ramp and stop walking. Thus, whether this synchronization succeeds the next cycle follows the same motion, achieving a stable walking or leading to failure. Furthermore, the roll motion determines the failing state if the stable walking has not been achieved. If the maximum roll angle is too small, the robot would stop walking after a few steps as the foot clearance is not sufficient. On the contrary, it would fall down if the maximum roll angle is too large where the artificial muscle-tendon units are unable to drive the robot return to upright position.

The maximum roll angle can be determined by two factors, the stiffness and the preload of the medial/lateral artificial muscle-tendon units. They generate torques in the ankle joint especially around the subtalar axis, stopping the roll motion when a determined angle is reached and diving the robot to its upright position. High stiffness and preload will decrease the maximum roll angle and vice versa.

6.3.3 Stopping

This problem is mainly due to the deceleration of the robot which is affected by many factors such as too small slope angle, high stiffness in the artificial muscle-tendon units, inappropriate initial conditions and tolerance errors of the ramp.

If the slope angle, the potential energy of the robot is insufficient to drive the robot walk. This also happened when the robot walked on the uneven surface of the ramp

caused by the tolerance errors. The slope angle slightly changes in some specific region as the surface of the ramp cannot be ideally flat. The robot would decelerate to stop when it reaches the area where the slope angle suddenly decreases.

Inappropriate initial conditions lead to stopping after launching. Too small initial roll angle will reduce the initial kinematic energy and cannot create clearance between the foot and the ramp for swing motion.

Furthermore, the too high stiffness of the artificial muscle-tendon can also affect the landing producing the overmuch torque around the ankle joint. The roll motion in the stance leg and swing motion in the swing leg are all limited to small ranges that would not be able to make the robot achieve stable walking. When the maximum roll angle is reached and stance leg starts to return to upright position, the swing cycle of the contralateral leg just begins. The foot will collide with the ramp instead of landing parallel.

6.3.4 Falling

The reason for falling is the acceleration of the robot at every step. This acceleration is due to uncontrolled roll and swinging motions during walking caused by factors such as small stiffness in the artificial muscle-tendon units, inappropriate initial conditions and tolerance errors of the ramp. The roll angle is never exactly constant, and it slightly varies during the walking motion; however, for some cases this roll motion gets too large at some specific steps exceeding the critical value and accelerating the robot until falling. Therefore, there are 2 motions that should be controlled in order to avoid this acceleration, the roll motion in the coronal plane and the swinging of the legs.

The roll motion is controlled by the extension of the artificial muscle-tendon units around the ankle and the initial conditions in the launching process. It would be improved by adding some device in order to accurately control the maximum roll angle as a function of the desired step length.

The swinging of the legs can be controlled by the artificial muscle-tendon units around the hip and the maximum roll angle that is reached in a gait cycle. If the swinging is not enough for stable walking, one of the solution is to increase the roll motion of the stance leg. If the swing motion is too large, decrease in the maximum roll angle or adding more artificial muscle-tendon units to the hip joint in the sagittal plane may be helpful. Further research on falling could be done in the future.

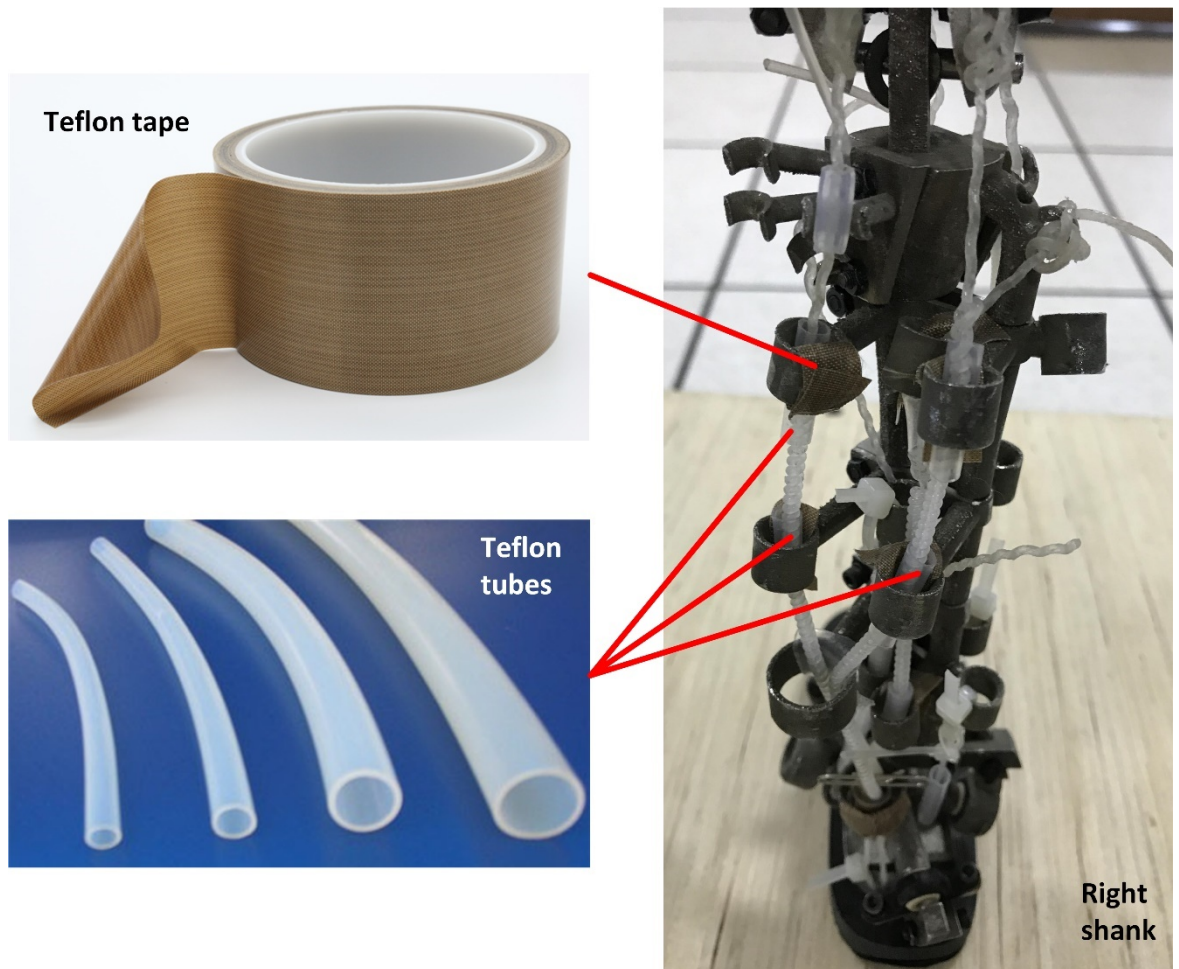


Figure 6.8 Lubrication of the right shank using Teflon tape and Teflon tubes.

6.3.5 Frictions

During the initial test, the motions around the joints was hysteric, i.e., the resilience of the artificial muscles was poor. For instance, the foot cannot return to its neutral position when the ankle was dorsiflexed along the talocrural or inverted along the subtalar joint even with a small stiffness in the artificial muscle-tendon units. The coiled fibres always stuck with the edge of the bushing in the skeleton which guided the muscle paths.

Thus, Teflon tapes and Teflon tubes made of Polytetrafluoroethylene (PTFE) were used to lubricate the surface between the muscle fibres and the skeletal body of the robot, of which the friction coefficient is as low as 0.04. For example in the right shank, Teflon tapes were attached on the contacting surface between the muscle fibres and the skeleton, and Teflon tubes covered the surface of muscle fibres (see Figure 6.8). This feature was adopted in the whole body of the robot.

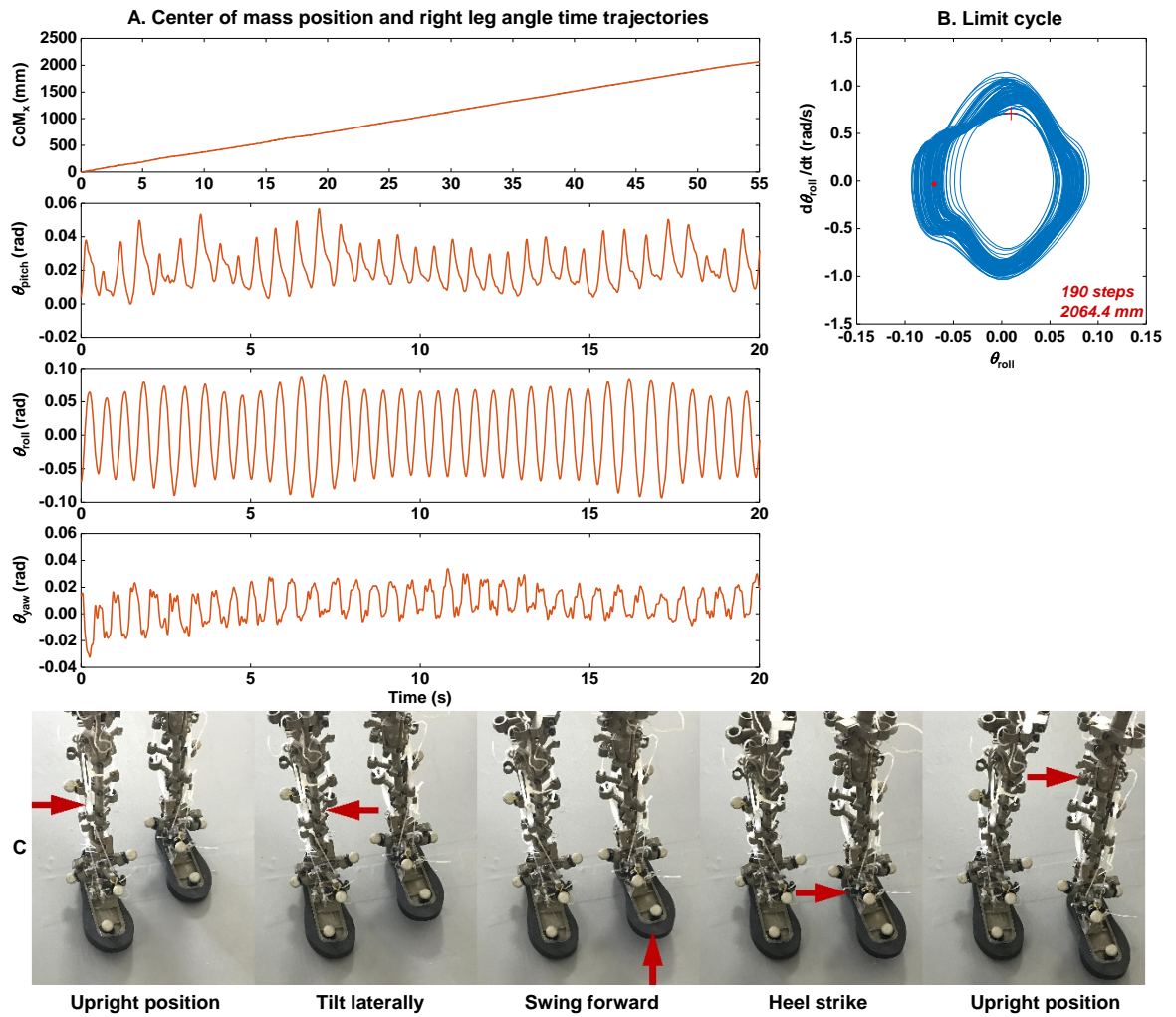


Figure 6.9 Walking test of the robot. (A) Centre of mass in the progression direction and right leg angle time trajectories in terms of pitch, roll and yaw motion. (B) State space plot of the limit cycles in the roll axis (frontal plane). Red dot is the initial conditions (around 0.07 rad and 0 rad/s) and plus sign is the end state. (C) Walking sequence of one step.

6.4 Repeated Test

To certify the new paradigm of developing humanoid robot, repeated tests were conducted on a ramp without any actuation and control. The upper body including head, middle and upper trunk, and arms was ignored as the lower body governs bipedal locomotion especially in normal walking.

6.4.1 Repeated Tests for Passive Walking

A robust steady-state motion (Figure 6.9C) was found during the test on a 2.44-m-long

ramp with slope angle of 0.118 radians. With good practice, the robot can walk steadily in 100% of launches, which has achieved 26 consecutive successful walking tests (Supplementary Video 3). It walked the full length of the ramp in above 96% of trials, whereas inappropriate initial conditions were the primary cause of those launches in which the robot stopped or fell before reaching the end of the ramp. Figure 6.9 displays the time trajectories of centre of mass (CoM) position and right leg angle, the stability with the limit cycle, and the walking gait of one test. Pitch motion in this case is the leg swing in the sagittal plane, roll motion for achieving foot clearance is a gentle rocking movement in the frontal plane, and yaw motion is the twist and turn in the transverse plane. In this test, the robot achieved 190 steps and 2064.4 mm distance travelled (Figure 6.9B) with a very reproducible cycle in pitch, roll and yaw motion (Figure 6.9A).

6.4.2 Gait cycle

In the robot walking, according to the interaction between the foot and the ground, the gait cycle was divided in two main phases, i.e. the stance phase, during which the foot was in contact with the ground, and the swing phase, in which the foot was in the air (see Figure 6.9C and Supplementary Video 4). Each phase has a different functional goal that stance ensures body progression while maintaining upright position whereas swing is performed to advance the leg and to prepare for the next step. As for the timing, the temporal distribution of the two phases is approximately 52% for stance and 48% for swing. The stance phase of robot walking is shorter than that of human walking which is around 60% because toe-off and push-off of the foot do not exist in robot walking due to stiff toe joints and no actuation.

However, the walking sequence indicates that the robot is obviously not human-like in a number of ways. It is missing upper body parts, and the knees are locked with the legs. There are no toes in the feet, which cannot provide balance and thrust during walking. As power comes from gravity, there are no muscle contractions or torques to accelerate the swinging leg which affects the robot's motion. With all of these shortcomings, it is astonishing that the robot still walks so stably by today's robotics standards.

6.4.3 CoM

The position of the CoM of the robot during passive walking on the ramp were measured. For a steady walk, the projections of the CoM along three axes are shown Figure 6.10. The

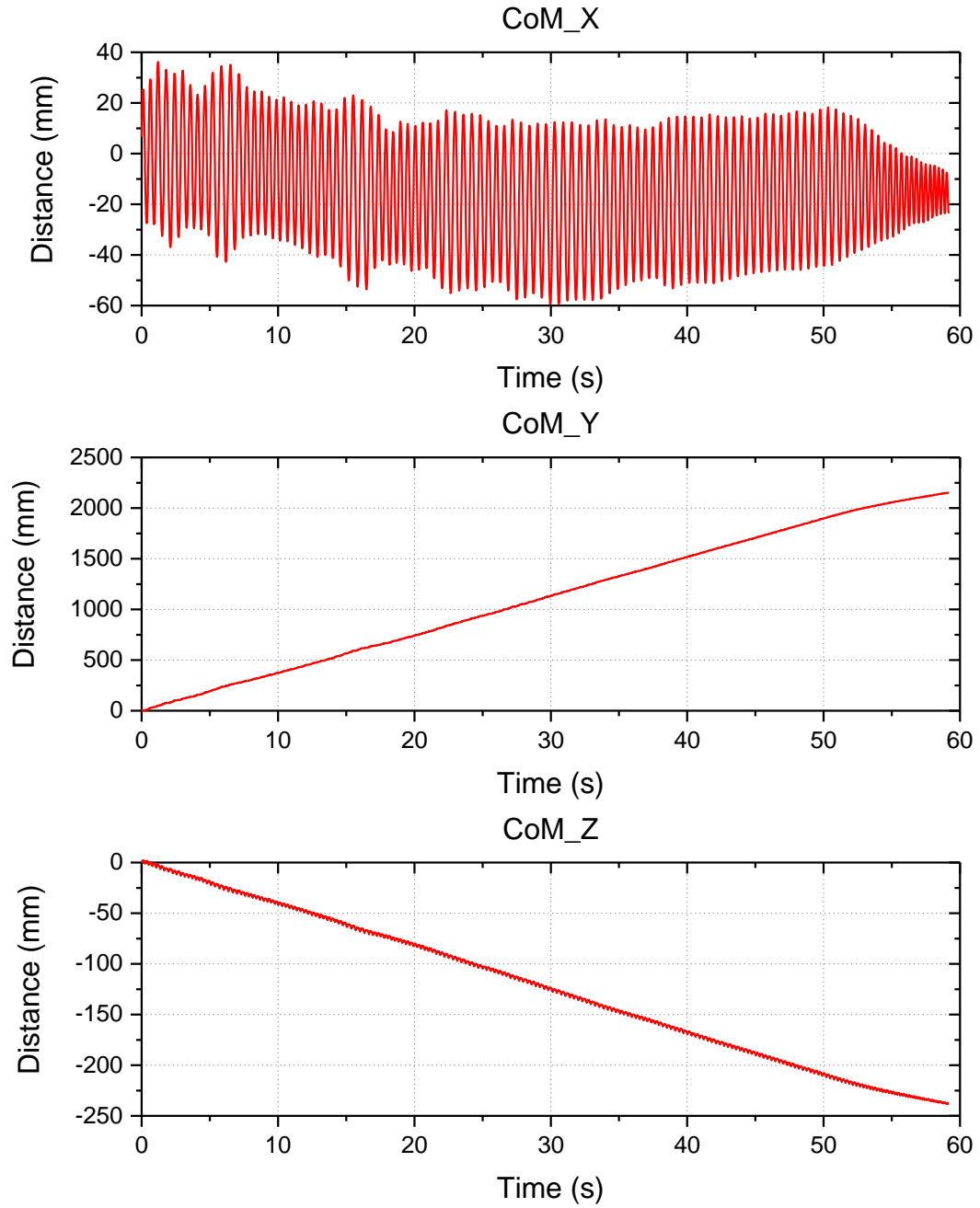


Figure 6.10 CoM of the robot during passive walking. The global X-axis is to the right (top), the Y-axis is in the direction of progression (middle) and the Z-axis is vertical (bottom).

CoM made sideways excursions of $-60\sim 40\text{ mm}$ in medial-lateral direction, forwarded 2150.9 mm in progression and declined 237.4 mm in vertical direction. The robot stopped walking in the edge of the ramp with -23.2 mm sideways in the medial-lateral direction which is 0.0487 times the leg length. Similar to the simulation result in section 5.2.2, the trajectories of CoM in the sagittal plane, especially along the Z axis, had certain

fluctuation during walking (see Figure 6.10, bottom). These oscillations were caused by the completely passive walking gait of the robot (roll motion of the stance leg and swing of the contralateral leg).

6.4.4 Motion of the Ankle Joint

The general pattern of human ankle motion during normal walking has been studied extensively [286-288], but there are some difference for robot walking. From initial foot contact through foot flat, the talocrural joint plantarflexes, the subtalar joint everts, and the foot pronates. The subtalar joint everts partly because the contact point of the foot is lateral to the ankle joint centre and the centre of gravity (CoG) starts to change to another leg, thus producing a valgus thrust on the subtalar joint. In the initial contact of contralateral foot, with dorsiflexion of the talocrural joint and inversion of the subtalar joint, the foot is capable of propulsion.

The rotating angles in the talocrural joint and subtalar joint cannot be directly measured from the 3D motion capture system as only the kinematic data of reflective markers attached on the robot are recorded. Thus, the motions in the ankle are calculated from the trajectory of the markers.

From initial foot contact, the talocrural joint is in slight plantarflexion which increased until foot flat, but it rapidly reverses to dorsiflexion during the latter part of stance as the body passes over the foot. The motion then returns to upright position during swing until the next initial contact. Rotation of talocrural joint during normal walking averages 1.8° plantarflexion and 2.2° dorsiflexion, with a total motion of 4° . Maximum plantarflexion occurs at foot flat, and maximum dorsiflexion occurs at the end of the stance phase. At initial contact, the talocrural joint is almost neutral (Figure 6.11, top). From initial contact to foot flat, the ankle plantarflexes (i.e., extends) to a maximum of 1.8° as the foot is lowered to the ramp surface. At the end of stance, the ankle dorsiflexes (i.e., flexes) to a maximum of 2.2° as the leg rotates anteriorly and medially over the supporting foot. During the early stage of swing, the ankle rapidly plantarflexes to neutral position as the robot weight is transferred onto the contralateral leg to attain foot clearance. The talocrural joint is in neutral position during the rest of swing.

The subtalar joint rotates in stance, which affects the weight-bearing alignment of the entire robot. Unlike human walking, the motion at the subtalar joint is bigger than the

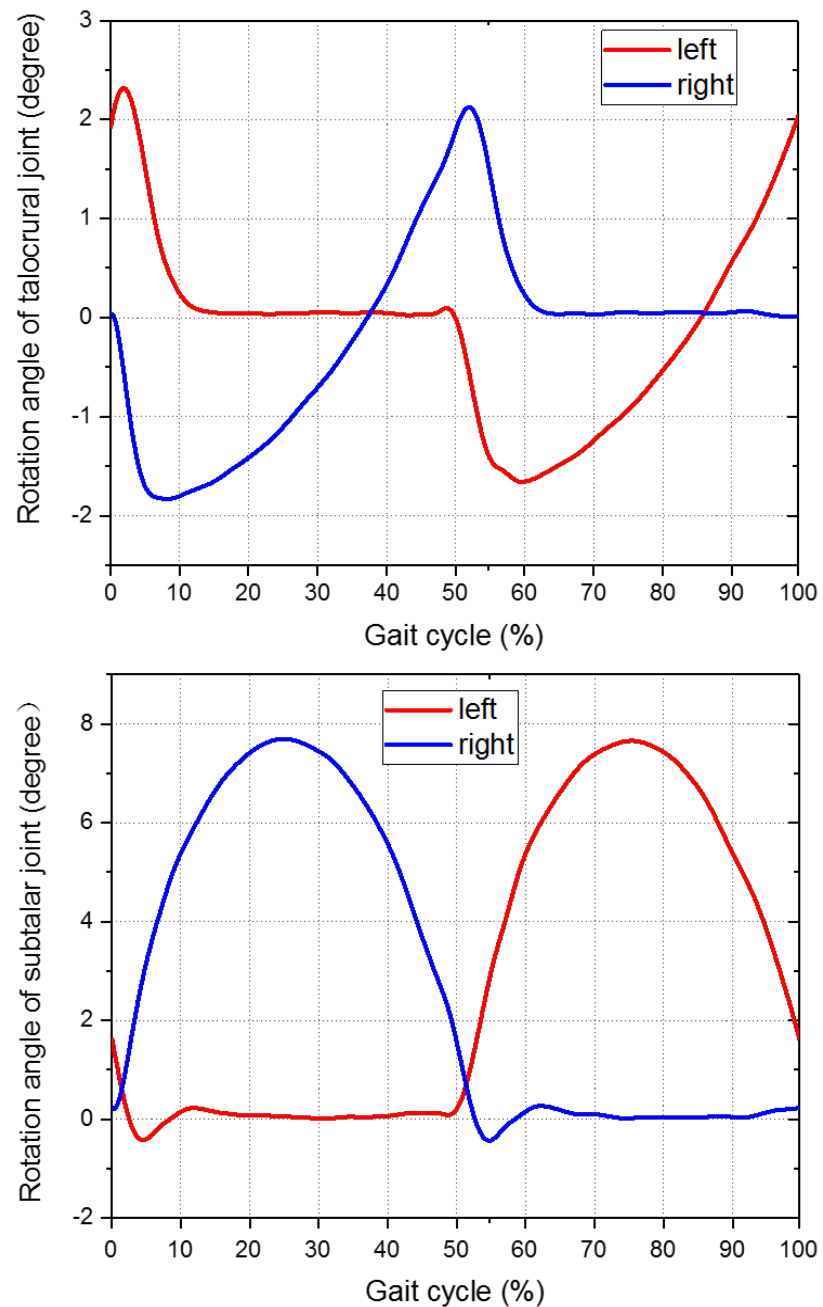


Figure 6.11 Rotation angle of talocrural joint (top) and subtalar joint (bottom) in the ankle during robot walking. Zero value in the talocrural joint means that the robot is in upright position, positive and negative angle represents that it inclines forward (dorsiflexion) and backward (plantarflexion) in sagittal plane respectively. Zero value in the subtalar joint means that the robot is in upright position, positive and negative angle represents that it tilts laterally (eversion) and medially (inversion) in coronal plane respectively.

talocrural joint as it provides foot clearance that is performed by knee flexion and

extension in humans. And subtalar rotation is the motion which permits the foot to adapt to various surfaces. During initial contact, the subtalar joint begins everting until peak eversion is reached by the middle of stance (see Figure 6.11, bottom) which averages 7.7° . This rapid eversion is followed by gradual inversion, with peak inversion achieved by early of swing. The foot drifts back to neutral position during swing. Subtalar eversion is one of the mechanisms to absorb shock as the robot weight is transferred onto the supporting foot during stance. When the robot's centre of mass (CoM) is translated more laterally as stance progresses, the tension of the artificial muscle units in the medial side of the leg increases and drives the foot to invert. Subtalar inversion helps to bring about stability of the foot and propel the transfer of CoM to the other leg.

6.4.5 Ground Reaction Forces

Ground reaction forces (GRFs) during passive walking on the ramp are measured by the force plates (see Figure 6.12), starting from the heel strike of the right foot. Unlike the results in Adams simulation (see section 5.2.3) or in the gait measurements of human walking [270], the starting and ending point of the vertical and horizontal component of the GRFs during robot walking do not equal to zero, because the forces are indirectly measured from the combination of the ramp and three force plates. When one leg is in the late stance phase, the other leg starts to enter the heel strike phase, i.e., the double stance phase is also recorded not the swing phase. The GRFs include the stance phase of both legs where the first half is the measurement of the right leg and the second half is that of the left leg. Accordingly, the first peak or valley comes sooner than the simulation results or human gait measurements as the force in the late stance of the contralateral leg is also recorded at the beginning.

For the vertical component, the passive peak of the right leg and the active peak of the left leg are integrated together. The valley value around 6 N/kg is similar as that in human walking, while the peak value above 9 N/kg is smaller than 12 N/kg in humans. The peak value of the lateral component is higher than humans, almost 2 N/kg versus -0.6 N/kg , caused by the larger roll motion of the robot. There is no positive value in the horizontal force, which suggests that the propulsion generated from the robot cannot be compared with humans. The push off of the foot does not exist in the passive walking which provides most of the propulsive force in human walking. All the data of human walking are from the research done by Ren et al [270].

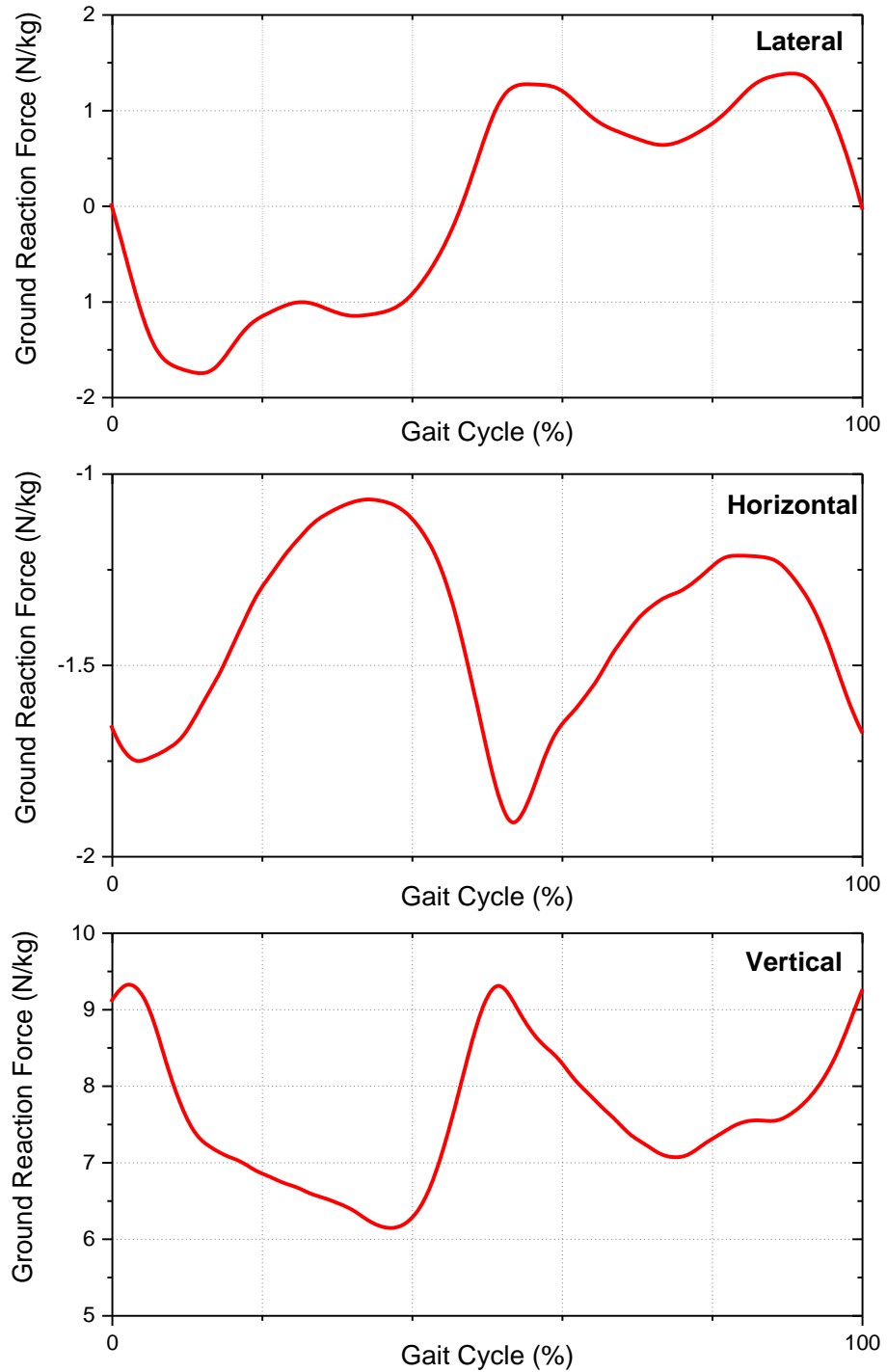


Figure 6.12 Ground reaction forces during one passive walking gait including medial-lateral (top), horizontal (middle), and vertical (bottom) forces in the physical test.

6.4.6 Muscle Settings

The artificial muscles coiled from fishing lines are the determinant factor which affects the walking of the robot by changing the stiffness and the preload. Among them, the extensor

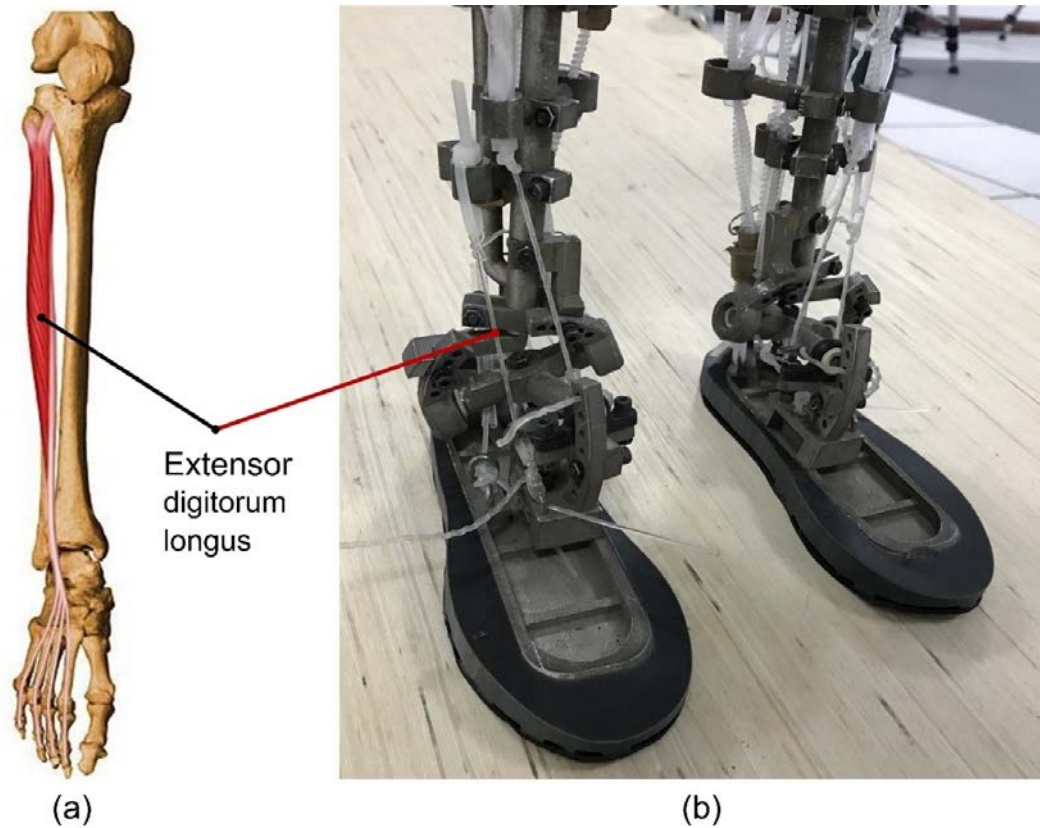


Figure 6.13 Extensor digitorum longus muscle (a) in human body and (b) in the robot.

digitum longus is a muscle of the anterior component of the leg in which the function is to dorsiflex the foot and extend the toes. The insertion was simplified to a single point on the top of the foot in the robot (see Figure 6.13b) instead of distal phalanges of digit 2-5 in humans (see Figure 6.13a).

The results showed that adjusting the preload in the extensor digitorum longus muscle severely changes the motion of passive walking on the ramp. The roll motion becomes too large leading to falling after several steps if the preload is high, while the swing motion is insufficient leading to stopping if the preload is small. Furthermore, a slight changing in the preload would make the robot walk sideways. If the preload in the left extensor digitorum longus increase, it will automatically steer toward the right direction; a decrease in the preload will lead the robot walking toward the left direction. Although this variation can change the walking pattern, the adjustable range is relatively small in which the stable walking should be performed. Too high or small preload in the extensor digitorum longus would lead to failure.

As there are not suitable sensors (e.g. position sensors for spherical joints) due to the

high complexity of the skeletal structures, the tracking of the robot dynamics is impossible. I cannot evaluate the performance of the robot because of the lack of quantified kinematic and kinetic data from experiment. These data can be easily measured in conventional robots using commercial sensors usually implemented in the joints and under the foot.

6.5 Functional Analysis

Functional analysis has been tested to demonstrate the potentials of using this robot platform to examine the underlying mechanisms of human agile movements, mainly for the internal functions of human MSK and its interactions with the environment. All the data were then low-pass filtered with a cut-off 10 Hz. Each test of different configurations was repeated ten times to allow selection of a representative gait trial with same initial conditions.

Humans navigate complex terrain in their daily lives. From natural trails to uneven sidewalks, humans often encounter surfaces that are not smooth. Terrain has many features that might affect locomotion, such as unevenness, damping and coefficient of friction. I have preliminarily investigated the effect of the terrain texture and friction on biped walking in section 3.2 and 3.3. The internal mechanics of human body varies with different individuals, for instance, the muscle properties, joint configurations and foot shape are not identical for different human subjects. However, all of them are able to perform stable walking. I try to explain how these factors affect biped locomotion in Section 3.4-3.6, particularly in walking.

6.5.1 Uneven terrain

To provide some insight into how terrain texture affects locomotion, I tested biped walking on different uneven terrains. Mean texture depth (MTD) is used as the index of unevenness, which is determined by the ASTM sand patch method that is applying and smoothing a known volume of sand or glass spheres to make a “pancake” on the terrain surface [289]. MTD is calculated by measuring the area of the pancake and dividing this area into the known volume [290, 291],

$$\text{MTD} = \frac{4 \cdot V}{\pi \cdot D^2} \quad (6.1)$$

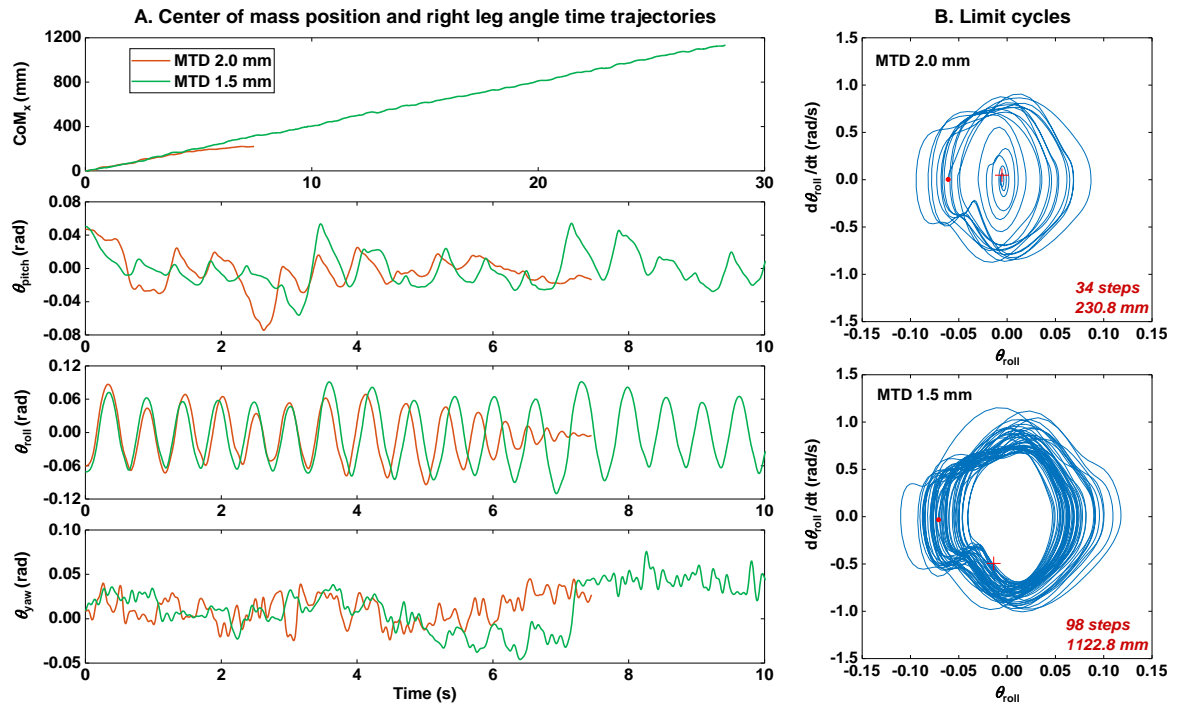


Figure 6.14 Robot walking experiments on 1.4-m-long uneven terrains of MTD 2.0 mm and 1.5 mm. (A) Centre of mass in the progression direction and right leg angle time trajectories in terms of pitch, roll and yaw motion. (B) State space plot of the limit cycles in the roll axis (frontal plane). Red dot is the initial conditions (0.06-0.07 rad and 0 rad/s) and plus sign is the end state.

where V is the volume of sand or glass spheres, and D is the average patch diameter.

The robot travelled the full length of the MTD-2.0-mm terrain but stopped on the MTD-1.5-mm terrain after few steps (Supplementary Video 5 and Figure 6.14A). When placed on MTD-1.5-mm terrain, the robot produces stably periodic trajectories of θ_{roll} at all times (Figure 6.14B). But on MTD-2.0-mm terrain, it generates inadequate walking cycles and converges to a stopping point (Figure 6.14). More distance travelled (1122.8 vs. 230.8 mm) and number of steps (98 vs. 34 steps) are achieved on the terrain of low unevenness (Figure 6.14) indicating that the robot cannot recover to steady state if too heavy external perturbations exists in the route. The results imply that the unevenness of the terrain severely affects the stability of biped walking.

6.5.2 Pavement friction

High friction surface made from polyvinyl chloride (PVC) and low friction surface made

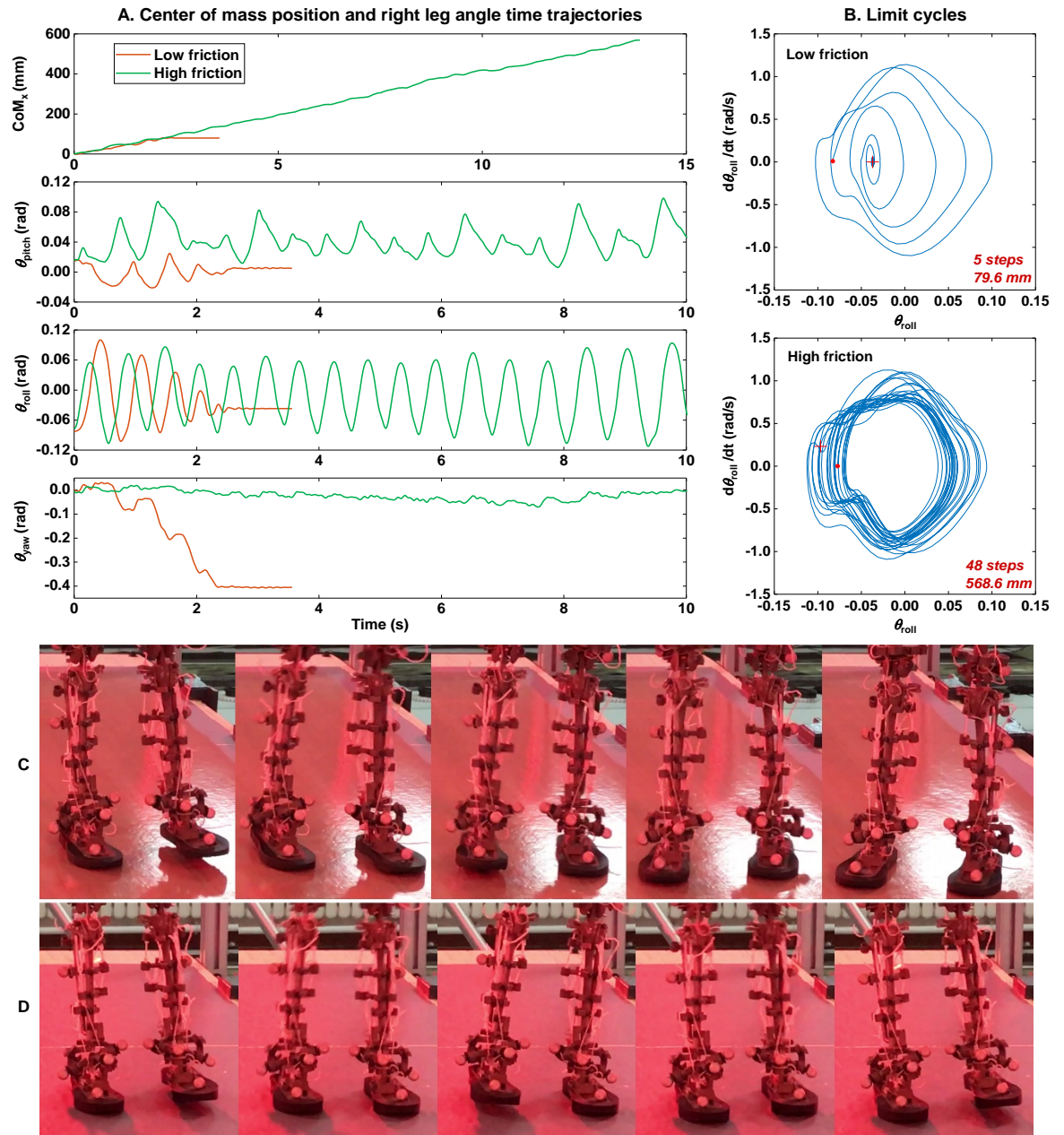


Figure 6.15 Robot walking experiments on low and high friction pavement. (A) Centre of mass in the progression direction and right leg angle time trajectories in terms of pitch, roll and yaw motion. (B) State space plot of the limit cycles in the roll axis (frontal plane). Red dot is the initial conditions (0.07-0.08 rad and 0 rad/s) and plus sign is the end state. Walking sequence on (C) low and (D) high friction pavement.

from Polytetrafluoroethylene (PTFE) were attached on the pavement to go into the effect of terrain friction on biped walking. The friction coefficient of the high friction surface is 0.4-0.5, much higher than the low friction surface of 0.05-0.1. The robot performed stable

walking after releasing on the high friction surface, however, it stopped on the low friction pavement after few steps (Supplementary Video 6 and Figure 6.15B). An intriguing movement observed in the test was that the robot turned sideways and slid on the low friction pavement (Figure 6.15C) due to insufficient propulsive and breaking force as well as high ground reaction torque, compared to walking straight on the high friction surface (Figure 6.15D). An intensely increasing yaw motion (up to 0.4 radians in 2.2 seconds) in the transverse plane occurs on the low friction surface, yet this motion on the high friction pavement remains stable in a small range of ± 0.05 rad (Figure 6.15A). It can be concluded that the pavement friction can alter the gait pattern of biped walking by transforming the contact conditions between the foot and the environment in terms of adhesive force and moment.

6.5.3 Muscle stiffness

To purvey some knowledge into how the muscle stiffness impacts biped locomotion, a soft (1.83 N/mm), a medium (3.66 N/mm) and a hard (4.58 N/mm) Gastrocnemius musculotendon unit were tested on the robot. The Soft-GAS robot fell forward after walking only 4 steps (Supplementary Video 7). The Hard-GAS robot travelled more steps than the Soft-Gas (Figure 6.16B), yet still ended in falling backward or sideways (Supplementary Video 7). There is a drastic growth in the pitch angle of walking with soft Gastrocnemius musculotendon unit, which increases up to 1 radian in 2 seconds (Figure 6.16A), leading to falling forward (Figure 6.16C). Following a series of relatively stable cycles before 4.5 s, the pitch angle of the test using hard Gastrocnemius unit starts to gradually decline (Figure 6.16A), resulting in falling backward (Figure 6.16D). In contrast, medium Gastrocnemius musculotendon unit allows the robot to walk stably, presenting quite small variations in the pitch motion (Figure 6.16A). Therefore, too high or too low stiffness of Gastrocnemius will induce failure during walking, especially in the sagittal plane, suggesting that proper muscle stiffness is rewarding for the propulsion of biped walking.

6.5.4 Joint axis

The axes of rotation of human ankle (talocrural and subtalar) are oblique to the ground in neutral position, i.e., standing upright. The robot ankle has been adjusted to different angles of rotating axes (parallel and oblique ankle) to understand the natural regulation of

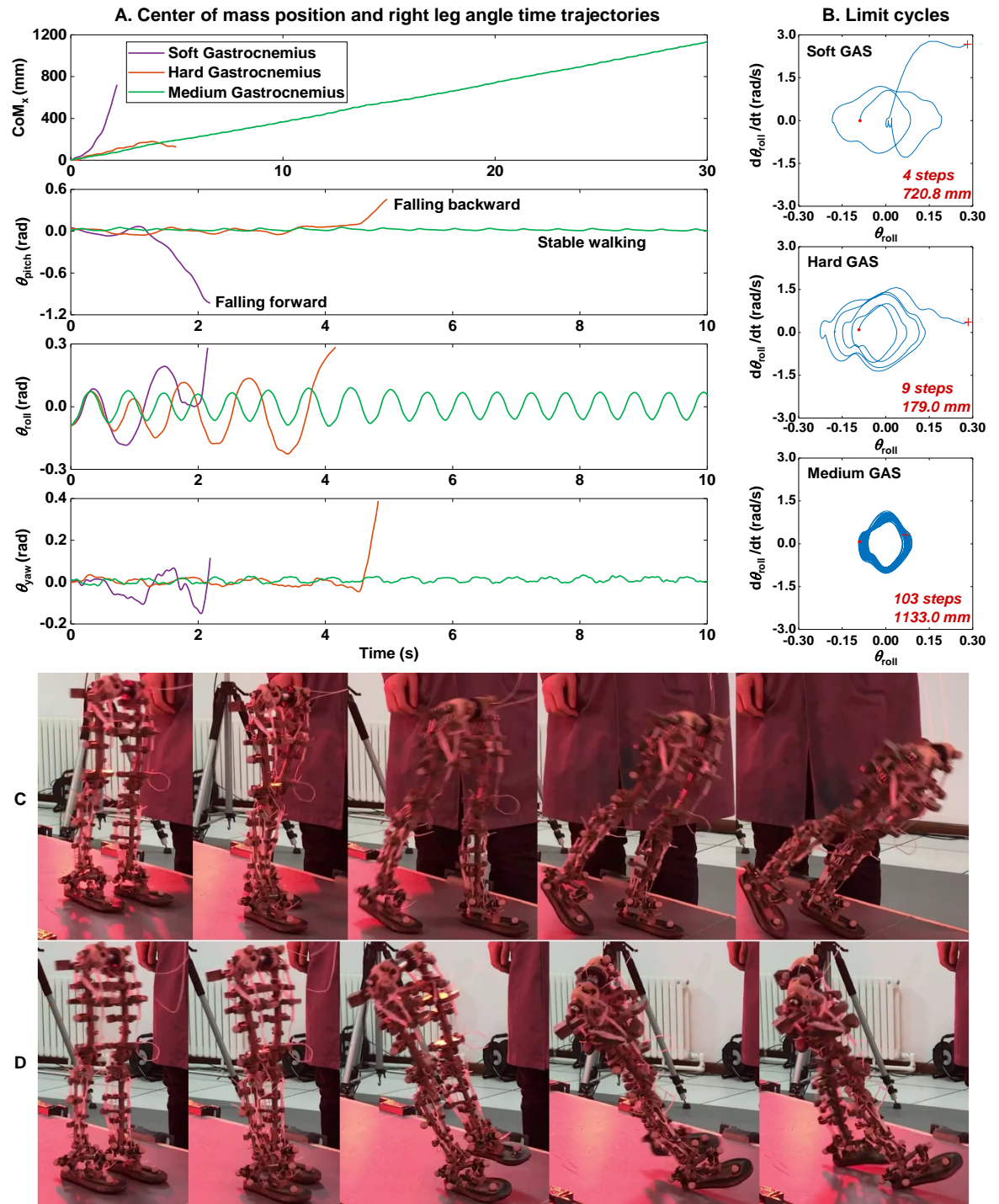


Figure 6.16 Robot walking experiments configured with three different Gastrocnemius (GAS) musculotendon units in terms of stiffness. (A) Centre of mass in the progression direction and right leg angle time trajectories in terms of pitch, roll and yaw motion. (B) State space plot of the limit cycles in the roll axis (frontal plane). Red dot is the initial conditions (0.08-0.09 rad and 0 rad/s) and plus sign is the end state. Sequence of (C) the Soft-GAS walking and (D) the Hard-GAS walking.

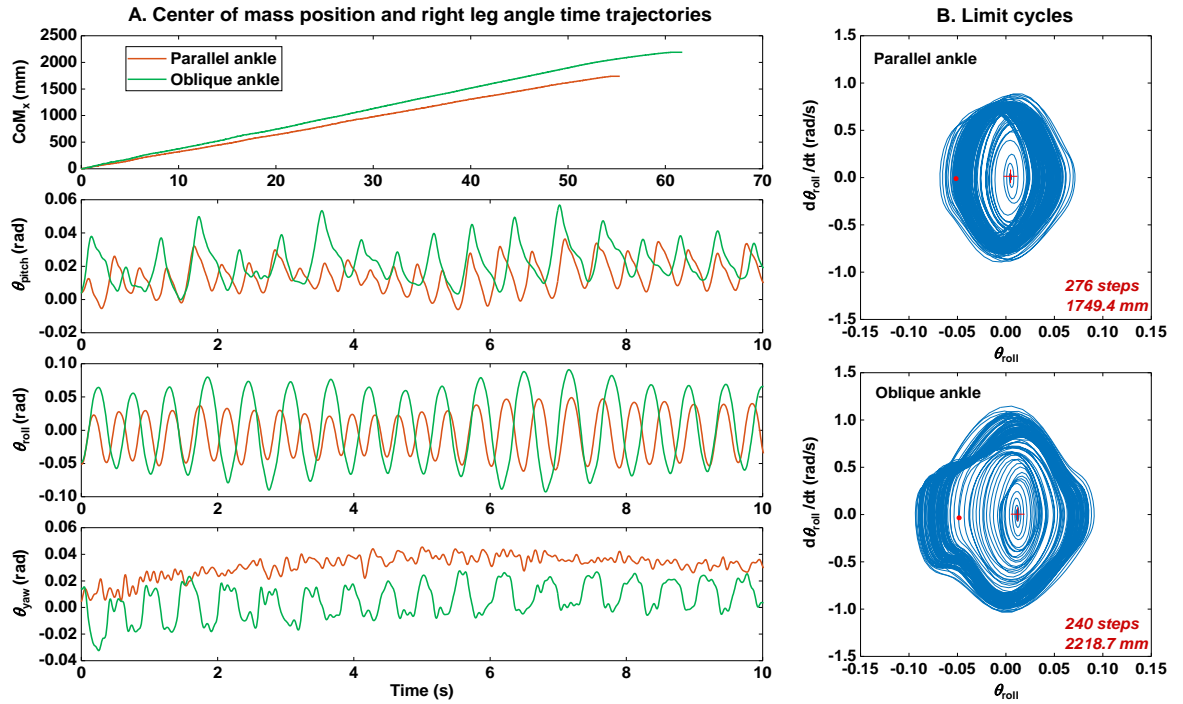


Figure 6.17 Robot walking experiments with parallel ankle and oblique ankle. (A) Centre of mass in the progression direction and right leg angle time trajectories in terms of pitch, roll and yaw motion. (B) State space plot of the limit cycles in the roll axis (frontal plane). Red dot is the initial conditions (about 0.05 rad and 0 rad/s) and plus sign is the end state.

ankle functions during walking motion. The parallel ankle is set to 0° in both the talocrural and subtalar joint, that is, the axes are paralleled to the ground when the robot is in neutral/upright position. They are changed to 18° talocrural angle and 21° subtalar angle in the oblique ankle. The robot configured with oblique ankle can travel more distance than parallel ankle, walking full length and about 3/4 of the ramp respectively (Supplementary Video 8), 2218.7 vs. 1749.4 mm (Figure 6.17A). Actually, the oblique ankle could prolong the walking gait if the ramp length is extended (Supplementary Video 8). The robot can achieve larger step length when setting with oblique ankle, travelling longer distance but fewer steps (Figure 6.17B). Furthermore, the range of the limit cycles in the roll axis at setting of oblique ankle is higher than that of parallel ankle (Figure 6.17B), leading to a larger basin of attraction [292] in this dimension.

The results in the physical test agree with the simulations in section 5.3. In both physical test and computer simulations in Adams, the robot with oblique angle in the ankle

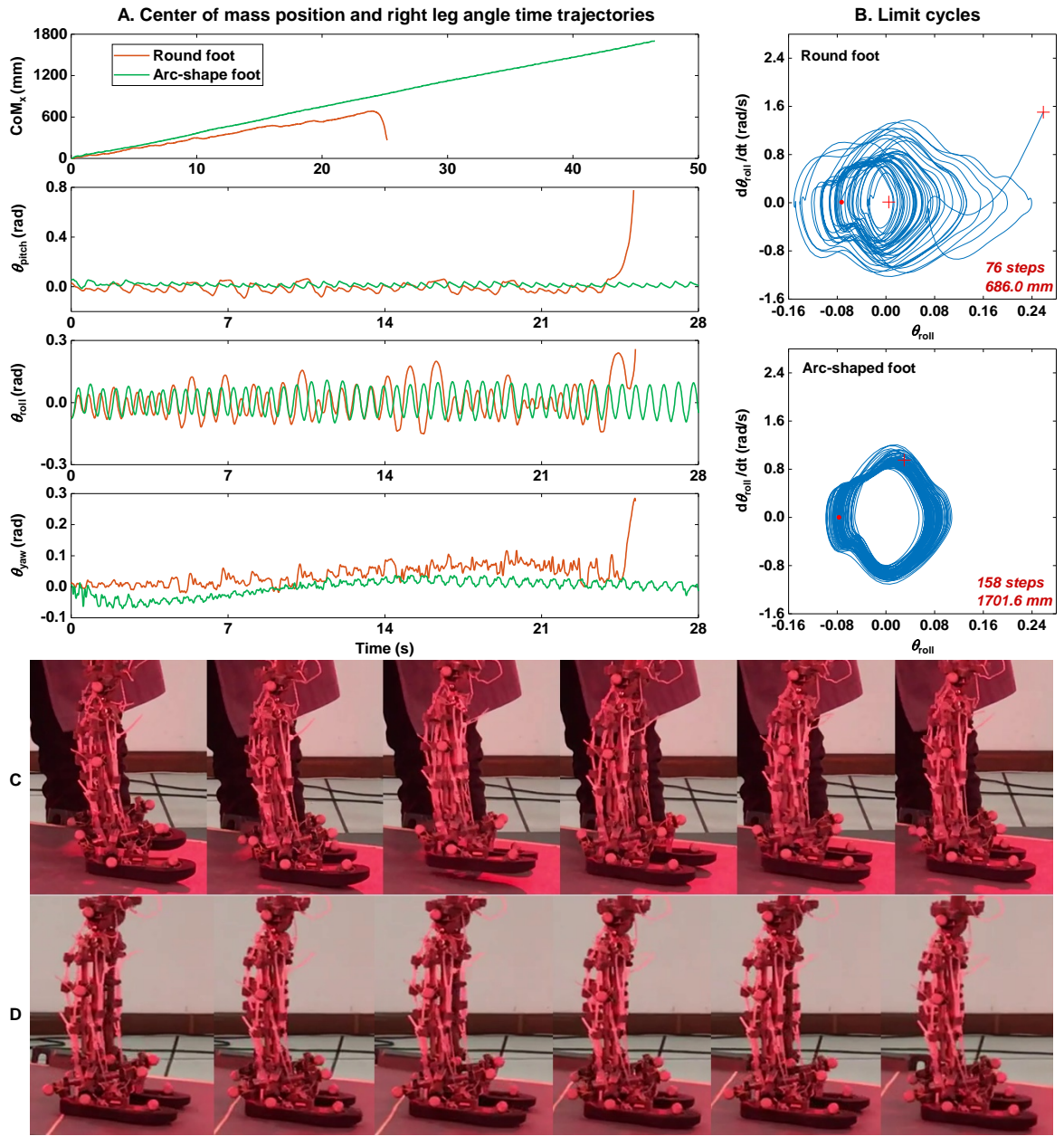


Figure 6.18 Robot walking experiments with arc-shaped foot and round foot. (A) Centre of mass in the progression direction and right leg angle time trajectories in terms of pitch, roll and yaw motion. (B) State space plot of the limit cycles in the roll axis (frontal plane). Red dot is the initial conditions (0.07-0.08 rad and 0 rad/s) and plus sign is the end state. (C) Hobbling sequence of round foot. (D) Normal walking of arc-shaped foot.

can travel more distance than the distance discovered when the ankle setting is 0° in the talocrural and subtalar angle. The results infer that the obliqueness of joint axis in the ankle is beneficial for the capacity of long-distance biped walking.

6.5.5 Foot shape

An arc-shaped and a round foot were 3D printed to exploit the influence of foot shape on biped walking. A hobbling gait that the right leg swung backward and forward alternately (Figure 6.18C and Supplementary Video 9) was found in the walking of setting with round foot, different from normal gait of arc-shaped foot that the leg always swung forward (Figure 6.18D). Although the round foot travelled 84 steps (Figure 6.18B), a falling backward failure occurred when the foot was not able to support dynamically stable walking (Supplementary Video 9). The variations of the periodic pitch angle at setting of round foot, from -0.006 to 0.015 rad, are much larger than that of arc-shaped foot, from -0.06 to 0.10 rad before falling (Figure 6.18A). The arc-shaped foot advantages the robot to walk longer distance (1337.6 vs. 623.1 mm) and more steps (122 vs. 84), as well as with greater stability (more stable limit cycles of roll motion), than the round foot (Figure 6.18B). The results suggest that the arc-shaped foot makes the robot walk more naturally and stably, and the longitudinal arch of foot can provide more economical biped locomotion (e.g., walking and running) in terms of energy.

6.6 Conclusion

This 3D printed bipedal robot can walk down a ramp in the physical test. I used trial, error, and correction process to adjust the coordination between the skeletal system, muscular system of the robot and the environment. Experimental installations for physical tests were explained. 3D motion capture system, Vicon, was used to measure the trajectories of the body and joint of the robot. Three Kistler force plates were arranged on the ground to record the GRFs during walking. A ramp in which the slope angle can be altered gradually was designed as the pavement for passive walking.

Preliminary tests were used to determine the best conditions for the robot. Launching procedure along other key factors affecting walking pattern was discussed. Successful initial conditions for a determined configuration of slope angle, muscle-tendon units, etc. may not work for a slightly different robot setting. Roll motion occurring in the stance leg is one of the most important factors for passive walking, in which the maximum roll angle should be controlled properly. There are several parameters that can lead the robot to failure (falling or stopping), such as the slope angle, the stiffness in the artificial muscle-tendon units, initial conditions and tolerance errors of the ramp.

Repeated tests were conducted on the ramp with a tilted angle of 6.75° . The axes of rotation in the ankle joint was set to 0° talocrural angle and 0° subtalar angle. The robot can perform stable passive walking in 100% of launches, i.e., 26 consecutive successful tests (see attached Supplementary Video 3). It walked the full length of a 2.44 m ramp in about 95% of launches, whereas inappropriate initial conditions, e.g., slope angle, released roll angle and released velocity, seem to be the primary cause of those launches in which the robot stopped or fell down before reaching the end of the ramp. Gait cycle and related biomechanical events were discussed in which the stance phase of robot walking is shorter than that of human walking. The ankle motion in one gait cycle has been studied, mainly for the rotation of the talocrural and subtalar joint. Unlike human walking, the motion at the subtalar joint is bigger than the talocrural joint as it provides foot clearance that is performed by knee flexion and extension in humans. The trajectories of the centre of mass in three directions during passive walking were obtained using Vicon motion capture system. Three-axis Ground reaction forces in one gait cycle were measured using the force plates. Besides, the material properties in the artificial muscle-tendon units are very sensitive for passive walking. The preload in the extensor digitorum longus muscle had a distinct impact on the success of walking. A slight change in the preload would make the robot walk sideways.

However, there are not quantified index for assessing the stability of 3D passive walkers (although 2D walkers have an index called Gait Sensitivity Norm [293, 294] to evaluate the stability). The common indicator for stable walking is whether it can perform human-like pattern motion, e.g., flexion of the knee if it has, swing of the arm if it has, coupled motion between the upper limbs and the lower limbs and tilted angle of the robot during walking [148]. In fact, the passive walking of the robot is in some way like the infants where the knee joint can be considered as being locked and the foot clearance is achieved by the roll motion of the stance.

The contributions to knowledge in this chapter include the following:

- Used a humanoid robot with the same biomechanical properties as the human subject to study human musculoskeletal biomechanics;
- Found that the unevenness of the terrain severely affects the stability of biped walking;
- Found that pavement friction can alter the gait pattern of biped walking by

transforming the contact conditions between the foot and the environment;

- Found that proper muscle stiffness is rewarding for the propulsion of biped walking;
- Found that the obliqueness of joint axis in the ankle is beneficial for the capacity of long-distance biped walking;
- Found that the longitudinal arc of the foot makes the robot walk more naturally and stably.

Chapter 7

Conclusions and Future Work

7.1 Conclusions

In this PhD project, a new approach of developing bipedal robot inspired from human musculoskeletal biomechanics was illustrated. Human musculoskeletal system provides a simplification of control during human motions and becomes an effective tool to improve the understanding of the underlying principles of human behaviour, however even the recent research in robotics does not completely take advantage of this kind of phenomenon.

Most current conventional robots imitated the human walking exclusively by computing the exact trajectory of each joint and controlling itself by sophisticated algorithm and actuators. Although other passive dynamic walking robots partly achieved human-like locomotion, they overlooked the significance of the mechanical properties and muscle arrangements to human movements.

Recently, some research teams have successfully developed a series of musculoskeletal robots. However, those robots only replicated parts of human MSK, either from an anthropometric point of view or neglecting the accuracy of muscle arrangement (e.g., insertion, origin, muscle path which affect moment arm during motion) and kinematic parameters (e.g., joint axis of rotation) especially for biped locomotion. For example, Asano et al [295] proposed a human mimetic humanoid with a high degree of anatomical fidelity to the human structure which was capable of whole-body motions, yet the muscle unit and the joint axis are still not human-like. Above all, none of those robots can perform stable walking which is of great concern to bipedal robots.

The above-mentioned robots share high similarity with human in terms of the shape of the skeletal structure and the arrangement of the muscle, and they can conduct desired

motions under various control methods. However, none of them can perform biped locomotion pattern which is of great concern for humanoid robot. This is because those robots are mainly focused on mimicking movements in the upper body of human body rather than the biped locomotion, and the biomechanics including kinematic (e.g., joint rotation axis) and kinetic (e.g., mechanics of the body segment) characteristics of the musculoskeletal system in lower limbs has not been explored thoroughly.

Thus, I developed a biped robot inspired from human musculoskeletal biomechanics, which replicates the whole body of human with some simplification in the upper body such as ribs. The mechanics of each skeletal part (e.g., mass distribution and moment of inertia) are almost same as human's and the kinematics of the key joints (e.g., joint centre and axis of rotation) are comparable to human's. The artificial muscular system is designed based on human musculoskeletal geometry, and each muscle-tendon unit share identical path with corresponding muscle volume of human. It acts on and equilibrates the skeletal part not only by itself but also combined with each other, e.g., the artificial muscle-tendon unit of Gastrocnemius and Soleus have been inserted to the foot by one Achilles's tendon. The robot can walk on a ramp without any control, only relying on the natural dynamics of the skeletal body and the balance of the artificial muscular system. This robot possesses the key features of anthropomimetic robot such as bones, muscles, tendons and joints, and could also achieve biped locomotion such as walking that is basic capacity for passive walker.

A 3D whole-body musculoskeletal model including the skin, skeleton and muscles of a healthy male was reconstructed from the Visible Human Project to examine the anatomy, structure and geometry of human MSK. Anthropometric data, key kinematic parameters and musculoskeletal geometry were measured and analysed to provide key design parameters for the bio-robot. The human body was considered as 14 segments including the head and neck, the upper, middle and lower (pelvis) trunk, two upper arms, two forearms, two thighs, two shanks and two feet. The joint centre of the rotating axis of 12 major anatomical joint (e.g., the ankle, knee, hip, shoulder and elbow, etc.) were obtained. In addition, the musculoskeletal geometries (including the insertion, origin and muscle path) for 68 main functional muscle groups including 6 in the head and neck, 20 in the trunk, 10 in two arms, 18 in two thighs and 14 in two shanks were carefully determined.

On the basis of biomechanical analysis of human body, the robot was designed and

assembled in NX software in which each body segment shares similar mechanics with humans. All joints used commercial plastic bearing to limit motion range. Angle adjusting mechanism was designed in the knee (7 levels from -5° to 25°) and ankle (5 levels from 0° to 36° in the talocrural joint and 7 levels from 0° to 42° in the subtalar joint) to study how the joint angle affects normal walking in the future. Then, the skeletal parts of the robot were scaled to half of the real human subject in dimensions and 3D printed using stainless steel. A whole-body muscular system was designed based on various artificial muscle-tendon units coiled from Nylon 6 monofilament fishing lines. The material property of the unit varies according to different diameter of the fibre and load in twist insertion.

A computational model was designed to simulate passive walking on the ramp in Adams. Parameters related to the simulation were defined including the joints, ground contact, artificial muscle and the variables which affects walking pattern. The model has been validated to achieve stable walking after launching with a determined initial condition. It could walk 3547.5 mm long. The position of the CoM and velocity were predicted during walking. The ankle motions mainly in the talocrural joint and subtalar joint were recorded and analysed. Roll motion in the subtalar joint is larger than human walking as it need to create foot clearance by tilting the robot laterally rather than knee bending. Ground reaction forces in a walking gait were measured. The general patterns in all three axes are comparable to humans, but the peak values are different, i.e., the peak values of main biomechanical events in GRFs during the robot walking are all higher than that in humans except the breaking peak. This might be caused by the different walking pattern of the robot that no knee flexion exists and the range of roll motion are much larger than humans. Spring forces in the anterior, posterior, medial and lateral position in the ankle were analysed. The fact that the forces in the anterior-posterior springs are much higher than that in the medial-lateral springs complies with humans where Tibialis Anterior, Soleus and Gastrocnemius muscles are much stronger than other muscles around the ankle. The *CoT* of the robot for passive walking was 0.21 compared to *CoT* 0.2 of human walking. The biped walking of the robot has the same energy efficiency as human walking.

The design of experiment was conducted by changing the angles of the talocrural (from 0° to 36°) and subtalar (from 0° to 42°) joint axis. Distance travelled and the ending status (falling or stopping) were recorded for all 1591 trials. The results showed that no stable walking can be performed by the robot for a subtalar angle of more than 29° or a

talocrural angle of more than 24° . The stable region in which the robot can travel more than 1100 mm on the ramp located in the narrow strip from the combination of 0° - 0° to 24° - 29° (the former is the talocrural angle and the latter is the subtalar angle). The distance travelled of stable passive walking firstly decreases to a valley with the increase of the stable angle. Then, an inverted “U” curve occurred between the distance travelled and the ankle angle until the edge of the stable region. The best configuration in the ankle is 16° talocrural angle and 23° subtalar angle, where the robot can travel on the ramp up to 4166.2 mm, 17.4 % longer than the distance travelled under the setting of 0° in the talocrural and subtalar angle (parallel to the ground when standing). The most stable regions for passive walking are 10° ~ 20° talocrural angles and 16° ~ 26° subtalar angles. It can be intuitive thinking that the oblique axis of rotation in the ankle may facilitate normal walking for biped robots.

This 3D printed bipedal robot can walk down a ramp in the physical test. Experimental installations including 3D motion capture system (Vicon) and three Kistler force plates were used to measure the kinematic and kinetic data of the body and joint in the robot. A ramp in which the slope angle can be altered gradually was designed as the pavement for passive walking. Preliminary tests were used to determine the best conditions for the robot. Launching procedure along other key factors affecting walking pattern was discussed. Successful initial conditions for a determined configuration of slope angle, muscle-tendon units, etc. may not work for a slightly different robot setting. Roll motion occurred in the stance leg is one of the most important factors for passive walking, in which the maximum roll angle should be controlled properly. There are several parameters that can lead the robot to failure (falling or stopping), such as the slope angle, the stiffness in the artificial muscle-tendon units, initial conditions and tolerance errors of the ramp. Teflon tapes and tubes were used as lubrication between the artificial muscle-tendon units and the 3D printed skeletal body of the robot.

Repeated tests were conducted on the ramp with a tilted angle of 6.75° . The axes of rotation in the ankle joint was set to 0° talocrural angle and 0° subtalar angle. The robot can perform stable passive walking in 100% of launches, i.e., 26 consecutive successful tests (see Supplementary Video 3). It walked the full length of a 2.44 m ramp in about 95% of launches, whereas inappropriate initial conditions, e.g., slope angle, released roll angle and released velocity, seem to be the primary cause of those launches in which the robot stopped or fell down before reaching the end of the ramp. The position of the CoM of the

robot during passive walking on the ramp were measured where the trajectories of CoM in the sagittal plane, especially along the Z axis, had certain fluctuation during walking. These oscillations were caused by the completely passive walking gait of the robot (roll motion of the stance leg and swing of the contralateral leg).

Gait cycle and related biomechanical events were discussed in which the stance phase of robot walking is shorter than that of human walking. The ankle motion in one gait cycle has been studied, mainly for the rotation of the talocrural and subtalar joint. Unlike human walking, the motion at the subtalar joint is bigger than the talocrural joint as it provides foot clearance that is performed by knee flexion and extension in humans. The walking sequence indicates that the robot is obviously not human-like in a number of ways. It is missing upper body parts, and the knees are locked with the legs. There are no toes in the feet, which cannot provide balance and thrust during walking. As power comes from gravity, there are no muscle contractions or torques to accelerate the swinging leg which affects the robot's motion. With all of these shortcomings, it is astonishing that the robot still walks so stably by today's robotics standards.

Ground reaction forces were measured during walking including the stance phase of both legs where the first half is the measurement of the right leg and the second half is that of the left leg. The swing phase of the leg was not recorded because the forces are indirectly measure from the combination of the ramp and three force plates. The first peak or valley in each component of the measured GRFs comes sooner than the simulation results or human gait measurements as the force in the late stance of the contralateral leg is also recorded at the beginning. For the vertical component, the passive peak of the right leg and the active peak of the left leg are integrated together. The valley value around 6 N/kg is similar as that in human walking, while the peak value above 9 N/kg is smaller than 12 N/kg in humans. The peak value of the lateral component is higher than humans, almost 2 N/kg versus -0.6 N/kg , caused by the larger roll motion of the robot. There is no positive value in the horizontal force, which suggests that the propulsion generated from the robot cannot be compared with humans. The push off of the foot does not exist in the passive walking which provides most of the propulsive force in human walking.

Besides, the material properties in the artificial muscle-tendon units are very sensitive for passive walking. The preload in the extensor digitorum longus muscle had a distinct impact on the success of walking. A slight change in the preload would make the robot

walk sideways.

However, there are not quantified index for assessing the stability of 3D passive walkers (although 2D walkers has an index called Gait Sensitivity Norm [293, 294] to evaluate the stability). The common indicator for stable walking is whether it can perform human-like pattern motion, e.g., flexion of the knee if it has, swing of the arm if it has, coupled motion between the upper limbs and the lower limbs and tilted angle of the robot during walking [148].

Most notably, this is the first study to our knowledge to develop a bipedal walking robot with the same musculoskeletal biomechanics (e.g., anthropometric data, key kinematic parameters and musculoskeletal geometry) as a real human subject replacing the mechanical structure and the muscular system. Image processing, reverse engineering, inverse dynamics, CAD, and 3D printing technique allow us to study, analyse and imitate the anatomy and characteristics from a specific person, not from generalized model or anatomy books which may lead to different or inaccurate mechanical properties and muscle arrangements.

Since understanding agile movements requires a systematic approach that explores the interaction of all involved components (the musculoskeletal system, the nervous system, and the environment), a more elaborate model that takes into account more aspects of the human neuro-musculo-skeletal system (e.g. with anthropopathic skeletal body structures, multiple muscles, and multi-layered neural control levels) is a key research aspect to make a contribution to human biology. It is important to choose the appropriate features and functional parts of human biology to replicate in the robot. As not all structures and features during human locomotion are dispensable for robot locomotion, only replicating the key relevant features to design a bio-inspired bipedal robot is required.

Concluding, I provide a new paradigm for developing bipedal robot which takes inspiration from human MSK and uses multidisciplinary knowledge along with advanced manufacturing technologies. Furthermore, this paradigm for developing bipedal robot can be also considered as a new approach to develop exoskeletons and prostheses based on human musculoskeletal system.

7.2 Future Work

In future, the 3D printed musculoskeletal robot can be used as a platform to examine

biological hypotheses and fundamental mechanical principles of the human body in fields such as biomechanics, physiology, rehabilitation science and engineering.

In this thesis, the successful walking of the physical test was only accomplished with the 0° talocrural angle and 0° subtalar angle in the ankle. Although the ankle function, particularly the angle of the rotating axis of the talocrural and subtalar joint, has been studied using simulation in Adams, the physical tests on the ramp with different ankle setups should be included in the future.

Further research of the walking performance on various uneven terrains with different mean texture depths (MTD) will be carried out to better investigate the ability of resisting disturbance during walking. As the kinematic and kinetic data can be measured using the motion capture system combined with the force plates, the benefits that the oblique rotating axis in the ankle joint may act on the walking performance could be observed and systematically analysed.

Another line of research is to study effect of other joints such as the knee or hip joint on the walking ability, where the ankle joint settings may have synergistic functions. Also, the upper body could be added to explore how the arm swing coordinates with the lower limbs during walking. In short, there are a number of areas that can be considered for future work.

The platform can be used in several new applications of human biological research that have not been considered previously. For example, human joint consists of complex surface profile, well-arranged ligaments and other soft tissues. The hard elements (e.g., bones) withstand expression and the soft tissues (e.g., ligaments) maintain tension when executing agile movements, which is the evolution of humans through natural selection in millions of years. The robot can be used to investigate the fundamental principle of this graceful mechanism by redesigning a bionic joint with same structure as the human subject and systematically changing the morphology in experiments. In addition, other clinical applications are also possible in such fields as sports science and rehabilitation. Many athletes or sports trainers suffer from chronic pain caused by tendinitis or severe injuries, e.g., rupture of Achilles tendon usually occurred in football or basketball players. If the robot can replicate complicated behaviours involving the skeletal and the muscular system, the analysis of corresponding muscle activities during motions will profit them a lot. Furthermore, the humanoid robot gives an alternative perspective to be used in testing

exoskeletons and prostheses.

Bibliography

- [1] B. Siciliano and O. Khatib, *Handbook of Robotics* (Handbook of Robotics). 2008, pp. 1-4.
- [2] C. Breazeal and B. Scassellati, "Robots that imitate humans," *Trends in Cognitive Sciences*, vol. 6, no. 11, pp. 481-487, Nov 2002.
- [3] B. Webb, "Can robots make good models of biological behaviour?," *Behavioral and brain sciences*, vol. 24, no. 06, pp. 1033-1050, 2001.
- [4] B. Webb, "Robots in invertebrate neuroscience," *Nature*, vol. 417, no. 6886, pp. 359-363, May 16 2002.
- [5] A. J. Ijspeert, "Biorobotics: using robots to emulate and investigate agile locomotion," *Science*, vol. 346, no. 6206, pp. 196-203, Oct 10 2014.
- [6] T. McGeer, "Passive dynamic walking," *International Journal of Robotics Research*, vol. 9, no. 2, pp. 62-82, 1990.
- [7] P. Manoonpong, T. Geng, T. Kulvicius, B. Porr, and F. Wörgötter, "Adaptive, Fast Walking in a Biped Robot under Neuronal Control and Learning," *PLoS Computational Biology*, vol. 3, no. 7, pp. 1305-1320, 2007.
- [8] M. F. Eilenberg, H. Geyer, and H. Herr, "Control of a Powered Ankle-Foot Prosthesis Based on a Neuromuscular Model," *IEEE Transactions on Neural Systems and Rehabilitation Engineering*, vol. 18, no. 2, pp. 164-173, Apr 2010.
- [9] H. M. Herr and A. M. Grabowski, "Bionic ankle-foot prosthesis normalises walking gait for persons with leg amputation," *Proceedings of the Royal Society B-Biological Sciences*, vol. 279, no. 1728, pp. 457-464, Feb 7 2012.
- [10] C. Azevedo, B. Espiau, B. Amblard, and C. Assaiante, "Bipedal locomotion: toward unified concepts in robotics and neuroscience," *Biological Cybernetics*, vol. 96, no. 2, pp. 209-228, Feb 2007.
- [11] P. B. Wieber, "On the stability of walking systems," in *Proceedings of the International Workshop on Humanoid and Human Friendly Robotics*, 2002.

- [12] P. B. Wieber, "Constrained dynamics and parametrized control in biped walking," in *Proceedings of the International Symposium on Mathematical Theory of networks and systems*, 2000.
- [13] C. A. B. A. B. Espiau and C. Assaïante, "A Synthesis of Bipedal Locomotion in Human and Robots," 2004.
- [14] M. Vukobratović and J. Stepanenko, "On the stability of anthropomorphic systems," *Mathematical Biosciences*, vol. 15, no. 1-2, pp. 1-37, 1972.
- [15] A. Goswami, "Postural stability of biped robots and the foot-rotation indicator (FRI) point," *International Journal of Robotics Research*, vol. 18, no. 6, pp. 523-533, Jun 1999.
- [16] A. J. Ijspeert, "Central pattern generators for locomotion control in animals and robots: A review," *Neural Networks*, vol. 21, no. 4, pp. 642-653, May 2008.
- [17] J. Morimoto, G. Cheng, C. G. Atkeson, and G. Zeglin, "A simple reinforcement learning algorithm for biped walking," in *Proceedings of the 2004 IEEE International Conference on Robotics and Automation*, 2004, vol. 1-5, pp. 3030-3035.
- [18] Q. Z. Zhang, C. M. Chew, Y. L. Zhou, Q. L. Zhao, and P. Li, "Iterative learning control for biped walking," in *Proceedings of the 2010 IEEE International Conference on Mechatronics and Automation (ICMA 2010)*, Xi'an, China, 2010, pp. 237-241.
- [19] M. Vukobratović and B. Borovac, "Zero-moment point—thirty five years of its life," *International Journal of Humanoid Robotics*, vol. 1, no. 01, pp. 157-173, 2004.
- [20] S. Kajita *et al.*, "Biped walking pattern generation by using preview control of zero-moment point," in *Proceedings of the 2003 IEEE International Conference on Robotics and Automation*, Taipei, Taiwan, 2003, vol. 1-3, pp. 1620-1626.
- [21] J. Strom, G. Slavov, and E. Chown, "Omnidirectional Walking Using ZMP and Preview Control for the NAO Humanoid Robot," in *Proceedings of the 2009 Robot Soccer World Cup XIII*, 2010, vol. 5949, pp. 378-389.
- [22] S. Kagami, T. Kitagawa, K. Nishiwaki, T. Sugihara, M. Inaba, and H. Inoue, "A fast dynamically equilibrated walking trajectory generation method of humanoid robot," *Autonomous Robots*, vol. 12, no. 1, pp. 71-82, Jan 2002.

- [23] D. G. Hobbelen, *Limit cycle walking*. TU Delft, Delft University of Technology, 2008.
- [24] A. Goswami and V. Kallem, "Rate of change of angular momentum and balance maintenance of biped robots," in *Proceedings of the 2004 IEEE International Conference on Robotics and Automation*, 2004, vol. 1-5, pp. 3785-3790.
- [25] M. B. Popovic, A. Goswami, and H. Herr, "Ground reference points in legged locomotion: Definitions, biological trajectories and control implications," *International Journal of Robotics Research*, vol. 24, no. 12, pp. 1013-1032, Dec 2005.
- [26] S. Kajita *et al.*, "Resolved momentum control: Humanoid motion planning based on the linear and angular momentum," in *Proceedings of the 2003 IEEE/RSJ International Conference on Intelligent Robots and Systems (IROS)*, 2003, vol. 1-4, pp. 1644-1650.
- [27] B. W. Verdaasdonk, *Towards efficient and robust control of bipedal walking: basic models of posture and rhythmic movement*. University of Twente, 2008.
- [28] G. Endo, J. Nakanishi, J. Morimoto, and G. Cheng, "Experimental studies of a neural oscillator for biped locomotion with QRIO," in *Proceedings of the 2005 IEEE International Conference on Robotics and Automation (ICRA)*, 2005, vol. 1-4, pp. 596-602.
- [29] S. H. Hyon, J. Morimoto, and M. Kawato, "From Compliant Balancing to Dynamic Walking on Humanoid Robot: Integration of CNS and CPG," in *Proceedings of the 2010 IEEE International Conference on Robotics and Automation (ICRA)*, 2010, pp. 1084-1085.
- [30] J. Nakanishi, J. Morimoto, G. Endo, G. Cheng, S. Schaal, and M. Kawato, "Learning from demonstration and adaptation of biped locomotion," *Robotics and Autonomous Systems*, vol. 47, no. 2-3, pp. 79-91, Jun 30 2004.
- [31] F. Faber and S. Behnke, "Stochastic Optimization of Bipedal Walking using Gyro Feedback and Phase Resetting," in *Proceedings of the 2007 7th IEEE-RAS International Conference on Humanoid Robots*, 2007, pp. 203-209.
- [32] S. Kajita and B. Espiau, "Legged robots," in *Springer handbook of robotics*: Springer, 2008, pp. 361-389.

- [33] F. Allgöwer, T. A. Badgwell, J. S. Qin, J. B. Rawlings, and S. J. Wright, "Nonlinear predictive control and moving horizon estimation—an introductory overview," in *Advances in control*: Springer, 1999, pp. 391-449.
- [34] C. Azevedo, P. Poignet, and B. Espiau, "Artificial locomotion control: from human to robots," *Robotics and Autonomous Systems*, vol. 47, no. 4, pp. 203-223, Jul 31 2004.
- [35] A. D. Kuo, "Energetics of actively powered locomotion using the simplest walking model," *Journal of Biomechanical Engineering*, vol. 124, no. 1, pp. 113-120, 2002.
- [36] D. Renjewski and A. Seyfarth, "Robots in human biomechanics- A study on ankle push-off in walking," *Bioinspiration and Biomimetics*, vol. 7, no. 3, 2012.
- [37] R. Blickhan and R. J. Full, "Similarity in Multilegged Locomotion - Bouncing Like a Monopode," *Journal of Comparative Physiology a-Sensory Neural and Behavioral Physiology*, vol. 173, no. 5, pp. 509-517, Nov 1993.
- [38] M. H. Raibert, *Legged robots that balance*. MIT press, 1986.
- [39] T. Geng, "Online Regulation of the Walking Speed of a Planar Limit Cycle Walker via Model Predictive Control," *IEEE Transactions on Industrial Electronics*, vol. 61, no. 5, pp. 2326-2333, May 2014.
- [40] D. G. E. Hobbelen and M. Wisse, "Active Lateral Foot Placement for 3d Stabilization of a Limit Cycle Walker Prototype," *International Journal of Humanoid Robotics*, vol. 6, no. 1, pp. 93-116, Mar 2009.
- [41] Humanoid Robotics Institute, Waseda University. (2000). *Development of waseda robot*. Available: <http://www.humanoid.waseda.ac.jp/booklet/katobook.html>
- [42] I. Kato and H. Tsuiki., "The hydraulically powered biped walking machine with a high carrying capacity," in *Proceedings of the 4th International Symposium on External Control of Human Extremities*, Dubrovnik, Yugoslavia, 1972, pp. 410-421.
- [43] I. Kato. (1973) Development of WABOT-I. *The University of Tokyo press*. 173-214.
- [44] H. O. Lim and A. Takanishi, "Biped walking robots created at Waseda University: WL and WABIAN family," *Philosophical Transactions of the Royal Society A: Mathematical, Physical and Engineering Sciences*, vol. 365, no. 1850, pp. 49-64, 2007.

- [45] Y. Ogura *et al.*, "Development of a new humanoid robot WABIAN-2," in *Proceedings of the 2006 IEEE International Conference on Robotics and Automation (ICRA)*, 2006, vol. 1-10, pp. 76-81.
- [46] Y. Sugahara *et al.*, "Walking up and down stairs carrying a human by a biped locomotor with parallel mechanism," in *Proceedings of the 2005 IEEE/RSJ International Conference on Intelligent Robots and Systems*, 2005, vol. 1-4, pp. 3425-3430.
- [47] K. Hirai, "Current and future perspective of Honda humanoid robot," in *Proceedings of the 1997 IEEE/RSJ International Conference on Intelligent Robots and Systems*, 1997, vol. 2, pp. 500-508.
- [48] M. Hirose and K. Ogawa, "Honda humanoid robots development," *Philosophical Transactions: Mathematical, Physical and Engineering Sciences*, vol. 365, no. 1850, pp. 11-9, Jan 15 2007.
- [49] K. Hirai, "The Honda humanoid robot: development and future perspective," *Industrial Robot*, vol. 26, no. 4, pp. 260-266, 1999.
- [50] Y. Sakagami, R. Watanabe, C. Aoyama, S. Matsunaga, N. Higaki, and K. Fujimura, "The intelligent ASIMO: System overview and integration," in *Proceedings of the 2002 IEEE/RSJ International Conference on Intelligent Robots and Systems*, EPFL, Lausanne, Switzerland, 2002, vol. 3, pp. 2478-2483.
- [51] Y. H. M. Hirose, T. Takenaka, K. Hirai, "Development of humanoid robot ASIMO," *Honda R&D Technical Review*, vol. 13, no. 1, pp. 1-6, 2001.
- [52] Honda. (2015). *ASIMO - The Honda Worldwide ASIMO Site*. Available: <http://world.honda.com/ASIMO/>
- [53] D. Levi Strauss, "Robot dreams (Honda creates Asimo, a humanoid prototype)," *Aperture*, no. 175, pp. 20-20, Sum 2004.
- [54] J. Chestnutt, M. Lau, G. Cheung, J. Kuffner, J. Hodgins, and T. Kanade, "Footstep planning for the Honda ASIMO humanoid," in *Proceedings of the 2005 IEEE International Conference on Robotics and Automation (ICRA)*, 2005, vol. 1-4, pp. 629-634.
- [55] B. Schaub, "Asimo learns how to jaywalk," *New Scientist*, vol. 193, no. 2590, pp. 24-24, Feb 10 2007.
- [56] J. Chestnutt, P. Michel, J. Kuffner, and T. Kanade, "Locomotion among dynamic obstacles for the Honda ASIMO," in *Proceedings of the 2007 IEEE/RSJ*

- International Conference on Intelligent Robots and Systems*, 2007, vol. 1-9, pp. 2578-2579.
- [57] V. Ng-Thow-Hing *et al.*, "The Memory Game: Creating a human-robot interactive scenario for ASIMO," in *Proceedings of the 2008 IEEE/RSJ International Conference on Robots and Intelligent Systems*, 2008, vol. 1-3, pp. 779-786.
- [58] S. Y. Okita, V. Ng-Thow-Hing, and R. Sarvadevabhatla, "Learning Together: ASIMO Developing an Interactive Learning Partnership with Children," in *Proceedings of the 18th IEEE International Symposium on Robot and Human Interactive Communication*, 2009, vol. 1-2, pp. 1023-1028.
- [59] H. Inoue and H. Hirukawa, "Explorations of humanoid robot applications," in *Proceedings of the IEEE-RAS International Conference on Humanoid Robots*, 2001.
- [60] Y. Nakamura *et al.*, "Humanoid robot simulator for the METI HRP Project," *Robotics and Autonomous Systems*, vol. 37, no. 2-3, pp. 101-114, Nov 30 2001.
- [61] K. Kaneko *et al.*, "Humanoid robot HRP-2," in *Proceedings of the 2004 IEEE International Conference on Robotics and Automation*, New Orleans, LA, USA, 2004, vol. 2004, pp. 1083-1090.
- [62] AIST. (2007). *Humanoid Robot HRP*. Available: <https://unit.aist.go.jp/is/humanoid/index.html>
- [63] AIST. (2006, 13 July). *Development of a humanoid robot based on technical transfer from AIST*. Available: <http://www.aist.go.jp/aist%20e/latest%20research/2006/20060713/20060713.html>
- [64] K. Yokoi, F. Kanehiro, K. Kaneko, K. Fujiwara, S. Kajita, and H. Hirukawa, "Experimental study of biped locomotion of humanoid robot HRP-1S," *Experimental Robotics VIII*, vol. 5, pp. 75-84, 2003.
- [65] K. Yokoi, F. Kanehiro, K. Kaneko, S. Kajita, K. Fujiwara, and H. Hirukawa, "Experimental study of humanoid robot HRP-1S," *International Journal of Robotics Research*, vol. 23, no. 4-5, pp. 351-362, Apr-May 2004.
- [66] H. Hirukawa *et al.*, "Humanoid robotics platforms developed in HRP," *Robotics and Autonomous Systems*, vol. 48, no. 4, pp. 165-175, Oct 31 2004.
- [67] K. Kaneko *et al.*, "Humanoid robot HRP-2," in *Proceedings of the 2004 IEEE International Conference on Robotics and Automation*, 2004, vol. 1-5, pp. 1083-1090.

- [68] B. Verrelst, O. Stasse, K. Yokoi, and B. Vanderborght, "Dynamically stepping over obstacles by the humanoid robot HRP-2," in *Proceedings of the 2006 6th IEEE-RAS International Conference on Humanoid Robots*, 2006, vol. 1-2, pp. 117-123.
- [69] S. Miossec, K. Yokoi, and A. Kheddar, "Development of a software for motion optimization of robots - Application to the kick motion of the HRP-2 robot," in *Proceedings of the 2006 IEEE International Conference on Robotics and Biomimetics*, 2006, vol. 1-3, pp. 299-304.
- [70] O. Stasse *et al.*, "Towards Autonomous Object Reconstruction for Visual Search by the Humanoid Robot HRP-2," in *Proceedings of the 2007 7th IEEE-RAS International Conference on Humanoid Robots*, 2007, pp. 151-158.
- [71] F. Kanehiro *et al.*, "Distributed control system of humanoid robots based on real-time ethernet," in *Proceedings of the 2006 IEEE/RSJ International Conference on Intelligent Robots and Systems*, 2006, vol. 1-12, pp. 2471-2477.
- [72] K. Akachi *et al.*, "Development of humanoid robot HRP-3P," in *Proceedings of the 2005 5th IEEE-RAS International Conference on Humanoid Robots*, 2005, pp. 50-55.
- [73] K. Kaneko, K. Harada, F. Kanehiro, G. Miyamori, and K. Akachi, "Humanoid Robot HRP-3," in *Proceedings of the 2008 IEEE/RSJ International Conference on Robots and Intelligent Systems*, 2008, vol. 1-3, pp. 2471-2478.
- [74] K. Kaneko *et al.*, "Humanoid Robot HRP-4-Humanoid Robotics Platform with Lightweight and Slim Body -," in *Proceedings of the 2011 IEEE/RSJ International Conference on Intelligent Robots and Systems*, 2011, pp. 4400-4407.
- [75] F. Dietz, S. Franken, K. Yoshida, H. Nakamura, J. Kappler, and V. Gieselmann, "The family of hepatoma-derived growth factor proteins: characterisation of a new member HRP-4 and classification of its subfamilies," *Biochemical Journal*, vol. 366, pp. 491-500, Sep 1 2002.
- [76] JSK Laboratory. (2001, 17 July). *Perception-Action Integrated Humanoid Robot : H6 & H7*. Available: http://www.jsk.t.u-tokyo.ac.jp/research/h6/H6_H7.html
- [77] K. Nishiwaki, T. Sugihara, S. Kagami, F. Kanehiro, M. Inaba, and H. Inoue, "Design and development of research platform for perception-action integration in humanoid robot: H6," in *Proceedings of 2000 the IEEE/RSJ International*

- Conference on Intelligent Robots and Systems (IROS 2000)*, 2000, vol. 1-3, pp. 1559-1564.
- [78] S. Kagami, K. Nishiwaki, T. Sugihara, J. J. Kuffner, M. Inaba, and H. Inoue, "Design and implementation of software research platform for humanoid robotics: H6," in *Proceedings of the 2001 IEEE International Conference on Robotics and Automation*, 2001, vol. I-IV, pp. 2431-2436.
- [79] S. Kagami, K. Nishiwaki, J. J. Kuffner, Y. Kuniyoshi, M. Inaba, and H. Inoue, "Online 3D vision, motion planning and bipedal locomotion control coupling system of humanoid robot: H7," in *Proceedings of the 2002 IEEE/RSJ International Conference on Intelligent Robots and Systems*, 2002, vol. 1-3, pp. 2557-2562.
- [80] K. Nishiwaki, S. Kagami, Y. Kuniyoshi, M. Inaba, and H. Inoue, "Online generation of humanoid walking motion based on a fast generation method of motion pattern that follows desired ZMP-H7," in *Proceedings of the 2002 IEEE/RSJ International Conference on Intelligent Robots and Systems*, EPFL, Lausanne, Switzerland, 2002, vol. 3, pp. 2684-2689.
- [81] S. Kagami *et al.*, "Measurement and comparison of humanoid H7 walking with human being," *Robotics and Autonomous Systems*, vol. 48, no. 4, pp. 177-187, 2004.
- [82] Toyota. (2003). *Toyota Robot Overview*. Available: http://www.toyota.co.jp/en/news/04/1203_1d.html
- [83] Y. Tsusaka and Y. Ota, "Wire-driven bipedal robot," in *Proceedings of the 2006 IEEE/RSJ International Conference on Intelligent Robots and Systems*, Beijing, China, 2006, vol. 1-12, pp. 3958-3963.
- [84] R. Tajima, D. Honda, and K. Suga, "Fast Running Experiments Involving a Humanoid Robot," in *Proceedings of the 2009 IEEE International Conference on Robotics and Automation (ICRA)*, Kobe, Japan, 2009, vol. 1-7, pp. 1418-1423.
- [85] R. Tajima and K. Suga, "Motion having a flight phase: Experiments involving a one-legged robot," in *Proceedings of the 2006 IEEE/RSJ International Conference on Intelligent Robots and Systems*, 2006, vol. 1-12, pp. 1726-1731.
- [86] I. W. Park, J. Y. Kim, J. G. Lee, and J. H. Oh, "Mechanical design of the humanoid robot platform, HUBO," *Advanced Robotics*, vol. 21, no. 11, pp. 1305-1322, Nov 2007.

- [87] J. H. Oh, D. Hanson, W. S. Kim, I. Y. Han, J. Y. Kim, and I. W. Park, "Design of android type humanoid robot Albert HUBO," in *Proceedings of the 2006 IEEE/RSJ International Conference on Intelligent Robots and Systems*, 2006, vol. 1-12, pp. 1428-1433.
- [88] K. Jung-Hoon, K. Jung-Yup, and O. Jun-Ho, "Weight-adaptive walking of the passenger-carrying biped robot, HUBO FX-1," in *Proceedings of the 2010 10th IEEE-RAS International Conference on Humanoid Robots*, 2010, pp. 33-39.
- [89] J. H. Kim, I. W. Park, and J. H. Oh, "Design of Lower Limbs for a Humanoid Biped Robot," *International Journal of Human friendly Welfare Robotic System*, vol. 2, no. 4, pp. 5-10, 2002.
- [90] J. H. Kim, S. W. Park, I. W. Park, and J. H. Oh, "Development of a Humanoid Biped Walking Robot Platform KHR-1—Initial Design and Its Performance Evaluation," in *Proceedings of the 3rd IARP International Workshop on Humanoid and Human Friendly Robotics*, Tsukuba, Japan, 2002, pp. 14-21.
- [91] I. W. Park, J. Y. Kim, S. W. Park, and J. H. Oh, "Development of humanoid robot platform KHR-2 (KAIST humanoid robot-2)," in *Proceedings of the 2004 4th IEEE/RAS International Conference on Humanoid Robots*, 2004, vol. 1-2, pp. 292-310.
- [92] I. W. Park, J. Y. Kim, J. Lee, and J. H. Oh, "Mechanical design of humanoid robot platform KHR-3 (KAIST humanoid robot-3 : HUBO)," in *Proceedings of the 2005 5th IEEE-RAS International Conference on Humanoid Robots*, 2005, pp. 321-326.
- [93] C. Baek-Kyu, P. Sang-Sin, and O. Jun-Ho, "Controllers for running in the humanoid robot, HUBO," in *Proceedings of the 9th IEEE-RAS International Conference on Humanoid Robots*, 2009, pp. 385-390.
- [94] S. Lohmeier, K. Löffler, M. Gienger, H. Ulbrich, and F. Pfeiffer, "Computer system and control of biped "Johnnie"," in *Proceedings of THE 2004 IEEE International Conference on Robotics and Automation*, New Orleans, LA, 2004, vol. 2004, pp. 4222-4227.
- [95] S. Lohmeier, T. Buschmann, and H. Ulbrich, "Humanoid Robot LOLA," in *Proceedings of the 2009 IEEE International Conference on Robotics and Automation (ICRA)*, Kobe, Japan, 2009, vol. 1-7, pp. 2516-2521.

- [96] F. Pfeiffer, K. Löffler, and M. Gienger, "The Concept of Jogging JOHNNIE," in *Proceedings of the IEEE International Conference on Robotics and Automation*, 2002, vol. 3, pp. 3129-3135.
- [97] K. Löffler, M. Gienger, and F. Pfeiffer, "Sensors and control concept of walking "Johnnie"," *International Journal of Robotics Research*, vol. 22, no. 3-4, pp. 229-239, 2003.
- [98] K. Löffler, M. Gienger, F. Pfeiffer, and H. Ulbrich, "Sensors and control concept of a biped robot," *IEEE Transactions on Industrial Electronics*, vol. 51, no. 5, pp. 972-980, 2004.
- [99] S. Lohmeier, T. Buschmann, H. Ulbrich, and F. Pfeiffer, "Modular joint design for performance enhanced humanoid robot LOLA," in *Proceedings of the 2006 IEEE International Conference on Robotics and Automation (ICRA)*, Orlando, Florida, USA, 2006, vol. 1-10, pp. 88-93.
- [100] H. Ulbrich, T. Buschmann, and S. Lohmeier, "Development of the humanoid robot LOLA," *Applied Mechanics and Materials*, vol. 5-6, pp. 529-540, 2006.
- [101] T. Buschmann, S. Lohmeier, and H. Ulbrich, "Humanoid robot Lola: Design and walking control," *Journal of Physiology-Paris*, vol. 103, no. 3-5, pp. 141-148, May-Sep 2009.
- [102] T. Buschmann, S. Lohmeier, and H. Ulbrich, "Design and Control of the Humanoid Walking Robot Lola," *At-Automatisierungstechnik*, vol. 58, no. 11, pp. 613-621, 2010.
- [103] V. Favot, M. Schwienbacher, T. Buschmann, S. Lohmeier, and H. Ulbrich, "The Humanoid Robot LOLA - Experimental Results," *Numerical Analysis and Applied Mathematics, Vols I-Iii*, vol. 1281, pp. 398-401, 2010.
- [104] C. Chevallereau *et al.*, "RABBIT: A testbed for advanced control theory," *IEEE Control Systems Magazine*, vol. 23, no. 5, pp. 57-79, Oct 2003.
- [105] K. Sreenath, H. W. Park, I. Poulakakis, and J. W. Grizzle, "A Compliant Hybrid Zero Dynamics Controller for Stable, Efficient and Fast Bipedal Walking on MABEL," *International Journal of Robotics Research*, vol. 30, no. 9, pp. 1170-1193, Aug 2011.
- [106] J. W. Grizzle, J. Hurst, B. Morris, H. W. Park, and K. Sreenath, "MABEL, A New Robotic Bipedal Walker and Runner," in *Proceedings of the 2009 American*

- Control Conference*, Hyatt Regency Riverfront, St. Louis, MO, USA, 2009, vol. 1-9, pp. 2030-2036.
- [107] Z. Q. Peng, Q. Huang, X. J. Zhao, T. Xiao, and K. J. Li, "Online trajectory generation based on off-line trajectory for biped humanoid," in *Proceedings of the 2004 IEEE International Conference on Robotics and Biomimetics (ROBIO)*, Shenyang, China, 2004, pp. 752-756.
- [108] T. Xiao, Q. Huang, J. X. Li, W. M. Zhang, and K. J. Li, "Trajectory calculation and gait change on-line for humanoid teleoperation," in *Proceedings of the IEEE International Conference on Mechatronics and Automation (ICMA)*, Luoyang, China, 2006, vol. 1-3, pp. 1614-1619.
- [109] J. Hofschulte, M. Seebode, and W. Gerth, "Parallel manipulator hip joint for a bipedal robot," *Climbing and Walking Robots*, pp. 601-609, 2005.
- [110] C. Azevedo, N. Andreff, and S. Arias, "Bipedal walking: from gait design to experimental analysis," *Mechatronics*, vol. 14, no. 6, pp. 639-665, Jul 2004.
- [111] M. Arbulú, D. Kaynov, L. Cabas, and C. Balaguer, "The Rh-1 full-size humanoid robot: Design, walking pattern generation and control," *Applied Bionics and Biomechanics*, vol. 6, no. 3-4, pp. 301-344, 2009.
- [112] G. A. Pratt, "Legged robots at MIT: What's new since Raibert," *IEEE Robotics & Automation Magazine*, vol. 7, no. 3, pp. 15-19, Sep 2000.
- [113] H. W. Park, K. Sreenath, J. W. Hurst, and J. W. Grizzle, "Identification of a Bipedal Robot with a Compliant Drivetrain," *IEEE Control Systems Magazine*, vol. 31, no. 2, pp. 63-88, Apr 2011.
- [114] L. Zhang, Q. Huang, Q. S. Liu, T. Liu, D. G. Li, and Y. P. Lu, "A Teleoperation System for a Humanoid Robot with Multiple Information Feedback and Operational Modes," in *Proceedings of the IEEE International Conference on Robotics and Biomimetics (ROBIO)*, Hong Kong, China, 2005, pp. 290-294.
- [115] L. A. Stankevich, "Intellectual robots in Russia: experience of development and RoboCup participation," presented at the Proceedings of the 9th Conference Speech and Computer, Saint-Petersburg, Russia, 20th - 22th September 2004, 2004.
- [116] R. Caballero, M. Armada, and P. Alarcon, "Development and experimental evaluation of sensorial system for SILO-2 biped robot," in *Proceedings of the 2006*

- International Conference of Climbing and Walking Robots (CLAWAR 2006)*, 2006, pp. 386-395.
- [117] J. Pratt, C. M. Chew, A. Torres, P. Dilworth, and G. Pratt, "Virtual model control: an intuitive approach for bipedal locomotion-Spring Flamingo," *International Journal of Robotics Research*, vol. 20, no. 2, pp. 129-143, 2001.
- [118] Y. Kuroki, "A small biped entertainment robot- SONY SDR-3X," in *Proceedings of the 2001 International Symposium on Micromechatronics and Human Science (MHS 2001)*, 2001, pp. 3-4.
- [119] T. Ishida, "A small biped entertainment robot SDR-4X II," in *Proceedings of the 2003 IEEE International Symposium on Computational Intelligence in Robotics and Automation*, Kobe, Japan, 2003, vol. 3, pp. 1046-1051 vol.3.
- [120] M. Fujita, Y. Kuroki, T. Ishida, and T. T. Doi, "A small humanoid robot SDR-4X for entertainment applications," in *Proceedings of the 2003 IEEE/ASME International Conference on Advanced Intelligent Mechatronics*, Kobe, Japan, 2003, vol. 2, pp. 938-943 vol.2.
- [121] T. Ishida, Y. Kuroki, and J. Yamaguchi, "Development of mechanical system for a small biped entertainment robot," in *Proceedings of the 12th IEEE International Workshop on Robot and Human Interactive Communication*, 2003, pp. 297-302.
- [122] T. Ishida, Y. Kuroki, and J. Yamaguchi, "Mechanical system of a small biped entertainment robot," in *Proceedings of the 2003 IEEE/RSJ International Conference on Intelligent Robots and Systems (IROS)*, Las Vegas, Nevada, 2003, vol. 2, pp. 1129-1134.
- [123] Y. Kuroki *et al.*, "Motion creating system for a small biped entertainment robot," in *Proceedings of the 2003 IEEE/RSJ International Conference on Intelligent Robots and Systems (IROS)*, Las Vegas, Nevada, USA, 2003, vol. 2, pp. 1394-1399.
- [124] Sony. (2000, 21 November). *Sony Develops Small Biped Entertainment Robot*. Available: http://www.sony.net/SonyInfo/News/Press_Archive/200011/00-057E2/
- [125] D. Gouaillier *et al.*, "Mechatronic design of NAO humanoid," in *Proceedings of the 2009 IEEE International Conference on Robotics and Automation*, Kobe, Japan, 2009, vol. 1-7, pp. 2124-2129.

- [126] F. Wang, Y. N. Wang, S. G. Wen, and S. Y. Zhao, "Nao Humanoid Robot Gait Planning Based on the Linear Inverted Pendulum," in *Proceedings of the 2012 24th Chinese Control and Decision Conference (CCDC)*, 2012, pp. 986-990.
- [127] C. Y. Wei, J. C. Xu, C. Wang, P. Wiggers, and K. Hindriks, "An Approach to Navigation for the Humanoid Robot Nao in Domestic Environments," *Towards Autonomous Robotic Systems*, vol. 8069, pp. 298-310, 2014.
- [128] S. H. Wen, K. M. Othman, A. B. Rad, Y. X. Zhang, and Y. S. Zhao, "Indoor SLAM Using Laser and Camera with Closed-Loop Controller for NAO Humanoid Robot," *Abstract and Applied Analysis*, 2014.
- [129] T. Deutsch, C. Muchitsch, H. Zeilinger, M. Bader, M. Vincze, and R. Lang, "Cognitive Decision Unit Applied to Autonomous Biped Robot NAO," in *Proceedings of the 2011 9th IEEE International Conference on Industrial Informatics (INDIN)*, 2011.
- [130] S. Kajita *et al.*, "Cybernetic human HRP-4C: A humanoid robot with human-like proportions," in *14th International Symposium of Robotic Research, ISRR 2009* vol. 70, ed. Lucerne, 2011, pp. 301-314.
- [131] M. S. Erden, "Emotional Postures for the Humanoid-Robot Nao," *International Journal of Social Robotics*, vol. 5, no. 4, pp. 441-456, Nov 2013.
- [132] K. Kaneko, F. Kanehiro, M. Morisawa, K. Miura, S. Nakaoka, and S. Kajita, "Cybernetic human HRP-4C," in *Proceedings of the 9th IEEE-RAS International Conference on Humanoid Robots (Humanoids 2009)*, Paris, France, 2009, pp. 7-14.
- [133] K. Kaneko *et al.*, "Hardware Improvement of Cybernetic Human HRP-4C for Entertainment Use," in *Proceedings of the 2011 IEEE/RSJ International Conference on Intelligent Robots and Systems*, 2011, pp. 4392-4399.
- [134] K. Miura, F. Kanehiro, K. Kaneko, S. Kajita, and K. Yokoi, "Quick Slip-Turn of HRP-4C on its Toes," in *Proceedings of the 2012 IEEE International Conference on Robotics and Automation (ICRA)*, 2012, pp. 3527-3528.
- [135] Boston Dynamics. (2011). *PETMAN - An Anthropomorphic Robot* Available: http://www.bostondynamics.com/robot_petman.html
- [136] Boston Dynamics. (2013). *Atlas - The Agile Anthropomorphic Robot*. Available: http://www.bostondynamics.com/robot_Atlas.html
- [137] Committee on Full-System Testing and Evaluation of Personal Protection Equipment Ensembles in Simulated Chemical-Warfare Environments, National

- Research Council (U.S.), *Soldier Protective Clothing and Equipment: Feasibility of Chemical Testing Using a Fully Articulated Robotic Mannequin*. Washington D.C., 2008.
- [138] PAL Robotics. (2014). *REEM-C: Robotics Research*. Available: <http://www.pal-robotics.com/en/products/reem-c/>
- [139] J. H. Kim and J. H. Oh, "Realization of dynamic walking for the humanoid robot platform KHR-1," *Advanced Robotics*, vol. 18, no. 7, pp. 749-768, 2004.
- [140] D. Grunberg, R. Ellenberg, Y. E. Kim, and P. Y. Oh, *From RoboNova to HUBO: Platforms for Robot Dance* (Progress in Robotics). 2009, pp. 19-24.
- [141] J. Shan and F. Nagashima, "Neural locomotion controller design and implementation for humanoid robot HOAP-1," in *Proceedings of the 20th Annual Conference of the Robotics Society of Japan*, Osaka, Japan, 2002.
- [142] R. Zaier and F. Nagashima, "Motion Generation of Humanoid Robot based on Polynomials Generated by Recurrent Neural Network," in *Proceedings of the the First Asia International Symposium on Mechatronics (AISM 2004)*, Xi'an, China, 2004, pp. 659-664.
- [143] T. Tawara *et al.*, "Morph: A desktop-class humanoid capable of acrobatic behavior," *International Journal of Robotics Research*, vol. 23, no. 10-11, pp. 1097-1103, Oct-Nov 2004.
- [144] Y. Okumura *et al.*, "morph3: a compact-size humanoid robot system capable of acrobatic behavior," *Advanced Robotics*, vol. 18, no. 7, pp. 699-710, 2004.
- [145] F. Yamasaki, T. Matsui, T. Miyashita, and H. Kitano, "PINO The humanoid that walk," in *Proceedings of the First IEEE-RAS International Conference on Humanoid Robots*, 2000.
- [146] F. Yamasaki, T. Matsui, T. Miyashita, and H. Kitano, *Pino the humanoid: A basic architecture* (Proceedings of the 2000 Robot Soccer World Cup IV). Springer, 2001, pp. 269-278.
- [147] J. D. Boyling, "The Biomechanics and Motor Control of Human Gait - Winter, Da," *Ergonomics*, vol. 32, no. 4, pp. 453-453, Apr 1989.
- [148] S. Collins, A. Ruina, R. Tedrake, and M. Wisse, "Efficient bipedal robots based on passive-dynamic walkers," *Science*, vol. 307, no. 5712, pp. 1082-1085, Feb 18 2005.

- [149] T. McGeer, "Passive Dynamic Walking," *The International Journal of Robotics Research*, vol. 9, no. 2, pp. 62-82, 1990.
- [150] T. McGeer, "Passive walking with knees," in *Proceedings of the 1990 IEEE International Conference on Robotics and Automation*, 1990, pp. 1640-1645 vol.3.
- [151] I. A. Johnston, "Muscles, Reflexes, and Locomotion - McMahon,T," *Science*, vol. 226, no. 4680, pp. 1308-1308, 1984.
- [152] Y. Ikemata, A. Sano, and H. Fujimoto, "A physical principle of gait generation and its stabilization derived from mechanism of fixed point," in *Proceedings of the 2006 IEEE International Conference on Robotics and Automation (ICRA)*, Orlando, Florida, USA, 2006, vol. 1-10, pp. 836-841.
- [153] R. Tedrake, T. W. Zhang, M. F. Fong, and H. S. Seung, "Actuating a simple 3D passive dynamic walker," in *Proceedings of the 2004 IEEE International Conference on Robotics and Automation*, New Orleans, LA, USA, 2004, vol. 1-5, pp. 4656-4661.
- [154] S. H. Collins, M. Wisse, and A. Ruina, "A three-dimensional passive-dynamic walking robot with two legs and knees," *International Journal of Robotics Research*, vol. 20, no. 7, pp. 607-615, Jul 2001.
- [155] T. Narukawa, K. Yokoyama, M. Takahashi, and K. Yoshida, "Design and Construction of a Simple 3D Straight-Legged Passive Walker with Flat Feet and Ankle Springs," *Journal of System Design and Dynamics*, vol. 3, no. 1, pp. 1-12, 2009.
- [156] T. Narukawa, K. Yoshida, K. Yokoyama, and M. Takahashi, *An experimental study of three-dimensional passive dynamic walking with flat feet and ankle springs*. INTECH Open Access Publisher, 2010.
- [157] T. Narukawa, K. Yokoyama, M. Takahashi, and K. Yoshida, "A Simple 3D Straight-Legged Passive Walker with Flat Feet and Ankle Springs," in *Proceedings of the 2008 IEEE/RSJ International Conference on Robots and Intelligent Systems*, Nice, France, 2008, vol. 1-3, pp. 2952-2957.
- [158] Delft Biorobotics Laboratory. (2015). *Bipedal walking and running robots*. Available: <http://www.3me.tudelft.nl/en/about-the-faculty/departments/biomechanical-engineering/research/dbl-delft-biorobotics-lab/bipedal-robots/>

- [159] R. Q. van der Linde, "Passive bipedal walking with phasic muscle contraction," *Biological Cybernetics*, vol. 81, no. 3, pp. 227-237, Sep 1999.
- [160] R. Q. van der Linde, "Design, analysis, and control of a low power joint for walking robots, by phasic activation of McKibben muscles (vol 15, pg 599, 1999)," *IEEE Transactions on Robotics and Automation*, vol. 15, no. 6, pp. 1145-1145, Dec 1999.
- [161] M. Wisse and R. Q. Van der Linde, *Delft pneumatic bipeds*. Springer Science & Business Media, 2007.
- [162] M. Wisse, A. L. Schwab, R. Q. van der Linde, and F. C. T. van der Helm, "How to keep from falling forward: Elementary swing leg action for passive dynamic walkers," *IEEE Transactions on Robotics*, vol. 21, no. 3, pp. 393-401, Jun 2005.
- [163] M. Wisse and J. van Frankenhuyzen, "Design and construction of MIKE; A 2-D autonomous biped based on passive dynamic walking," *Adaptive Motion of Animals and Machines*, pp. 143-154, 2006.
- [164] M. Wisse, A. L. Schwab, and F. C. T. van der Helm, "Passive dynamic walking model with upper body," *Robotica*, vol. 22, pp. 681-688, Nov-Dec 2004.
- [165] M. Wisse, D. G. E. Hobbelen, and A. L. Schwab, "Adding an upper body to passive dynamic walking robots by means of a bisecting hip mechanism," *IEEE Transactions on Robotics*, vol. 23, no. 1, pp. 112-123, Feb 2007.
- [166] M. Wisse, "Essentials of dynamic walking-Analysis and design of two-legged robots," PhD, Delft University of Technology, 2004.
- [167] M. Wisse, "Three additions to passive dynamic walking; actuation, an upper body, and 3D stability," in *Proceedings of the 2004 4th IEEE/RAS International Conference on Humanoid Robots*, 2004, vol. 1-2, pp. 113-132.
- [168] M. Wisse and A. L. Schwab, "Skateboards, bicycles, and three-dimensional biped walking machines: Velocity-dependent stability by means of lean-to-yaw coupling," *International Journal of Robotics Research*, vol. 24, no. 6, pp. 417-429, Jun 2005.
- [169] M. Wisse, G. Feliksdal, J. Van Frankenhuyzen, and B. Moyer, "Passive-Based Walking Robot," *Robotics & Automation Magazine, IEEE*, vol. 14, no. 2, pp. 52-62, 2007.

- [170] S. H. Collins and A. Ruina, "A Bipedal Walking Robot with Efficient and Human-Like Gait," in *Proceedings of the 2005 IEEE International Conference on Robotics and Automation*, Barcelona, Spain, 2005, pp. 1983-1988.
- [171] T. W. Z. Russ Tedrake, H Sebastian Seung, "Learning to walk in 20 minutes," *Yale University*, 2005.
- [172] R. L. Tedrake, "Applied Optimal Control for Dynamically Stable Legged Locomotion-Toddler," PhD, Massachusetts Institute of Technology, 2004.
- [173] J. D. Karssen, "Design and construction of the Cornell Ranger, a world record distance walking robot," *Internship Final Report*, 2007.
- [174] P. A. Bhounsule, J. Cortell, and A. Ruina, "Design and control of Ranger: an energy-efficient, dynamic walking robot," in *Proceedings of the 15th International Conference on Climbing and Walking Robots and the Support Technologies for Mobile Machines*, 2012, pp. 441-448.
- [175] P. A. Bhounsule, "A controller design framework for bipedal robots: trajectory optimization and event-based stabilization," PhD Thesis, Cornell University, 2012.
- [176] P. A. Bhounsule *et al.*, "Low-bandwidth reflex-based control for lower power walking: 65 km on a single battery charge," *The International Journal of Robotics Research*, vol. 33, no. 10, pp. 1305-1321, 2014.
- [177] B. Verrelst, R. Van Ham, B. Vanderborght, F. Daerden, D. Lefeber, and J. Vermeulen, "The pneumatic biped "Lucy" actuated with pleated pneumatic artificial muscles," *Autonomous Robots*, vol. 18, no. 2, pp. 201-213, Mar 2005.
- [178] B. Verrelst, B. Vanderborght, J. Vermeulen, R. Van Ham, J. Naudet, and D. Lefeber, "Control architecture for the pneumatically actuated dynamic walking biped "Lucy"," *Mechatronics*, vol. 15, no. 6, pp. 703-729, Jul 2005.
- [179] B. Vanderborght, B. Verrelst, R. Van Ham, and D. Lefeber, "Controlling a bipedal walking robot actuated by pleated pneumatic artificial muscles," *Robotica*, vol. 24, pp. 401-410, Jul-Aug 2006.
- [180] B. Vanderborght, *Dynamic stabilisation of the biped Lucy powered by actuators with controllable stiffness*. Springer Science & Business Media, 2010.
- [181] B. Verrelst *et al.*, "Motion generation and control for the pneumatic biped "lucy"," *International Journal of Humanoid Robotics*, vol. 3, no. 1, pp. 67-103, Mar 2006.

- [182] J. Vermeulen, B. Verrelst, D. Lefeber, P. Kool, and B. Vanderborght, "A real-time joint trajectory planner for dynamic walking bipeds in the sagittal plane," *Robotica*, vol. 23, pp. 669-680, Nov-Dec 2005.
- [183] J. Vermeulen, B. Verrelst, B. Vanderborght, D. Lefeber, and P. Guillaume, "Trajectory planning for the walking biped "Lucy"," *International Journal of Robotics Research*, vol. 25, no. 9, pp. 867-887, Sep 2006.
- [184] J. Vermeulen, D. Lefeber, B. Verrelst, and B. Vanderborght, "Trajectory planning for the walking biped "Lucy"," *Climbing and Walking Robots*, pp. 665-676, 2005.
- [185] B. Vanderborght, B. Verrelst, R. Van Ham, M. Van Damme, B. M. Y. Duran, and P. Beyl, "Exploiting natural dynamics to reduce energy consumption by controlling the compliance of soft actuators," *International Journal of Robotics Research*, vol. 25, no. 4, pp. 343-358, Apr 2006.
- [186] Y. Nakanishi *et al.*, "Design Approach of Biologically-Inspired Musculoskeletal Humanoids Invited Paper," *International Journal of Advanced Robotic Systems*, vol. 10, Apr 2013.
- [187] Y. Asano, K. Okada, and M. Inaba, "Design principles of a human mimetic humanoid: Humanoid platform to study human intelligence and internal body system," *Science Robotics*, vol. 2, no. 13, Dec 20 2017.
- [188] I. Mizuuchi *et al.*, "The design and control of the flexible spine of a fully tendon-driven humanoid "Kenta"," in *Proceedings of the 2002 IEEE/RSJ International Conference on Intelligent Robots and Systems*, EPFL, Lausanne, Switzerland, 2002, vol. 1-3, pp. 2527-2532.
- [189] T. Yoshikai, S. Yoshida, I. Mizuuchi, D. Sato, M. Inaba, and H. Inoue, "Multi-sensor guided behaviors in whole body tendon-driven humanoid Kenta," in *Proceedings of the IEEE International Conference on Multisensor Fusion and Integration for Intelligent Systems*, 2003, pp. 9-14.
- [190] I. Mizuuchi *et al.*, "Realization of standing of the musculoskeletal humanoid Kotaro by reinforcing muscles," in *Proceedings of the 2006 6th IEEE-RAS International Conference on Humanoid Robots*, 2006, vol. 1-2, pp. 176-181.
- [191] Y. Sodeyama, I. Mizuuchi, T. Yoshikai, Y. Nakanishi, and M. Inaba, "A shoulder structure of muscle-driven humanoid with shoulder blades," in *Proceedings of the 2005 IEEE/RSJ International Conference on Intelligent Robots and Systems*, 2005, vol. 1-4, pp. 1077-1082.

- [192] I. Mizuuchi *et al.*, "An Advanced Musculoskeletal Humanoid Kojiro," in *Proceedings of the 2007 7th IEEE-RAS International Conference on Humanoid Robots*, New York, USA, 2007, pp. 294-299.
- [193] K. Hongo, Y. Nakanishi, Y. Namiki, I. Mizuuchi, and M. Inaba, "Automatic Parameter Adjustment of Reflexive Walking of a Musculo-Skeletal Humanoid," in *Proceedings of the 2008 8th IEEE-RAS International Conference on Humanoid Robots (Humanoids 2008)*, 2008, pp. 16-21.
- [194] Y. Sodeyarna, T. Yoshikai, T. Nishino, I. Mizuuchi, and M. Inaba, "The designs and motions of a shoulder structure with a wide range of movement using bladebone-collarbhone structures," in *Proceedings of the 2007 IEEE/RSJ International Conference on Intelligent Robots and Systems*, San Diego, CA, USA, 2007, vol. 1-9, pp. 3635-3640.
- [195] Y. Nakanishi, Y. Namiki, J. Urata, I. Mizuuchi, and M. Inaba, "Design of Tendon Driven Humanoid's Lower Body Equipped with Redundant and High-powered Actuators," in *Proceedings of the 2007 IEEE/RSJ International Conference on Intelligent Robots and Systems (IROS)*, San Diego, CA, USA, 2007, pp. 3623-3628.
- [196] T. Kozuki *et al.*, "Design Methodology for the Thorax and Shoulder of Human Mimetic Musculoskeletal Humanoid Kenshiro -A Thorax structure with Rib like Surface -," in *Proceedings of the 2012 IEEE/RSJ International Conference on Intelligent Robots and Systems (IROS)*, 2012, pp. 3687-3692.
- [197] Y. Asano *et al.*, "Lower Thigh Design of Detailed Musculoskeletal Humanoid "Kenshiro"," in *Proceedings of the 2012 IEEE/RSJ International Conference on Intelligent Robots and Systems (IROS)*, 2012, pp. 4367-4372.
- [198] T. Kozuki *et al.*, "Design of Upper limb by Adhesion of Muscles and Bones-Detail Human Mimetic Musculoskeletal Humanoid Kenshiro," in *Proceedings of the 2013 IEEE/RSJ International Conference on Intelligent Robots and Systems (IROS)*, 2013, pp. 935-940.
- [199] Y. Asano *et al.*, "Human Mimetic Musculoskeletal Humanoid Kengoro toward Real World Physically Interactive Actions," *2016 IEEE-RAS 16th International Conference on Humanoid Robots (Humanoids)*, pp. 876-883, 2016.
- [200] Y. Asano *et al.*, "Achievement of Twist Squat by Musculoskeletal Humanoid with Screw-Home Mechanism," in *Proceedings of the 2013 IEEE/RSJ International Conference on Intelligent Robots and Systems (IROS)*, 2013, pp. 4649-4654.

- [201] K. Radkhah, C. Maufroy, M. Maus, D. Scholz, A. Seyfarth, and O. von Stryk, "Concept and Design of the Biobiped1 Robot for Human-Like Walking and Running," *International Journal of Humanoid Robotics*, vol. 8, no. 3, pp. 439-458, Sep 2011.
- [202] TU Darmstadt. (2010). *BioBiped project website*. Available: <http://www.biobiped.de/index/>
- [203] !!! INVALID CITATION !!! [204-206].
- [204] F. Iida, J. Rummel, and A. Seyfarth, "Bipedal walking and running with spring-like biarticular muscles," *Journal of Biomechanics*, vol. 41, no. 3, pp. 656-667, 2008.
- [205] A. Seyfarth, F. Iida, R. Tausch, M. Stelzer, O. von Stryk, and A. Karguth, "Towards Bipedal Jogging as a Natural Result of Optimizing Walking Speed for Passively Compliant Three-Segmented Legs," *The International Journal of Robotics Research*, vol. 28, no. 2, pp. 257-265, 2009.
- [206] D. Scholz, S. Kurowski, K. Radkhah, and O. V. Stryk, "Bio-inspired motion control of the musculoskeletal BioBiped1 robot based on a learned inverse dynamics model," in *Proceedings of the 2011 11th IEEE-RAS International Conference on Humanoid Robots (Humanoids)*, Bled, Slovenia, 2011, pp. 395-400.
- [207] K. Radkhah and O. von Stryk, "Actuation Requirements for Hopping and Running of the Musculoskeletal Robot BioBiped1," in *Proceedings of the 2011 IEEE/RSJ International Conference on Intelligent Robots and Systems*, 2011.
- [208] K. Radkhah, T. Lens, and O. von Stryk, "Detailed Dynamics Modeling of BioBiped's Monoarticular and Biarticular Tendon-Driven Actuation System," in *Proceedings of the 2012 IEEE/RSJ International Conference on Intelligent Robots and Systems (IROS)*, Vilamoura, Algarve, Portugal, 2012, pp. 4243-4250.
- [209] M. A. Sharbafi, K. Radkhah, O. Von Stryk, and A. Seyfarth, "Hopping control for the musculoskeletal bipedal robot: BioBiped," in *Proceedings of the 2014 IEEE/RSJ International Conference on Intelligent Robots and Systems (IROS 2014)*, Chicago, IL, USA, 2014, pp. 4868-4875.
- [210] R. Niiyama, S. Nishikawa, and Y. Kuniyoshi, "Athlete Robot with applied human muscle activation patterns for bipedal running," in *Proceedings of the 2010 10th IEEE-RAS International Conference on Humanoid Robots (Humanoids)*, 2010, pp. 498-503.

- [211] R. Niiyama and Y. Kuniyoshi, "Design of a musculoskeletal athlete robot: A biomechanical approach," in *Proceedings of the 12th International Conference on Climbing and Walking Robots and the Support Technologies for Mobile Machines (CLAWAR 2009)*, Istanbul, 2010, pp. 173-180.
- [212] N. Ryuma and K. Yasuo, "Design principle based on maximum output force profile for a musculoskeletal robot," *Industrial Robot: An International Journal*, vol. 37, no. 3, pp. 250-255, 2010/05/03 2010.
- [213] R. Niiyama, S. Nishikawa, and Y. Kuniyoshi, "Biomechanical Approach to Open-Loop Bipedal Running with a Musculoskeletal Athlete Robot," *Advanced Robotics*, vol. 26, no. 3-4, pp. 383-398, 2012.
- [214] C. G. Atkeson *et al.*, "Using humanoid robots to study human behavior," *IEEE Intelligent Systems & Their Applications*, vol. 15, no. 4, pp. 46-55, Jul-Aug 2000.
- [215] M. Kawato, "Brain controlled robots," *HFSP Journal*, vol. 2, no. 3, pp. 136-142, Jun 2008.
- [216] J. D. Millan, "Brain-controlled robots," *IEEE Intelligent Systems*, vol. 23, no. 3, pp. 74-76, May-Jun 2008.
- [217] M. Kawato, "Brain-controlled robots," in *Proceedings of the 2008 IEEE International Conference on Robotics and Automation*, 2008, vol. 1-9, pp. Dr21-Dr21.
- [218] T. Chaminade and G. Cheng, "Social cognitive neuroscience and humanoid robotics," *Journal of Physiology-Paris*, vol. 103, no. 3-5, pp. 286-295, May-Sep 2009.
- [219] A. Ude, C. G. Atkeson, and M. Riley, "Programming full-body movements for humanoid robots by observation," *Robotics and Autonomous Systems*, vol. 47, no. 2-3, pp. 93-108, Jun 30 2004.
- [220] M. Riley, A. Ude, C. Atkeson, and G. Cheng, "Coaching: An approach to efficiently and intuitively create humanoid robot behaviors," in *Proceedings of the 2006 6th IEEE-RAS International Conference on Humanoid Robots*, 2006, vol. 1-2, pp. 567-574.
- [221] M. Riley, A. Ude, and C. G. Atkeson, "Methods for motion generation and interaction with a humanoid robot: Case studies of dancing and catching," in *AAAI and CMU Workshop on Interactive Robotics and Entertainment*, Pittsburgh, USA, April 30-May 1, 2000, pp. 35-42.

- [222] D. C. Bentivegna, C. G. Atkeson, A. UDE, and G. Cheng, "Learning to act from observation and practice," *International Journal of Humanoid Robotics*, vol. 1, no. 04, pp. 585-611, 2004.
- [223] D. C. Bentivegna, C. G. Atkeson, and G. Cheng, "Learning tasks from observation and practice," *Robotics and Autonomous Systems*, vol. 47, no. 2-3, pp. 163-169, Jun 30 2004.
- [224] J. G. Hale and F. E. Pollick, "'Sticky Hands': Learning and generalization for cooperative physical interactions with a humanoid robot," *IEEE Transactions on Systems, Man and Cybernetics Part C: Applications and Reviews*, vol. 35, no. 4, pp. 512-521, 2005.
- [225] N. S. Pollard, J. K. Hodgins, M. J. Riley, and C. G. Atkeson, "Adapting human motion for the control of a humanoid robot," in *Proceedings of the 2002 IEEE International Conference on Robotics and Automation*, 2002, vol. I-IV, pp. 1390-1397.
- [226] A. J. Ijspeert, J. Nakanishi, and S. Schaal, "Movement imitation with nonlinear dynamical systems in humanoid robots," in *Proceedings of the 2002 IEEE International Conference on Robotics and Automation*, 2002, vol. I-IV, pp. 1398-1403.
- [227] T. Shibata and S. Schaal, "Biomimetic gaze stabilization based on feedback-error-learning with nonparametric regression networks," *Neural Networks*, vol. 14, no. 2, pp. 201-216, Mar 2001.
- [228] G. Cheng *et al.*, "CB: a humanoid research platform for exploring neuroscience," *Advanced Robotics*, vol. 21, no. 10, pp. 1097-1114, 2007.
- [229] G. Cheng *et al.*, "CB: A humanoid research platform for exploring NeuroScience," in *Proceedings of the 2006 6th IEEE-RAS International Conference on Humanoid Robots*, 2006, vol. 1-2, pp. 182-187.
- [230] G. Cheng *et al.*, "CB: Exploring neuroscience with a humanoid research platform," in *Proceedings of the 2008 IEEE International Conference on Robotics and Automation*, Pasadena, CA, USA, 2008, vol. 1-9, pp. 1772-1773.
- [231] J. Morimoto *et al.*, "Modulation of simple sinusoidal patterns by a coupled oscillator model for biped walking," in *Proceedings of the 2006 IEEE International Conference on Robotics and Automation (ICRA 2006)*, Orlando, Florida, USA, 2006, vol. 1-10, pp. 1579-1584.

- [232] G. Endo, J. Morimoto, T. Matsubara, J. Nakanishi, and G. Cheng, "Learning CPG sensory feedback with policy gradient for biped locomotion for a full-body humanoid," in *Proceedings of the National Conference on Artificial Intelligence*, 2005, vol. 20, no. 3, p. 1267.
- [233] G. Cheng, N. Fitzsimmons, J. Morimoto, M. Lebedev, M. Kawato, and M. Nicolelis, "Bipedal locomotion with a humanoid robot controlled by cortical ensemble activity," in *Abstracts-Society for Neuroscience*, 2007, vol. 517, p. 22.
- [234] J. Morimoto, G. Endo, J. Nakanishi, and G. Cheng, "A biologically inspired biped locomotion strategy for humanoid robots: Modulation of sinusoidal patterns by a coupled oscillator model," *IEEE Transactions on Robotics*, vol. 24, no. 1, pp. 185-191, Feb 2008.
- [235] S. Hyon and G. Cheng, "Gravity Compensation and Full-Body Balancing for Humanoid Robots," in *Proceedings of the 2006 6th IEEE-RAS International Conference on Humanoid Robots*, 2006, pp. 214-221.
- [236] S. H. Hyon, J. G. Hale, and G. Cheng, "Full-body compliant human-humanoid interaction: Balancing in the presence of unknown external forces," *IEEE Transactions on Robotics*, vol. 23, no. 5, pp. 884-898, Oct 2007.
- [237] S. H. Hyon and G. Cheng, "Disturbance rejection for biped humanoids," in *Proceedings of the 2007 IEEE International Conference on Robotics and Automation*, 2007, vol. 1-10, pp. 2668-2675.
- [238] A. Ude, V. Wyart, L. H. Lin, and G. Cheng, "Distributed visual attention on a humanoid robot," in *Proceedings of the 2005 5th IEEE-RAS International Conference on Humanoid Robots*, 2005, pp. 381-386.
- [239] A. Toda, H. Imamizu, M. A. Sato, Y. Wada, and M. Kawato, "Reconstruction of temporal movement from single-trial non-invasive brain activity: A hierarchical Bayesian method," *Neural Information Processing, Part Ii*, vol. 4985, pp. 1027-1036, 2008.
- [240] T. Geng, B. Porr, and F. Worgotter, "Fast biped walking with a sensor-driven neuronal controller and real-time online learning," *International Journal of Robotics Research*, vol. 25, no. 3, pp. 243-259, Mar 2006.
- [241] T. Geng, B. Porr, and F. Worgotter, "A reflexive neural network for dynamic biped walking control," *Neural Computation*, vol. 18, no. 5, pp. 1156-1196, May 2006.

- [242] G. Sandini, G. Metta, and D. Vernon, "RobotCub: An open framework for research in embodied cognition," in *Proceedings of the 2004 4th IEEE/RAS International Conference on Humanoid Robots*, 2004, vol. 1-2, pp. 13-32.
- [243] G. Metta *et al.*, "The RobotCub project--an open framework for research in embodied cognition," in *Proceedings of the IEEE-RAS International Conference on Humanoid Robots*, 2006, no. BIOROB-CONF-2006-014.
- [244] N. G. Tsagarakis *et al.*, "iCub: the design and realization of an open humanoid platform for cognitive and neuroscience research," *Advanced Robotics*, vol. 21, no. 10, pp. 1151-1175, 2007.
- [245] N. Nosengo, "The bot that plays ball," *Nature*, vol. 460, no. 7259, pp. 1076-1078, Aug 27 2009.
- [246] N. G. Tsagarakis, B. Vanderborght, M. Laffranchi, and D. G. Caldwell, "The Mechanical Design of the New Lower Body for the Child Humanoid robot 'iCub'," in *Proceedings of the 2009 IEEE-RSJ International Conference on Intelligent Robots and Systems*, 2009, pp. 4962-4968.
- [247] A. Parmiggiani *et al.*, "The design of the iCub humanoid robot," *International Journal of Humanoid Robotics*, vol. 9, no. 4, Dec 2012.
- [248] Italian Institute of Technology. (2010). *iCub--RobotCub Project*. Available: <http://www.robotcub.org/>
- [249] G. Sandini, G. Metta, and D. Vernon, "The iCub Cognitive Humanoid Robot: An Open-System Research Platform for Enactive Cognition," *50 Years of Artificial Intelligence*, vol. 4850, pp. 358-369, 2007.
- [250] G. Metta, G. Sandini, D. Vernon, L. Natale, and F. Nori, "The iCub humanoid robot: An open platform for research in embodied cognition," in *Proceedings of the 8th Workshop on Performance Metrics for Intelligent Systems, PerMIS'08*, Gaithersburg, MD, 2008, pp. 50-56.
- [251] G. Metta *et al.*, "The iCub humanoid robot: An open-systems platform for research in cognitive development," *Neural Networks*, vol. 23, no. 8-9, pp. 1125-1134, Oct-Nov 2010.
- [252] D. Vernon, G. Metta, and G. Sandini, "The iCub cognitive architecture: Interactive development in a humanoid robot," in *Proceedings of the 2007 IEEE 6th International Conference on Development and Learning*, 2007, pp. 93-98.

- [253] K. Narioka, R. Niiyama, Y. Ishii, and K. Hosoda, "Pneumatic musculoskeletal infant robots," in *Proceedings of the the 2009 IEEE/RSJ International Conference on Intelligent Robots and Systems*, 2009.
- [254] T. Takuma and K. Hosoda, "Controlling the walking period of a pneumatic muscle walker," *International Journal of Robotics Research*, vol. 25, no. 9, pp. 861-866, Sep 2006.
- [255] K. Narioka and K. Hosoda, "Designing Synergistic Walking of a Whole-Body Humanoid Driven by Pneumatic Artificial Muscles: An Empirical Study," *Advanced Robotics*, vol. 22, no. 10, pp. 1107-1123, 2008.
- [256] R. Niiyama and Y. Kuniyoshi, "Pneumatic biped with an artificial musculoskeletal system," in *Proceedings of the 4th International Symposium on Adaptive Motion of Animals and Machines (AMAM2008)*, 2008, pp. 80-81.
- [257] K. Narioka and K. Hosoda, "Motor development of an pneumatic musculoskeletal infant robot," in *Proceedings of the 2011 IEEE International Conference on Robotics and Automation (ICRA)*, 2011, pp. 963-968.
- [258] L. Torburn, "The Biomechanics and Motor Control of Human Gait - Normal, Elderly and Pathological, 2nd Edition - Winter, Da," *Journal of Rehabilitation Research and Development*, vol. 29, no. 3, pp. 76-77, Sum 1992.
- [259] P. Holmes, R. J. Full, D. Koditschek, and J. Guckenheimer, "The dynamics of legged locomotion: Models, analyses, and challenges," *Siam Review*, vol. 48, no. 2, pp. 207-304, Jun 2006.
- [260] L. Ren, Z. H. Qian, and L. Q. Ren, "Biomechanics of Musculoskeletal System and Its Biomimetic Implications: A Review," *Journal of Bionic Engineering*, vol. 11, no. 2, pp. 159-175, Apr 2014.
- [261] M. J. Ackerman, "The visible human project®: From body to bits," in *2016 38th Annual International Conference of the IEEE Engineering in Medicine and Biology Society (EMBC)*, Orlando, FL, USA, 16-20 August 2016, 2016, pp. 3338-3341.
- [262] V. Spitzer, M. J. Ackerman, A. L. Scherzinger, and D. Whitlock, "The visible human male: A technical report," *Journal of the American Medical Informatics Association*, vol. 3, no. 2, pp. 118-130, Mar-Apr 1996.
- [263] M. J. Ackerman, "The Visible Human Project," *Proceedings of the IEEE*, vol. 86, no. 3, pp. 504-511, 1998.

- [264] W. P. Segars and B. M. W. Tsui, "MCAT to XCAT: The Evolution of 4-D Computerized Phantoms for Imaging Research," *Proceedings of the IEEE*, vol. 97, no. 12, pp. 1954-1968, Dec 2009.
- [265] W. P. Segars, G. Sturgeon, S. Mendonca, J. Grimes, and B. M. W. Tsui, "4D XCAT phantom for multimodality imaging research," *Medical Physics*, vol. 37, no. 9, pp. 4902-4915, Sep 2010.
- [266] G. S. K. Fung, K. Stierstorfer, W. P. Segars, K. Taguchi, T. G. Flohr, and B. M. W. Tsui, "XCAT/DRASIM: A Realistic CT/Human-Model Simulation Package," in *Conference on Medical Imaging 2011 - Physics of Medical Imaging*, Lake Buena Vista, FL, USA, 13-17 February 2011, 2011, vol. 7961.
- [267] P. de Leva, "Adjustments to Zatsiorsky-Seluyanov's segment inertia parameters," *Journal of Biomechanics*, vol. 29, no. 9, pp. 1223-1230, Sep 1996.
- [268] J. Valentin, "Basic anatomical and physiological data for use in radiological protection: reference values: ICRP Publication 89," *Annals of the ICRP*, vol. 32, no. 3, pp. 175-176, 2002.
- [269] J. V. G. A. Durnin and Womersley, J., "Body Fat Assessed from Total-Body Density and Its Estimation from Skinfold Thickness - Measurements on 481 Men and Women Aged from 16 to 72 Years," *British Journal of Nutrition*, vol. 32, no. 1, pp. 77-97, 1974.
- [270] L. Ren, R. K. Jones, and D. Howard, "Whole body inverse dynamics over a complete gait cycle based only on measured kinematics," *Journal of Biomechanics*, vol. 41, no. 12, pp. 2750-2759, Aug 28 2008.
- [271] M. H. Weik, "Computer-aided Design and Manufacturing," in *Computer Science and Communications Dictionary*, Boston, MA: Springer US, 2001.
- [272] Siemens. (2007, May 7, 2007). *Siemens Closes Acquisition of UGS; Introduces Business as UGS PLM Software*. Available: https://www.plm.automation.siemens.com/en/about_us/newsroom/press/press_release.cfm?Component=34092&ComponentTemplate=822
- [273] Siemens. (2018). *NX main page*. Available: <https://www.plm.automation.siemens.com/global/en/products/nx/>
- [274] J. Cui *et al.*, "Combinatorial search of thermoelastic shape-memory alloys with extremely small hysteresis width," *Nature Materials*, vol. 5, no. 4, pp. 286-290, Apr 2006.

- [275] J. Tangorra, P. Anquetil, T. Fofonoff, A. Chen, M. Del Zio, and I. Hunter, "The application of conducting polymers to a biorobotic fin propulsor," *Bioinspiration & Biomimetics*, vol. 2, no. 2, pp. S6-S17, Jun 2007.
- [276] J. S. Leng, X. Lan, Y. J. Liu, and S. Y. Du, "Shape-memory polymers and their composites: Stimulus methods and applications," *Progress in Materials Science*, vol. 56, no. 7, pp. 1077-1135, Sep 2011.
- [277] P. Miaudet *et al.*, "Shape and temperature memory of nanocomposites with broadened glass transition," *Science*, vol. 318, no. 5854, pp. 1294-1296, Nov 23 2007.
- [278] F. Carpi, S. Bauer, and D. De Rossi, "Stretching Dielectric Elastomer Performance," *Science*, vol. 330, no. 6012, pp. 1759-1761, Dec 23 2010.
- [279] M. D. Lima *et al.*, "Electrically, Chemically, and Photonically Powered Torsional and Tensile Actuation of Hybrid Carbon Nanotube Yarn Muscles," *Science*, vol. 338, no. 6109, pp. 928-932, Nov 16 2012.
- [280] C. S. Haines *et al.*, "Artificial Muscles from Fishing Line and Sewing Thread," *Science*, vol. 343, no. 6173, pp. 868-872, Feb 21 2014.
- [281] C. S. Haines, N. Li, G. M. Spinks, A. E. Aliev, J. T. Di, and R. H. Baughman, "New twist on artificial muscles," *Proceedings of the National Academy of Sciences, USA*, vol. 113, no. 42, pp. 11709-11716, Oct 18 2016.
- [282] N. Alexander and H. Schwameder, "Effect of sloped walking on lower limb muscle forces," *Gait & Posture*, vol. 47, pp. 62-67, Jun 2016.
- [283] S. H. Collins, M. Wisse, and A. Ruina, "A three-dimensional passive-dynamic walking robot with two legs and knees," *The International Journal of Robotics Research*, vol. 20, no. 7, pp. 607-615, Jul 2001.
- [284] D. P. Noonan, P. Mountney, D. S. Elson, A. Darzi, and G. Z. Yang, "A Stereoscopic Fibroscope for Camera Motion and 3D Depth Recovery during Minimally Invasive Surgery," in *Proceedings of 2009 IEEE International Conference on Robotics and Automation (ICRA)*, 2009, vol. 1-7, pp. 3274-3279.
- [285] K. Yamane and J. Hodgins, "Simultaneous Tracking and Balancing of Humanoid Robots for Imitating Human Motion Capture Data," in *Proceedings of 2009 IEEE-RSJ International Conference on Intelligent Robots and Systems*, 2009, pp. 2510-2517.

- [286] L. W. Lamoreux, "Kinematic measurements in the study of human walking," *Bulletin of Prosthetics Research*, vol. 10, no. 15, pp. 3-84, 1971.
- [287] D. G. Wright, S. M. Desai, and W. H. Henderson, "Action of the Subtalar and Ankle-Joint Complex during the Stance Phase of Walking," *Journal of Bone & Joint Surgery American Volume*, vol. 46, pp. 361-82, March 1964.
- [288] M. P. Murray, A. B. Drought, and R. C. Kory, "Walking Patterns of Normal Men," *Journal of Bone & Joint Surgery American Volume*, vol. 46, pp. 335-60, March 1964.
- [289] A. S. E965, *Standard test method for measuring pavement macrotexture depth using a volumetric technique*. West Conshohocken, PA: American Society for Testing and Materials (ASTM) International, 2015.
- [290] N. Fisco and H. Sezen, "Comparison of Surface Macrotexture Measurement Methods," *Journal of Civil Engineering and Management*, vol. 19, pp. S153-S160, 2013.
- [291] H. Sezen and N. Fisco, "Evaluation and Comparison of Surface Macrotexture and Friction Measurement Methods," *Journal of Civil Engineering and Management*, vol. 19, no. 3, pp. 387-399, 2013.
- [292] A. L. Schwab and M. Wisse, "Basin of attraction of the simplest walking model," in *Proceedings of ASME Design Engineering Technical Conferences and Computers and Information in Engineering Conference (IDETC/CIE)*, Pittsburgh, Pennsylvania, USA, 2001, vol. 6, pp. 531-539.
- [293] D. G. E. Hobbelen and M. Wisse, "Ankle actuation for Limit Cycle Walkers," *International Journal of Robotics Research*, vol. 27, no. 6, pp. 709-735, Jun 2008.
- [294] D. G. E. Hobbelen and M. Wisse, "A disturbance rejection measure for limit cycle walkers: The Gait Sensitivity Norm," *IEEE Transactions on Robotics*, vol. 23, no. 6, pp. 1213-1224, Dec 2007.
- [295] Y. Asano, K. Okada, and M. Inaba, "Design principles of a human mimetic humanoid: Humanoid platform to study human intelligence and internal body system," *Science Robotics*, vol. 2, no. 13, pp. 1-11, 2017.

Appendix A

Distance Travelled in Simulation

Subtalar angle (°)	Talocrural angle (°)	Distance Travelled (mm)	Ending Status
0.00	0.00	3547.500	stopping
1.00	0.00	141.990	stopping
2.00	0.00	2528.200	stopping
3.00	0.00	99.447	stopping
4.00	0.00	280.640	falling
5.00	0.00	74.872	stopping
6.00	0.00	157.100	stopping
7.00	0.00	80.290	stopping
8.00	0.00	67.471	stopping
9.00	0.00	131.850	stopping
10.00	0.00	103.160	stopping
11.00	0.00	81.135	stopping
12.00	0.00	64.040	stopping
13.00	0.00	97.900	stopping
14.00	0.00	85.257	stopping
15.00	0.00	107.660	stopping
16.00	0.00	88.534	stopping
17.00	0.00	83.673	stopping
18.00	0.00	74.052	stopping
19.00	0.00	69.587	stopping
20.00	0.00	48.960	stopping
21.00	0.00	52.358	stopping
22.00	0.00	46.746	stopping
23.00	0.00	32.388	stopping
24.00	0.00	41.408	stopping
25.00	0.00	41.774	stopping
26.00	0.00	36.542	stopping
27.00	0.00	39.679	stopping
28.00	0.00	37.521	stopping

29.00	0.00	41.453	stopping
30.00	0.00	37.643	stopping
31.00	0.00	37.569	stopping
32.00	0.00	34.311	stopping
33.00	0.00	29.927	stopping
34.00	0.00	35.557	stopping
35.00	0.00	34.865	stopping
36.00	0.00	35.114	stopping
37.00	0.00	33.552	stopping
38.00	0.00	28.414	stopping
39.00	0.00	33.300	stopping
40.00	0.00	30.275	stopping
41.00	0.00	27.379	stopping
42.00	0.00	28.214	stopping
0.00	1.00	1139.000	falling
1.00	1.00	1241.700	falling
2.00	1.00	1276.700	falling
3.00	1.00	1089.900	stopping
4.00	1.00	1594.200	stopping
5.00	1.00	145.590	stopping
6.00	1.00	178.680	stopping
7.00	1.00	214.930	stopping
8.00	1.00	81.748	stopping
9.00	1.00	155.370	stopping
10.00	1.00	59.622	stopping
11.00	1.00	93.993	stopping
12.00	1.00	122.060	stopping
13.00	1.00	136.430	stopping
14.00	1.00	112.690	stopping
15.00	1.00	61.339	stopping
16.00	1.00	120.110	stopping
17.00	1.00	97.440	stopping
18.00	1.00	86.023	stopping
19.00	1.00	64.242	stopping
20.00	1.00	48.916	stopping
21.00	1.00	51.198	stopping
22.00	1.00	45.128	stopping
23.00	1.00	36.665	stopping
24.00	1.00	35.003	stopping
25.00	1.00	37.353	stopping
26.00	1.00	42.522	stopping
27.00	1.00	39.763	stopping

28.00	1.00	38.945	stopping
29.00	1.00	38.536	stopping
30.00	1.00	36.962	stopping
31.00	1.00	38.472	stopping
32.00	1.00	36.339	stopping
33.00	1.00	38.313	stopping
34.00	1.00	34.418	stopping
35.00	1.00	39.218	stopping
36.00	1.00	32.332	stopping
37.00	1.00	33.517	stopping
38.00	1.00	32.623	stopping
39.00	1.00	34.157	stopping
40.00	1.00	29.070	stopping
41.00	1.00	32.465	stopping
42.00	1.00	29.134	stopping
0.00	2.00	1129.000	falling
1.00	2.00	243.690	falling
2.00	2.00	1371.900	falling
3.00	2.00	842.680	falling
4.00	2.00	593.700	falling
5.00	2.00	1653.900	stopping
6.00	2.00	85.084	falling
7.00	2.00	174.950	falling
8.00	2.00	205.780	stopping
9.00	2.00	235.500	stopping
10.00	2.00	119.210	stopping
11.00	2.00	106.440	stopping
12.00	2.00	134.180	stopping
13.00	2.00	82.335	stopping
14.00	2.00	93.961	stopping
15.00	2.00	149.300	stopping
16.00	2.00	139.540	stopping
17.00	2.00	102.780	stopping
18.00	2.00	57.845	stopping
19.00	2.00	68.804	stopping
20.00	2.00	67.624	stopping
21.00	2.00	48.404	stopping
22.00	2.00	60.283	stopping
23.00	2.00	39.065	stopping
24.00	2.00	46.849	stopping
25.00	2.00	48.144	stopping
26.00	2.00	41.471	stopping

27.00	2.00	46.398	stopping
28.00	2.00	42.382	stopping
29.00	2.00	42.755	stopping
30.00	2.00	39.967	stopping
31.00	2.00	40.086	stopping
32.00	2.00	39.192	stopping
33.00	2.00	37.979	stopping
34.00	2.00	36.555	stopping
35.00	2.00	33.060	stopping
36.00	2.00	36.534	stopping
37.00	2.00	35.934	stopping
38.00	2.00	32.481	stopping
39.00	2.00	28.240	stopping
40.00	2.00	30.839	stopping
41.00	2.00	31.369	stopping
42.00	2.00	32.839	stopping
0.00	3.00	519.850	falling
1.00	3.00	947.840	falling
2.00	3.00	556.270	falling
3.00	3.00	300.370	falling
4.00	3.00	567.130	falling
5.00	3.00	154.450	falling
6.00	3.00	583.430	falling
7.00	3.00	1006.700	stopping
8.00	3.00	351.050	stopping
9.00	3.00	156.510	stopping
10.00	3.00	93.852	stopping
11.00	3.00	76.192	stopping
12.00	3.00	132.460	stopping
13.00	3.00	268.960	stopping
14.00	3.00	287.860	stopping
15.00	3.00	154.770	stopping
16.00	3.00	139.420	stopping
17.00	3.00	95.484	stopping
18.00	3.00	132.520	stopping
19.00	3.00	67.407	stopping
20.00	3.00	49.290	stopping
21.00	3.00	59.410	stopping
22.00	3.00	63.420	stopping
23.00	3.00	54.896	stopping
24.00	3.00	54.646	stopping
25.00	3.00	43.111	stopping

26.00	3.00	47.440	stopping
27.00	3.00	45.868	stopping
28.00	3.00	42.209	stopping
29.00	3.00	48.663	stopping
30.00	3.00	44.910	stopping
31.00	3.00	36.019	stopping
32.00	3.00	37.783	stopping
33.00	3.00	37.860	stopping
34.00	3.00	34.437	stopping
35.00	3.00	32.214	stopping
36.00	3.00	30.120	stopping
37.00	3.00	36.958	stopping
38.00	3.00	32.476	stopping
39.00	3.00	36.279	stopping
40.00	3.00	33.283	stopping
41.00	3.00	33.399	stopping
42.00	3.00	28.824	stopping
0.00	4.00	491.560	falling
1.00	4.00	479.920	falling
2.00	4.00	450.690	falling
3.00	4.00	687.150	falling
4.00	4.00	526.060	falling
5.00	4.00	87.545	falling
6.00	4.00	782.450	falling
7.00	4.00	185.670	falling
8.00	4.00	171.780	stopping
9.00	4.00	116.730	stopping
10.00	4.00	584.490	stopping
11.00	4.00	153.940	stopping
12.00	4.00	64.521	stopping
13.00	4.00	273.490	stopping
14.00	4.00	183.080	stopping
15.00	4.00	265.860	stopping
16.00	4.00	140.550	stopping
17.00	4.00	171.290	stopping
18.00	4.00	90.740	stopping
19.00	4.00	66.772	stopping
20.00	4.00	76.366	stopping
21.00	4.00	54.317	stopping
22.00	4.00	63.244	stopping
23.00	4.00	48.118	stopping
24.00	4.00	58.185	stopping

25.00	4.00	46.494	stopping
26.00	4.00	53.257	stopping
27.00	4.00	49.980	stopping
28.00	4.00	44.333	stopping
29.00	4.00	46.576	stopping
30.00	4.00	41.912	stopping
31.00	4.00	33.564	stopping
32.00	4.00	39.630	stopping
33.00	4.00	40.393	stopping
34.00	4.00	39.970	stopping
35.00	4.00	31.056	stopping
36.00	4.00	36.533	stopping
37.00	4.00	33.994	stopping
38.00	4.00	30.006	stopping
39.00	4.00	34.890	stopping
40.00	4.00	30.256	stopping
41.00	4.00	32.073	stopping
42.00	4.00	25.545	stopping
0.00	5.00	504.670	falling
1.00	5.00	460.290	falling
2.00	5.00	723.160	falling
3.00	5.00	411.720	falling
4.00	5.00	743.010	falling
5.00	5.00	722.240	falling
6.00	5.00	470.800	falling
7.00	5.00	396.560	falling
8.00	5.00	1349.800	stopping
9.00	5.00	810.490	stopping
10.00	5.00	327.020	stopping
11.00	5.00	636.940	stopping
12.00	5.00	199.110	stopping
13.00	5.00	294.000	stopping
14.00	5.00	635.600	stopping
15.00	5.00	145.250	stopping
16.00	5.00	158.090	stopping
17.00	5.00	103.620	stopping
18.00	5.00	72.363	stopping
19.00	5.00	85.676	stopping
20.00	5.00	85.205	stopping
21.00	5.00	464.710	stopping
22.00	5.00	60.174	stopping
23.00	5.00	51.431	stopping

24.00	5.00	47.377	stopping
25.00	5.00	68.954	stopping
26.00	5.00	53.489	stopping
27.00	5.00	38.940	stopping
28.00	5.00	47.238	stopping
29.00	5.00	45.185	stopping
30.00	5.00	40.698	stopping
31.00	5.00	39.096	stopping
32.00	5.00	39.796	stopping
33.00	5.00	38.685	stopping
34.00	5.00	36.499	stopping
35.00	5.00	38.082	stopping
36.00	5.00	35.627	stopping
37.00	5.00	31.584	stopping
38.00	5.00	35.354	stopping
39.00	5.00	30.611	stopping
40.00	5.00	28.293	stopping
41.00	5.00	31.615	stopping
42.00	5.00	28.169	stopping
0.00	6.00	536.250	falling
1.00	6.00	311.910	falling
2.00	6.00	316.630	falling
3.00	6.00	530.250	falling
4.00	6.00	494.570	falling
5.00	6.00	500.580	falling
6.00	6.00	343.840	falling
7.00	6.00	411.550	falling
8.00	6.00	438.600	falling
9.00	6.00	1271.600	stopping
10.00	6.00	191.530	stopping
11.00	6.00	295.460	falling
12.00	6.00	92.530	stopping
13.00	6.00	617.810	stopping
14.00	6.00	143.250	stopping
15.00	6.00	646.140	stopping
16.00	6.00	472.650	stopping
17.00	6.00	124.760	stopping
18.00	6.00	193.010	stopping
19.00	6.00	72.903	stopping
20.00	6.00	67.057	stopping
21.00	6.00	76.033	stopping
22.00	6.00	72.248	stopping

23.00	6.00	50.588	stopping
24.00	6.00	62.650	stopping
25.00	6.00	56.384	stopping
26.00	6.00	58.328	stopping
27.00	6.00	47.943	stopping
28.00	6.00	44.725	stopping
29.00	6.00	45.468	stopping
30.00	6.00	40.430	stopping
31.00	6.00	43.137	stopping
32.00	6.00	41.788	stopping
33.00	6.00	32.636	stopping
34.00	6.00	45.358	stopping
35.00	6.00	34.047	stopping
36.00	6.00	25.811	stopping
37.00	6.00	40.452	stopping
38.00	6.00	35.325	stopping
39.00	6.00	27.684	stopping
40.00	6.00	30.252	stopping
41.00	6.00	28.197	stopping
42.00	6.00	24.611	stopping
0.00	7.00	344.230	falling
1.00	7.00	359.230	falling
2.00	7.00	351.570	falling
3.00	7.00	438.820	falling
4.00	7.00	446.330	falling
5.00	7.00	558.520	falling
6.00	7.00	445.260	falling
7.00	7.00	452.530	falling
8.00	7.00	300.320	falling
9.00	7.00	479.390	falling
10.00	7.00	1461.000	stopping
11.00	7.00	755.600	falling
12.00	7.00	1072.000	falling
13.00	7.00	345.380	stopping
14.00	7.00	642.830	stopping
15.00	7.00	356.590	stopping
16.00	7.00	663.440	stopping
17.00	7.00	96.765	stopping
18.00	7.00	172.880	stopping
19.00	7.00	184.540	stopping
20.00	7.00	111.190	stopping
21.00	7.00	63.120	stopping

22.00	7.00	64.188	stopping
23.00	7.00	63.230	stopping
24.00	7.00	58.283	stopping
25.00	7.00	54.895	stopping
26.00	7.00	60.158	stopping
27.00	7.00	53.557	stopping
28.00	7.00	50.022	stopping
29.00	7.00	44.003	stopping
30.00	7.00	49.205	stopping
31.00	7.00	44.606	stopping
32.00	7.00	40.152	stopping
33.00	7.00	44.230	stopping
34.00	7.00	35.952	stopping
35.00	7.00	36.391	stopping
36.00	7.00	33.408	stopping
37.00	7.00	34.988	stopping
38.00	7.00	33.122	stopping
39.00	7.00	33.389	stopping
40.00	7.00	25.497	stopping
41.00	7.00	28.161	stopping
42.00	7.00	25.411	stopping
0.00	8.00	419.640	falling
1.00	8.00	324.100	falling
2.00	8.00	386.740	falling
3.00	8.00	575.320	falling
4.00	8.00	372.060	falling
5.00	8.00	607.410	falling
6.00	8.00	496.060	falling
7.00	8.00	368.420	falling
8.00	8.00	297.490	falling
9.00	8.00	179.010	falling
10.00	8.00	786.390	falling
11.00	8.00	239.280	falling
12.00	8.00	622.460	falling
13.00	8.00	472.770	falling
14.00	8.00	568.840	stopping
15.00	8.00	2281.200	stopping
16.00	8.00	679.320	stopping
17.00	8.00	298.750	stopping
18.00	8.00	102.350	stopping
19.00	8.00	100.870	stopping
20.00	8.00		stopping

21.00	8.00	83.985	stopping
22.00	8.00	82.468	stopping
23.00	8.00	67.271	stopping
24.00	8.00	64.021	stopping
25.00	8.00	69.751	stopping
26.00	8.00	66.594	stopping
27.00	8.00	53.333	stopping
28.00	8.00	45.451	stopping
29.00	8.00	44.318	stopping
30.00	8.00	44.480	stopping
31.00	8.00	44.167	stopping
32.00	8.00	39.890	stopping
33.00	8.00	42.514	stopping
34.00	8.00	40.553	stopping
35.00	8.00	41.603	stopping
36.00	8.00	42.783	stopping
37.00	8.00	37.277	stopping
38.00	8.00	35.416	stopping
39.00	8.00	32.871	stopping
40.00	8.00	31.491	stopping
41.00	8.00	27.074	stopping
42.00	8.00	28.454	stopping
0.00	9.00	370.870	falling
1.00	9.00	303.530	falling
2.00	9.00	312.980	falling
3.00	9.00	313.960	falling
4.00	9.00	463.660	falling
5.00	9.00	360.920	falling
6.00	9.00	273.570	falling
7.00	9.00	548.870	falling
8.00	9.00	706.350	falling
9.00	9.00	348.290	stopping
10.00	9.00	430.180	falling
11.00	9.00	925.300	stopping
12.00	9.00	493.130	falling
13.00	9.00	645.000	stopping
14.00	9.00	583.860	stopping
15.00	9.00	1937.300	stopping
16.00	9.00	694.990	stopping
17.00	9.00	666.790	stopping
18.00	9.00	153.860	stopping
19.00	9.00	224.080	stopping

20.00	9.00	125.900	stopping
21.00	9.00	99.517	stopping
22.00	9.00	201.930	stopping
23.00	9.00	82.415	stopping
24.00	9.00	77.348	stopping
25.00	9.00	67.265	stopping
26.00	9.00	66.699	stopping
27.00	9.00	61.326	stopping
28.00	9.00	59.546	stopping
29.00	9.00	45.740	stopping
30.00	9.00	44.381	stopping
31.00	9.00	45.579	stopping
32.00	9.00	37.396	stopping
33.00	9.00	47.368	stopping
34.00	9.00	39.845	stopping
35.00	9.00	37.582	stopping
36.00	9.00	42.854	stopping
37.00	9.00	33.139	stopping
38.00	9.00	42.007	stopping
39.00	9.00	30.345	stopping
40.00	9.00	30.934	stopping
41.00	9.00	29.401	stopping
42.00	9.00	29.804	stopping
0.00	10.00	345.030	falling
1.00	10.00	302.470	falling
2.00	10.00	417.990	falling
3.00	10.00	330.330	falling
4.00	10.00	311.010	falling
5.00	10.00	300.720	falling
6.00	10.00	390.420	falling
7.00	10.00	300.040	falling
8.00	10.00	564.360	falling
9.00	10.00	452.620	falling
10.00	10.00	632.470	falling
11.00	10.00	209.600	falling
12.00	10.00	457.010	falling
13.00	10.00	1271.700	falling
14.00	10.00	1249.200	falling
15.00	10.00	674.380	stopping
16.00	10.00	1625.100	stopping
17.00	10.00	692.840	stopping
18.00	10.00	182.750	stopping

19.00	10.00	107.390	stopping
20.00	10.00	123.650	stopping
21.00	10.00	125.530	stopping
22.00	10.00	77.242	stopping
23.00	10.00	88.877	stopping
24.00	10.00	81.240	stopping
25.00	10.00	77.969	stopping
26.00	10.00	79.394	stopping
27.00	10.00	75.229	stopping
28.00	10.00	53.658	stopping
29.00	10.00	51.787	stopping
30.00	10.00	59.135	stopping
31.00	10.00	51.592	stopping
32.00	10.00	44.566	stopping
33.00	10.00	42.876	stopping
34.00	10.00	40.466	stopping
35.00	10.00	40.909	stopping
36.00	10.00	41.130	stopping
37.00	10.00	35.721	stopping
38.00	10.00	32.655	stopping
39.00	10.00	31.017	stopping
40.00	10.00	29.753	stopping
41.00	10.00	28.021	stopping
42.00	10.00	26.515	stopping
0.00	11.00		falling
1.00	11.00	475.550	falling
2.00	11.00	528.290	falling
3.00	11.00	331.770	falling
4.00	11.00	1854.200	falling
5.00	11.00	323.170	falling
6.00	11.00	313.740	falling
7.00	11.00	385.570	falling
8.00	11.00	332.640	falling
9.00	11.00	393.330	falling
10.00	11.00	600.090	falling
11.00	11.00	480.030	falling
12.00	11.00	460.570	falling
13.00	11.00	714.740	stopping
14.00	11.00	857.390	falling
15.00	11.00	987.950	falling
16.00	11.00	668.480	stopping
17.00	11.00	3055.900	falling

18.00	11.00	1942.000	stopping
19.00	11.00	129.550	stopping
20.00	11.00	519.000	stopping
21.00	11.00	127.460	stopping
22.00	11.00	67.847	stopping
23.00	11.00	116.790	stopping
24.00	11.00	92.152	stopping
25.00	11.00	88.016	stopping
26.00	11.00	65.966	stopping
27.00	11.00	61.828	stopping
28.00	11.00	52.280	stopping
29.00	11.00	49.537	stopping
30.00	11.00	54.846	stopping
31.00	11.00	50.837	stopping
32.00	11.00	43.150	stopping
33.00	11.00	52.108	stopping
34.00	11.00	38.702	stopping
35.00	11.00	43.277	stopping
36.00	11.00	39.341	stopping
37.00	11.00	37.306	stopping
38.00	11.00	38.455	stopping
39.00	11.00	31.905	stopping
40.00	11.00	27.195	stopping
41.00	11.00	24.816	stopping
42.00	11.00	23.466	stopping
0.00	12.00	316.800	falling
1.00	12.00	312.370	falling
2.00	12.00	308.680	falling
3.00	12.00	245.560	falling
4.00	12.00	319.870	falling
5.00	12.00	339.360	falling
6.00	12.00	336.630	falling
7.00	12.00	280.970	falling
8.00	12.00	285.320	falling
9.00	12.00	524.370	falling
10.00	12.00	445.000	falling
11.00	12.00	585.870	falling
12.00	12.00	367.480	falling
13.00	12.00	289.740	falling
14.00	12.00	451.780	falling
15.00	12.00	200.060	falling
16.00	12.00	638.180	falling

17.00	12.00	2376.800	falling
18.00	12.00	1745.800	stopping
19.00	12.00	1912.400	stopping
20.00	12.00	2083.900	stopping
21.00	12.00	162.040	stopping
22.00	12.00	117.960	stopping
23.00	12.00	118.300	stopping
24.00	12.00	90.605	stopping
25.00	12.00	83.356	stopping
26.00	12.00	77.905	stopping
27.00	12.00	70.592	stopping
28.00	12.00	71.197	stopping
29.00	12.00	51.342	stopping
30.00	12.00	56.730	stopping
31.00	12.00	49.863	stopping
32.00	12.00	45.958	stopping
33.00	12.00	38.302	stopping
34.00	12.00	44.057	stopping
35.00	12.00	41.135	stopping
36.00	12.00	39.954	stopping
37.00	12.00	35.851	stopping
38.00	12.00	30.636	stopping
39.00	12.00	32.760	stopping
40.00	12.00	29.620	stopping
41.00	12.00	27.104	stopping
42.00	12.00	24.940	stopping
0.00	13.00	114.860	falling
1.00	13.00	347.290	falling
2.00	13.00	309.750	falling
3.00	13.00	395.580	falling
4.00	13.00	340.810	falling
5.00	13.00	305.910	falling
6.00	13.00	332.750	falling
7.00	13.00	227.420	falling
8.00	13.00	310.790	falling
9.00	13.00	271.240	falling
10.00	13.00	316.660	falling
11.00	13.00	284.740	falling
12.00	13.00	379.650	falling
13.00	13.00	358.390	falling
14.00	13.00	350.710	falling
15.00	13.00	608.770	falling

16.00	13.00	769.980	falling
17.00	13.00	865.920	stopping
18.00	13.00	281.600	falling
19.00	13.00	1306.800	stopping
20.00	13.00	124.860	stopping
21.00	13.00	149.120	stopping
22.00	13.00	139.390	stopping
23.00	13.00	114.020	stopping
24.00	13.00	93.987	stopping
25.00	13.00	103.690	stopping
26.00	13.00	84.574	stopping
27.00	13.00	80.333	stopping
28.00	13.00	54.085	stopping
29.00	13.00	57.998	stopping
30.00	13.00	59.102	stopping
31.00	13.00	55.926	stopping
32.00	13.00	46.137	stopping
33.00	13.00	44.123	stopping
34.00	13.00	43.631	stopping
35.00	13.00	38.220	stopping
36.00	13.00	41.636	stopping
37.00	13.00	37.581	stopping
38.00	13.00	31.868	stopping
39.00	13.00	36.297	stopping
40.00	13.00	25.923	stopping
41.00	13.00	28.581	stopping
42.00	13.00	25.092	stopping
0.00	14.00	681.740	falling
1.00	14.00	324.270	falling
2.00	14.00	360.290	falling
3.00	14.00	315.130	falling
4.00	14.00	332.640	falling
5.00	14.00	355.230	falling
6.00	14.00	295.090	falling
7.00	14.00	462.840	falling
8.00	14.00	316.250	falling
9.00	14.00	321.780	falling
10.00	14.00	432.760	falling
11.00	14.00	288.220	falling
12.00	14.00	301.420	falling
13.00	14.00	288.630	falling
14.00	14.00	277.610	falling

15.00	14.00	363.120	falling
16.00	14.00	411.940	falling
17.00	14.00	334.750	falling
18.00	14.00	1083.800	falling
19.00	14.00		stopping
20.00	14.00	1080.100	stopping
21.00	14.00	1769.900	stopping
22.00	14.00	275.800	stopping
23.00	14.00	2552.200	stopping
24.00	14.00	382.150	stopping
25.00	14.00	102.150	stopping
26.00	14.00	89.866	stopping
27.00	14.00	81.259	stopping
28.00	14.00	71.057	stopping
29.00	14.00	85.781	stopping
30.00	14.00	60.448	stopping
31.00	14.00	55.107	stopping
32.00	14.00	45.441	stopping
33.00	14.00	49.047	stopping
34.00	14.00	45.298	stopping
35.00	14.00	44.138	stopping
36.00	14.00	39.674	stopping
37.00	14.00	35.356	stopping
38.00	14.00	32.444	stopping
39.00	14.00	28.657	stopping
40.00	14.00	26.196	stopping
41.00	14.00	25.250	stopping
42.00	14.00	23.183	stopping
0.00	15.00	224.510	falling
1.00	15.00	354.040	falling
2.00	15.00	552.830	falling
3.00	15.00	282.620	falling
4.00	15.00	340.350	falling
5.00	15.00	337.150	falling
6.00	15.00	249.240	falling
7.00	15.00	319.200	falling
8.00	15.00	401.880	falling
9.00	15.00	390.290	falling
10.00	15.00	389.420	falling
11.00	15.00	332.940	falling
12.00	15.00	541.000	falling
13.00	15.00	320.750	falling

14.00	15.00	363.760	falling
15.00	15.00	391.770	falling
16.00	15.00	212.590	falling
17.00	15.00	637.440	falling
18.00	15.00	712.140	falling
19.00	15.00	1032.900	stopping
20.00	15.00	1273.500	stopping
21.00	15.00	2441.900	stopping
22.00	15.00	1204.000	stopping
23.00	15.00	1081.300	stopping
24.00	15.00	160.270	stopping
25.00	15.00	104.290	stopping
26.00	15.00	96.037	stopping
27.00	15.00	97.498	stopping
28.00	15.00	81.618	stopping
29.00	15.00	62.448	stopping
30.00	15.00	87.386	stopping
31.00	15.00	57.440	stopping
32.00	15.00	45.081	stopping
33.00	15.00	45.519	stopping
34.00	15.00	48.181	stopping
35.00	15.00	43.268	stopping
36.00	15.00	46.009	stopping
37.00	15.00	36.550	stopping
38.00	15.00	26.773	stopping
39.00	15.00	29.995	stopping
40.00	15.00	28.003	stopping
41.00	15.00	28.417	stopping
42.00	15.00	24.078	stopping
0.00	16.00	363.160	falling
1.00	16.00	347.510	falling
2.00	16.00	259.920	falling
3.00	16.00	397.180	falling
4.00	16.00	406.960	falling
5.00	16.00	376.880	falling
6.00	16.00	313.510	falling
7.00	16.00	321.090	falling
8.00	16.00	344.350	falling
9.00	16.00	336.210	falling
10.00	16.00	398.740	falling
11.00	16.00	306.370	falling
12.00	16.00	312.550	falling

13.00	16.00	295.900	falling
14.00	16.00	293.480	falling
15.00	16.00	276.200	falling
16.00	16.00	361.990	falling
17.00	16.00	329.720	falling
18.00	16.00	432.960	falling
19.00	16.00	552.300	falling
20.00	16.00	225.240	falling
21.00	16.00	1286.600	stopping
22.00	16.00	1602.800	falling
23.00	16.00	4166.249	stopping
24.00	16.00		stopping
25.00	16.00	726.190	stopping
26.00	16.00	109.950	stopping
27.00	16.00	94.268	stopping
28.00	16.00	68.749	stopping
29.00	16.00	69.640	stopping
30.00	16.00	60.707	stopping
31.00	16.00	59.528	stopping
32.00	16.00	55.164	stopping
33.00	16.00	49.422	stopping
34.00	16.00	52.185	stopping
35.00	16.00	46.455	stopping
36.00	16.00	41.753	stopping
37.00	16.00	35.928	stopping
38.00	16.00	37.795	stopping
39.00	16.00	29.227	stopping
40.00	16.00	28.960	stopping
41.00	16.00	27.175	stopping
42.00	16.00	25.222	stopping
0.00	17.00	292.430	falling
1.00	17.00	234.600	
2.00	17.00	340.120	falling
3.00	17.00	325.640	stopping
4.00	17.00	290.280	falling
5.00	17.00	343.050	falling
6.00	17.00	396.110	falling
7.00	17.00	272.530	falling
8.00	17.00	333.540	falling
9.00	17.00	326.150	falling
10.00	17.00	254.510	falling
11.00	17.00	293.140	falling

12.00	17.00	310.260	falling
13.00	17.00	364.440	falling
14.00	17.00	305.360	falling
15.00	17.00	306.100	falling
16.00	17.00	373.050	falling
17.00	17.00	319.250	falling
18.00	17.00	407.330	falling
19.00	17.00	563.950	falling
20.00	17.00	1015.000	falling
21.00	17.00	628.130	falling
22.00	17.00	1591.100	stopping
23.00	17.00	1800.400	stopping
24.00	17.00	2478.500	stopping
25.00	17.00		stopping
26.00	17.00	106.540	stopping
27.00	17.00	109.560	stopping
28.00	17.00	90.383	stopping
29.00	17.00	71.579	stopping
30.00	17.00	63.643	stopping
31.00	17.00	62.059	stopping
32.00	17.00	55.271	stopping
33.00	17.00	48.307	stopping
34.00	17.00	43.039	stopping
35.00	17.00	43.909	stopping
36.00	17.00	40.882	stopping
37.00	17.00	37.513	stopping
38.00	17.00	31.852	stopping
39.00	17.00	30.035	stopping
40.00	17.00	25.996	stopping
41.00	17.00	29.256	stopping
42.00	17.00	25.275	stopping
0.00	18.00	341.670	falling
1.00	18.00	464.730	falling
2.00	18.00	337.750	falling
3.00	18.00	341.870	falling
4.00	18.00	296.640	falling
5.00	18.00	269.560	falling
6.00	18.00	317.390	falling
7.00	18.00	320.320	falling
8.00	18.00	346.040	falling
9.00	18.00	563.620	falling
10.00	18.00	243.930	falling

11.00	18.00	284.770	falling
12.00	18.00	325.130	falling
13.00	18.00	462.050	falling
14.00	18.00	301.980	falling
15.00	18.00	274.770	falling
16.00	18.00	296.760	falling
17.00	18.00	520.320	falling
18.00	18.00	250.600	falling
19.00	18.00	603.380	falling
20.00	18.00	872.250	stopping
21.00	18.00	768.450	stopping
22.00	18.00	736.430	stopping
23.00	18.00	959.030	stopping
24.00	18.00	1649.700	stopping
25.00	18.00	247.610	stopping
26.00	18.00	204.370	stopping
27.00	18.00	101.150	stopping
28.00	18.00	86.399	stopping
29.00	18.00	83.703	stopping
30.00	18.00	68.398	stopping
31.00	18.00	58.357	stopping
32.00	18.00	51.558	stopping
33.00	18.00	53.967	stopping
34.00	18.00	48.884	stopping
35.00	18.00	38.982	stopping
36.00	18.00	40.773	stopping
37.00	18.00	31.969	stopping
38.00	18.00	37.493	stopping
39.00	18.00	27.598	stopping
40.00	18.00	25.947	stopping
41.00	18.00	24.824	stopping
42.00	18.00	25.626	stopping
0.00	19.00	366.840	falling
1.00	19.00	481.600	falling
2.00	19.00	406.980	stopping
3.00	19.00	399.710	stopping
4.00	19.00	321.390	falling
5.00	19.00	287.220	falling
6.00	19.00	264.850	falling
7.00	19.00	211.650	falling
8.00	19.00	266.700	falling
9.00	19.00	205.530	falling

10.00	19.00	264.620	falling
11.00	19.00	338.560	falling
12.00	19.00	318.450	falling
13.00	19.00	266.180	falling
14.00	19.00	390.330	falling
15.00	19.00	270.440	falling
16.00	19.00	303.470	falling
17.00	19.00	390.790	falling
18.00	19.00	214.550	falling
19.00	19.00	349.090	falling
20.00	19.00	300.650	falling
21.00	19.00	542.380	falling
22.00	19.00	556.830	falling
23.00	19.00	703.770	falling
24.00	19.00	1096.300	stopping
25.00	19.00	2503.500	stopping
26.00	19.00	2578.300	stopping
27.00	19.00	103.870	stopping
28.00	19.00	102.040	stopping
29.00	19.00	98.081	stopping
30.00	19.00	62.551	stopping
31.00	19.00	59.599	stopping
32.00	19.00	57.406	stopping
33.00	19.00	47.817	stopping
34.00	19.00	45.132	stopping
35.00	19.00	42.194	stopping
36.00	19.00	37.539	stopping
37.00	19.00	34.856	stopping
38.00	19.00	29.173	stopping
39.00	19.00	27.643	stopping
40.00	19.00	27.359	stopping
41.00	19.00	25.371	stopping
42.00	19.00	25.801	stopping
0.00	20.00	376.650	falling
1.00	20.00	362.110	falling
2.00	20.00	338.290	falling
3.00	20.00	402.060	falling
4.00	20.00	369.930	falling
5.00	20.00	670.100	falling
6.00	20.00	249.600	falling
7.00	20.00	333.920	falling
8.00	20.00	245.030	falling

9.00	20.00	325.760	falling
10.00	20.00	271.900	falling
11.00	20.00	357.910	falling
12.00	20.00	254.010	falling
13.00	20.00	218.350	falling
14.00	20.00	222.590	falling
15.00	20.00	298.590	falling
16.00	20.00	301.150	falling
17.00	20.00	273.590	stopping
18.00	20.00	388.270	falling
19.00	20.00	373.740	falling
20.00	20.00	259.280	falling
21.00	20.00	281.240	falling
22.00	20.00	563.250	falling
23.00	20.00	391.970	falling
24.00	20.00	141.600	falling
25.00	20.00	708.530	stopping
26.00	20.00	2472.700	stopping
27.00	20.00	207.880	stopping
28.00	20.00	101.660	stopping
29.00	20.00	67.846	stopping
30.00	20.00	67.212	stopping
31.00	20.00	61.630	stopping
32.00	20.00	55.159	stopping
33.00	20.00	55.560	stopping
34.00	20.00	43.436	stopping
35.00	20.00	37.162	stopping
36.00	20.00	38.923	stopping
37.00	20.00	35.509	stopping
38.00	20.00	30.486	stopping
39.00	20.00	29.312	stopping
40.00	20.00	25.681	stopping
41.00	20.00	24.659	stopping
42.00	20.00	24.808	stopping
0.00	21.00	279.340	stopping
1.00	21.00	469.980	falling
2.00	21.00	373.390	falling
3.00	21.00	278.410	falling
4.00	21.00	260.750	falling
5.00	21.00	242.540	falling
6.00	21.00	269.030	stopping
7.00	21.00	375.390	falling

8.00	21.00	225.310	stopping
9.00	21.00	294.500	falling
10.00	21.00	309.800	falling
11.00	21.00	185.010	falling
12.00	21.00	209.990	falling
13.00	21.00	227.010	falling
14.00	21.00	217.700	falling
15.00	21.00	225.440	falling
16.00	21.00	288.630	falling
17.00	21.00	307.690	falling
18.00	21.00	288.000	falling
19.00	21.00	298.100	falling
20.00	21.00	360.380	stopping
21.00	21.00	442.480	stopping
22.00	21.00	414.250	falling
23.00	21.00	388.020	falling
24.00	21.00	558.910	falling
25.00	21.00	762.710	stopping
26.00	21.00	987.550	stopping
27.00	21.00	956.920	stopping
28.00	21.00	3460.100	stopping
29.00	21.00	107.830	stopping
30.00	21.00	68.474	stopping
31.00	21.00	51.195	stopping
32.00	21.00	56.248	stopping
33.00	21.00	49.587	stopping
34.00	21.00	50.378	stopping
35.00	21.00	41.175	stopping
36.00	21.00	41.347	stopping
37.00	21.00	34.347	stopping
38.00	21.00	30.556	stopping
39.00	21.00	28.825	stopping
40.00	21.00	29.017	stopping
41.00	21.00	25.323	stopping
42.00	21.00	25.730	stopping
0.00	22.00	247.710	falling
1.00	22.00	743.990	falling
2.00	22.00	365.870	falling
3.00	22.00	373.250	falling
4.00	22.00	398.560	falling
5.00	22.00	257.540	falling
6.00	22.00	277.450	falling

7.00	22.00	293.650	falling
8.00	22.00	385.740	falling
9.00	22.00	307.870	falling
10.00	22.00	227.910	falling
11.00	22.00	181.030	falling
12.00	22.00	220.240	falling
13.00	22.00	288.170	falling
14.00	22.00	294.520	falling
15.00	22.00	317.710	falling
16.00	22.00		falling
17.00	22.00	304.230	falling
18.00	22.00	171.790	falling
19.00	22.00	274.980	falling
20.00	22.00	378.370	falling
21.00	22.00	323.400	falling
22.00	22.00	445.290	falling
23.00	22.00	301.270	falling
24.00	22.00	673.270	falling
25.00	22.00	655.470	stopping
26.00	22.00	624.710	stopping
27.00	22.00	2129.700	stopping
28.00	22.00	160.580	stopping
29.00	22.00	232.710	stopping
30.00	22.00	78.660	stopping
31.00	22.00	64.144	stopping
32.00	22.00	63.528	stopping
33.00	22.00	44.657	stopping
34.00	22.00	42.927	stopping
35.00	22.00	42.742	stopping
36.00	22.00	33.983	stopping
37.00	22.00	32.953	stopping
38.00	22.00	31.683	stopping
39.00	22.00	28.448	stopping
40.00	22.00	27.998	stopping
41.00	22.00	26.895	stopping
42.00	22.00	25.491	stopping
0.00	23.00	398.990	stopping
1.00	23.00	624.450	falling
2.00	23.00	312.340	falling
3.00	23.00	163.230	falling
4.00	23.00	320.830	stopping
5.00	23.00	259.030	falling

6.00	23.00	298.760	stopping
7.00	23.00	239.480	falling
8.00	23.00	264.340	falling
9.00	23.00	273.430	falling
10.00	23.00	344.150	falling
11.00	23.00	379.880	falling
12.00	23.00	331.850	falling
13.00	23.00	219.780	falling
14.00	23.00	244.110	falling
15.00	23.00	268.440	falling
16.00	23.00	231.200	falling
17.00	23.00	321.290	falling
18.00	23.00	308.590	falling
19.00	23.00	292.480	falling
20.00	23.00	364.820	falling
21.00	23.00	431.860	falling
22.00	23.00	164.580	falling
23.00	23.00	299.010	falling
24.00	23.00	335.110	stopping
25.00	23.00	300.560	stopping
26.00	23.00	646.680	stopping
27.00	23.00	1234.600	stopping
28.00	23.00	207.610	stopping
29.00	23.00	128.580	stopping
30.00	23.00	94.633	stopping
31.00	23.00	54.047	stopping
32.00	23.00	55.173	stopping
33.00	23.00	51.482	stopping
34.00	23.00	43.679	stopping
35.00	23.00	33.649	stopping
36.00	23.00	33.881	stopping
37.00	23.00	32.900	stopping
38.00	23.00	29.600	stopping
39.00	23.00	28.659	stopping
40.00	23.00	27.914	stopping
41.00	23.00	26.982	stopping
42.00	23.00	26.421	stopping
0.00	24.00	539.620	falling
1.00	24.00	412.760	falling
2.00	24.00	402.900	falling
3.00	24.00	495.900	falling
4.00	24.00	347.590	falling

5.00	24.00	513.530	falling
6.00	24.00	252.350	falling
7.00	24.00	363.270	falling
8.00	24.00	214.720	falling
9.00	24.00	357.060	falling
10.00	24.00	411.610	falling
11.00	24.00	221.900	falling
12.00	24.00	232.740	falling
13.00	24.00	233.590	falling
14.00	24.00	235.040	falling
15.00	24.00	227.310	falling
16.00	24.00	343.540	falling
17.00	24.00	280.570	falling
18.00	24.00	310.250	falling
19.00	24.00	320.910	falling
20.00	24.00	291.850	falling
21.00	24.00	689.380	falling
22.00	24.00	386.000	falling
23.00	24.00	473.250	falling
24.00	24.00	759.540	falling
25.00	24.00	240.650	falling
26.00	24.00	504.940	falling
27.00	24.00	1130.400	stopping
28.00	24.00	575.410	stopping
29.00	24.00	1264.900	stopping
30.00	24.00	70.758	stopping
31.00	24.00	70.377	stopping
32.00	24.00	53.207	stopping
33.00	24.00	40.993	stopping
34.00	24.00	75.429	stopping
35.00	24.00	45.562	stopping
36.00	24.00	35.098	stopping
37.00	24.00	30.839	stopping
38.00	24.00	29.485	stopping
39.00	24.00	28.790	stopping
40.00	24.00	28.080	stopping
41.00	24.00	27.948	stopping
42.00	24.00	25.918	stopping
0.00	25.00	383.960	falling
1.00	25.00	397.490	stopping
2.00	25.00	409.470	falling
3.00	25.00	135.850	falling

4.00	25.00	252.930	falling
5.00	25.00	348.700	falling
6.00	25.00	383.230	falling
7.00	25.00	287.620	falling
8.00	25.00	233.570	falling
9.00	25.00	301.580	falling
10.00	25.00	384.190	falling
11.00	25.00	386.660	falling
12.00	25.00	374.910	falling
13.00	25.00	361.040	falling
14.00	25.00	232.790	falling
15.00	25.00	308.490	falling
16.00	25.00	224.560	falling
17.00	25.00	188.800	falling
18.00	25.00	363.420	falling
19.00	25.00	310.620	falling
20.00	25.00	141.810	falling
21.00	25.00	413.360	falling
22.00	25.00	604.260	falling
23.00	25.00	381.330	stopping
24.00	25.00	427.890	falling
25.00	25.00	519.180	falling
26.00	25.00	432.270	stopping
27.00	25.00	398.320	stopping
28.00	25.00	609.640	stopping
29.00	25.00	113.270	stopping
30.00	25.00	118.400	stopping
31.00	25.00	57.973	stopping
32.00	25.00	41.990	stopping
33.00	25.00	54.508	stopping
34.00	25.00	35.502	stopping
35.00	25.00	35.076	stopping
36.00	25.00	37.165	stopping
37.00	25.00	32.674	stopping
38.00	25.00	31.400	stopping
39.00	25.00	29.582	stopping
40.00	25.00	28.582	stopping
41.00	25.00	27.994	stopping
42.00	25.00	27.276	stopping
0.00	26.00		stopping
1.00	26.00	472.220	falling
2.00	26.00	339.200	falling

3.00	26.00	392.610	falling
4.00	26.00	370.620	falling
5.00	26.00	342.160	falling
6.00	26.00	251.130	stopping
7.00	26.00	321.280	falling
8.00	26.00	222.720	stopping
9.00	26.00	335.320	falling
10.00	26.00	226.130	falling
11.00	26.00	223.560	falling
12.00	26.00	243.730	falling
13.00	26.00	244.400	falling
14.00	26.00	282.770	falling
15.00	26.00	259.090	falling
16.00	26.00	344.390	falling
17.00	26.00	323.200	falling
18.00	26.00	442.140	falling
19.00	26.00	323.320	falling
20.00	26.00	255.000	falling
21.00	26.00	310.140	falling
22.00	26.00	294.940	falling
23.00	26.00	280.120	falling
24.00	26.00	460.070	falling
25.00	26.00	340.030	falling
26.00	26.00	304.440	falling
27.00	26.00	319.330	stopping
28.00	26.00	564.640	stopping
29.00	26.00	169.250	stopping
30.00	26.00	76.946	stopping
31.00	26.00	51.000	stopping
32.00	26.00	56.768	stopping
33.00	26.00	55.123	stopping
34.00	26.00	42.106	stopping
35.00	26.00	36.402	stopping
36.00	26.00	34.622	stopping
37.00	26.00	32.180	stopping
38.00	26.00	31.219	stopping
39.00	26.00	29.596	stopping
40.00	26.00	29.486	stopping
41.00	26.00	28.416	stopping
42.00	26.00	27.281	stopping
0.00	27.00	373.370	stopping
1.00	27.00	403.600	stopping

2.00	27.00	411.830	falling
3.00	27.00	461.000	falling
4.00	27.00	361.600	falling
5.00	27.00	444.460	falling
6.00	27.00	404.940	falling
7.00	27.00	379.780	stopping
8.00	27.00	299.880	stopping
9.00	27.00	673.470	falling
10.00	27.00	570.840	falling
11.00	27.00	321.580	falling
12.00	27.00	245.130	falling
13.00	27.00	343.670	falling
14.00	27.00	237.930	falling
15.00	27.00	358.510	falling
16.00	27.00	257.370	falling
17.00	27.00	350.240	falling
18.00	27.00	358.690	falling
19.00	27.00	327.080	falling
20.00	27.00	326.130	falling
21.00	27.00	302.030	falling
22.00	27.00	282.210	falling
23.00	27.00	265.220	falling
24.00	27.00	348.320	falling
25.00	27.00	349.500	falling
26.00	27.00	382.170	stopping
27.00	27.00	233.080	stopping
28.00	27.00	685.540	stopping
29.00	27.00	77.703	stopping
30.00	27.00	61.989	stopping
31.00	27.00	69.221	stopping
32.00	27.00	72.367	stopping
33.00	27.00	61.588	stopping
34.00	27.00	40.044	stopping
35.00	27.00	37.594	stopping
36.00	27.00	36.090	stopping
37.00	27.00	32.950	stopping
38.00	27.00	32.261	stopping
39.00	27.00	29.436	stopping
40.00	27.00	29.974	stopping
41.00	27.00	28.341	stopping
42.00	27.00	28.189	stopping
0.00	28.00	429.150	falling

1.00	28.00	362.200	stopping
2.00	28.00	428.630	stopping
3.00	28.00	363.230	falling
4.00	28.00	381.210	falling
5.00	28.00	711.660	falling
6.00	28.00	371.440	stopping
7.00	28.00	234.210	stopping
8.00	28.00	152.960	falling
9.00	28.00	340.980	stopping
10.00	28.00	250.770	falling
11.00	28.00	244.750	falling
12.00	28.00	552.560	falling
13.00	28.00	241.810	falling
14.00	28.00	265.480	falling
15.00	28.00	274.090	falling
16.00	28.00	243.690	falling
17.00	28.00	364.600	falling
18.00	28.00	356.170	falling
19.00	28.00	340.280	falling
20.00	28.00	317.980	falling
21.00	28.00	306.820	falling
22.00	28.00	514.170	falling
23.00	28.00	289.300	falling
24.00	28.00	346.770	falling
25.00	28.00	394.200	stopping
26.00	28.00	291.670	stopping
27.00	28.00	444.010	stopping
28.00	28.00	469.020	stopping
29.00	28.00	651.380	stopping
30.00	28.00	77.480	stopping
31.00	28.00	71.807	stopping
32.00	28.00	59.188	stopping
33.00	28.00	44.697	stopping
34.00	28.00	45.223	stopping
35.00	28.00	41.919	stopping
36.00	28.00	32.944	stopping
37.00	28.00	31.923	stopping
38.00	28.00	32.476	stopping
39.00	28.00	30.766	stopping
40.00	28.00	30.162	stopping
41.00	28.00	29.281	stopping
42.00	28.00	28.312	stopping

0.00	29.00	434.180	falling
1.00	29.00	410.380	stopping
2.00	29.00	486.000	falling
3.00	29.00	466.380	falling
4.00	29.00	477.070	falling
5.00	29.00	608.650	stopping
6.00	29.00	367.430	falling
7.00	29.00	281.590	falling
8.00	29.00	270.220	falling
9.00	29.00	407.730	falling
10.00	29.00	321.950	falling
11.00	29.00	332.320	falling
12.00	29.00	327.430	falling
13.00	29.00	223.680	falling
14.00	29.00	269.530	falling
15.00	29.00	259.430	falling
16.00	29.00	269.110	falling
17.00	29.00	229.430	falling
18.00	29.00	235.550	falling
19.00	29.00	358.970	stopping
20.00	29.00	302.250	falling
21.00	29.00	318.760	falling
22.00	29.00	307.480	falling
23.00	29.00	371.060	falling
24.00	29.00	479.510	falling
25.00	29.00	277.060	stopping
26.00	29.00	262.720	stopping
27.00	29.00	450.590	stopping
28.00	29.00	424.970	stopping
29.00	29.00	126.400	stopping
30.00	29.00	75.212	stopping
31.00	29.00	77.909	stopping
32.00	29.00	72.077	stopping
33.00	29.00	54.270	stopping
34.00	29.00	43.236	stopping
35.00	29.00	35.738	stopping
36.00	29.00	36.936	stopping
37.00	29.00	31.705	stopping
38.00	29.00	31.663	stopping
39.00	29.00	30.329	stopping
40.00	29.00	29.109	stopping
41.00	29.00	29.179	stopping

42.00	29.00	27.847	stopping
0.00	30.00	424.790	stopping
1.00	30.00	335.470	falling
2.00	30.00	445.560	stopping
3.00	30.00	378.950	falling
4.00	30.00	454.200	falling
5.00	30.00	333.330	falling
6.00	30.00	370.890	stopping
7.00	30.00	330.280	falling
8.00	30.00	363.810	falling
9.00	30.00	260.130	falling
10.00	30.00	261.850	falling
11.00	30.00	228.560	falling
12.00	30.00	280.370	stopping
13.00	30.00	398.880	falling
14.00	30.00	314.530	falling
15.00	30.00	273.070	falling
16.00	30.00	274.240	falling
17.00	30.00	443.200	falling
18.00	30.00	223.920	falling
19.00	30.00	340.240	falling
20.00	30.00	517.700	falling
21.00	30.00	341.380	falling
22.00	30.00	481.620	falling
23.00	30.00	298.280	stopping
24.00	30.00	285.180	falling
25.00	30.00	442.310	stopping
26.00	30.00	343.790	stopping
27.00	30.00	365.500	stopping
28.00	30.00	443.800	stopping
29.00	30.00	115.940	stopping
30.00	30.00	99.687	stopping
31.00	30.00	62.897	stopping
32.00	30.00	38.388	stopping
33.00	30.00	39.562	stopping
34.00	30.00	38.544	stopping
35.00	30.00	33.919	stopping
36.00	30.00	30.986	stopping
37.00	30.00	32.032	stopping
38.00	30.00	31.694	stopping
39.00	30.00	30.584	stopping
40.00	30.00	30.803	stopping

41.00	30.00	28.486	stopping
42.00	30.00	27.764	stopping
0.00	31.00	460.950	stopping
1.00	31.00	420.180	stopping
2.00	31.00	330.120	falling
3.00	31.00	359.020	stopping
4.00	31.00	442.770	falling
5.00	31.00	377.030	falling
6.00	31.00	398.300	falling
7.00	31.00	326.580	falling
8.00	31.00	352.760	stopping
9.00	31.00	267.650	falling
10.00	31.00	239.090	falling
11.00	31.00	315.960	falling
12.00	31.00	279.130	falling
13.00	31.00	363.280	falling
14.00	31.00	307.250	stopping
15.00	31.00	265.930	falling
16.00	31.00	260.560	falling
17.00	31.00	317.530	falling
18.00	31.00	338.900	falling
19.00	31.00	346.440	falling
20.00	31.00	375.620	falling
21.00	31.00	376.630	falling
22.00	31.00	305.440	falling
23.00	31.00	299.960	falling
24.00	31.00	291.200	falling
25.00	31.00	417.070	falling
26.00	31.00	451.560	stopping
27.00	31.00	453.860	stopping
28.00	31.00	435.170	stopping
29.00	31.00	80.899	stopping
30.00	31.00	60.121	stopping
31.00	31.00	66.192	stopping
32.00	31.00	39.195	stopping
33.00	31.00	35.917	stopping
34.00	31.00	37.747	stopping
35.00	31.00	33.842	stopping
36.00	31.00	33.984	stopping
37.00	31.00	31.010	stopping
38.00	31.00	31.223	stopping
39.00	31.00	30.793	stopping

40.00	31.00	29.384	stopping
41.00	31.00	29.603	stopping
42.00	31.00	28.089	stopping
0.00	32.00	748.120	stopping
1.00	32.00	680.860	falling
2.00	32.00	463.980	falling
3.00	32.00	249.650	falling
4.00	32.00	355.800	stopping
5.00	32.00	333.500	falling
6.00	32.00	429.210	falling
7.00	32.00	360.160	falling
8.00	32.00	262.270	stopping
9.00	32.00	284.730	falling
10.00	32.00	296.690	falling
11.00	32.00		falling
12.00	32.00	395.680	falling
13.00	32.00	427.130	stopping
14.00	32.00	401.190	falling
15.00	32.00	381.450	falling
16.00	32.00	250.510	falling
17.00	32.00	271.370	falling
18.00	32.00	263.190	stopping
19.00	32.00	607.940	falling
20.00	32.00	304.640	falling
21.00	32.00	343.080	falling
22.00	32.00	340.830	falling
23.00	32.00	190.740	falling
24.00	32.00	308.500	falling
25.00	32.00	293.020	falling
26.00	32.00	289.710	stopping
27.00	32.00	172.310	stopping
28.00	32.00	172.210	stopping
29.00	32.00	507.850	stopping
30.00	32.00	84.191	stopping
31.00	32.00	56.220	stopping
32.00	32.00	45.431	stopping
33.00	32.00	36.802	stopping
34.00	32.00	36.899	stopping
35.00	32.00	34.616	stopping
36.00	32.00	33.194	stopping
37.00	32.00	31.450	stopping
38.00	32.00	30.700	stopping

39.00	32.00	31.096	stopping
40.00	32.00	29.165	stopping
41.00	32.00	29.522	stopping
42.00	32.00	26.360	stopping
0.00	33.00	844.930	stopping
1.00	33.00	455.690	stopping
2.00	33.00	443.200	falling
3.00	33.00	401.970	falling
4.00	33.00	344.670	falling
5.00	33.00	263.830	stopping
6.00	33.00	333.530	falling
7.00	33.00	246.670	falling
8.00	33.00	299.370	stopping
9.00	33.00	347.210	falling
10.00	33.00	392.830	falling
11.00	33.00	247.510	falling
12.00	33.00	361.050	stopping
13.00	33.00	311.590	stopping
14.00	33.00	282.100	falling
15.00	33.00	363.980	falling
16.00	33.00	358.330	falling
17.00	33.00	237.920	falling
18.00	33.00	245.420	falling
19.00	33.00	400.570	falling
20.00	33.00	322.040	falling
21.00	33.00	360.500	falling
22.00	33.00	362.020	falling
23.00	33.00	322.270	falling
24.00	33.00	557.980	falling
25.00	33.00	389.060	stopping
26.00	33.00	347.150	stopping
27.00	33.00	455.220	stopping
28.00	33.00	422.020	stopping
29.00	33.00	47.287	stopping
30.00	33.00	47.120	stopping
31.00	33.00	41.184	stopping
32.00	33.00	35.839	stopping
33.00	33.00	36.964	stopping
34.00	33.00	33.028	stopping
35.00	33.00	34.162	stopping
36.00	33.00	33.476	stopping
37.00	33.00	32.715	stopping

38.00	33.00	31.708	stopping
39.00	33.00	31.913	stopping
40.00	33.00	30.991	stopping
41.00	33.00	26.873	stopping
42.00	33.00	29.142	stopping
0.00	34.00	786.500	stopping
1.00	34.00	752.960	stopping
2.00	34.00	715.450	stopping
3.00	34.00	369.090	stopping
4.00	34.00	345.230	
5.00	34.00	350.210	stopping
6.00	34.00	415.730	stopping
7.00	34.00	251.190	stopping
8.00	34.00	356.820	stopping
9.00	34.00	324.420	stopping
10.00	34.00	251.350	stopping
11.00	34.00	374.480	stopping
12.00	34.00	370.340	stopping
13.00	34.00	327.080	stopping
14.00	34.00	324.310	stopping
15.00	34.00	355.200	stopping
16.00	34.00	370.660	stopping
17.00	34.00	172.130	stopping
18.00	34.00	258.150	stopping
19.00	34.00	350.160	stopping
20.00	34.00	346.680	stopping
21.00	34.00	437.340	stopping
22.00	34.00	353.570	stopping
23.00	34.00	332.880	stopping
24.00	34.00	289.590	stopping
25.00	34.00	300.580	stopping
26.00	34.00	278.610	stopping
27.00	34.00	435.810	stopping
28.00	34.00	375.030	stopping
29.00	34.00	73.340	stopping
30.00	34.00	43.658	stopping
31.00	34.00	42.952	stopping
32.00	34.00	45.589	stopping
33.00	34.00	36.233	stopping
34.00	34.00	35.564	stopping
35.00	34.00	33.016	stopping
36.00	34.00	34.037	stopping

37.00	34.00	33.172	stopping
38.00	34.00	30.971	stopping
39.00	34.00	31.989	stopping
40.00	34.00	31.259	stopping
41.00	34.00	30.197	stopping
42.00	34.00	29.375	stopping
0.00	35.00	158.730	stopping
1.00	35.00	535.470	stopping
2.00	35.00	989.270	stopping
3.00	35.00	568.090	falling
4.00	35.00	582.980	stopping
5.00	35.00	369.930	stopping
6.00	35.00	349.650	falling
7.00	35.00	339.530	falling
8.00	35.00	379.630	falling
9.00	35.00	295.240	falling
10.00	35.00	356.220	falling
11.00	35.00	285.170	stopping
12.00	35.00	277.400	falling
13.00	35.00	242.170	falling
14.00	35.00	265.600	falling
15.00	35.00	410.950	falling
16.00	35.00	270.480	falling
17.00	35.00	271.250	falling
18.00	35.00	255.590	falling
19.00	35.00	439.020	falling
20.00	35.00	424.860	falling
21.00	35.00	236.590	falling
22.00	35.00	328.090	falling
23.00	35.00	464.580	stopping
24.00	35.00	321.430	falling
25.00	35.00	374.790	falling
26.00	35.00	400.690	falling
27.00	35.00	480.070	stopping
28.00	35.00	393.270	stopping
29.00	35.00	505.920	stopping
30.00	35.00	86.903	stopping
31.00	35.00	36.001	stopping
32.00	35.00	64.078	stopping
33.00	35.00	36.195	stopping
34.00	35.00	34.683	stopping
35.00	35.00	34.666	stopping

36.00	35.00	34.783	stopping
37.00	35.00	33.434	stopping
38.00	35.00	33.281	stopping
39.00	35.00	32.601	stopping
40.00	35.00	29.617	stopping
41.00	35.00	30.461	stopping
42.00	35.00	29.200	stopping
0.00	36.00	188.000	stopping
1.00	36.00	236.080	stopping
2.00	36.00	630.790	stopping
3.00	36.00	1028.200	stopping
4.00	36.00	399.640	stopping
5.00	36.00	533.930	falling
6.00	36.00	366.390	stopping
7.00	36.00	458.990	stopping
8.00	36.00	341.030	stopping
9.00	36.00	390.110	falling
10.00	36.00	335.490	stopping
11.00	36.00	347.470	falling
12.00	36.00	337.070	falling
13.00	36.00	329.800	falling
14.00	36.00	327.360	falling
15.00	36.00	363.360	falling
16.00	36.00	336.260	falling
17.00	36.00	229.430	stopping
18.00	36.00	253.420	falling
19.00	36.00	389.200	stopping
20.00	36.00	333.050	falling
21.00	36.00	327.690	falling
22.00	36.00	436.230	falling
23.00	36.00	334.380	falling
24.00	36.00	339.750	stopping
25.00	36.00	376.620	falling
26.00	36.00	478.020	stopping
27.00	36.00	307.060	stopping
28.00	36.00	82.563	stopping
29.00	36.00	89.167	stopping
30.00	36.00	40.089	stopping
31.00	36.00	38.263	stopping
32.00	36.00	38.195	stopping
33.00	36.00	38.176	stopping
34.00	36.00	35.606	stopping

35.00	36.00	35.471	stopping
36.00	36.00	35.781	stopping
37.00	36.00	34.169	stopping
38.00	36.00	33.059	stopping
39.00	36.00	31.039	falling
40.00	36.00	27.131	stopping
41.00	36.00	28.329	stopping
42.00	36.00	28.000	stopping